University of Pennsylvania
ScholarlyCommons

Publicly Accessible Penn Dissertations

1-1-2013

# PDT in the Thoracic Cavity: Spectroscopic Methods and Fluence Modeling for Treatment Planning

Julia Meo
*University of Pennsylvania*, meo.julia@gmail.com

Follow this and additional works at: http://repository.upenn.edu/edissertations

 Part of the Optics Commons

Recommended Citation
Meo, Julia, "PDT in the Thoracic Cavity: Spectroscopic Methods and Fluence Modeling for Treatment Planning" (2013). *Publicly Accessible Penn Dissertations*. 898.
http://repository.upenn.edu/edissertations/898

This paper is posted at ScholarlyCommons. http://repository.upenn.edu/edissertations/898
For more information, please contact libraryrepository@pobox.upenn.edu.

# PDT in the Thoracic Cavity: Spectroscopic Methods and Fluence Modeling for Treatment Planning

**Abstract**
PDT for the thoracic cavity provides a promising cancer treatment modality, but improvements in treatment planning, particularly in PDT dosimetry, can be made to improve uniformity of light delivery. When a cavity of arbitrary geometry is illuminated, the fluence increases due to multiple-scattered photons, referred to as the Integrating Sphere Effect (ISE). Current pleural PDT treatment protocol at the University of Pennsylvania monitors light fluence (hereafter simply fluence, measured in W/cm2) via seven isotropic detectors sutured at different locations in thoracic cavity of a patient. This protocol monitors light at discrete locations, but does not provide a measurement of fluence for the thoracic cavity as a whole. Current calculation of light fluence includes direct light only and thus does not account for the unique optical properties of each tissue type present, which in turn affects the accuracy of the calculated light distribution in the surrounding tissue and, in turn, the overall cell death and treatment efficacy.

Treatment planning for pleural PDT can be improved, in part, by considering the contribution of scattered light, which is affected by the two factors of geometry and in vivo optical properties. We expanded the work by Willem Star in regards to the ISE in a spherical cavity. A series of Monte Carlo (MC) simulations were run for semi-infinite planar, spherical, and ellipsoidal geometries for a range of optical properties. The results of these simulations are compared to theory and numerical solutions for fluence in the cavity and at the cavity-medium boundary. The development via MC simulations offers a general method of calculating the required light fluence specialized to each patient, based on the treatment surface area.

The scattered fluence calculation is dependent on in vivo optical properties (μa and μs') of the tissues treated. Diffuse reflectance and fluorescence spectroscopy methods are used to determine the optical properties and oxygenation (reflectance measurements) and drug concentration (fluorescence measurements) of different tissues in vivo, before and after treatment, in patients enrolled the Phase I HPPH study ongoing at the University of Pennsylvania.

This work aims to provide the building blocks essential to pleural PDT treatment planning by more accurately calculating the required fluence using a model that accounts for the effects of treatment geometry and optical properties measured in vivo.

**Degree Type**
Dissertation

**Degree Name**
Doctor of Philosophy (PhD)

**Graduate Group**
Physics & Astronomy

**First Advisor**
Timothy C. Zhu

This dissertation is available at ScholarlyCommons: http://repository.upenn.edu/edissertations/898

**Second Advisor**
Jarod C. Finlay

**Keywords**
PDT, Radiative Transport, Spectroscopy

**Subject Categories**
Optics | Physics

This dissertation is available at ScholarlyCommons: http://repository.upenn.edu/edissertations/898

PDT IN THE THORACIC CAVITY:
SPECTROSCOPIC METHODS AND FLUENCE MODELING FOR TREATMENT PLANNING

Julia Lauren Meo

A DISSERTATION

in

Physics and Astronomy

Presented to the Faculties of the University of Pennsylvania

in

Partial Fulfillment of the Requirements for the

Degree of Doctor of Philosophy

2013

Supervisor of Dissertation

Timothy C. Zhu, Ph.D.
Professor of Radiation Oncology
Adjunct Associate Professor of Physics

Co-Supervisor of Dissertation

Jarod C. Finlay, Ph.D.
Assistant Professor of Radiation Oncology
Adjunct Assistant Professor of Physics

Graduate Group Chairperson

Randall Kamien
*Vicki and William Abrams Professor in the Natural Sciences*

Dissertation Committee:

Dr. Arjun Yodh, Professor of Physics

Dr. James Aguirre, Assistant Professor of Physics

Dr. Mark Goulian, Professor of Physics

Dr. Joel Karp, Professor of Physics

# DEDICATION

*To my parents for their endless love and support, and to my husband, Nick, for his patience and confidence in me.*

# ABSTRACT

PDT IN THE THORACIC CAVITY: SPECTROSCOPIC METHODS AND FLUENCE MODELING FOR TREATMENT PLANNING

Julia L. Meo

Dr. Timothy C. Zhu

Dr. Jarod C. Finlay

PDT for the thoracic cavity provides a promising cancer treatment modality, but improvements in treatment planning, particularly in PDT dosimetry, can be made to improve uniformity of light delivery. When a cavity of arbitrary geometry is illuminated, the fluence increases due to multiple-scattered photons, referred to as the Integrating Sphere Effect (ISE). Current pleural PDT treatment protocol at the University of Pennsylvania monitors light fluence (hereafter simply fluence, measured in $W/cm^2$) via seven isotropic detectors sutured at different locations in thoracic cavity of a patient. This protocol monitors light at discrete locations, but does not provide a measurement of fluence for the thoracic cavity as a whole. Current calculation of light fluence includes direct light only and thus does not account for the unique optical properties of each tissue type present, which in turn affects the accuracy of the calculated light distribution in the surrounding tissue and, in turn, the overall cell death and treatment efficacy.

Treatment planning for pleural PDT can be improved, in part, by considering the contribution of scattered light, which is affected by the two factors of geometry and in vivo optical properties. We expanded the work by Willem Star in regards to the ISE in a spherical cavity. A series of Monte Carlo (MC) simulations were run for semi-infinite planar, spherical, and

ellipsoidal geometries for a range of optical properties. The results of these simulations are compared to theory and numerical solutions for fluence in the cavity and at the cavity-medium boundary. The development via MC simulations offers a general method of calculating the required light fluence specialized to each patient, based on the treatment surface area.

The scatter fluence calculation is dependent on in vivo optical properties ($\mu_a$ and $\mu_s$') of the tissues treated. Diffuse reflectance and fluorescence spectroscopy methods are used to determine the optical properties and oxygenation (reflectance measurements) and drug concentration (fluorescence measurements) of different tissues in vivo, before and after treatment, in patients enrolled the Phase I HPPH study ongoing at the University of Pennsylvania.

This work aims to provide the building blocks essential to pleural PDT treatment planning by more accurately calculating the required fluence using a model that accounts for the effects of treatment geometry and optical properties measured in vivo.

# Table of Contents

# List of Tables

# List of Figures

# Chapter 1

# Introduction

## 1.1 Photodynamic Therapy

Photodynamic therapy (PDT) is a cancer treatment modality that consists of light, a photosensitizing drug, and singlet oxygen, $^1O_2$, to cause local cell damage as a method of killing cancerous tissues. PDT has been applied to a wide variety of cancers including cancers of the bladder[1-8], the prostate[9-24], and of the head and neck[25]. While still in development to become a common cancer treatment, PDT is already FDA approved for skin[26-31], esophageal[32], bladder [1-8], and ophthalmic cancers[33]. PDT is a localized treatment method, unlike systemic chemotherapy, sparing healthy cells. Unlike radiation therapy, using ionizing radiation, it does not cause long term cumulative damage to the patient as it does not appear to target DNA [34]. The advantages of PDT are clear but much work needs to be done in optimizing treatment doses, PDT delivery methods, and PDT dosimetry before it can become a standard cancer treatment option to patients with a variety of malignancies.

Current PDT treatment protocol for pleural PDT at the Hospital of the University of Pennsylvania (UPHS) is to administer a photosensitizing drug to the patient, either systematically at the appropriate time before surgery and light application. This is referred to as the drug-light interval. Light at a drug specific wavelength is then administered to the cancerous region on the patient's body after the drug-light interval has passed. This light administration in combination with the photosensitizer activates a reactive singlet oxygen species $^1O_2$, causing local cell damage thereby killing the cancerous tissue. At the UPHS, the fluence, or light dose, for pleural PDT is administered at a predetermined dose and is not dependent on the unique qualities of the patient for thoracic cavity treatment[35]. Fluence is monitored, in the instance of PDT for the thoracic cavity, by isotropic detectors sutured to the patient's thoracic cavity by the surgeon. Once these detectors indicate the prescribed total light dose is reached, the light source is turned off, and PDT is considered complete.

### *1.1.1 Photosensitizers*

The development of photosensitizers is ongoing, with sensitivity designed to be in the "therapeutic window" (650-850 nm) where the hemoglobin spectrum does not dominate (see Figure 1.1). In this window, for light sources whose wavelength is between 650-850 nm, light penetrates deeper into the tissue as optical absorption is lower than in other parts of the spectrum, reaching a greater area of tissue and causing more cell death overall. In this work, we consider two photosensitizers: benzoporphyrin derivative monoacid (BPD) and 2-[1-hexyloxyethyl]-2-devinyl pyropheophorbide-a (HPPH).

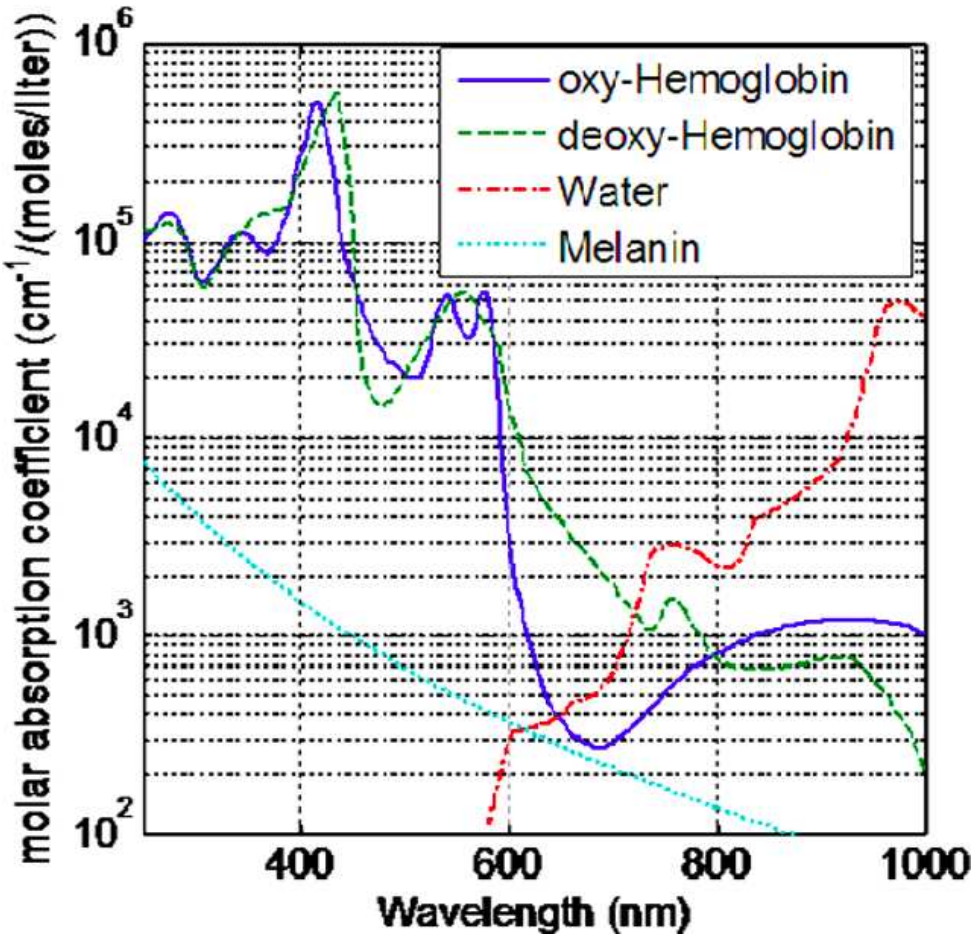


Figure 1.1: Molar absorption coefficients of common absorbents.

Note the relative dip in absorption between 600 and 800 nm; this is the “therapeutic window”.

As Allison et al. state in their review of photosensitizers[36], the ideal photosensitizer would possess low toxicity, reliable activation at longer wavelengths (above 630 nm), short sensitivity to sunlight, low cost, and good availability. The first generation of photosensitizers was porphyrin based, as is the BPD used here in the canine study. Porphyrin based photosensitizer development began in the 1970s and early 1980s. Second generation porphyrin photosensitizers, such as BPD, are porphyrin derivatives or synthetics. Another class of photosensitizers are chlorin based, such as the HPPH used in the Phase I UPHS HPPH study

presented in this work. Each family of photosensitizers has its advantages and disadvantages, depending on the type of tissue they are intended to treat. Photosensitizer development is ongoing, striving to find a drug that meets the requirements of an ideal photosensitizer.

BPD is a second generation, porphryin-based photosensitizer. Its activation wavelength is 690 nm, allowing for greater light penetration depth than many first generation photosensitizers, whose activation wavelength was lower in the spectrum. It has a relatively short period of light sensitivity (4-5 days), allowing patients to recover from acute photosensitivity. A study of BPD as treatment for peritoneal carcinomatosis in canines was conducted at UPHS. This study evaluated 15 canines with varying photosensitizer dose as well as varying light fluence. The work presented here focuses on the spectroscopic methods used during this study; obtaining optical properties, hemoglobin levels, oxygenation and photosensitizer concentration of the canine intraperitoneal cavity.

The second photosensitizer we consider, HPPH, is a chlorin-based photosensitizer that has an absorption peak at 665 nm. It has been used to treat head and neck, esophageal, and lung cancers[37]. Currently, there is a Phase I study being conducted at UPHS and Roswell Park Cancer Institute, treating patients with malignant pleural mesothelioma (MPM) using HPPH. This thesis uses measurements of optical properties, fluence, and source position data from this ongoing study.

### *1.1.2 PDT and optical properties*

PDT efficacy is dependent on several factors. Drug uptake, light distribution in tissue, and the geometry of the treatment region all affect the amount of cell damage that occurs. Light distribution in tissue, depends in part on the absorption coefficient ($\mu_a$) and the reduced

scattering coefficient ($\mu_s'$), of the tissue being treated. The absorption coefficient is defined as the probability of photon absorption per unit distance and is measured in $cm^{-1}$. The scattering coefficient, $\mu_s$, is the probability of photon scattering per unit distance in $cm^{-1}$. The reduced scattering coefficient then is defined by $\mu_s'=\mu_s(1-g)$ where *g* is the mean cosine of the phase function. By measuring these optical properties we are able to better determine what incident light irradiance is needed for optimum treatment using the appropriate fluence model. The geometry of the treatment region affects light distribution as well. Current protocol assumes all treatment regions are planar and semi-infinite. PDT in cavity geometry, however, experiences an increase in fluence caused by light reflecting off the cavity walls. By obtaining knowledge of in ivo optical properties and correctly modeling the fluence in the treatment region, more uniform light fluence can be achieved.

## 1.2 Malignant Pleural Mesothelioma

### *1.2.1 A brief introduction to lung cancers*

Pleural cancers, including malignant pleural mesothelioma (MPM), non-small cell lung cancer, and early small cell lung cancer, are historically difficult to treat and offer a prognosis of 6 to 15 months[38]. Primary pleural cancers are rare, with mesothelioma being the most common. The source of malignant mesothelioma lies in the lining cells of the pleura and peritoneal cavities[39]. Naturally occurring MPM is rare but exposure to asbestos, which was used heavily in construction post World War II, increase the risk to developing MPM. Asbestos use was largely abandoned in the Western World during the 1980s, but the long latency of MPM (15 to 60 years)[39] means the instances of MPM continue to rise, particularly among men.

The difficulty in treating MPM lies in the ability of the treatment team to eradicate all cancerous cells from the pleural cavity, as MPM often demonstrates widespread local

disease[34, 40]. There is no standard treatment for pleural cancers [38, 41] though treatment often begins with a surgical resection of the lung, parietal pleura, and the ipsilateral diaphragm and pericardium [38]. While this procedure is vital in removing the bulk of the cancerous tissue, it is impossible to remove this tissue without leaving behind a quantity of cancer cells in the thoracic cavity [41]. Consequently, several different treatment modalities are being investigated which combine surgical debulking with a follow-up treatment to kill off remaining cancer cells. These modalities include chemotherapy, radiation therapy, and PDT. Chemotherapy, both systematic and intrapleural, has not shown to eradicate cancer cells significantly, and radiation therapy is limited in its application because of the need to spare nearby vital organs such as the liver and remaining lung[38].

### *1.2.2 PDT as a treatment modality for MPM*

PDT, by consequence of its limited light penetration into the tissue, is able to spare these vital organs and sterilize remaining cancer cells. It offers a promising treatment option to pleural cancer patients, particularly when coupled with the traditional methods of cancer treatment as it does not present additional toxicities to affect the original treatment plan [41]. In 1996, a Phase III trial was completed using the photosensitizer Photofrin to treat MPM[39]. The study found that for surgeries where complete macroscopic resection was performed in conjunction with PDT, the mean survival time was approximately 36 months, whereas in patients where incomplete resection and PDT were performed the mean survival time was about 12 months. With the development of second-generation photosensitizers and complete resection, PDT applied to MPM offers a strong treatment method. The work presented here utilizes data collected during the ongoing Phase I HPPH study, using mediated PDT to treat MPM. In

particular, observations of optical properties and drug concentration are considered during treatment.

### 1.3 Infrared Navigation System for Treatment

In this work, we present the development of a novel method to guide the PDT treatment in order to achieve more uniform distribution of light fluence. Within the thoracic cavity, the light delivery is continuously administered by a moving point source applied by the clinician. We introduce a real-time infrared (IR) tracking camera to track the movement of the light source. The same tracking device is also used to determine the surface contour of the treatment area at the beginning of PDT treatment (see Figure 1.2). It is at this point in the PDT treatment where real-time dosimetry guidance becomes most critical. As the clinician applies the light source, the knowledge of how well each particular area of the thoracic cavity is irradiated has the potential to make the entire treatment process more effective and efficient. The light source position data gathered by this system is then applied to the fluence model we developed for a cavity geometry and is displayed on screen as a fluence map, to be used for the clinician's guidance in applying the light source (see Figure 1.3).

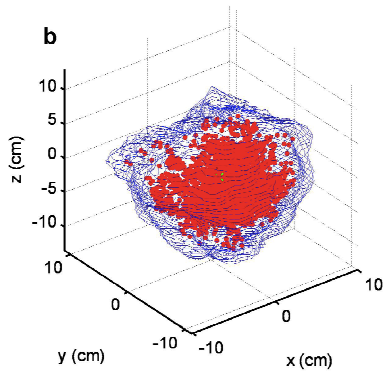


Figure 1.2: Contour of torso shaped phantom with IR tracking data.

A contour is first taken of the perimeter of the phantom. Position data of the moving light sources (denoted by the red circles) is gathered via the IR tracking system[42].

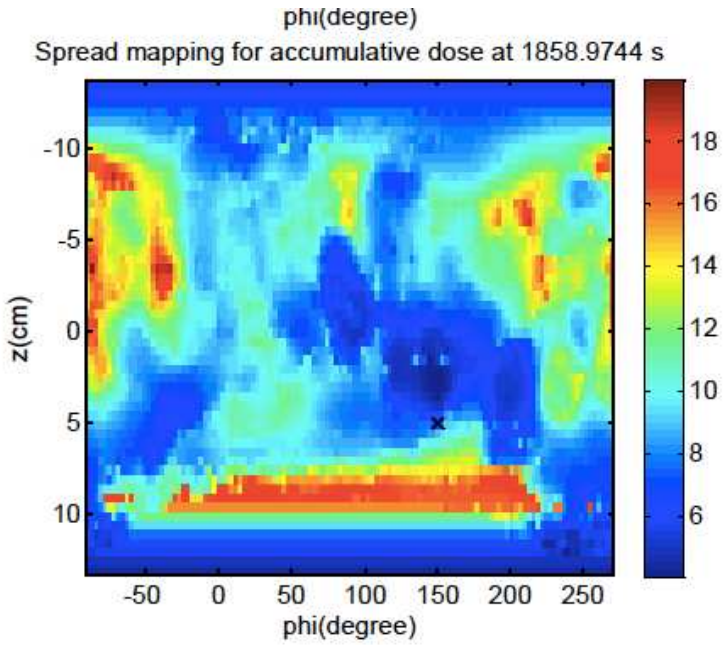


Figure 1.3: Calculated light fluence using IR tracking data

Calculated light fluence using IR tracking data in a human torso-shaped phantom. The black **x** marks the location of the isotropic detector, monitoring the fluence as current standard protocol dictates.[42]

## 1.4 Light Propagation and PDT

In PDT, the degree of cancerous cell death is dependent, in part, on how much light is able to reach the targeted tissue. Light transport in biological matter is governed primarily by the scattering and absorption of photons. These properties are characterized by the absorption coefficient, $\mu_a$ and the reduced scattering coefficient, $\mu_s'$.

### *1.4.1 Radiative transport model*

This light propagation is described by a series of equations and boundary conditions known as diffusion theory of light transport. The radiative transport equation (RTE), which will be further discussed in section 2.1, can be solved using several different approximations. We focus on the diffusion approximation as a solution to the RTE. The diffusion approximation first assumes the number of photon scattering events is much greater than the number of photon

absorption events ($\mu_s$'>>$\mu_a$). This is a reasonable assumption in most biological tissues in the near infrared range (NIR) (see Section 2.8). A full treatment of the diffusion approximation is discussed in Section 2.2. The diffusion approximation solution is dependent on the optical properties of the tissue as well as the geometry of the treatment area.

### *1.4.2 Monte Carlo Simulations*

Where the diffusion approximations fails, namely when $\mu_s$' is not much greater than $\mu_a$ or where the change in current density is greater than one mean free path, or the asymmetric light scattering is important, other methods can be applied to solve for the light distribution in the tissue. We use Monte Carlo (MC) simulations (Section 3.4-3.7), a common method of fluence modeling[43, 44] . MC simulations are based on the random walks of photons traveling through a medium.

In these simulations we control the geometry, number of photons, and optical properties of the system. The weight of the photon changes as each photon progresses via a uniformly distributed random number generator after each scattering and absorption interaction. By tracking the photons throughout the simulation we determine the total fluence, direct light fluence, and scattered light fluence in the tissue. The results of the MC simulation are then compared to the fluence calculated by the diffusion approximation solution or empirical solution. We consider several different boundary conditions, tissue optical properties, the properties of the medium inside the cavity, attenuation, and geometries to simulate treatment conditions during PDT.

## 1.5 Light Fluence Distribution and PDT Dosimetry

### *1.5.1 PDT dosimetry*

PDT dosimetry, the measurement of photodynamic effect in tissue, is dependent not only on the light distribution in the target tissue but also on the oxygenation of the tissue and drug uptake of the target tissue[35, 45-48]. The current treatment protocol for both the BPD canine study and the Phase I HPPH study, however, specifies only the total incident light fluence and amount of photosensitizer administered[23, 32, 49] and does not account for the effects of overall drug uptake and oxygenation unique to each patient and each tissue type, nor does this protocol account for how the fluence changes in the tissue, versus fluence measured at the surface of the tissue. Currently there are two methods used in these studies to perform PDT dosimetry: a detector sutured into the tissue to measure fluence directly and a probe placed at the surface of the tissue to measure optical properties and/or tissue oxygenation and drug uptake and use these measurements to calculate fluence using an appropriate mathematical model post treatment[45]. Of course, it is optimal to minimize the trauma experienced by the tissue, making the noninvasive measurement of fluence more desirable for clinical applications. But this method needs to be developed such that it provides light dose in real-time, specified by the unique characteristics of the patient.

### *1.5.2 Fluence based Dosimetry*

The fluence at some depth in tissue is modeled by several methods. The foremost method, the diffusion approximation (see Section 2.2), is applied to fluence calculations often and is a function of $\mu_a$ and $\mu_s'$ and position. The diffusion approximation is not accurate near the tissue boundary; a distance of 1 mm or greater from the boundary is where this approximation holds. Other solutions are available to us, but are still dependent on $\mu_a$ and $\mu_s'$. Section 2.6 will go into further detail about methods used to determine these optical properties, but several

assumptions are made to model fluence. First, while biological tissues are known to be inhomogeneous, we assume them to be homogeneous in our models. Second, *ex vivo* measurements of $\mu_a$ and $\mu_s'$ are not necessarily equivalent to *in vivo* measurements of the same tissue. It is important, therefore, to obtain characteristic ranges of optical properties *in vivo* for fluence calculations. The $P_3$ approximation is advantageous to use when the diffusion approximation does not hold, eg. measurements close to the light source or where absorption is high. By measuring the optical properties using spectroscopic methods we can estimate how much light reaches tissues at certain depths and inform overall PDT dose.

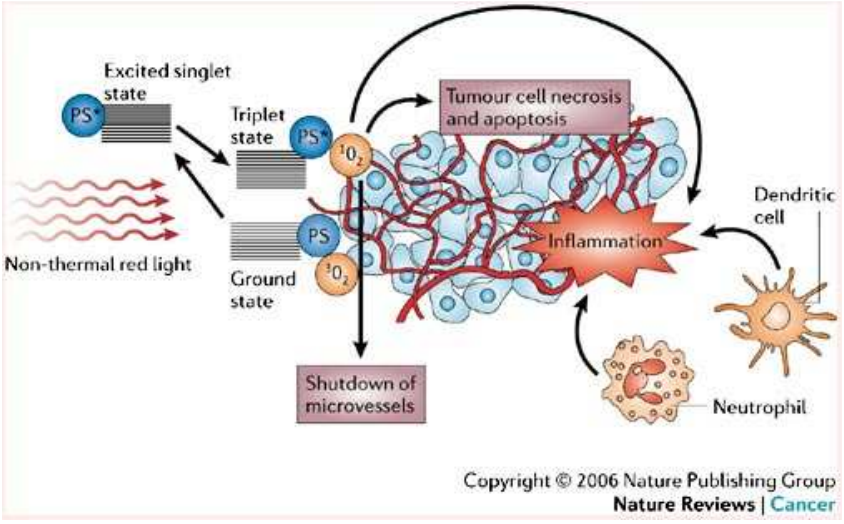


Figure 1.4: An Illustration of PDT Cytoxic effect

The photosensitizer (PS) absorbs light and an electron moves to the first short-lived excited singlet state. This is followed by intersystem crossing, in which the excited electron changes its spin and produces a longer-lived triplet state. The PS triplet transfers energy to ground-state triplet oxygen, which produces reactive singlet oxygen ($^1O_2$). $^1O_2$ can directly kill tumor cells by the induction of necrosis and/or apoptosis, can cause destruction of tumor vasculature and produces an acute inflammatory response[50].

### *1.5.3 Oxygenation and PDT*

The oxygenation levels of tissues are also an important factor in PDT dosimetry[23, 35, 51, 52]. The relationship between the PDT cytotoxic effect and singlet oxygen, $^1O_2$, is complex.

The photosensitizer begins in its ground state in a spectroscopic singlet, $S_0$. When light is absorbed, the molecules of photosensitizer are excited to their first singlet state, $S_1$. In the process of de-excitation, it transitions to the triplet state $T_1$ and then transfers energy to a $^3O_2$ molecule. This creates an extra $^1O_2$ molecule as the photosensitizer returns to its ground state. This process occurs many times, creating many $^1O_2$. It is the interaction of the $^1O_2$ with cellar targets that induce the cytotoxic effect (see Figure 1.4). Clearly, PDT requires the presence of oxygen to cause cell damage. If the treatment light intensity is too high, it may cause the tissue to become hypoxic, reducing the oxygen available to PDT. Monitoring the oxygenation of tissues during treatment helps to inform overall treatment outcome. Oxygenation in this work is monitored using spectroscopic methods *in vivo* (see Section 3.3). Blood carries oxygen to tissues, thus tissues with a higher blood supply, such as the liver, may be more susceptible to PDT than tissues without a rich blood supply. Shielding sensitive organs during treatment becomes important in the overall administration of PDT.

### *1.5.4 Photosensitizer uptake and dosimetry*

Finally, the drug uptake, unique to each patient and each tissue type, is another important factor in calculating accurate PDT dose. Because $\mu_a$ and $\mu_s$' are highly heterogeneous between different tissues types and between patients, the amount of drug absorbed can vary significantly. Photosensitizers used in PDT have a characteristic fluorescence signal[45] that can be observed during treatment. Photobleaching, which can occur during treatment, is defined as the destruction of fluorophores in the target tissue induced by irradiation. This destruction is mediated predominately by $^1O_2$ [35, 53, 54] for type II photosensitizers, destroying photosensitizer molecules. Spectroscopic fluorescence measurements (see Section 2.7) of a tissue before illumination will indicate the presence of the photosensitizer. Measurements

made during and after illumination may show a decrease in the amplitude of the fluorescent signal. By monitoring this signal, photobleaching may be observed and indicates the cytoxic effect has occurred. Many groups are monitoring the fluorescent signal of the photosensitizer in studies[23, 51, 52, 55, 56], and several are using this method in clinic[57, 58].

## 1.6 Spectroscopy

### *1.6.1 Diffuse reflectance spectroscopy*

Diffuse reflectance is the light reflected at many different angles off a surface, and the detection of the reflected light can provide information about the light distribution of the medium being studied. Diffuse reflectance spectroscopy is used here to determine the *in vivo* optical properties, $[Hb]_{tot}$, and oxygenation levels. Several different methods of reflectance spectroscopy have been developed, ranging from time-domain spectroscopy[17, 59, 60], frequency-domain spectroscopy[61-65], to continuous wave (CW) spatially-resolved spectroscopy. Using CW spatially-resolved spectroscopy, we determine the absorption and reduced scattering coefficients of tissues by fitting spectra with an algorithm[66], to be discussed in further detail in Section 3.3. Typical absorption and reduced scattering spectra of human tissue in vivo are displayed in Figure 1.5

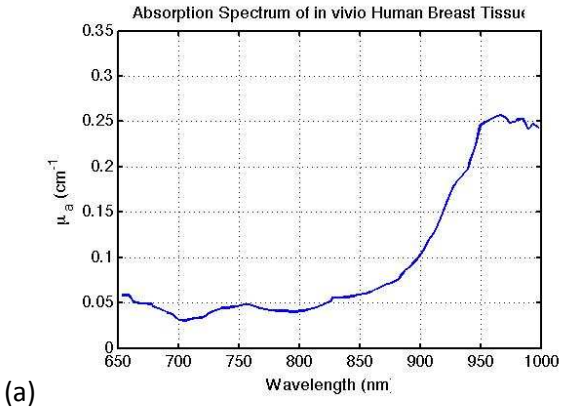


(a)

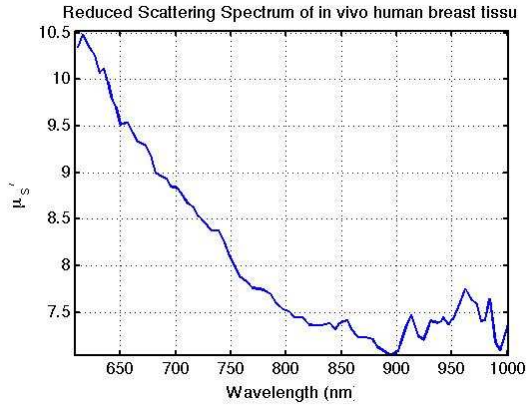


(b)

Figure 1.5: Absorption (a) and reduced scattering (b) spectra of human breast tissue in vivo measured by Cubeddu et al. [67]

The oxygenation of the tissue, important for determining the amount of expected cell death, can also be determined from fitting CW reflectance spectra[68], determining the amount oxygenated hemoglobin [$HbO_2$] and de-oxygenated hemoglobin [Hb] present in the tissue. The reflectance measurements performed for this work determine these properties for a wide variety of organ tissues *in vivo* in canines and humans, helping to further inform our fluence model.

### *1.6.2 Fluorescence spectroscopy*

The photosensitizers administered to the patient each have a characteristic fluorescence spectrum that can be observed via light detectors during surgeries. When some photosensitizers are exposed to its activation wavelength light for an extended period of time, photobleaching can occur and is observable by diffuse fluorescence spectroscopy. Observing photobleaching is one method of monitoring the PDT effect of irradiation of the treatment area[51]. By monitoring the shape of the photosensitizer's spectrum during treatment, we can determine the photodynamic dose[35] implicitly (observe a typical fluorescence spectrum in Figure 1.6).

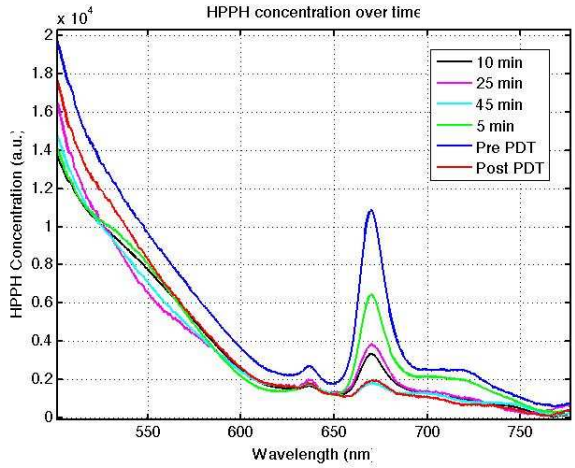


Figure 1.6: Measured fluorescence of HPPH over time

Measured tissue in vivo on a nude mouse. Note the amplitude of pre-PDT fluorescence (blue) to post-PDT fluorescence (red)

The measurements presented in this work were taken before and after treatment. Using the basis spectra of the fluorescence of BPD and HPPH, determined via a series of murine studies, we fit our fluorescence measurements made *in vivo* to determine drug concentration before

and after treatment. This is a useful tool is determining both drug uptake by a variety of tissues and also received light fluence.

### 1.7 Statement of Purpose

PDT treatment planning, particularly light fluence ("light dose" in clinic) calculation, has potential to be improved, and, in turn, improving PDT treatment outcome. When a cavity of arbitrary geometry, such as those observed in the Phase I HPPH study at UPHS, is illuminated, the overall fluence increases due to multiple scattered photons in what is known at the Integrating Sphere Effect (ISE)[5]. Current pleural PDT treatment protocol for treatment of the thoracic cavity at the UPHS monitors fluence discretely in the thoracic cavity of the patient. Light is delivered to the detectors to reach the predetermined prescribed total fluence. This protocol measures the light at discrete locations, and does not give the total fluence received by the whole cavity. Valuable information from in vivo spectroscopy measurements can provide total hemoglobin concentration and oxygenation of the treatment tissue in addition to optical properties.

Light dose calculation for pleural PDT can be improved by considering these two factors of geometry and in vivo spectroscopy data that has not previously been studied in the thoracic cavity and require further exploration.

To more accurately model the light dose in a cavity, we expanded the work presented by Willem Star[69] in regards to the ISE in a spherical cavity. A series of Monte Carlo (MC) simulations were run for semi-infinite planar, spherical, and ellipsoidal geometries for a range of optical properties. The results of these simulations are then compared to the theory as well as numerical solutions for fluence both in the cavity itself and at the cavity-tissue boundary. A

verification of these MC simulations offers a new method of determining the required light dose that is specialized to each treatment volume, shape and optical characteristics. The analytical theory Star presents, which will be derived in section 2.4, is dependent on the in vivo optical properties ($\mu_a$ and $\mu_s'$) of the tissues being treated. The optical properties are highly variable between tissue type and between patients[70]. Here we use spectroscopy methods to determine the in vivo optical properties for the tissues present in the interperitoneal region in canines and in the thoracic cavity in humans.

This thesis, by developing a fluence model for cavity geometries and determining the in vivo optical properties obtained during treatment, presents the tools to improve prescribed light fluence and specialize light dose to each patient in the future. We aim, with this work, to provide the building blocks essential to improving pleural PDT efficacy by more accurately calculating the required light dose using a model that accounts for the ISE and uses optical properties measured in vivo, obtained via spectroscopic measurements. With improved PDT treatment efficacy, the treatment plan and prognosis for patients with MPM has the potential to improve as well.

## 1.8 Outline

The work presented here is organized in the following manner: **Chapter 2** discusses in greater detail the diffusion approximation as applied to light transport in biological tissue. It also provides the theory and background information for the spectroscopic methods used to analyze data for this thesis. **Chapter 3** addresses the instrumentation and fitting algorithms used to obtain the optical properties, oxygenation levels, and drug concentration from diffuse reflectance and fluorescence measurements. The data collected from the BPD canine study and the HPPH Phase I clinical trial is also presented in Chapter 3. **Chapter 4** expands further on

fluence modeling and MC simulations used to calculate the fluence in different geometries. **Chapter 5** discusses the IR navigation system that is in development, which will utilize both the determined optical properties and the fluence model presented here. It is a novel tool, using the modeling developed here in conjunction with an infrared (IR) camera as a fluence tracking system for the clinician's use during pleural PDT. Finally, **Chapter 6** concludes this work by summarizing our findings and discussing future applications of the work completed here.

# Chapter 2

# Theory and Background

## 2.1 Introduction

In order to model light distribution in PDT and also to determine experimentally the properties of the tissues we treat, we must provide a rigorous theoretical description of light propagation in turbid media. This chapter provides the necessary mathematical framework. Section 2.2 describes the diffusion approximation to the radiative transfer equation (RTE) using simple boundary conditions and geometries. Section 2.3 goes further to describe the solution to the RTE when considering a semi-infinite, homogeneous, planar geometry for different approximations to the RTE. Section 2.4 focuses on the work of Star[69] and van Staveren[5] to describe the solution to the RTE in a spherical cavity geometry. Section 2.5 presents the theory behind determining the optical properties using diffuse reflectance measurements. Section 2.6 describes the theory behind the fluorescence measurements that are used for determining PDT

drug concentration. Finally, Section 2.8 presents a review of *in vivo* optical properties determined in human subjects from the literature.

## 2.2 Photon Diffusion Approximation

Radiative transport theory provides a mathematical model for the propagation of neutral particles through scattering and absorbing media. Ignoring the effects of polarization, phase, and inelastic scattering events, the radiance, $L(\mathbf{r},\hat{s}')$, defined as the power per unit area per unit solid angle in direction $\hat{s}$ at position $\mathbf{r}$, is described by the time independent Boltzmann equation [71]:

$$\nabla \cdot L(\vec{r},\hat{s})\hat{s} = -\mu_t L(\vec{r},\hat{s}) + \mu_s \int_{4\pi} L(\vec{r},\hat{s}') f(\hat{s},\hat{s}')\, d\Omega' + S(\vec{r},\hat{s}), \qquad (2.1)$$

where $\mu_t=\mu_a+\mu_s$, the absorption coefficient ($\mu_a$) is the probability of absorption per unit distance and the scattering coefficient ($\mu_s$) is the probability of scattering per unit distance. $S(r,\hat{s})$ represents the source term. The term $f(\hat{s},\hat{s}')$ is the scattering phase function, describing the probability that a photon incident in direction ŝ' will be scattered into direction ŝ. Equation ( 2.1 ) describes the gradient in radiance distribution, where $L(\mathbf{r},\hat{s})$ is decreased by absorption and photons that are scattered away from direction $\hat{s}$ (first term on the right hand side of the equation) and is increased by photons scattered into $\hat{s}$ and by the light source, $S(\mathbf{r},\hat{s})$ (remaining terms). The source term $S(\mathbf{r},\hat{s})$ is represented in a variety of ways, depending the light source used. For planar geometries, the light can be a wide beam with collimated incidence (referred to as a pencil beam or a wide beam with diffuse incidence. For spherical geometries, a point source is most commonly used in models. For cylindrical geometries, a long, linear light source is used. Each of these light sources are represented via appropriate and unique mathematical expressions. The two light sources used in this work are a pencil beam, used in our MC

simulations and later convolved to an isotropic point source for cavity geometries, and a simple isotropic point source.

The scattering phase function *f(ŝ,ŝ')* is assumed to depend only the deflection angle $\theta$ between *s* and *s'*. *f(ŝ,ŝ')* becomes a complicated function in turbid biological media, due to the high particle density and inhomogeneity of tissue. An accepted approximation for *f(ŝ,ŝ')* is the Henyey-Greenstein phase function[72]:

$$f_{HG}(cos\theta) = \left(\frac{1}{4\pi}\right)\frac{1-g^2}{(1+g^2-2gcos\theta)^{3/2}}, \quad (2.2)$$

where the general expression for *g* is the scattering anisotropy, expressed as:

$$g = \int_{4\pi} f(\hat{s},\hat{s}')d\Omega. \quad (2.3)$$

The quantity *g* is equal to the average of the scattering cosine $\theta$. The scattering anisotropy ranges from -1, which indicates backward scattering, to 1, which indicates forward scattering. If *g=0* then the scattering has no net preference for forward or backward scattering. In this work, we assume *g≈0.7-0.9*, accounting for the anisotropic scattering observed in tissue.

Equation ( 2.1 ) is analytically solvable in the instance of one-dimensional, idealized geometries, but these idealized situations are not applicable to calculating the light distribution in real-life experimental situations[71]. While several numerical methods have been employed to solve eqn. ( 2.1 ) for a particular geometry (eg. Kubelka-Munk[73] and Adding-Doubling[74] methods), the spherical harmonic approximation provides a series of approximations to simplify the solution, which expands the radiance and sources terms as a series of spherical harmonics and the scattering phase function as a series of Legendre polynomials:

$$L(\vec{r},\hat{s}) = \sum_{l=0}^{N}\sum_{m=-1}^{l}\sqrt{\frac{2l+1}{4\pi}}\phi_{lm}Y_{lm}(\hat{s}), \quad (2.4a)$$

$$S(\vec{r},\hat{s}) = \sum_{l=0}^{N}\sum_{m=-1}^{l}\sqrt{\frac{2l+1}{4\pi}}\sigma_{lm}Y_{lm}(\hat{s}), \quad (2.4b)$$

$$f(\hat{s}\cdot\hat{s}') = \sum_{l=0}^{N}\frac{2l+1}{4\pi}g_l P_l(\hat{s}\cdot\hat{s}'). \quad (2.4c)$$

The series of equation ( 2.4a ) are truncated at the $N^{th}$ term (referred as the $P_n$ approximation) and are then substituted into eqn. ( 2.1 ). For the diffusion approximation, *N=1*, with *l=0,1*, eqn. ( 2.4a ) becomes:

$$L(\vec{r},\hat{s}) = \frac{1}{4\pi}\phi(\vec{r}) + \frac{3}{4\pi}j(\vec{r})\cdot\hat{s} \quad (2.5a)$$

$$S(\vec{r},\hat{s}) = \frac{1}{4\pi}S_0(\vec{r}) + \frac{3}{4\pi}S_l(\vec{r})\cdot\hat{s}, \quad (2.5b)$$

$$f(\hat{s}\cdot\hat{s}) = \frac{1}{4\pi} + \frac{3}{4\pi}g(\hat{s}\cdot\hat{s}'). \quad (2.5c)$$

The radiance is composed of the fluence rate, $\phi(r)$, and the radiant flux, *F(r)*. The fluence rate is defined as the power incident on an infinitesimal sphere divided by the cross-sectional area of the sphere (eqn. ( 2.6 )), and the radiant flux is defined as the power transferred per unit area (eqn. ( 2.7 )).

$$\phi(\vec{r}) = \int_{4\pi} L(\vec{r}, \hat{s}) d\Omega \quad (2.6)$$

$$\mathrm{F}(\vec{r}) = \int_{4\pi} L(\vec{r}, \hat{s}) \cdot \hat{s} d\Omega \quad (2.7)$$

The divergence of the flux is found by substituting eqn. ( 2.5a ) into eqn. ( 2.1 ) and integrating over all solid angles eqn.( 2.8 ),

$$\nabla \cdot F(\vec{r}) = -\mu_a \phi(\vec{r}) + S_0(\vec{r}) \quad (2.8)$$

Using eqn.( 2.8 ), we can determine the gradient of the fluence by multiplying by $\hat{s}$ and once again integrating over all solid angles:

$$\frac{1}{3}\nabla\phi(\vec{r}) = -\left(\mu_s^{'} + \mu_a\right)F(\vec{r}) + S_1(\vec{r}). \quad (2.9)$$

The quantity $S_1(r)$ is zero everywhere when only isotropic sources are considered. The reduced scattering coefficient, $\mu_s' = (1-g)\mu_s$. Combining eqns. ( 2.8 ) and ( 2.9 ), we arrive at the time-independent diffusion equation for an isotropic source:

$$D\nabla^2\phi(\vec{r}) - \mu_a\phi(\vec{r}) = S_0(\vec{r}) \quad (2.10)$$

Here, $D = 1/3(\mu_a + \mu_s')$, is the diffusion constant. A simplified form of eqn. ( 2.1 ), eqn. ( 2.10 )allows us to solve for $\phi$ given a specified set of boundary conditions and geometry.

## 2.3 Semi-Infinite Approximations for fluence and reflectance

### *2.3.1 Analytic Approximation for a wide, diffuse light source*

Assuming the tissue to be a semi-infinite plane is a common practice for determining the light distribution from a wide, diffuse beam. In order to determine $\phi(r)$, the Green's function

is found as a solution to eqn.( 2.10 ) at some tissue depth $z_0$. We consider first the case where the refractive indices of the non-scattering and tissue match, where there is no photon current back into the tissue. This boundary condition is expressed as[75]:

$$\phi(r) + 2D\hat{n} \cdot \nabla\phi(\vec{r}) = 0 \qquad (2.11)$$

where $\hat{n}$ is a unit normal vector directed into the tissue. To solve eqn. ( 2.10 ) for a semi-infinite plane we use a photon dipole source and an extrapolated boundary condition. Equation ( 2.11 ) is fulfilled by setting the fluence equal to zero at a distance of *2D* above the planar surface (see Fig. 2). For the case of refractive index mismatch between the non-scattering medium and the tissue, the boundary condition is[76]:

$$\phi(\vec{r}) + 2AD\hat{n} \cdot \nabla\phi(\vec{r}) = 0, \qquad (2.12)$$

where *A* is a constant dependent on the Fresnel reflection coefficients and indices of refractions. The analytic expression for *A* is given by [66]. :

$$A = \frac{\frac{2}{(1-R_0)} - 1 + |cos\theta_c|^3}{1 - |\cos\theta_c|^2}, \qquad (2.13)$$

$R_0$ depends on the ratio of the indices of refraction, $n_{rel} = n_{air}/n_{tissue}$. $R_0=[(n_{rel}-1)/(n_{rel}+1)]^2$ [66]. For the case of matching indices of refraction, A=1. An empirical model was developed by Groenuis[77] for *A:*

$$\mathrm{A} = \frac{1 + r_d}{1 - r_d}, \qquad (2.14)$$

where $r_d$ is determined empirically by Egan and Hilgeman[78]:

( 2.15 )

Unless stated otherwise, eqn.( 2.14 ) and eqn.( 2.15 ) will be used hereafter for the values of *A* and $r_d$. For mismatched indices of refraction the boundary condition, eqn. ( 2.12 ), is satisfied if the fluence is set to zero at a extrapolated boundary at $z_b=2AD$ [79]. The distance $z_b$ is referred as the extrapolated boundary (see Figure 2.1) To implement the photon dipole model, an "image source" is placed distance $z_0+2z_b$ above the tissue surface for photon at a distance $z_0$ (where $z_0$ is the depth of the photon in the tissue).

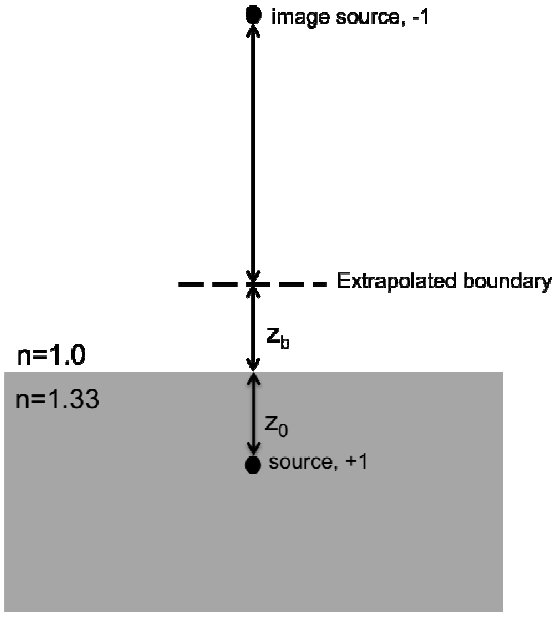


Figure 2.1: Configuration for extrapolated boundary conditions for an air-water interface.

The problem is then treated as though we are solving for the fluence for two point sources (real and image) in an infinite medium. The Green's function for an isotropic point at a position $(0,z_0)$ in an infinite medium is given as:

$$\phi(\rho, z) = \frac{1}{4\pi D}\frac{e^{-\mu_{eff} r_1}}{r_1}, \quad (2.16)$$

where $r_1=[(z-z_0)^2+\rho^2]^{1/2}$, with $\rho$ the radial distance from the point source. The total fluence for a semi-infinite planar medium with mismatched indices of refraction is:

$$\phi(\rho, z) = \frac{1}{4\pi D}\left(\frac{e^{-\mu_{eff} r_1}}{r_1} - \frac{e^{-\mu_{eff} r_2}}{r_2}\right), \quad (2.17)$$

where $r_2=[(z+z_0+2z_b)^2+\rho^2]^{1/2}$. Equation ( 2.17 ) is analytic diffusion approximation for fluence in a semi-infinite medium. The corresponding expression for reflectance will be derived in Section 2.6.2.

### *2.3.2 $P_3$ Approximation*

Following the work of Hull and Foster[68], the $P_3$ approximation to eqn. ( 2.1 ) is developed by expanding the spherical harmonics $Y_{lm}$ for the angular quantities in eqns. ( 2.4a ) and ( 2.4a ) to $l=3$ to solve eqn. ( 2.1 ). This expansion gives a set of 16 first order differential equations. This set can be further simplified to for a homogeneous medium with an isotropic point source. By symmetry this problem reduces to one dimension, resulting in only four differential equations that can be solved directly. This expansion, for a slab of infinite length and finite width, is a detailed derivation. For full derivation please see A.1 . From the final expansion, for a homogenous semi-infinite medium with an isotropic light source, the fluence is given as:

$$\varphi_0 = Ce^{(-\nu^- z)} + De^{(-\nu^+ z)} \quad (2.18)$$

where the $C$, $D$, $\nu^-$, and $\nu^+$ are defined in A.1 . The complicated expression of eqn. ( 2.20 ) was later verified [80] via MC simulations and phantom measurements and was found to be more accurate in calculating fluence than the analytic diffusion approximation approach.

For this treatment, the reflectance is given by determining how much light is transmitted across the boundary:

$$R_{det}(\rho; z_0) = \int_{\Omega_{det}} T_{fres}[\cos^{-1}(\hat{s} \cdot \hat{n})] L(r, \hat{s}; z_0)\, \hat{n} \cdot \hat{s}\, d\Omega, \quad (2.19)$$

where $T_{fres}$ is the Fresnel transmission factor, $\cos^{-1}(s \times n)$ describes the angle of incidence on the boundary, and $\Omega_{det}$ is the solid angle subtended by the detector. Equation ( 2.19 ) is the general expression for reflectance. When the term $L(r, \hat{s}; z_0)$ is expanded in spherical harmonics for $l$=1, this is the diffusion approximation. When this term is expanded to $l$=3, this becomes the $P_3$ approximation. The $P_3$ approximation overcomes the limitations of the diffusion theory approach, determining optical properties accurately where there is relatively high absorption and at short s-d separations. Yet the $P_3$ approximation also has its limitations and loses accuracy at small field sizes (<2 mm) [81].

## 2.4 Spherical Cavity Approximation

In clinical applications of intercavity PDT, such as the bladder or the thoracic cavity, it is useful to model light fluence in a cavity. The diffusion approximation can be applied to solve for the fluence by using the appropriate boundary conditions and accounting for light backscattered into a spherical cavity. To solve for the fluence in a spherical cavity we first consider the relationships between the net energy flux, radiance, and fluence. Recall eqn. ( 2.7 ) expresses the net energy flux in terms of radiance $L(r,\hat{s})$. Suppose the photon density distribution, $N(r,\hat{s})I$, is slightly anisotropic by a small shift $\varepsilon$ ($\varepsilon << 1$). The entire photon distribution density can then be expressed as:

$$N(\vec{r}, \hat{s}) = N_0(\vec{r}) \left[ \frac{1 + \varepsilon(\vec{r}) \hat{s} \cdot \hat{u}}{4\pi} \right] \quad (2.20)$$

where $\hat{u}$ is a unit vector pointing in the direction of interest. Using eqn. ( 2.20 ), the radiance, similar to eqn. ( 2.5a ) then becomes:

$$L(\vec{r},\hat{s}) = L_0(\vec{r})[1+\varepsilon(\vec{r})\hat{s}\cdot\hat{u}], \qquad (2.21)$$

Note that eqn.( 2.21 ) differs from eqn.( 2.5a ) in that here ***r*** represents the radial direction in a spherical coordinate system.

Combining eqn. ( 2.7 ) for the net energy flux and eqn. ( 2.21 )a new expression for radiance in terms of ***F(r)*** is determined:

$$L(\vec{r},\hat{s}) = L_0 + \frac{3}{4\pi}F(\vec{r})\cdot\hat{s}, \qquad (2.22)$$

where $4\pi L_0(\mathbf{r})=\phi(\mathbf{r})$. The flux ***F(r)*** has direction, however, and is broken up into two expressions: flux in positive direction, $F_{n+}(\mathbf{r})$, and flux in the negative direction, $F_{n-}(\mathbf{r})$:

$$F_{n+}(\vec{r}) = \int_{\hat{s}\cdot\hat{n}>0} L_0(\vec{r})(\hat{s}\cdot\hat{n})d\Omega + \int_{\hat{s}\cdot\hat{n}>0} \frac{3}{4\pi}F(\vec{r})\cdot\hat{s}(\hat{s}\cdot\hat{n})d\Omega, \qquad (2.23a)$$

$$F_{n-}(\vec{r}) = -\int_{\hat{s}\cdot\hat{n}<0} L_0(\vec{r})(\hat{s}\cdot\hat{n})d\Omega - \int_{\hat{s}\cdot\hat{n}<0} \frac{3}{4\pi}F(\vec{r})\cdot\hat{s}(\hat{s}\cdot\hat{n})d\Omega, \qquad (2.23b)$$

Simplifying eqn. ( 2.23a), we find new expressions for $F_{n+}(\mathbf{r})$ and $F_{n-}(\mathbf{r})$ in terms of ***F(r)***:

$$F_{n+}(\vec{r}) = \frac{\phi(\vec{r})}{4} + \frac{F(\vec{r})\cdot\hat{s}}{2}, \qquad (2.24a)$$

$$F_{n-}(\vec{r}) = \frac{\phi(\vec{r})}{4} - \frac{F(\vec{r}) \cdot \hat{s}}{2}, \qquad (2.24b)$$

Adding eqns. ( 2.23a) and ( 2.23a) together relates the total scattered fluence to the positive and negative fluxes:

$$\phi_s(\vec{r}) = 2[F_{n+}(\vec{r}) + F_{n-}(\vec{r})]. \qquad (2.25)$$

Equation ( 2.25 ) is an important result of diffusion theory and will be used to determine the fluence in a spherical cavity and its surrounding medium.

Following the derivation presented by Star [73], assume we have a spherical cavity of inner radius $r_c$ and whose outer radius approaches infinity. Because the cavity is radially symmetric, the problem reduces to one dimension. Further assuming we have an isotropic point source with power *P* such that $S(r)=P/4\pi r^2$, and applying eqn. ( 2.25 ), eqns. ( 2.8 ) and ( 2.9 ) become:

$$\frac{1}{r^2}\frac{\partial\left(F_{r+}(r) - F_{r-}(r)\right)}{\partial r} = -2\mu_a[F_{r+}(r) - F_{r-}(r)] + \mu_s \frac{P}{4\pi r^2} e^{-\mu_t(r-r_c)}, \qquad (2.26a)$$

$$\frac{\partial\left(F_{r+}(r) - F_{r-}(r)\right)}{\partial r} = -\frac{3}{2}\mu_{tr}[F_{r+}(r) - F_{r-}(r)] + \frac{3}{2} g\mu_s \frac{P}{4\pi r^2} e^{-\mu_t(r-r_c)}. \qquad (2.26b)$$

Equation ( 2.26a ) is then solved for the total fluence rate by applying the boundary condition of continuity at the cavity wall, $F_{r+}(r_c)=F_{r-}(r_c)$. The total fluence rate in the medium surrounding the cavity is determined to be:

$$\phi_t(r) = \frac{3S}{4\pi}\left\{\frac{\mu_{tr}e^{-\mu_{eff}(r-r_c)}}{r\left(1+\mu_{eff}r_c\right)} - \frac{2}{3}\frac{e^{-\mu_t(r-r_c)}}{r^2}\right\}. \quad (2.27)$$

Section 4.3 will expand upon eqn. ( 2.27 ) to determine the fluence rate within the cavity and to compare the diffusion approximation solution to integrating sphere theory. Accurate modeling of fluence in a cavity is important when considering treatment of the bladder, the thoracic cavity, and other treatment sites where the backscattered photons become important in determining PDT dosimetry, increasing the overall fluence.

## 2.5 Diffuse Reflectance

### *2.5.1 Introduction to models used to determine diffuse reflectance*

Several different techniques have been implemented to determine optical properties, hemoglobin concentration, $[Hb]_{tot}$, and tissue oxygenation ($StO_2$) *in vivo* using diffuse reflectance measurements. Time-resolved spectroscopy and frequency resolved spectroscopy of diffuse reflectance are two alternative methods but will not be explored further here, as they are beyond the scope of this thesis. Continuous wave spatially resolved spectroscopy is the experimental method applied here to determine the needed optical properties, $[Hb]_{tot}$, and $StO_2$. Knowledge of these properties helps to inform modeling of light distribution in tissue. This method records reflectance remitted from the target tissue at several different distances from the light source. The measured spectra are then fitted with the appropriate model to determine $\mu_a$ and $\mu_s'$, $[Hb]_{tot}$, and $StO_2$ (these fitting algorithms are discussed in detail in Chapter 3).

### *2.5.2 Extrapolated Boundary Conditions*

Farrell et al. [66] present a radially resolved, steady state model based on diffusion theory (see Section 2.2). Several assumptions are made. First, we assume the absorption is much less than the scattering in the target tissue ($\mu_a << \mu_s'$). Second, we assume measurements

of reflectance are made at least one free mean path from the light source. The first assumption generally holds in the therapeutic window (650-950 nm) and for the studies presented here this assumption is reasonable. Section 2.3.1 presents the framework for determining the reflectance in relation to fluence. Equations ( 2.11 ) and ( 2.12 ) are the boundary conditions that are applied to eqn.( 2.10 ) to arrive at the following relationship:

$$R(\rho, z) = -D\nabla\phi(\rho, z)|_{z=0}, \tag{2.28}$$

where $\rho$ represents the radial distance from the *z*-axis. Recalling Eqn.( 2.17 ), the Green's function for an isotropic point source, we solve for *R(ρ,z)*:

$$R(\rho, z_0) = -D\nabla\left\{\frac{1}{4\pi D}\left(\frac{e^{-\mu_{eff}r_1}}{r_1} - \frac{e^{-\mu_{eff}r_2}}{r_2}\right)\right\}. \tag{2.29}$$

Recalling that $r_1$ and $r_2$ are functions of $z, z_0, z_b$, and $\rho$ Eqn.( 2.31 ) becomes[60]:

$$R(\rho) = \frac{1}{4\pi}\left[z_0\left(\mu_{eff} + \frac{1}{r_1}\right)\frac{e^{-\mu_{eff}}}{r_1^2} + (z_0 + 2z_b)\left(\mu_{eff} + \frac{1}{r_2}\right)\frac{e^{-\mu_{eff}r_2}}{r_2^2}\right]. \tag{2.30}$$

To determine the total diffuse reflectance, we integrate eqn.( 2.30 ), weighted by the source strength of all interaction sites along the *z*-axis (see Figure 2.1), over the entire target tissue surface:

$$R_d(z_0) = \int_0^\infty R(\rho, z_0)2\pi\rho\, d\rho. \tag{2.31}$$

$$R_d(z_0) = \frac{1}{2}\left(e^{-\mu_{eff}z_0} + e^{-\mu_{eff}(z_0+2z_b)}\right). \tag{2.32}$$

Eqn.( 2.32 ) is further simplified by the following relationships:

$$z_b = 2AD = \frac{2A}{3\mu_t{}'} \quad (2.33)$$

$$\frac{\mu_{eff}}{\mu_t{}'} = [3(1-a')]^{1/2}. \quad (2.34)$$

and assuming the diffusion approximation, the total diffuse reflectance becomes[66]:

$$\rho = \frac{a'}{2}\left(1 + e^{-\frac{4}{3}A\sqrt{3(1-a')}}\right)e^{-A\sqrt{3(1-a')}}. \quad (2.35)$$

Equation ( 2.35 ) is an important expression. By fitting measured reflectance data with this expression we are able to determine $\mu_a$ and $\mu_s$' unique to each tissue measured so essential to light fluence modeling. Keinle et al. discuss the three common boundary conditions: zero boundary condition (ZBC), extrapolated boundary condition (EBC), and partial current boundary condition[60], and conclude the EBC treatment of the reflectance-fluence relationship determines optical properties within 10-15% of the actual values. This makes the EBC treatment the most effective method of determining optical properties, total hemoglobin concentration, and oxygenation from diffuse reflectance measurements when using a diffusion theory[66, 79, 82].

### *2.5.3 Diffusion theory-$P_3$ hybrid model*

While diffusion theory is commonly applied to determine $\mu_a$ and $\mu_s$' and $[Hb]_{tot}$ and $StO_2$ from reflectance measurements, this method has limitations. Diffusion theory is not applicable for tissues with high absorption nor at source-detector (s-d) distances less than one free mean path. The expression for reflectance (eqn. ( 2.19 )) derived using the $P_3$ approximation overcomes the limitations of the diffusion theory approach, determining optical properties more accurately where there is relatively high absorption and at short s-d separations. Using the

hybrid $P_3$ model[68] allows us to determine these properties with even greater accuracy near the boundary.

## 2.6 Fluorescence

Fluorescence measurements *in vivo* are used to determine photosensitizer concentration. Fluorescent light is emitted by fluorophores naturally present in tissue and also by photosensitizers used in PDT. The naturally occurring fluorescence is referred as autofluorescence and, as discussed in Chapter 3.2.3, is accounted for when determining drug concentration. Fluorophores, molecules that emit light when excited by light of a particular wavelength, each have a unique fluorescence spectrum that allows the determination of optical properties and drug concentration. The fluorescence signal is measured using a variety of methods. In this work, a fiber optic probe is used. One fiber emits the excitation light while a second fiber detects the resulting fluorescence emission.

Although we do not use our fluorescence measurements to determine optical properties in this work, it is worth discussing briefly. The fluorescence signal is generated by a collection of fluorophores present in the target tissue. The fluorescent emission is isotropic and its source function is described by[83]:

$$S_0 = \mu_{af}(r)\phi_x(r)\sigma_f(\lambda_x/\lambda_m), \quad (2.36)$$

where $\sigma_f$ and $\mu_{af}$ are the fluorescence quantum yield and excitation-wavelength absorption coefficient of the fluorophore, respectively, $\phi_x(r)$ is the fluence of excitation light, and the wavelength ratio ($\lambda_x/\lambda_m$) accounts for the difference in photon energy between the excitation and emission wavelengths. We assume the fluorophores are uniformly distributed throughout the target tissue and also have uniform quantum yield. The detected fluorescence signal is then

a function of the optical properties of the tissue, the fluence at the excitation wavelength, and position.

Measured fluorescence data is also used to determine the photosensitizer concentration in tissues in-vivo, which in turn is another method of implicit PDT dosimetry[35]. The fitting algorithm used to determine the drug concentration in tissues is discussed in detail in 3.3.2. Photosensitizers each have a unique fluorescence spectrum. By monitoring the spectrum before and after illumination, we can determine the relative concentration of the Photosensitizer in the measured tissues. Photobleaching, where fluorophores are destroyed from exposure to $^1O_2$, becomes important as it can serve as an indicator of how much tissue damage occurs. We measure photobleaching as the loss of fluorescence emission during treatment. The magnitude of photobleaching observed depends on the incident fluence rate, the oxygenation of the target tissue, and the optical properties of the target tissue. Several different models exist to describe the relationship between the fluorescence emission of a photosensitizer and these factors [35, 53]. The fluorescence spectra measured may be distorted by the absorption and scattering of the tissue[84]. A method for accounting for this distortion using the corresponding reflectance data is discussed in 3.3.2.

## 2.7 Range of Optical Properties

The *in vivo* optical properties $\mu_a$ and $\mu_s$' vary greatly between tissue type and often between tissue of the same type from different specimens. An overall range of $\mu_a$ and $\mu_s$', however, can be found in the literature. The absorption coefficient, $\mu_a$, is determined by the presence of chromophores in the tissue. Chromophores are the light-absorbent components of tissue. Each chromophore has its own unique absorption spectrum, and the concentration of different chromophores create the overall absorption spectrum of a tissue. The dominant

chromophores in tissues are hemoglobin (deoxyhemoglobin and oxyhemoglobin) and, in skin melanin. Hemoglobin is a red-colored protein that carries oxygen from the lungs to the rest of the body within red blood cells. It is the sum total of oxyhemoglobin (oxygen bound hemoglobin) and deoxyhemoglobin. The absorption spectra of oxyhemoglobin and deoxyhemoglobin differ (see Figure 1.1). Analysis of the measured absorption spectra of tissues can reveal the oxygenation of the tissues, which is, as discussed in Section 2.5, an important factor in PDT dosimetry. The brown-black pigment melanin is an important absorbing chromophore in the skin. Melanin absorbs light between ~330 nm and 700 nm and is a particularly strong scattering source in the ultraviolet part of the spectrum (see Figure 1.1). The concentration of each absorber can be determined by analyzing the full spectrum of $\mu_a(\lambda)$ for a particular tissue.

The reduced scattering coefficient $\mu_s'$ is dependent on the presence of cells and cell morphology. Light is scattered by cell nuclei at large incident angles, the cells themselves at small incident angles, mitochondria, lysosomes, and Golgi apparatus. $\mu_s'$ decreases monotonically with increasing wavelength and is often modeled by Mie theory. In Mie theory, scattering sources are treated as individual spheres that are distributed either monodispersely or polydispersely and interact with a planar electromagnetic wave. The scattering is dependent on the radii of the spheres and the index of refraction and can be shown to be mostly in the forward direction. Mourant et al. [85-87] conducted several studies of scattering in biological tissues and concluded that about 40% of scattering is caused by the cells nuclei and their sub-structures. Other organelles in the cell cytoplasm contribute greatly to scattering at large incident angles.

Table 2.1 lists the measurements of optical properties of in vivo ($\mu_a$ and $\mu_s$') human tissue at room temperature (22$^o$ C) for treatment wavelengths commonly used for PDT; the method used to obtain the optical properties is also listed. Figure 2.2 presents the spectra of human tissues in vivo for $\mu_a$ and $\mu_s$' as a function of wavelength. The data was taken from the literature for respective tissue and optical properties, and were fitted with a series of best-fit lines ($R^2 > 90$) using the software package STATA$^{TM}$. The data then compared to the resulting fit to the best-fit line, and a 95% confidence interval was obtained from this comparison (denoted by the gray band in Figure 2.2). For wavelengths $\lambda$> 690 nm where the absorption of hemoglobin is no longer dominant, tissue optical properties will be affected strongly by the absorption of photosensitizer. As a result, the spatial distribution and dynamic photobleaching of the photosensitizer will affect the in vivo optical properties. For example, the peak observed at 740 nm in prostate tissue is caused by the presence of a photosensitizing drug, Motexafin Lutetium. The result of this analysis is the overall trend in $\mu_a$ and $\mu_s$' as a function of wavelength for particular human tissues *in vivo* observed in the available literature.

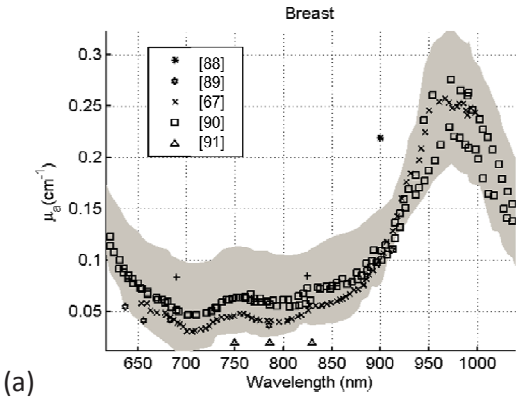
Breast
[88]
[89]
[67]
[90]
[91]
$\mu_a$ (cm$^{-1}$)
Wavelength (nm)

(a)

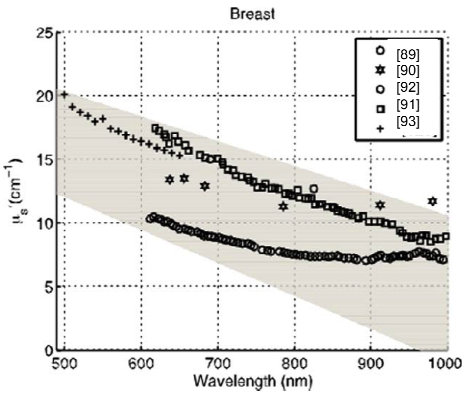
Breast
[89]
[90]
[92]
[91]
[93]
$\mu_s'$ (cm$^{-1}$)
Wavelength (nm)

(b)

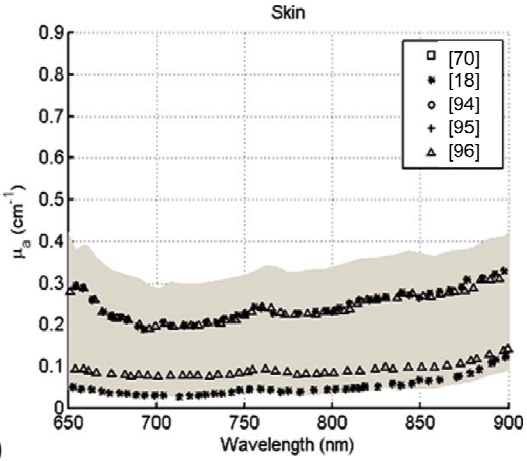
Skin
[70]
[18]
[94]
[95]
[96]
$\mu_a$ (cm$^{-1}$)
Wavelength (nm)

(c)

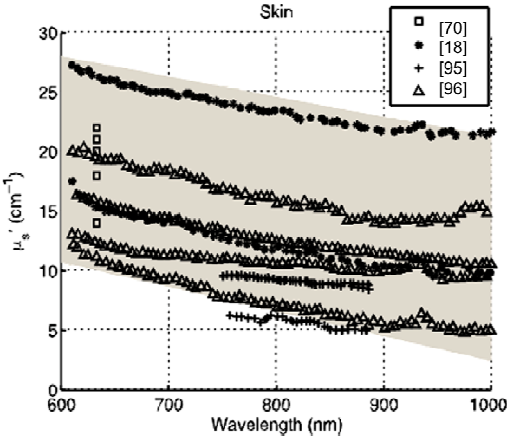
Skin
[70]
[18]
[95]
[96]
$\mu_s'$ (cm$^{-1}$)
Wavelength (nm)

(e)

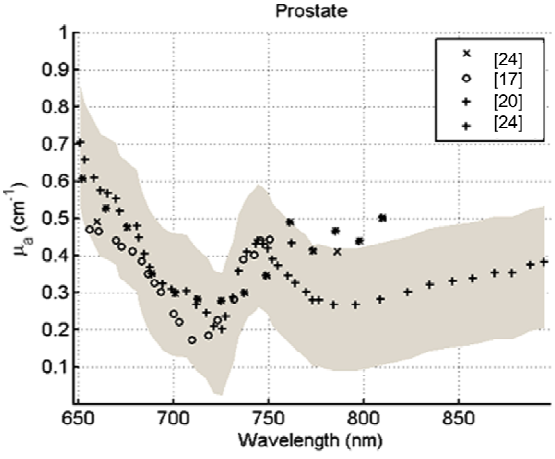
Prostate
[24]
[17]
[20]
[24]
$\mu_a$ (cm$^{-1}$)
Wavelength (nm)

(f)

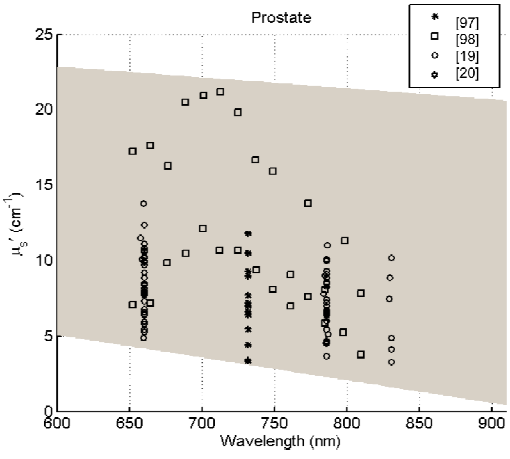
Prostate
[97]
[98]
[19]
[20]
$\mu_s'$ (cm$^{-1}$)
Wavelength (nm)

(g)

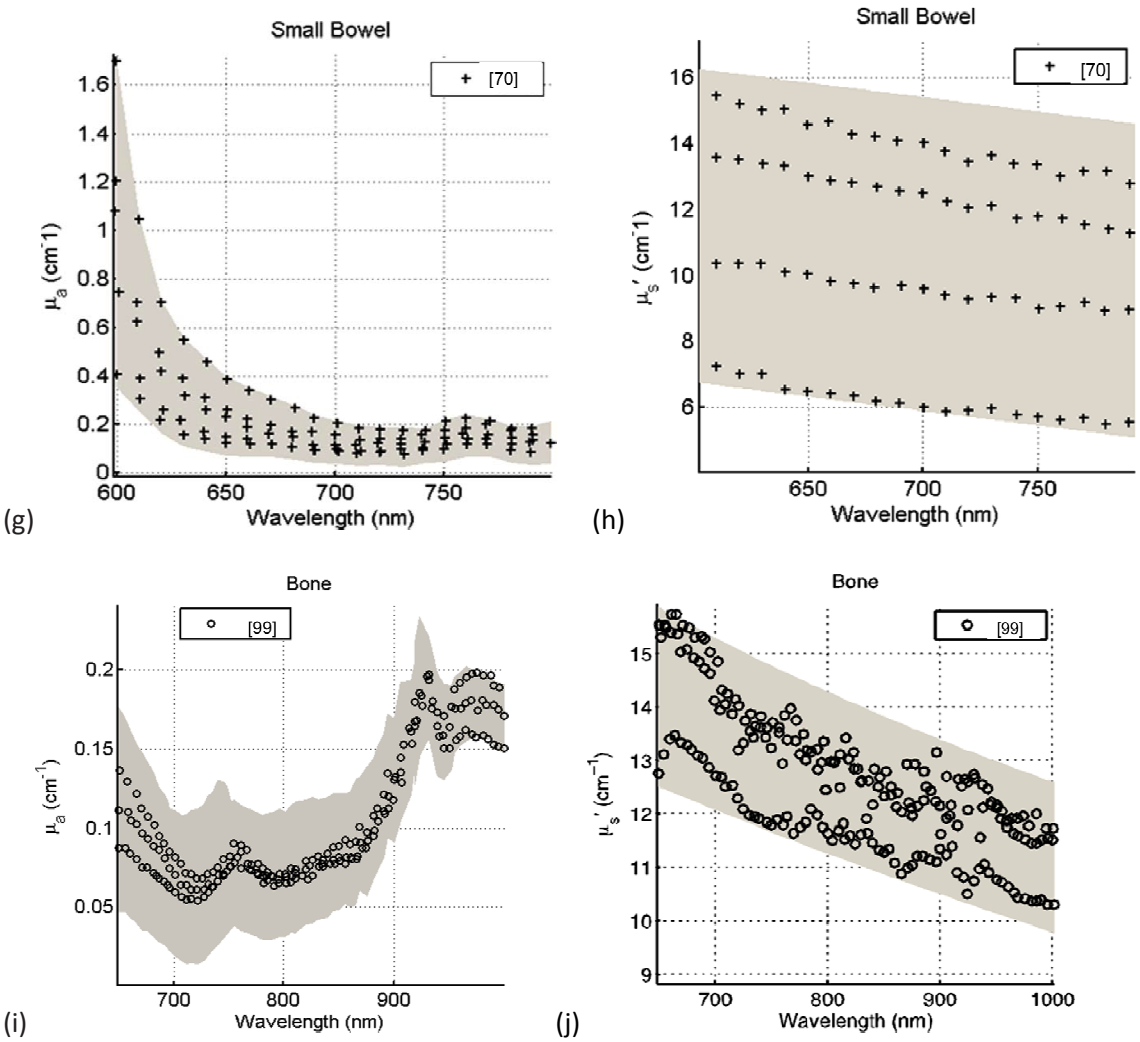


Figure 2.2: Absorption and Scattering coefficients for human tissue in vivo

Absorption and Scattering coefficients of human tissue in vivo versus wavelength for breast (a) [67, 88-91], (b) [89-93], b); skin (c) [18, 70, 94-96], (d)[18, 70, 95, 96]; prostate (e) [11, 17, 20, 24], (f)[19, 20, 97, 98]; small bowel (g) [70],(h) [70]; and bone (i) [99], (j) [99]. The grey shaded region is the range of $\mu_a$ and $\mu_s'$ with a 95% confidence interval based on review of the literature.

Table 2.1: In vivo optical properties at commonly used treatment wavelengths for PDT

| Tissue | λ (nm) | $\mu_a$ ($cm^{-1}$) | $\mu_s'$ ($cm^{-1}$) | Experimental Method | References |
|---|---|---|---|---|---|
| **Bladder** | 532 | 0.27-0.71 | 1.28-3.30 | 4 | [100] |
| | 630 | 0.28-0.76 | 2.5-6.37 | 4 | [100] |
| **Bone** | 650 | 0.09-0.14 | 12.5-15.8 | 1 | [99] |
| | 760 | 0.07-0.09 | 11.9-14.1 | 1 | [99] |
| **Brain** | 420 | 0.01-3.51 | 18.75-55.83 | 4 | [100] |
| | 532 | 0.02-3.84 | 0.10-46.3 | 4 | [100] |
| | 630 | 0.02-0.50 | 3.72-21.97 | 4 | [100-102] |
| | 760 | 0.11-0.17 | 4.0-10.5 | 1, 2 | [103, 104] |
| | 780 | 0.078-0.089 | 8.42-9.16 | 2 | [105] |
| **Breast** | 660 | 0.037-0.110 | 11.4-13.5 | 1,4 | [67, 89-91, 93, 106] |
| | 760 | 0.031-0.10 | 8.3-12.0 | 1,4 | [91, 93, 106-109] |
| | 900 | 0.096-0.29 | 3.33-5.86 | 1,4 | [88, 91, 106, 110] |
| Tumor | 530 | 0.60-0.86 | 28.0-32.1 | 4 | [92] |
| | 690 | 0.070-0.10 | 14.7-17.3 | 2 | [94] |
| | 895 | 0.068-0.102 | 12.4-13.1 | 2 | [94] |
| **Bowel** | | | | | |
| Small | 630 | 0.19-0.21 | 8.95-10.05 | 4 | [70, 111] |
| Large | 630 | 0.12-0.18 | 10.11-10.42 | 4 | [70, 111] |
| **Diaphragm** | 661 | 0.15-1.08 | 9.65-21.7 | 4 | [112] |
| **Heart** | 630 | 0.03-1.55 | 17.56-75.06 | 4 | [113] |
| | 661 | 0.12-0.18 | 5.22-90.80 | 4 | [112] |
| **Liver** | 630 | 1.15-1.56 | 21.6-30.4 | 4 | [70, 111] |
| **Lung** | 630 | 0.16-1.36 | 1.07-83.81 | 4 | [113] |
| | 661 | 0.49-0.88 | 21.14-22.52 | 4 | [112] |
| **Pericardium** | 630 | 0.13-0.33 | 13.0-21.9 | 4 | [70, 111] |
| **Prostate** | 630 | 0.05-1.0 | 3.41-17.02 | 4 | [98, 114] |
| | 650 | 0.14-0.61 | 5.24-22.68 | 4 | [19, 98, 115] |
| | 672 | 0.09-0.72 | 7.1-25.0 | 1,3 | [17, 18, 98, 115] |
| | 732 | 0.09-0.72 | 3.37-29.8 | 4 | [17, 24, 115] |
| | 762 | 0.11-1.6 | 1.2-40.0 | 2 | [15, 17, 20, 21, 115] |
| **Skin** | 630 | 0.05-1.11 | 2.26-20.95 | 1,4 | [11, 70, 113, 116, 117] |
| | 661 | 0.51-0.64 | 2.24-5.77 | 4 | [93, 112, 118] |
| | 800 | 0.16-0.23 | 6.80-9.84 | 1 | [93, 95, 96] |

*1. Time of flight absorption spectroscopy* *2. Frequency Resolved Spectroscopy*
*3. CW Absorption Transmittance Spectrsocopy* *4. CW Absorption Reflectance Spectroscopy*

# Chapter 3

# Spectroscopy

### 3.1 Introduction

Diffuse reflectance and fluorescence spectroscopy is a vital tool in optimizing PDT. The studies presented here use a fiber optic probe that sequentially measures the reflectance spectra and the fluorescence spectra of the tissue. As discussed in chapter two, reflectance measurements are used to determine not only the *in vivo* optical properties of the tissue, but also, with a series of fitting algorithms, the oxygenation saturation and blood concentration of the tissues. Although these properties can change during treatment and are unique to each patient and each tissue type, *in vivo* measurements provide an overall range of properties that one can expect to observe in further studies. *In vivo* fluorescence measurements provide a method of monitoring treatment beyond current standard protocol. The pre clinical canine BPD trial presents *in vivo* reflectance and fluorescence data previously unavailable in the literature. Working with the photosensitized BPD also provides an opportunity to further understand the behavior and effects of this photosensitizer. The Phase I HPPH trial also provides *in vivo*

reflectance and fluorescence data for the first time. An analysis of these two studies informs our dosimetric model and may potentially improve PDT efficacy.

## 3.2 Instrumentation

Reflectance and fluorescence measurements were made using a fiber optic probe that was made in-house. The probe, shown in Figure 3.1, is made of two source fibers and 9 detector fibers. One source fiber is illuminated by a tungsten lamp (Avalight, Avantes, Inc.) for reflectance measurements. The source fiber is turned on while the nine detectors collect the reflected light (see Figure 3.1). The second source fiber is illuminated by a low intensity laser (wavelength=403 nm). This is the excitation light for fluorescence measurements. Once reflectance data is collected, the white light source fiber is turned off and the 403 nm light source is turned on and data is collected. All eleven fibers are bundled together, with fiber separations depicted in Figure 3.2. The entire probe is encased by Black heatshrink over 8.5 mm (ID) Stayput Steel cable (Armor Associates SP-8.5).

Figure 3.1: Spectroscopic Probe

Spectroscopic probe head (left) and trigger button (right). Light sources are on the far right of the probe head, with detectors placed at increasing distance. The LED light on the probe handle indicates to clinician when the measurement system is ready to be used.

The data collection process is triggered by a push button, which is controlled by the clinician. All collected light is coupled to a CCD based spectrograph (InSpectrum, Roper Scientific, Princeton, NJ), recording a spectrum from each detector. Spectroscopic measurements were obtained in the following order by the CCD: diffuse reflectance (white light on), background (no source on), and fluorescence (403 nm laser on). The cycling sequence was repeated six times for each measurement and later averaged to reduce noise.

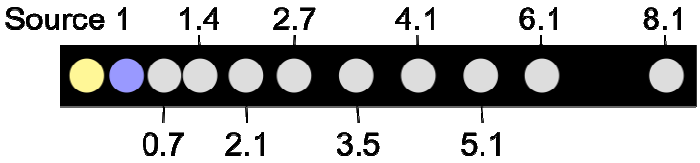


Figure 3.2: Source detector separations in cm

Source 1 is the white light source used for reflectance measurements, the second circle represents the 403 nm light source used for fluorescence measurements.

The data collected by the spectrograph is stored and then processed before it is fit using the algorithms described in section 3.3. Data is corrected for CCD offset and instrument variation. The CCD offset is corrected by subtraction of an averaged dark frame (the background measurement collected). To correct for the instrument spectral response, measurements made in an integrating sphere are used. The probe is placed at the center of an integrating sphere. The use of an integrating sphere, which is coated in white reflecting paint, allows us to record in variation in fiber throughput, light source variation, and the spectral response of the CCD. Measured reflectance is divided by the spectrum obtained in the integrating sphere. The six frames collected are averaged together and normalized by the maximum of each spectrum and then saved for further analysis.

### 3.3 Fitting Algorithms

Once the reflectance and fluorescence data is processed the following fitting algorithms are

applied where appropriate. Radially (Section 3.3.1) and spectrally (Section 3.3.2) fitting of diffuse reflectance measurement allow us to determine the optical properties and the hemoglobin and oxygenation levels respectively. Spectrally resolved fitting of fluorescence data, using the appropriate basis spectrum, determines the relative photosensitizer concentration. The outputs of each fitting process provide valuable information for determining light fluence distribution, as discussed further in Chapter 4.

### *3.3.1 Diffuse reflectance radially resolved fitting*

As mentioned in section 2.3.2, Hull and Foster [68] developed an expression for reflectance using the $P_3$ approximation. Equation( 2.19 ) is used to fit the radial profile of reflectance measurements to determine the optical properties of the measured tissue. Applying the $P_3$ approximation in this manner is advantageous over the diffusion approximation for reflectance because it is valid at small source-detector separations, which allows for smaller measuring instruments to be used in the clinic.

Nichols et al. [119] applied the solution for reflectance derived by Farrell et al. [66], a diffusion approximation based solution, to fit the radial profile of reflectance measurements to determine the optical properties of turbid media. For the work presented here, we apply the same overall fitting technique, only using Hull and Foster's $P_3$ approximation for reflectance as opposed to Farrell's. We normalize the measure reflectance:

$$R_{d,norm} = \frac{R_d(\rho)}{R_{d(\rho_{norm})}}, \qquad (3.1)$$

where $R_d(\rho_{norm})$ is measured reflectance at a known distance $\rho_{norm}$. In this way we consider only the shape of measured spectrum, independent of intensity. A theoretical reflectance radial

profile is fitted to the measured reflectance radial profile using a nonlinear optimization algorithm, *fminsearch*, available in Matlab, to determine $\mu_a$ and $\mu_s$' via radial distance fitting.

The function *fminsearch* is an unconstrained nonlinear optimization algorithm based on the work of Lagarias et al. [120]. It finds the minimum of a scalar function of several variables given an initial estimate. In this instance, an initial estimate of $\mu_a$ and $\mu_s$' are given to generate the theoretical radial profile. We assume eqn. ( 2.19 ) is continuously differentiable and run *fminsearch* iteratively until the difference between the theoretical spectrum and measured spectrum is minimized. The minimum reached is a local minimum only. If the initial values for $\mu_a$ and $\mu_s$' differ drastically from the true $\mu_a$ and $\mu_s$' then another, local, minimum may be reached, returning incorrect values for $\mu_a$ and $\mu_s$'. We conducted a phantom study, with known optical properties, to test how the initial values of $\mu_a$ and $\mu_s$' given to the fitting algorithm affect final values of $\mu_a$ and $\mu_s$'.

Four liquid phantoms were made using black India ink (for absorption), Intralipid™ (for scattering), and water. The absorption coefficient of the India ink was determined using an absorption spectrum spectrometer (Ocean Optics cuvette holder, TE-cooled CCD spectrograph) from a series of measurements made using nine different concentrations of the same ink used in the phantom measurements. Each of the four phantoms (see Table 3.1) was measured a total of four times, with five frames per measurement, collected by the 9 detectors of the probe described in section 3.2. Our purpose in making repeated measurements was to observe the spread in resulting optical properties from a series of measurements on the same sample.

Table 3.1: Tissue Phantom Optical Properties

| Phantom | $\mu_a$ ($cm^{-1}$) | $\mu_s'$ ($cm^{-1}$) |
|---|---|---|
| A | 1.2 | 16.5 |
| B | 1.22 | 18.0 |
| C | 1 | 25 |
| D | 0.5 | 15 |

We tested how dependent the resulting optical properties from our fitting algorithm are on the initial guess used in the algorithm. We do this by fitting the phantom data (of well-known optical properties) repeatedly, using different initial guesses and comparing the output of the algorithm. We present the results from Phantom A ($\mu_a$=1.2 ($cm^{-1}$) and $\mu_s'$=16.5 ($cm^{-1}$)) here, with initial guesses listed in Table 3.2.

Table 3.2: Initial Guesses for Phantom A

| Optical Properties | Index Number | $\mu_a$ ($cm^{-1}$) | $\mu_s'$ ($cm^{-1}$) |
|---|---|---|---|
| | 1 | 1.0 | 10 |
| | 2 | 0.5 | 15 |
| | 3 | 1.0 | 15 |
| | 4 | 0.5 | 18 |
| | 5 | 1.0 | 18 |
| | 6 | 1.5 | 18 |
| | 7 | 0.5 | 20 |
| | 8 | 1.0 | 20 |
| | 9 | 1.5 | 20 |

Of the four phantoms measured, three displayed a downward sloping, negative correlation between $\mu_a$ and $\mu_s'$ (see Figure 3.3). The concentration of data points, however, appears to be random between phantoms. Each set of data for each phantom was fitted using the known optical properties of that phantom as the initial guess for the optimization algorithm.

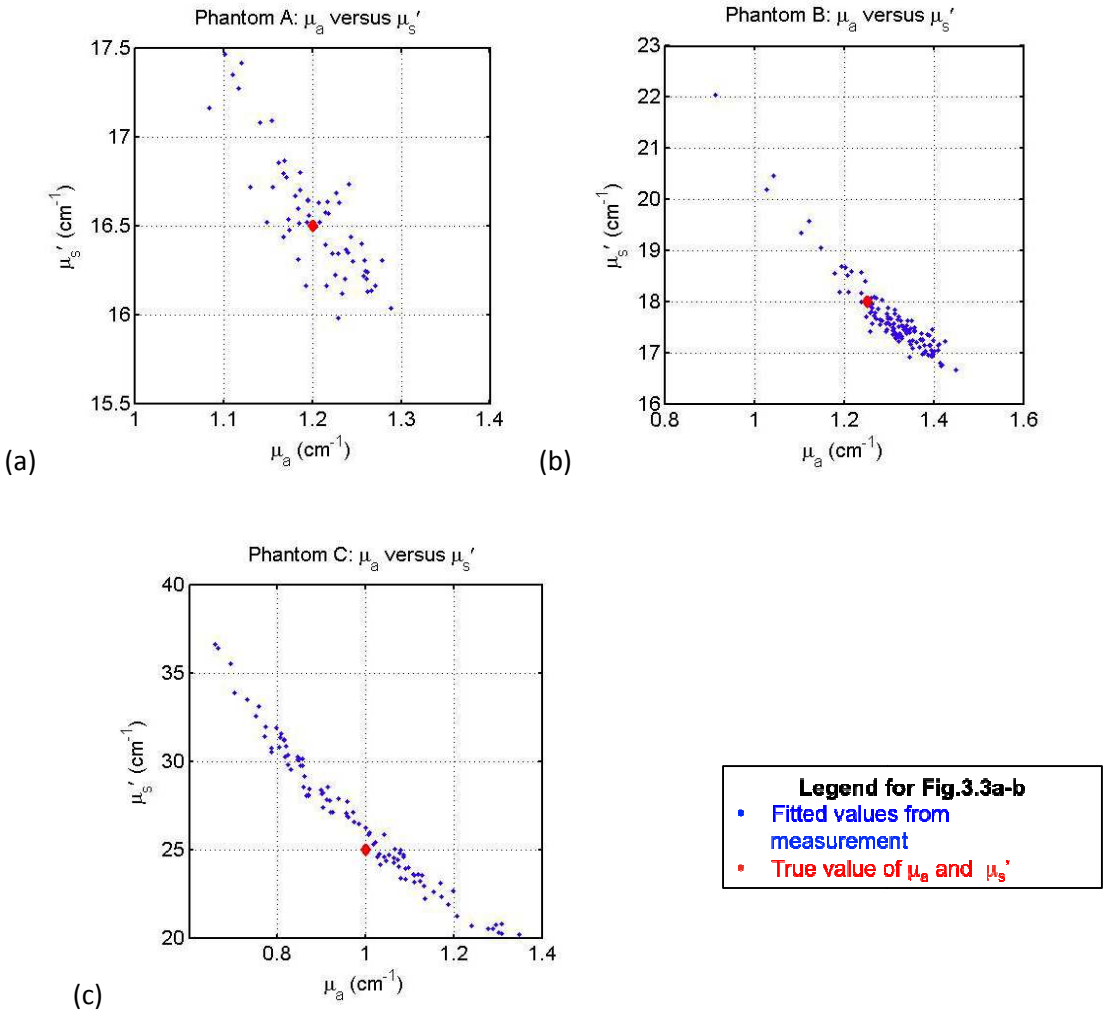


Figure 3.3: $\mu_s'$ vs. $\mu_a$ of measured phantoms

(a) Resulting optical properties from four concurrent measurements, where each measurement has five frames with data being collected by nine detectors for Phantom A ($\mu_a$=1.2 ($cm^{-1}$), $\mu_s'$=16.5 ($cm^{-1}$)). For this set of measurements the data points are randomly, but relatively evenly distributed about the actual optical properties of the phantom. (b) Resulting optical properties from four concurrent measurements for Phantom B ($\mu_a$=1.22 ($cm^{-1}$), $\mu_s'$=18.0 ($cm^{-1}$)). For this set of measurements the data points are more concentrated at $\mu_a$ above the actual value of the phantom and above the known $\mu_s'$. (c) Resulting optical properties from four concurrent measurements for Phantom C ($\mu_a$=1.0 ($cm^{-1}$), $\mu_s'$=25 ($cm^{-1}$)). For this set of measurements the data points are evenly distributed about the actual optical properties of the phantom but display a greater range in optical properties than the previous two phantoms.

From our fitting process, using a range of initial guesses, we found overwhelmingly that for ideal, homogeneous data the initial guess given to our fitting algorithm has less effect on the

final result of the fitting algorithm than the experimental variation in the measurement (see Figure 3.4).While providing the algorithm with an incorrect initial guess does shift the resulting fitted optical properties about the actual values, it does not result in fitted optical properties that are greater than 10% different from $\mu_s'$ and 11% different from $\mu_a$.

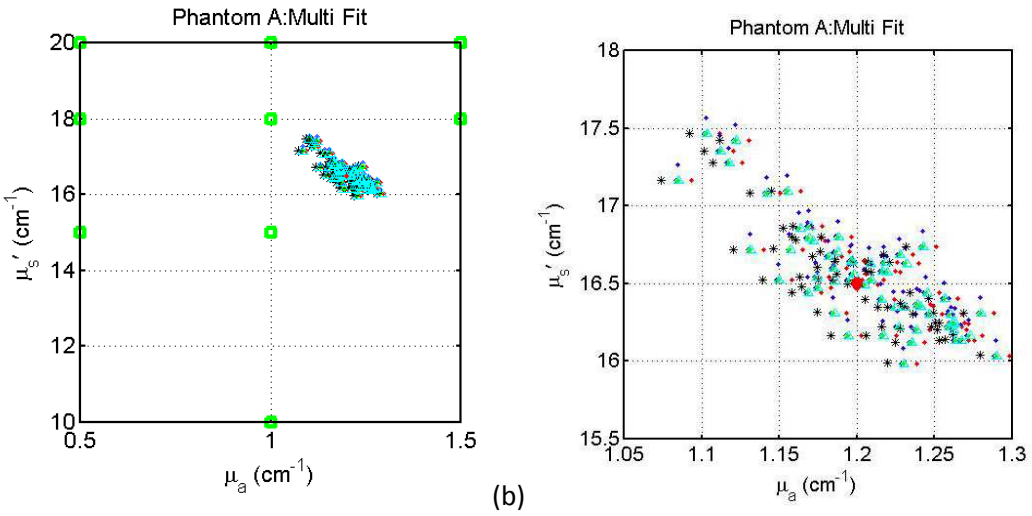


Figure 3.4: Optical properties from fitting algorithm for phantom A

(a) Range of optical properties for a range of initial guess used in fitting algorithm. Initial guesses are denoted by the green squares (for values of initial guesses, see Table 3.2). Resulting values of optical properties are denoted by small, colored markers clustered about the known values of $\mu_a$=1.2 ($cm^{-1}$) and $\mu_s'$=16.5 $cm^{-1}$). (b) Zooming in on the spread of optical properties generated by the range of initial guesses plotted in Fig.(a). Note that many data points are layered on top of each other for different initial guesses as the resulting values do not change. Actual values of $\mu_a$ and $\mu_s'$ of Phantom A is denoted by the large red dot.

### *3.3.2 Diffuse reflectance spectrally resolved fitting*

Using a radially resolved fitting algorithm allows us to determine the optical properties of the measured tissues directly. In the past, the resulting optical properties were used to determine the concentration of common absorbers such as hemoglobin and deoxyhemoglobin indirectly[68, 119, 121]. By building on the work of Finlay and Foster[80], implementing a spectrally resolved fitting algorithms allows the direct determination of absorber

concentrations. This technique also uses the diffusion $P_3$ hybrid-model to model light propagation in tissue (see A.1 for full derivation and application). Using this model and the determined values of $\mu_a$ and $\mu_s'$ (as described below), the diffuse reflectance is calculated at each wavelength to create entire theoretical reflectance spectrum.

The fitting process results in a vector **a,** whose components characterize the reflectance spectrum being analyzed. The first two components of **a** describe the absorber concentrations in the measurements of interest[83]:

$$\mu_a(\lambda) = a_1\mu_{aHbO_2}(\lambda) + a_2\mu_{aHb}(\lambda), \quad (3.2)$$

The absorption spectra of hemoglobin (Hb) and deoxyhemoglobin ($HbO_2$) taken from the literature[122]. The coefficients $\boldsymbol{a_1}$ and $\boldsymbol{a_2}$ are the concentrations of $HbO_2$ and Hb respectively. Only $HbO_2$ and Hb are considered when computing the absorption of a tissue measurement as, for the studies in this work, all measurements were made on internal organs where whole blood is expected to be the dominant absorber. The remaining two components of vector **a** describe the scattering, according to an approximation based on Mie theory[85]:

$$\mu_s' = a_3\left(\frac{\lambda}{\lambda_0}\right)^{-a_4}, \quad (3.3)$$

The parameter $\boldsymbol{a_3}$ is the value of $\mu_s'$ at $\lambda_0$, the normalization wavelength. The normalization wavelength is chosen to be the treatment wavelength.. The parameter $\boldsymbol{a_4}$ is determined by the specific distribution of scatterers and varies from 0.37 for particles much larger than $\lambda$ to 4.0 for particles much smaller than $\lambda$.

From the vector **a**, a theoretical reflectance spectrum is created and fitted to the measured spectrum. Using the optimization function *fminsearch* as before, the fitting process

runs through iterations until an optimum theoretical spectrum is determined. The four components of **a** are stored and taken to be the best fit values for concentrations of $HbO_2$ and Hb, and reduced scattering. The quantities $HbO_2$ and Hb, given in μM, are often best expressed in terms of total hemoglobin and the oxygenation saturation. Using the hemoglobin oxygen saturation equation:

$$SO_2 = \frac{[HbO_2]}{[HbO_2] + [Hb]}. \quad (3.4)$$

The fitting process gives [Hb] and [$HbO_2$]; using these results and eqn.( 3.4 ) we determine $StO_2$.

### *3.3.3 Fluorescence spectra fitting for Photosensitizer concentration*

The measured fluorescence spectra are a combination of the fluorescence of several fluorophores present in the tissue. Photosensitizers such as BPD and HPPH each have a distinctive fluorescence spectrum. By fitting the measured fluorescence spectrum of a tissue that is injected with a photosensitizer, before and after treatment light is applied, we are able to observe the change in the amount of photosensitizer present. A measured fluorescence spectrum of tissue where a photosensitizer is present must also use the autofluorescence spectrum (see 3.4.1 Autofluorescence), in addition to the photosensitizer spectrum to accurately to fit for phototsensitizer concentration. Corrections for the effects of absorption and scattering in the tissue are also applied to obtain the true fluorescence spectrum of a photosensitizer.

We used the fitting algorithm developed by Finlay et al.[123] to obtain photosensitizer concentrations from fluorescence measurements. The measured fluorescence spectrum is divided by the corresponding reflectance spectrum to account for the effects of absorption and scattering [124]. The spectrum is then fitted as a linear combination of fluorescence basis

spectra using a single value decomposition (SVD) algorithm in MATLAB™. The SVD fitting algorithm is a non-iterative process, unlike *fminsearch*. The goal of the algorithm is to minimize the $\chi^2$ of the fit:

$$\chi^2 = \|Aa - b\|^2, \quad (3.5)$$

where $A=(1/\sigma)\boldsymbol{X}$ with $\boldsymbol{X}$ as the basis matrix and $\sigma$ representing the uncertainties of the measurements, $\boldsymbol{a}$ is a vector of amplitudes of the vectors to be determined by the fit, and $\boldsymbol{b}=(1/\sigma)\boldsymbol{y}$, where $\boldsymbol{y}$ is the vector of the measured data. These basis vectors are not necessarily orthogonal, providing the motivation to use the SVD method over the traditional least squares fitting technique. Press et al. [125] provides an application of SVD fitting, which we will outline below.

The singular value decomposition of matrix *A* from eqn. ( 3.5 ) is defined in the following manner:

$$A = UwV^T, \quad (3.6)$$

where *U* is an orthogonal matrix, *w* is the diagonal matrix whose elements are the singular values of decomposition, and $V^T$ is the transpose of the orthogonal matrix, *V*. The goal of SVD fitting is to determine a matrix *A* that minimizes $\chi^2$. The amplitudes of the fits are related to Eqn. ( 3.6 )via:

$$a = VmU^T b. \quad (3.7)$$

The variances of the amplitude of a (Eqn.( 3.7 )) are expressed in terms of V and *m:*

$$v_a = VmmV^T. \quad (3.8)$$

The uncertainty of *a* is determined by taking the square root of the elements of $v_a$. The matrix *m* is the diagonal matrix whose elements are the inverses of the corresponding elements of *w*. If the matrix *A* is singular, a substitution of *m* with *m** (defined below) is made to complete the fitting process. The elements of matrix *m** are defined as:

$$m_i^* = \frac{1}{w_i}, w_i > w_{\max}\gamma_{tol}$$

$$m_i^* = 0, w_i < w_{\max}\gamma_{tol}$$

where $w_{max}$ is the largest element of *w* and $\gamma_{tol}$ is a cutoff tolerance that is predetermined. The choice of $\gamma_{tol}$ can vary, as the resulting fit from an inappropriate choice of $\gamma_{tol}$ is very poor. An appropriate choice of $\gamma_{tol}$ is one where $\chi^2$ is at its minimum for *a,* (see Figure 3.5) this way we are able to determine a matrix *A* and vector ***a***, whose values minimize $\chi^2$ and result in the best fit, ***a*,** to the data, ***y***.

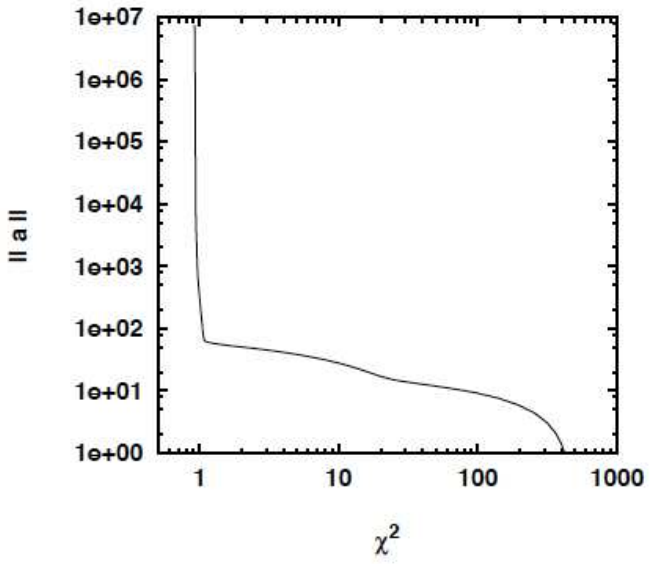


Figure 3.5: L-Curve of a typical in vivo fluorescence spectrum

The best choice of $\gamma_{tot}$ gives a fit where we are in the lower left-hand corner of the L-curve [83].

While the photosensitizer and autofluorescence are the dominant fluorophores in most measured spectra, a 61-term Fourier synthesis is included to account for unknown fluorophores whose fluorescence will affect the measured spectrum. The fluorescence emission spectrum is well approximated by a sum of Lorentzian curves. With this in mind, the Fourier transform of a Lorentzian is a decreasing exponential, allowing us to assign an appropriate weight to the Fourier components such that it decreases with increasing wavenumber. An added benefit of this method is that low weighting of higher frequency Fourier terms filters out high-frequency noise present in the data. In the fluorescence fitting process, the Fourier component is given much lower weighting (usually weight by 2.0) relative to that of the photosensitizer and autofluorescence (usually weighted by 100). Bringing these fitting components together, the total fluorescence is determined by:

$$f_{tot} = \sum_{i=1}^{N} A_i\,(100) f_s(\lambda) + 2.0B_0 + \sum_{k=1}^{30}\left(20e^{-k/20}\right) \times \left[B_k \sin\left(\frac{\pi k(\lambda-\lambda_i)}{\lambda_f-\lambda_i}\right) + C_k \cos\left(\frac{\pi k(\lambda-\lambda_i)}{\lambda_f-\lambda_i}\right)\right]. \quad (3.9)$$

Where $A_i$ and $f_i(\lambda)$ are the amplitude and basis spectrum of the $i^{th}$ of N total fluorophores present, respectively. The value of 20 in the exponentially decreasing weights was determined empirically[83]. And the spectral amplitudes, $A_i$, $B_k$, and $C_k$ ,are returned by the algorithm. These three amplitudes are the concentrations, in arbitrary units, of the photosensitizer, autofluorescence, and Fourier components.

To summarize, the measured fluorescence spectrum is divided by the corresponding reflectance spectrum to account for the effects of absorption and scattering. The spectrum is then fitted using the technique described in section 3.3.2, only using the SVD algorithm in place of *fminsearch*. Basis spectra of autofluorescence and photosensitizers are needed to fit the data

and isolate the fluorescence spectrum of the photosensitizer, which provides the drug concentration in the measured tissue. In addition to this, adding in Fourier components is necessary to account for unknown fluorophores.

## 3.4 Fluorescence Basis Spectra

### *3.4.1 Autofluorescence*

Many tissues display an inherent fluorescence, even without the presence of an added fluorophores such as a photosensitizer. Naturally present components, such as Nicotinamide adenine dinucleotide phosphate (NADPH), which is present in all living tissues, are fluorophores themselves. When obtaining our basis spectra and analyzing our measured fluorescence data it is imperative we account for the autofluorescence of the tissue. While the intensity of autofluorescence varies from tissue to tissue, these differences are minor. The autofluorescence can thus be measured on one type of tissue and then subsequently applied to all other fluorescence measurements.

To obtain this autofluorescence spectrum we conducted a series of measurements on two female nude mice. The mice were previously untreated and had not yet been administered the photosensitizer. A series of eleven measurements were made on Mouse 1 on the tail, haunch, and shoulder with a small probe similar in design to the one described in 3.2 Instrumentation. The fluorescence data was divided by the corresponding reflectance data to account for the effects of absorption and scattering. In processing these measurements, the mean was taken over all eleven measurements. From this mean spectrum, a scaled spectrum of protoporphyrin IX (PPIX) (0.4 times the normalized spectrum) was subtracted to remove a peak observed around 637 nm. A second peak around 676 nm was observed; to correct for this unexpected peak a Gaussian with a full width half max of 20 and maximum peak of one, scaled

by 900 was also subtracted from the mean spectrum. The resulting autofluorescence spectrum (Fig. 3.4) is a smooth spectrum, decreasing with wavelength. This autofluorescence spectrum is used in the determination of all following fluorescence basis spectra and fluorescence data in the BPD and HPPH studies.

### *3.4.2 BPD Basis Spectrum*

The basis spectrum of BPD used for data analysis was obtained from the treatment of two female, untumored, nude mice. Mice were anesthetized by inhalation of isoflurane in medical air (VetEquip anesthesia machine, VetEquip). Measurements were made on each mouse before drug administration on the tail, haunch, and shoulder (the treatment site). After being given a tail injection of 0.25 mg/kg BPD, the mice underwent a half hour drug-light interval and were treated with a 1 cm diameter laser-beam size (laser was placed 8 cm away from the treatment site) at a power of 58.9 mW. Measurements were made at before and after light delivery (treatment time was 55 minutes and 33 seconds) and at 5-minute intervals, causing brief interruptions in treatment. The data was corrected for CCD integration time and background was also subtracted before dividing the data by the corresponding reflectance to account for tissue optical heterogeneity.

The autofluorescence spectrum determined in section 3.4.1 was then subtracted from pre-treatment averaged measurements made at the treatment site, when the fluorescence amplitude is greatest. After this subtraction, a small peak was observed around 637 nm. We identified this peak to be similar to the fluorescence spectrum of the photosensitizer PPIX. A scaled PPIX basis spectrum (normalized basis spectrum multiplied by 0.4) was then subtracted from the measured BPD basis spectrum to obtain the spectrum used for data analysis (see Figure 3.6).

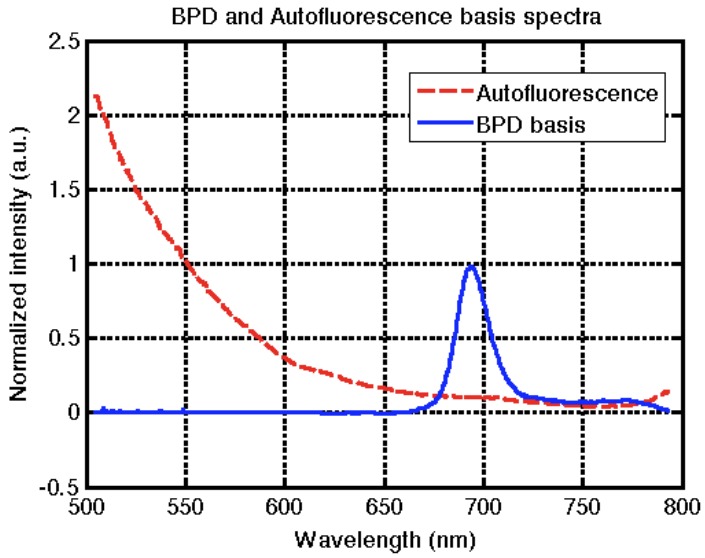


Figure 3.6: Autofluorescence and BPD basis spectra measured in nude mice

The autofluorescence was measured and processed as described in Section 3.4.1. The BPD basis spectra collected from nude mice demonstrates the characteristic fluorescence peak at 690 nm and normalized to 1 by dividing the whole spectrum by its maximum.

### *3.4.3 HPPH Basis Spectrum*

To determine the fluorescence basis spectrum of HPPH, the procedure described above is performed, using HPPH[1]. The basis spectra used for data analysis were obtained from the treatment of three nude mice with HPPH. Measurements were made on each mouse before drug administration on the tail, haunch, and shoulder (the treatment site). After being given a tail injection of 0.25 mg/kg of HPPH, the mice underwent a twenty-four drug-light interval and were treated with a 1 cm diameter laser-beam size at an irradiance of 75 mW/ $cm^2$ to a total fluence of 135 J/$cm^2$ (55.5 min). Measurements were made on each mouse before and after light delivery. The final mouse treated (Mouse Three) was measured at 10 minute intervals

[1] A study was performed, analyzing if the presence of difference solvents affected the HPPH basis spectrum. See

A.2 )

during treatment. The data was corrected for CCD spectral response and detector background signal. The effect of absorption and scattering were accounted for by dividing the fluorescence data by the corresponding reflectance data.

The autofluorescence spectrum is subtracted from the averaged measurements of the treated mice. The measurements were made at the treatment site pre-light delivery to obtain the HPPH basis spectrum (resulting spectrum is an average of 6 measurements, 6 pre treatment) when the fluorescence has its greatest amplitude. To confirm how consistent our HPPH basis spectrum from Mouse 1 is, we fitted the post-light delivery measurements made at the treatment site from Mouse 2 and 3 (see Figure 3.7) to obtain fits using a singular-value decomposition algorithm (discussed in greater detail below) for the HPPH fluorescence and autofluorescence.

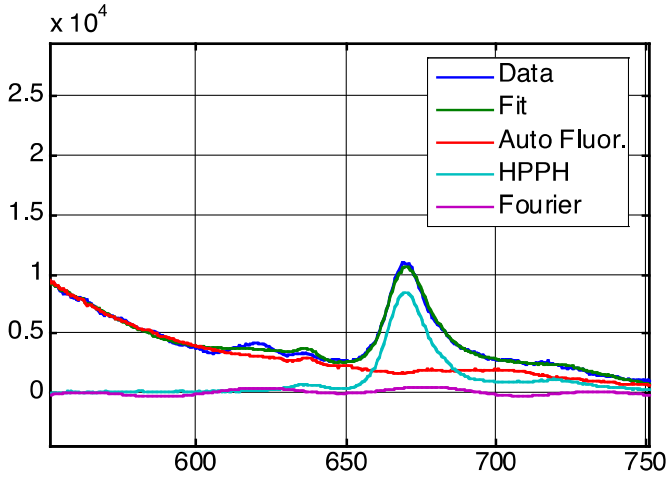


Figure 3.7: Fitted HPPH fluorescence data measured in nude mice as a function of wavelength (nm)

The Fourier component is used to account for any abnormalities that are not easily fit by the autofluorescence and HPPH basis spectra.

As observed in Figure 3.8 we are able to consistently obtain good fits using our HPPH spectra. As a further check our basis is compared to measurements made in a cuvette by Sunar et. al. [25](see Figure 3.8), where there is good agreement. The resulting HPPH spectrum from our mouse study is used for the fluorescence data analysis for all human in vivo data.

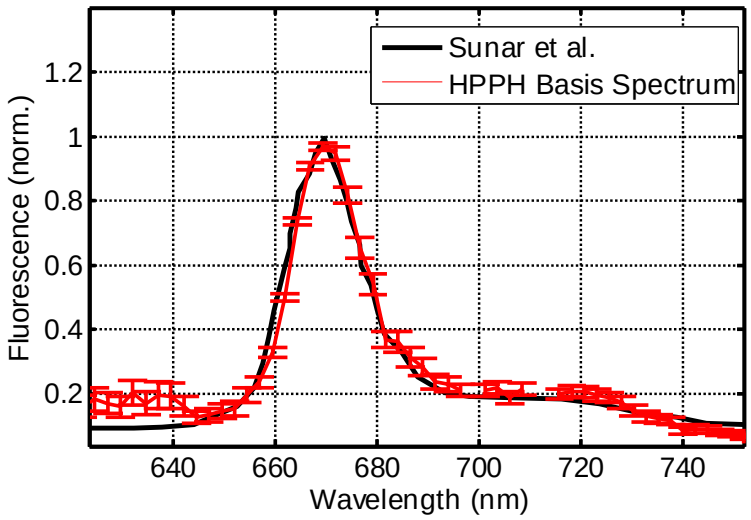


Figure 3.8: Measured HPPH basis spectrum compared to spectrum available in the literature

The two spectra agree within the error bars of the measured spectrum and show the characteristic fluorescence peak of HPPH.

Several photosensitizers' fluorescence spectra change throughout treatment due to the presence of photoproducts caused by chemical reactions induced in the drug. This made a study of HPPH photobleaching necessary in order to validate our basis spectra. The measurements made on the treatment site (the shoulder) of Mouse 3 at 5, 10, 25, and 45 minutes during light delivery (at each time interval three measurements were made at the treatment site) (see Figure 3.9a) display the expected decrease in HPPH fluorescence, indicating a decrease in the concentration of the drug. No significant change in spectral shape was observed further indicating there are no photoproducts induced by irradiation.

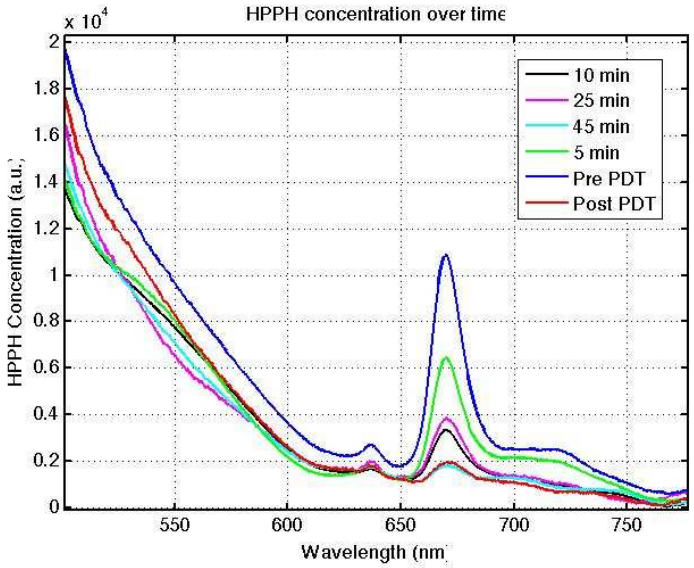


(a)

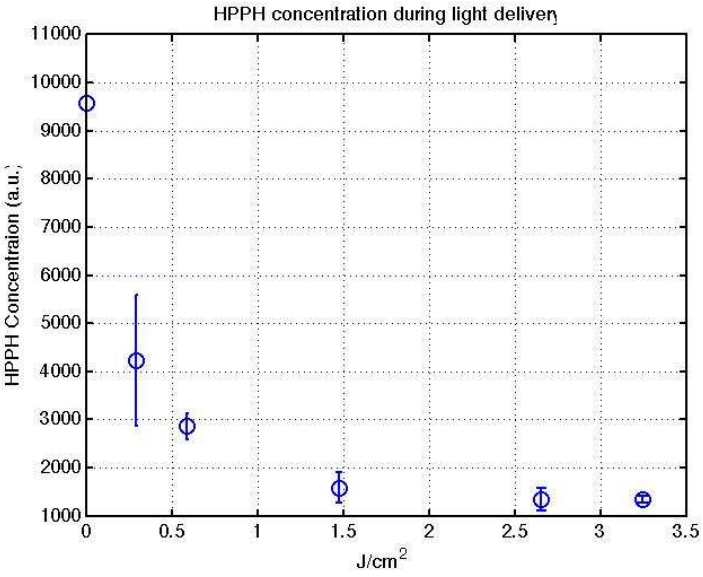


(b)

Figure 3.9: HPPH concentration over time

(a) Measured fluorescence during PDT in a nude mouse as a function of wavelength (nm). (b) HPPH concentration as a function of light delivered, demonstrates the expected decrease in HPPH concentration in the mouse.

Using the fitting algorithm described above, the concentration of HPPH in arbitrary units was found for each the measurements made during treatment. Plotted as a function of fluence rate (See Figure 3.9b), we see the expected monotonic decrease of HPPH concentration.

### 3.5 Measurements: BPD

The spectroscopic methods discussed in section 3.1-3.4 were used to evaluate the interperitoneal cavity of 15 healthy canines. This data was collected as a part of a pre clinical trial for the treatment peritoneal carcinomatosis (PC) using BPD.PC has low survival outcome and is difficult to treat with traditional radiation methods due the number of vital organs that need to be spared in the peritoneal region. The 15 dogs were given either 0.125 mg/kg or 0.25 mg/kg doses of BPD four hours before light administration (See Table 3.3)

Table 3.3: Treatment groups for BPD study

| Small Bowel Resection | | | |
|---|---|---|---|
| | | Light dose (J/cm2) | |
| Dog # | BPD dose | Overall | Anastomosis |
| 3 | 0.125mg/kg | 2 | 2 |
| 4 | 0.25mg/kg | 2 | 2 |
| 9 | 0.25mg/kg | 2 | 2 |
| 12 | 0.25mg/kg | 2 | 10 |
| 5 | 0.25mg/kg | 4 | 4 |
| 6 | 0.25mg/kg | 4 | 4 |
| 10 | 0.25mg/kg | 4 | 2 |
| 11**** | 0.25mg/kg | 4 | 2 |
| 13*** | 0.25mg/kg | 4 | 2 |
| 14*** | 0.25mg/kg | 4 | 2 |
| 15*** | 0.25mg/kg | 4 | 2 |
| 1 | 0.25mg/kg | 10 | 10** |
| 2 | 0.25mg/kg | 10 | 10* |
| | | | |
| No Small Bowel Resection | | | |
| | | Light dose (J/cm2) | |
| Dog # | BPD dose | Overall | Anastomosis |
| 7 | 0.25mg/kg | 4 | N/A |
| 8 | 0.25mg/kg | 4 | N/A |

*dog received PDT before small bowel resection
** dog received PDT after small bowel resection
*** cetuximab
****towel was placed over anastomosis

The dogs were kept in darkened rooms before light administration and all lighting in the operating room was covered by thin sheets of polyester filter (GamColor #480, GAM, Los Angeles, CA). The purpose of this filter is to reduce the light intensity at the peak absorption of BPD to avoid activation of BPD outside the treatment field. Light was administered using 8W diode laser with a peak at 690 nm (B&W Tek). The light administration procedure was similar to that described previously in [126]. The mesentery and small bowel were irradiated piecewise using a light field projected by a microlens. The cavity and the remaining organs were subsequently irradiated using a diffusing light wand, which was moved throughout the cavity to ensure uniform distribution of light. The total fluence delivered to the tissue surface was monitored by isotropic detectors placed on the surface of each section of the bowel, and at seven locations in the cavity: 1: the right upper quadrant lateral to the liver, near the border of the diaphragmatic attachments, 2: the left upper quadrant similarly near the border of the diaphragmatic attachments, 3: the left lower quadrant in the paracolic gutter, 4: the right lower quadrant, and 5: the pelvis anterior to the dome of the bladder.

Of the 15 canines, we obtained pre and post treatment measurements for 13. Measurements were made using the probe described in section 3.2 and the data was processed and fitted accordingly. The optical properties shown in Figure 3.10 and Figure 3.11 were obtained using the radially resolved fitting algorithm, taking the averages of $\mu_a$ and $\mu_s'$ between 685 nm to 695 nm, over the first four source-detector separations. The values for deoxyhemoglobin (Hb), oxyhemoglobin ($HbO_2$), total hemoglobin, and oxygenation were obtained by taking the average of the first four s-d separations with a wavelength range of 600-800 nm, using the spectrally resolved fitting algorithm. Total hemoglobin levels above 2500 uM were not included as hemoglobin levels above 2500 uM are unphysical[127]. BPD

concentrations shown in Figure 3.14 were obtained by fitting the first s-d separation spectrum using the fluorescence-fitting algorithm described above, and then dividing the BPD amplitude by the corresponding autofluorescence component to account for autofluorescence variation between subjects and tissue type. The variation in the fluorescence spectra caused by different $\mu_a$ and $\mu_s$' was accounted by dividing by the corresponding reflectance measurements We were unable to obtain fluorescence spectra for spleen tissue due to the high $\mu_a$ of the tissue.

### 3.6 Results: BPD

The tissues with measured spectra in the fifteen canine interperitoneal cavities are as follows: abdominal wall (Abdwall), aorta, bladder, bowel, colon, gall bladder, kidney, liver, rectum, and stomach. As observed in Figure 3.10 and Figure 3.11, the optical properties vary greatly, not only between different tissue types but also between different canine subjects. The optical properties also did not demonstrate any significant trend in changes post PDT. While relative ranges of tissues type observed, such as liver tissue demonstrating high $\mu_a$ and bladder tissue to have overall higher $\mu_s$', the great variation of optical properties in all tissues points to the need for real-time spectroscopy to truly calculate the most effective fluence dose not only for each subject, but also for each tissue type. This variation in optical properties is greater than the 10% variation observed in our phantom studies, and thus is assumed to be real variation, rather than variation caused by our fitting algorithms. Table 3.4 and Table 3.5 list the minimum and maximum values for $\mu_a$ and $\mu_s$' respectively for different tissue types.

Table 3.4: Minimum and maximum values for $\mu_a$ for BPD at 690 nm

| | Minimum ($cm^{-1)}$ | Maximum ($cm^{-1-)}$ |
|---|---|---|
| Abdominal Wall | 0.0011 | 0.245 |
| Aorta | 0.001 | 0.533 |
| Bladder | 0.001 | 0.976 |
| Bowel | 0.002 | 0.315 |
| Colon | 0.051 | 0.602 |
| Gall Bladder | 0.007 | 0.897 |
| Kidney | 0.0537 | 0.579 |
| Liver | 0.0114 | 1.080 |
| Rectum | 0.0058 | 0.145 |
| Spleen | 0.106 | 1.400 |
| Stomach | 0.01 | 0.149 |

Table 3.5: Minimum and maximum values for $\mu_s$' for BPD

| | Minimum ($cm^{-1}$) | Maximum ($cm^{-1}$) |
|---|---|---|
| Abdominal Wall | 0.859 | 14.600 |
| Aorta | 2.023 | 21.300 |
| Bladder | 3.660 | 33.500 |
| Bowel | 1.680 | 21.000 |
| Colon | 3.530 | 27.800 |
| Gall Bladder | 3.900 | 66.230 |
| Kidney | 13.500 | 29.100 |
| Liver | 2.030 | 82.600 |
| Rectum | 1.470 | 12.900 |
| Spleen | 17.500 | 50.600 |
| Stomach | 2.090 | 34.900 |

Figure 3.12 and Figure 3.13 also demonstrate wide-ranging variation. In Figure 3.12, there is no trend in changes in $[Hb]_{tot}$ post PDT. This indicates to us that PDT does not cause tissues to become hypoxic, which is a desirable clinical outcome. Again, the wide variation in

$[Hb]_{tot}$ between tissue types and subjects indicates real-time spectroscopy is necessary to truly know how PDT affects the $[Hb]_{tot}$ of a subject. The $StO_2$ levels (Figure 3.13) are of interest to us as they provide a way to measure photochemical oxygen consumption and vascular oxygenation. Figure 3.13 shows us PDT does cause significant vascular damage in the treated tissues. This is another desired clinical outcome as vascular hypoxia can cause tissues to be resistant to the more traditional cancer treatment methods: chemotherapy and radiotherapy. The number of different canine subjects with a measurement for a specific tissue type is listed in parentheses on the axis of Figure 3.10-Figure 3.14.

The concentration of BPD in tissues pre and post PDT (see Figure 3.14) demonstrates perhaps the widest range in determined values. While very generally we can observe that BPD concentration appears to decrease post PDT, this change is smaller than the overall variation in BPD concentration of different tissues and is therefore insignificant. This method of fluorescence spectroscopy, then, is too highly variable for use as a form PDT dosimetry. We observe no systematic photobleaching, further demonstrating how great this variation is.

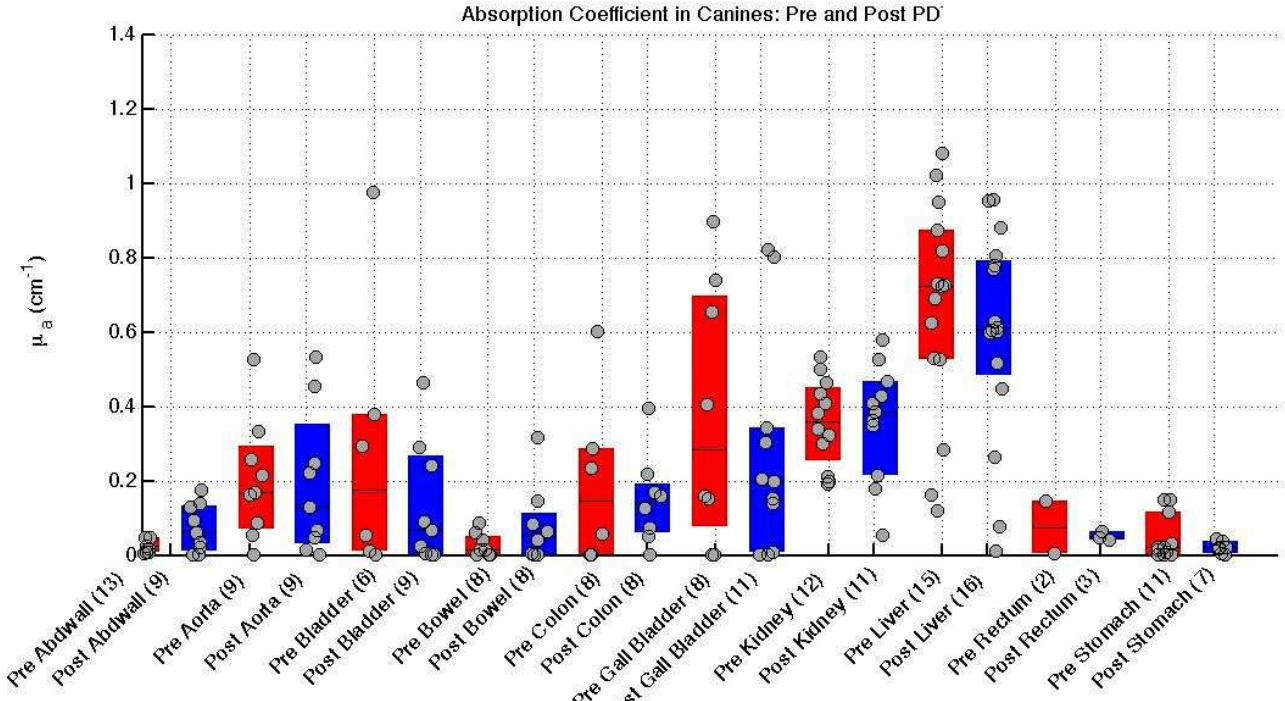


Figure 3.10: In vivo *absorption coefficient: Pre and Post PDT in canine BPD mediated PDT*

The pre PDT data (red) and post PDT data (blue) for each tissue type. The number of subjects for each tissue type are listed along the x-axis in parentheses. The individual data points are represented by gray circles. The box above the black line indicates the 75$^{th}$ percentile of the data, while the lower half represents the 25$^{th}$ percentile of data.

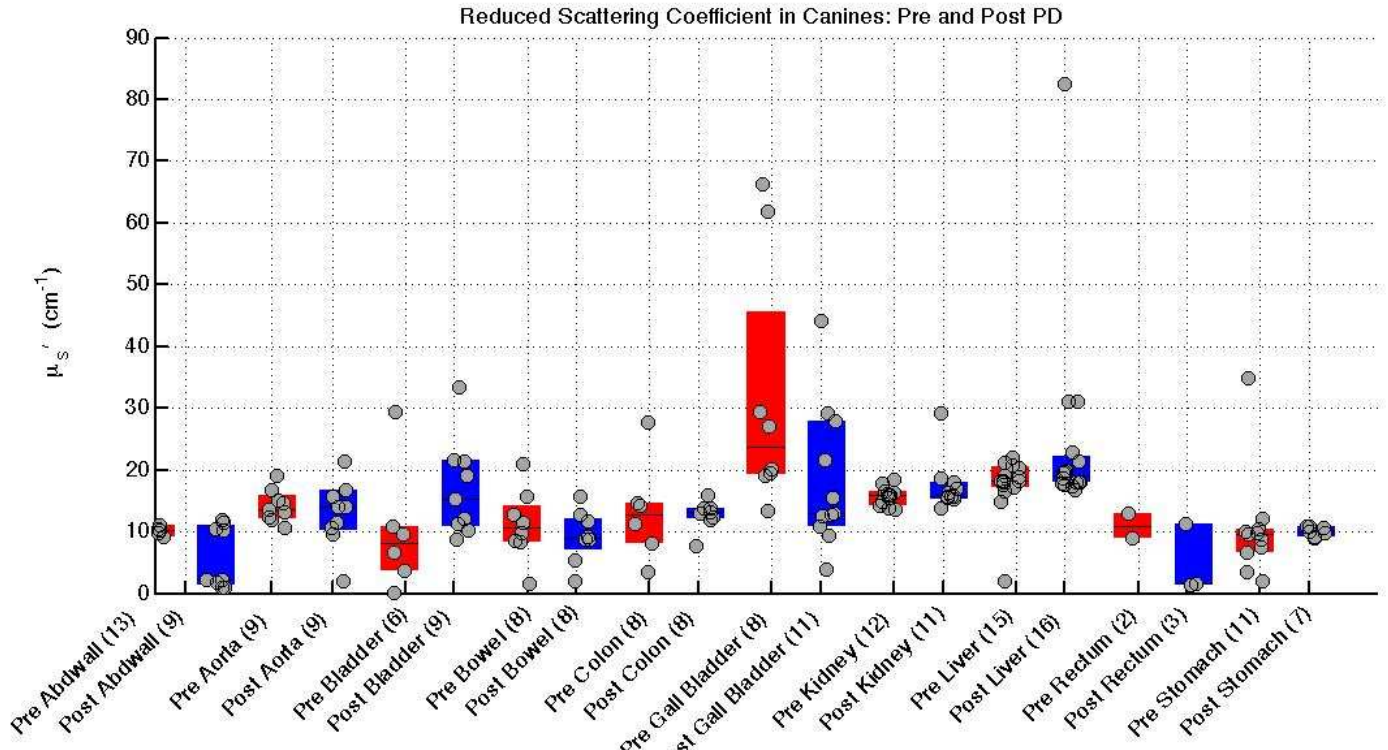


Figure 3.11: Reduced scattering coefficient pre and post PDT for canine BPD-mediated.

The pre PDT (red) and post PDT (blue) data for each tissue type. The same tissues that demonstrate higher absorption also demonstrate higher reduced scattering. The pre PDT data (red) and post PDT data (blue) for each tissue type. The number of subjects for each tissue type are listed along the x-axis in parentheses. The individual data points are represented by gray circles. The box above the black line indicates the 75$^{th}$ percentile of the data, while the lower half represents the 25$^{th}$ percentile of data.

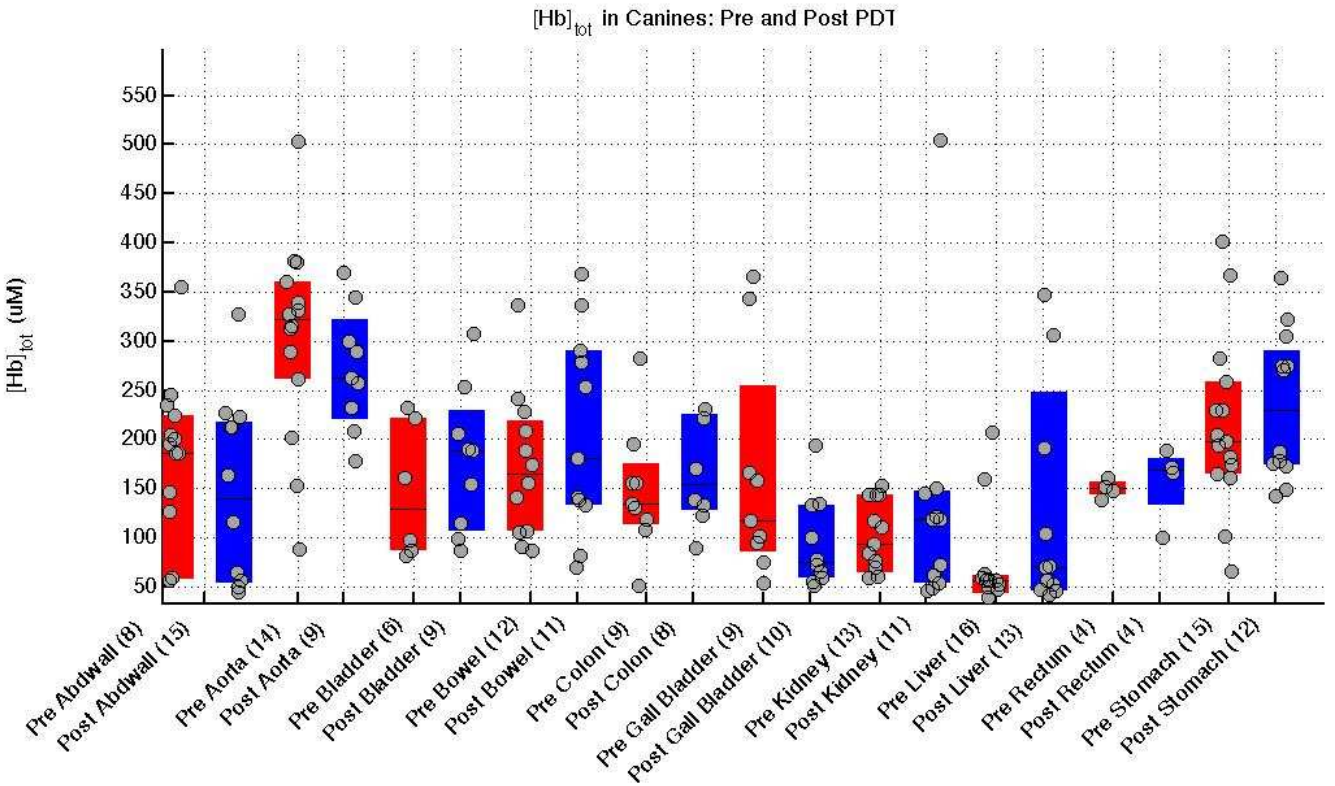


Figure 3.12: $[Hb]_{tot}$ in Canine interperitoneal cavities

The total hemoglobin of pre (red) and post (blue) PDT measurements obtained using spectral fitting. The pre PDT data (red) and post PDT data (blue) for each tissue type. The number of subjects for each tissue type are listed along the x-axis in parentheses. The individual data points are represented by gray circles. The box above the black line indicates the 75$^{th}$ percentile of the data, while the lower half represents the 25$^{th}$ percentile of data.

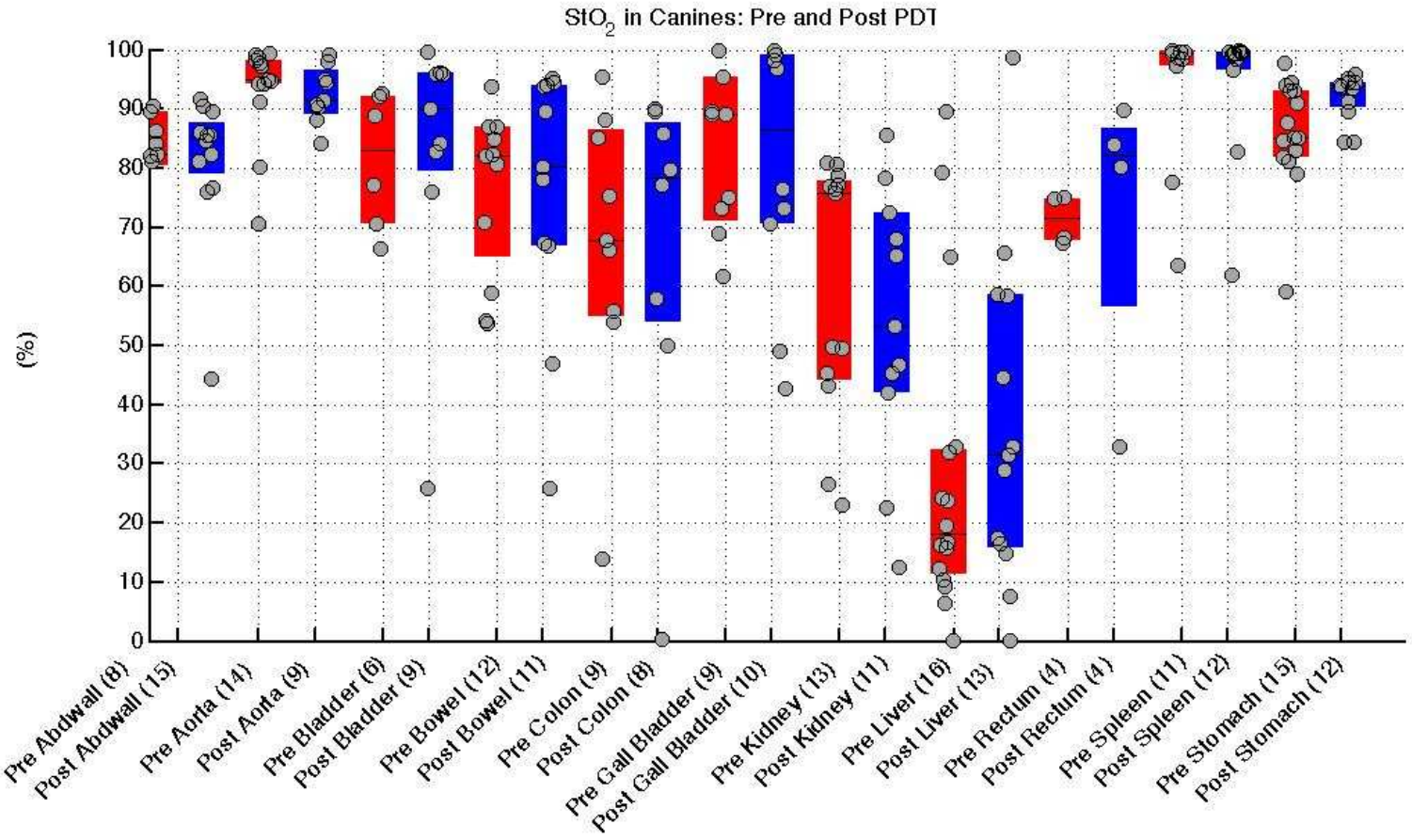


Figure 3.13: $StO_2$ in canine interperitoneal cavities pre and post PDT.

The pre PDT data (red) and post PDT data (blue) for each tissue type. The number of subjects for each tissue type are listed along the x-axis in parentheses. The individual data points are represented by gray circles. The box above the black line indicates the 75$^{th}$ percentile of the data, while the lower half represents the 25$^{th}$ percentile of data.

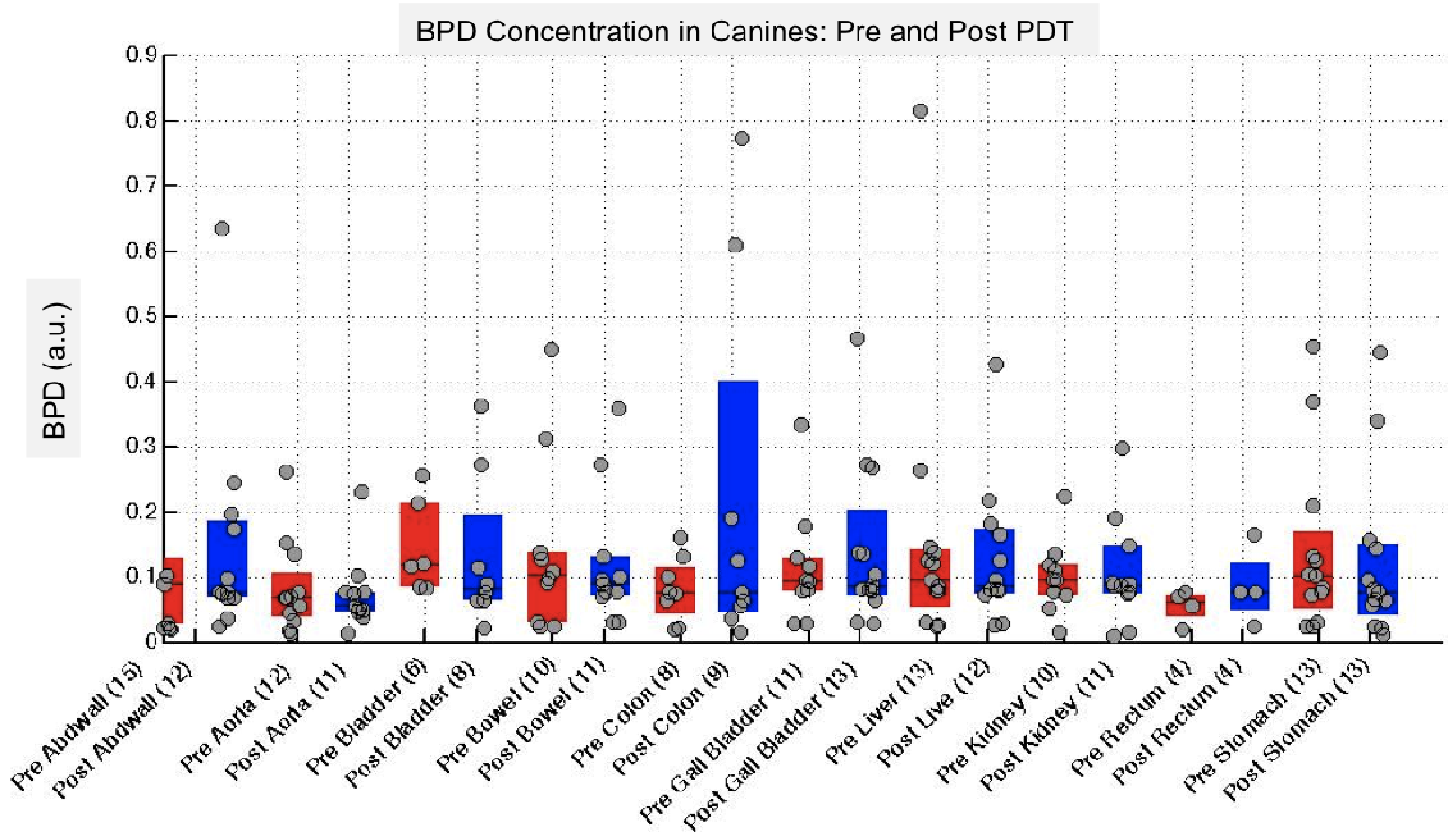


Figure 3.14: In vivo BPD concentration in canine interperitoneal cavities pre and post PDT

The concentration of BPD pre (red) and post (blue) PDT determined from in vivo fluorescence measurements. The pre PDT data (red) and post PDT data (blue) for each tissue type. The number of subjects for each tissue type are listed along the x-axis in parentheses. The individual data points are represented by gray circles. The box above the black line indicates the 75$^{th}$ percentile of the data, while the lower half represents the 25$^{th}$ percentile of data.

## 3.7 Measurements: HPPH

### *3.7.1 HPPH study introduction*

The same probe design described in section 3.2, and fitting algorithms used in section 3.6, we're used to collect data in-vivo in humans who were enrolled in the Phase I HPPH study first introduced in Chapter 1. The Phase I HPPH-mediated PDT study enrolls patients whose cancer is detected radiographically and is limited to a single hemithorax with pleural dissemination and whose pleural malignancy could be resected to a maximal thickness of 0.5 cm. All patients gave informed consent. The main objective of this study is to determine the maximum tolerated HPPH-mediated PDT dose in patients with pleural malignancies.

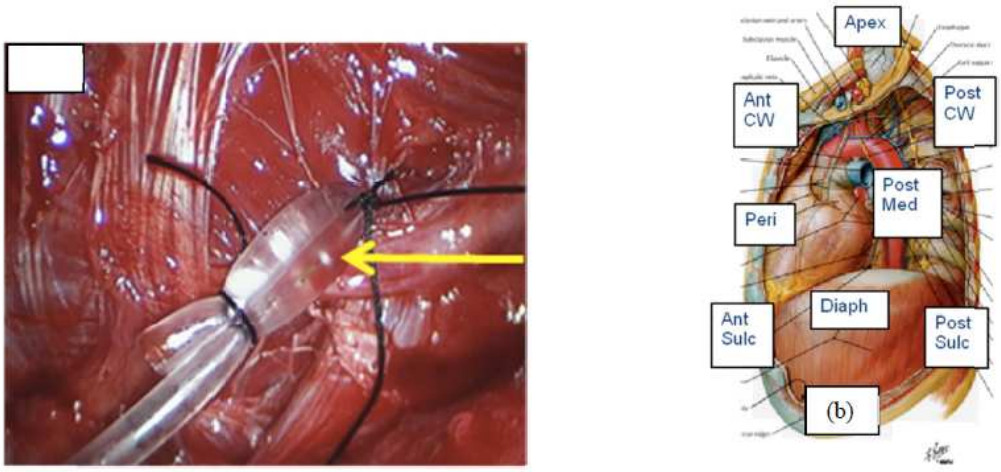


Figure 3.15: Detectors sutured into the thoracic cavity

a. Isotropic detector sutured in to the patient's chest wall and b. Anatomy of the thoracic cavity of the 8 isotropic detectors during pleural PDT: (1) Apex; (2) Anterior diaphragmatic sulcus (AS); (3) Posterior diaphragmatic sulcus (PS); (4) Pericardium (Peri);(5) Anterior chest wall (ACW); (6) Posterior chest wall (PCW); (7) Posterior mediastinum (PM); (8) Diaphragm (Diaph).[128]

The drug was first administered at a dose of 4 mg/m$^2$ and applied light fluence of 15 J/cm$^2$. Over the course of the study the light fluence was escalated to 60 J/cm$^2$ where the fluence was monitored by optical detectors sutured into the thoracic cavity of the patient (see

Figure 3.15). After debulking, the thoracic cavity was filled with a dilute Intralipid solution (0.01%) to facilitate more homogeneous delivery of light to the pleural walls. Light provided by a diode laser (B&W TEK, Inc. Newark, De) of 661 nm or 665 nm[2] was applied using a flat cut optical fiber (Medlight SA, Switzerland) sheathed within a endotracheal tube, where the balloon cuff was also filled with an Intralipid solution at 0.1% concentration. This delivery method was used to avoid burning tissues and protect the pleural walls (see ). Spectroscopic measurements were made pre and post light application, as in the BPD study (Section 3.5).

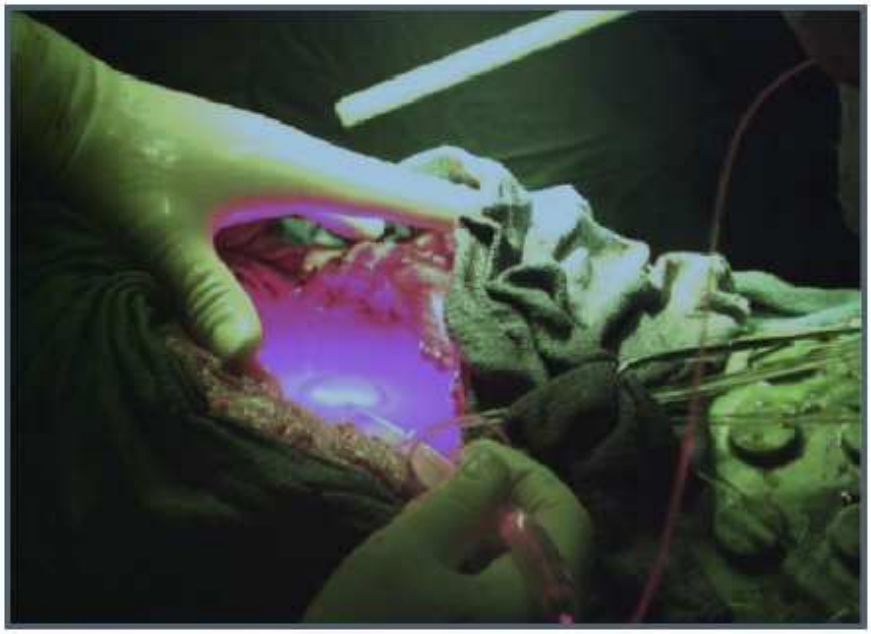

Figure 3.16: Application of light to the thoracic cavity during surgery.

A patient's thoracic cavity being treated with PDT in the clinic. Before the laser is turned on the isotropic detectors are sutured in a various points through the cavity after the bulk tumorous tissue is removed.

[2] The study began using the 661 nm laser, but after a study was done on the 665 laser (see A.3), this laser was put into use.

*3.7.2 Spectroscopy measurements*

The absorption coefficient, $\mu_a$ ($cm^{-1}$), and reduced scattering coefficient, $\mu_s'$ ($cm^{-1}$), were obtained by fitting reflectance spectra from the first four source-detector separations from 660 nm to 670 nm. The resulting values, seen in Figure 3.17 and Figure 3.18 are the average of $\mu_a$ and $\mu_s'$ from the four spectra respectively. We did not observe systematic differences in $\mu_a$ and $\mu_s'$ between measurements taken before and after irradiance. Figure 3.17 and Figure 3.18 show all values for $\mu_a$ and $\mu_s'$ respectively, with pre and post irradiance values plotted together. The number of different patients' tissues used to make each plot are listed in parentheses along the x-axis. It is interesting to note that lung tissue displays higher values for $\mu_a$ overall. The serratus tissue, on the other hand, shows lower overall $\mu_a$.

Reflectance fitting was used to determine values for $[Hb]_t$ that were above 2500 uM were not included in Figure 3.19 as values above 2500 uM are beyond the physical range of $[Hb]_t$ [127, 129]. While Figure 3.19 does display several data points well above the upper quartile of each tissue, overall data points are concentrated within the lower and upper quartiles, demonstrating that while there is patient to patient variation, each different tissue type has a distinct range of $[Hb]_t$ levels. As with the optical properties, there is no observable systematic difference between pre and post irradiance $[Hb]_t$ levels. This holds true for $StO_2$ levels, seen in Figure 3.20 as well. Here the data points are more widespread, indicating that oxygenation levels vary greatly both between patients and between different tissue types. Although, it can be observed that lung tissue does tend to have lower oxygenation levels than the surrounding tissues.

The measured fluorescence data, fitted for HPPH concentrations, is displayed in Figure 3.21. Only the spectrum from the first source-detector distance was fitted, as this spectrum had

the strongest signal and minimal noise. Data was fit from 600 nm to 790 nm and each fitted spectrum was divided by its corresponding autofluorescence spectrum to account for variation in autofluorescence between patients. Figure 3.21 shows that generally, HPPH levels are lower post irradiance, though this is not observed in all cases.

### 3.8 Results: HPPH

As in the BPD study in canines, the optical properties in Figure 3.17 and Figure 3.18 show great variation and no trend in changes of optical properties post PDT versus pre PDT. For clinical cases this result is particularly important. Current treatment protocol prescribes the fluence dose at a set level for all patients, as well as for all tissue types, based on the assumption that all tissue is optically homogeneous and the geometry of the target tissue does not affect overall fluence. Clearly Figure 3.17 and Figure 3.18 show there is great inhomogeneity between patients and between tissues. Assuming the target tissue is optically homogeneous, then, is quite unrealistic. For the most accurate fluence dose, these inhomogeneities must be accounted for, as light will penetrate into the different target tissues at substantially different amounts, resulting in non-uniform PDT treatments. As stated earlier, the observed variation is greater than the variation generated by our fitting algorithms and thus is real variation that must be accounted for. Table 3.6 and Table 3.7 list the minimum and maximum values for $\mu_a$ and $\mu_s$' respectively for different tissue types.

Figure 3.19 plots the $[Hb]_{tot}$ for the tissues measured, pre and post PDT. Generally, $[Hb]_{tot}$ decreases post PDT, but this is not observed in all cases (such as the esophagus) and the decrease in $[Hb]_{tot}$ is neither uniform nor statistically significant. The overall range in $[Hb]_{tot}$ does not display a trend, as the spread of values is different for each tissue type and also does not display a trend pre versus post PDT. This high variability indicates a need to

monitor $[Hb]_{tot}$ levels throughout treatment as each patient and tissue type is unique. Figure 3.20 shows that, generally, $StO_2$ decreases after PDT, but in no systematic or predictable way. Again we see the wide-ranging variability. The observed decrease in $StO_2$, however, is not great, demonstrating the PDT in the thoracic cavity does not cause tissue to become hypoxic, as observed in the canine study.

The HPPH concentration, plotted in Figure 3.21, continues to exhibit wide-ranging variability between tissue types and patients. As in the BPD canine study, this method of monitoring drug concentration does allow us to determine a model that would reliably predict drug concentration post PDT. As no systematic photobleaching is observed, the motivation for patient-by-patient drug concentration measuring becomes clear, particularly in light of the observed inhomogeneity.

Table 3.6: Minimum and maximum values for $\mu_a$ for HPPH

| | Minimum ($cm^{-1}$) | Maximum ($cm^{-1}$) |
|---|---|---|
| Aorta | 0.002 | 0.950 |
| Chest wall | 0.001 | 1.147 |
| Diaphragm | 0.004 | 2.517 |
| Esophagus | 0.036 | 0.649 |
| Lung | 0.062 | 2.517 |
| Pericardium | 0.005 | 1.519 |
| Serratus | 0.004 | 0.577 |

Table 3.7: Minimum and maximum values for $\mu_s'$ for HPPH

| | Minimum ($cm^{-1}$) | Maximum ($cm^{-1}$) |
|---|---|---|
| Aorta | 2.080 | 51.712 |
| Chest wall | 2.080 | 27.661 |
| Diaphragm | 2.170 | 57.886 |
| Esophagus | 10.679 | 50.529 |
| Lung | 14.355 | 61.624 |
| Pericardium | 11.015 | 52.754 |
| Serratus | 2.341 | 35.431 |

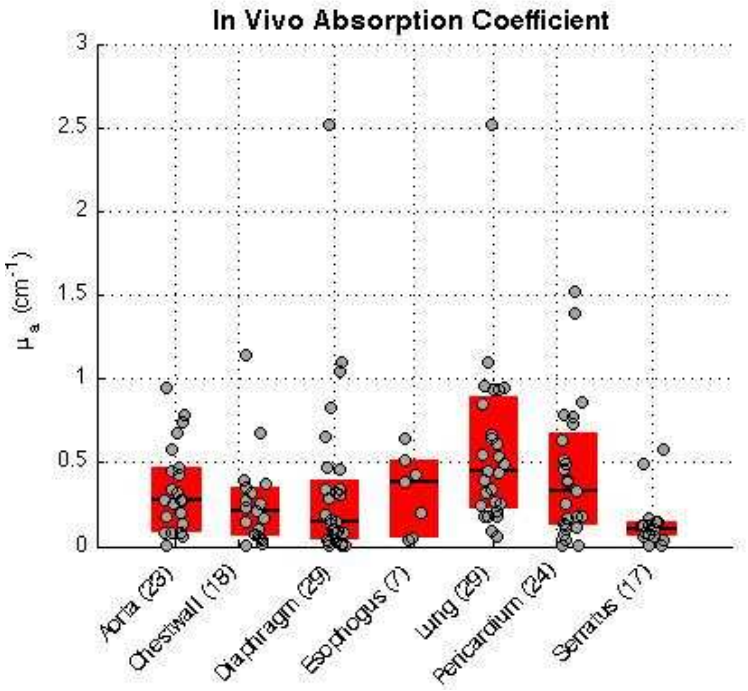


Figure 3.17: In vivo absorption coefficients measured in the thoracic cavities of humans for HPPH-mediated pleural PDT

The number of patients for each type of tissue is listed in parentheses along the x-axis. The mean value of $\mu_a$ is indicated by the line across the middle of each box, with the upper and lower quartiles determining the size of each box. The pre PDT data (red) and post PDT data (blue) for each tissue type. The number of subjects for each tissue type are listed along the x-axis in parentheses. The individual data points are represented by gray circles. The box above the black line indicates the 75$^{th}$ percentile of the data, while the lower half represents the 25$^{th}$ percentile of data.

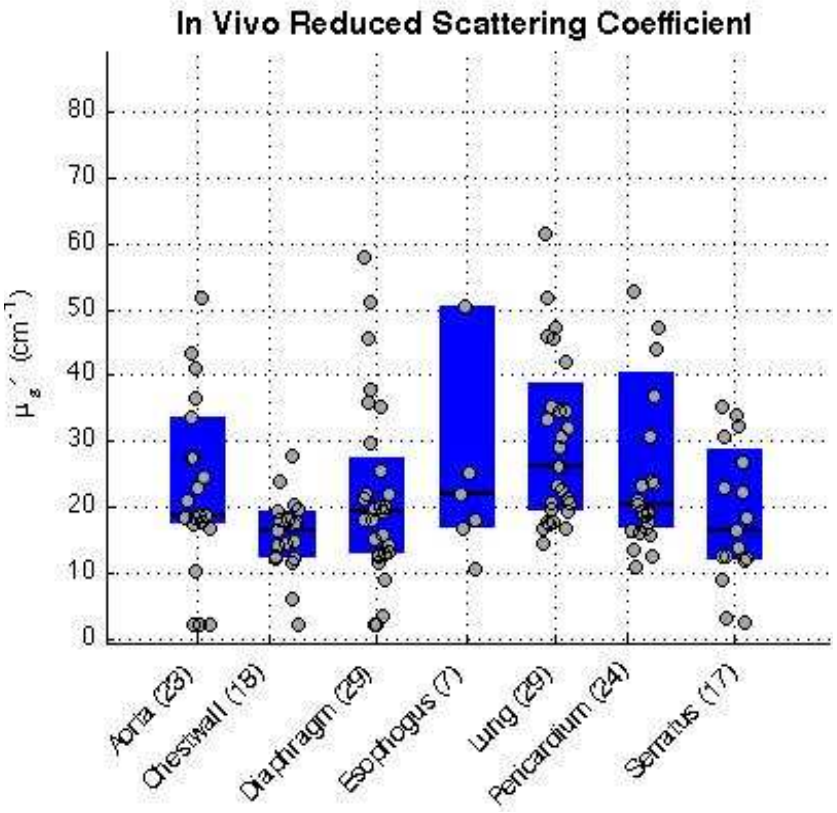


Figure 3.18: In vivo reduced scattering coefficients measured in patients for a variety of tissues.

The number of patients for each type of tissue is listed in parentheses along the x-axis. The mean value of $\mu_s'$ is indicated by the line across the middle of each box, with the upper and lower quartiles determining the size of each box. The pre PDT data (red) and post PDT data (blue) for each tissue type. The number of subjects for each tissue type are listed along the x-axis in parentheses. The individual data points are represented by gray circles. The box above the black line indicates the 75$^{th}$ percentile of the data, while the lower half represents the 25$^{th}$ percentile of data.

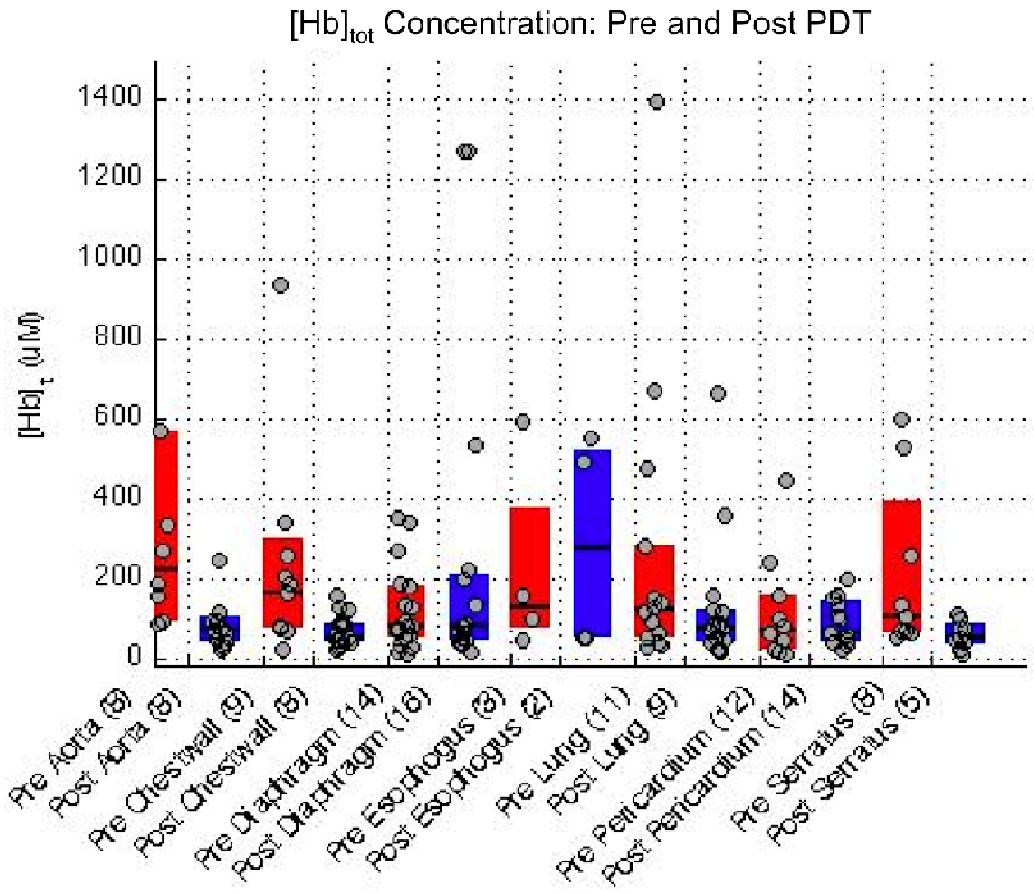


Figure 3.19: In vivo $[Hb]_{tot}$ (uM) measured in the thoracic cavity of patients

Pre (red) and Post (blue) PDT measurements for $[Hb]_{tot}$. The number of patients for each type of tissue is listed in parentheses along the x-axis. The mean value of $[Hb]_{tot}$ is indicated by the black line across the middle of each box plot, with the upper and lower quartiles determining the size of each box. The pre PDT data (red) and post PDT data (blue) for each tissue type. The number of subjects for each tissue type are listed along the x-axis in parentheses. The individual data points are represented by gray circles. The box above the black line indicates the 75$^{th}$ percentile of the data, while the lower half represents the 25$^{th}$ percentile of data.

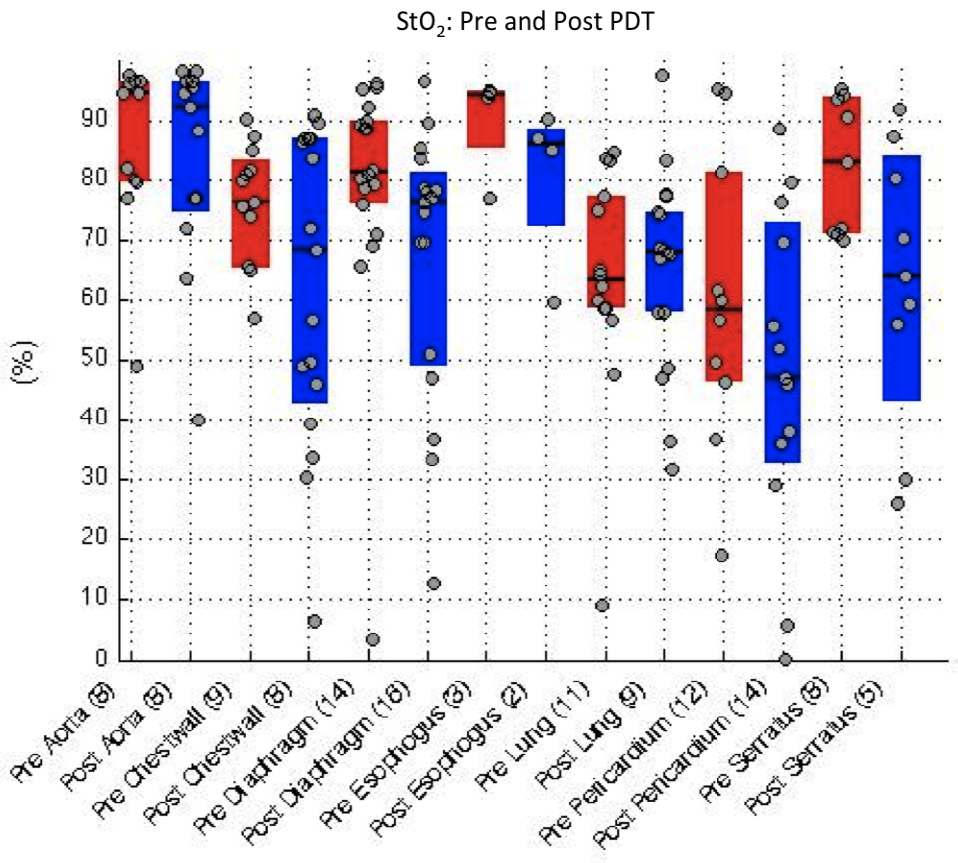


Figure 3.20: In vivo $StO_2$ measured in the thoracic cavity of patients, pre and post PDT

Pre (red) and Post (blue PDT measurements of $StO_2$. The number of patients for each type of tissue is listed in parentheses along the x-axis. The black line indicates the mean value of StO2 across the middle of each box plot, with the upper and lower quartiles determining the size of each box. The pre PDT data (red) and post PDT data (blue) for each tissue type. The number of subjects for each tissue type are listed along the x-axis in parentheses. The individual data points are represented by gray circles. The box above the black line indicates the 75$^{th}$ percentile of the data, while the lower half represents the 25$^{th}$ percentile of data.

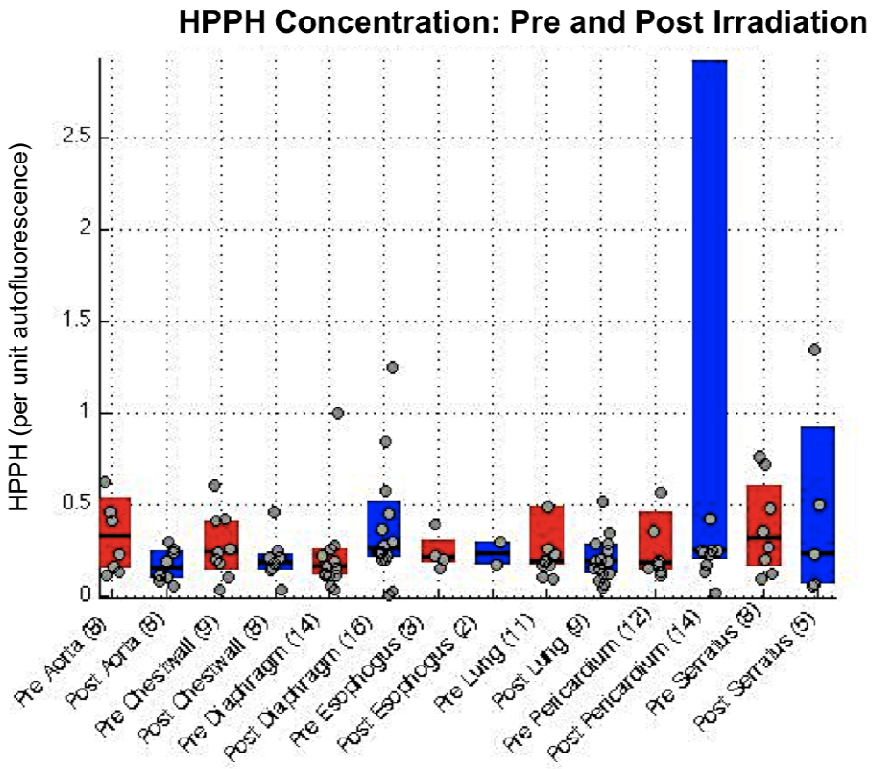


Figure 3.21: In vivo HPPH concentration measured in the thoracic cavity of patients, pre and post PDT

Pre (red) and Post (blue) PDT measurements of HPPH concentration. The number of patients for each type of tissue is listed in parentheses along the x-axis. The mean value of HPPH is indicated by the line across the middle of each box, with the red and blue bar representing the middle quartiles. The pre PDT data (red) and post PDT data (blue) for each tissue type. The number of subjects for each tissue type are listed along the x-axis in parentheses. The individual data points are represented by gray circles. The box above the black line indicates the 75$^{th}$ percentile of the data, while the lower half represents the 25$^{th}$ percentile of data.

## 3.9 Discussion

We successfully obtained in-vivo optical properties, $[Hb]_t$, oxygenation saturation, and drug concentration levels for both the canine BPD study and the Phase I Clinical HPPH trial. For both the BPD and HPPH studies, we determined the optical properties are not significantly affected by irradiation during PDT. These optical properties varied greatly between different tissue types, but, with the exception of several outliers, the $\mu_a$ and $\mu_s$' of each tissue types demonstrated a characteristic range between different subjects. These ranges of $\mu_a$ and $\mu_s$' can

inform PDT treatment planning in that we have a relative idea of which tissue types are more optically absorbing or scattering. The optical properties determined here will be used in fluence modeling in Chapter 4 and Chapter 5.

Table 3.8: Mean values of in-vivo optical properties for HPPH patients

| S/N | Tissue type | $\mu_a$ | std $\mu_a$ | $\mu_s'$ | std $\mu_s'$ | S/N | Tissue type | $\mu_a$ | std $\mu_a$ | $\mu_s'$ | std $\mu_s'$ |
|---|---|---|---|---|---|---|---|---|---|---|---|
| pat 1 | Chest wall | 0.2 | 0.0 | 12.2 | 0.4 | pat16 | Aorta | 0.3 | 0.0 | 18.5 | 0.1 |
| | Diaphragm | 0.3 | 0.0 | 12.5 | 0.1 | | Chest wall | 0.0 | 0.0 | 14.9 | 0.2 |
| | Esophagus | 0.0 | 0.0 | 50.5 | 4.7 | | Diaphragm | 0.1 | 0.2 | 13.0 | 5.0 |
| | Lung | 0.2 | 0.0 | 61.6 | 8.6 | | Lung | 1.1 | 0.0 | 30.7 | 0.4 |
| | Pericardium | 0.4 | 0.0 | 12.4 | 0.1 | | Pericardium | 0.3 | 0.0 | 21.2 | 0.2 |
| | Seratus | 0.1 | 0.0 | 34.1 | 1.7 | pat20 | Aorta | 0.6 | 0.1 | 51.7 | 5.1 |
| | Skin | 0.0 | 0.0 | 44.7 | 1.3 | | Esophagus | 0.4 | 0.0 | 16.6 | 0.1 |
| pat3 | Aorta | 0.3 | 0.0 | 43.5 | 1.3 | | Lung | 0.3 | 0.0 | 17.9 | 0.4 |
| | Chestwall | 0.0 | 0.0 | 32.0 | 0.5 | | Skin | 0.2 | 0.2 | 12.2 | 5.4 |
| | Diaphragm | 0.5 | 0.0 | 18.0 | 0.4 | pat21 | Aorta | 0.5 | 0.0 | 16.7 | 0.1 |
| | Lung | 0.2 | 0.0 | 34.7 | 1.2 | | Diaphragm | 0.1 | 0.0 | 37.8 | 1.7 |
| | Pericardium | 0.1 | 0.0 | 52.8 | 2.7 | | Lung | 0.6 | 0.0 | 17.7 | 0.1 |
| | Seratus | 0.1 | 0.1 | 27.0 | 1.1 | | Pericardium | 0.6 | 0.0 | 18.7 | 0.2 |
| | Skin | 0.3 | 0.1 | 5.3 | 0.9 | pat22 | Chest wall | 0.4 | 0.0 | 6.2 | 0.1 |
| | Tumor | 0.0 | 0.0 | 36.3 | 0.5 | | Diaphragm | 0.1 | 0.0 | 12.8 | 0.1 |
| pat5 | Diaphragm | 1.0 | 0.0 | 3.5 | 0.0 | | Esophagus | 0.6 | 0.0 | 18.2 | 0.3 |
| | Diaphragm | 1.1 | 0.1 | 13.1 | 0.3 | | Lung | 0.4 | 0.0 | 17.3 | 0.2 |
| | Lung | 0.5 | 0.0 | 21.4 | 0.3 | | Pericardium | 0.9 | 0.0 | 20.3 | 0.1 |
| | Pericardium | 0.3 | 0.0 | 19.0 | 0.3 | pat24 | Diaphragm | 0.7 | 0.0 | 21.2 | 0.6 |
| | Pleura | 1.0 | 0.1 | 3.1 | 0.1 | | Esophagus | 0.0 | 0.0 | 10.7 | 0.1 |
| | Seratus | 0.5 | 0.0 | 18.4 | 0.2 | | Lung | 0.2 | 0.0 | 32.2 | 1.5 |
| | Skin | 0.7 | 0.7 | 5.3 | 2.1 | | Pericardium | 1.4 | 0.6 | 47.2 | 10.8 |
| | Tumor | 0.1 | 0.0 | 15.7 | 0.2 | | Seratus | 0.1 | 0.0 | 12.6 | 0.2 |
| pat13 | Aorta | 0.4 | 0.2 | 22.9 | 3.1 | pat28 | Chest wall | 0.1 | 0.0 | 11.6 | 0.1 |
| | Chest wall | 0.3 | 0.0 | 14.1 | 0.1 | | Diaphragm | 0.3 | 0.0 | 15.3 | 0.2 |
| | Diaphragm | 0.0 | 0.0 | 45.6 | 1.4 | | Lung | 0.2 | 0.0 | 33.5 | 2.5 |
| | Lung | 0.1 | 0.0 | 45.8 | 2.7 | | Seratus | 0.1 | 0.0 | 12.1 | 0.2 |
| | Pericardium | 0.8 | 0.0 | 16.9 | 0.3 | pat34 | Aorta | 0.2 | 0.0 | 18.3 | 0.2 |
| | Seratus | 0.2 | 0.1 | 11.9 | 1.2 | | Chestwall | 0.1 | 0.0 | 2.1 | 0.1 |
| pat15 | Aorta | 0.3 | 0.0 | 18.8 | 0.2 | | Diaphragm | 0.3 | 0.0 | 19.5 | 0.2 |
| | Chest wall | 0.1 | 0.0 | 16.5 | 0.2 | | Lung | 0.9 | 0.0 | 26.1 | 0.3 |
| | Diaphragm | 0.1 | 0.0 | 14.0 | 0.1 | | | | | | |
| | Lung | 0.3 | 0.0 | 19.8 | 0.2 | | | | | | |
| | Pericardium | 0.1 | 0.0 | 16.1 | 0.2 | | | | | | |
| | Tumor | 0.1 | 0.0 | 15.1 | 0.2 | | | | | | |

The $[Hb]_t$ and oxygen saturation obtained from our measurements also display great variation between subjects and tissue types. Utilizing the $[Hb]_t$ and oxygen saturation to determine treatment outcome is beyond the scope of this work. However, our determined

values of $[Hb]_t$ and oxygen saturation will add new information to the work of others whose work focuses on the effects of total hemoglobin and oxygen saturation on treatment outcome and how these quantities can be used to improve PDT treatment planning. The determined concentrations of HPPH help to monitor the behavior of the photosensitizer during irradiation. From the results of the BPD and HPPH studies, we find generally, photosensitizer concentration decreases after irradiation. This outcome is expected, the activation of the photosensitizer when it is irradiated utilizes the drug to induce tissue damage. As observed in Figure 3.14 and Figure 3.21, photosensitizer remains in the tissue. The drug remaining in the tissue affects the photosensitivity the subject will experience post treatment.

Accounting for the great variation in all measured quantities in the two studies presented here shows the great need for real time, in vivo measurements during treatment. A fluence dose determined in this way is a large step from the current fluence dose protocol, which is based on a optically homogeneous, semi-infinite medium model. While the initial survival outcomes from the HPPH study are promising, it would be most interesting to observe how PDT treatment, tailored to each patient's unique properties, affect treatment outcome.

# Chapter 4

# Light Distribution Modeling

## 4.1 Introduction

The spectroscopy data presented in the preceding chapter provides only one element of several for optimizing PDT light dosimetry. As discussed by Zhu and Finlay [23], light fluence is currently based on both the incident light as well as received at the tissue surface. The total light distribution in the treatment tissue is a function, in part, of the tissues' properties, as determined in Chapter 3, and also a combination of direct and scattered light (note that factors such as tissues oxygenation are also important to PDT dosimetry, but are beyond the scope of the work presented here). Several PDT dosimetry systems attempt to monitor incident and scattered light at the tissue surface or interstitially [23, 24, 26, 130, 131], but light distribution modeling serves as a potential tool to optimize treatment planning. This chapter presents several studies of light distribution modeling in different geometries, building upon the work of existing methods[5, 43-45, 56].

MC simulations are a standard method of photon transport modeling[43, 132] and frequently used to verify analytic models. Beginning with the simplest scenario, we consider the fluence modeling in a semi-infinite media and improve upon existing empirical solutions[133] using Monte Carlo simulations (MC) for varying light field sizes. From the semi-infinite geometry

we move on to simulations in a spherical cavity. The expanded theory of fluence in a spherical cavity is compared to MC simulations of a spherical air cavity for a range of optical properties. We find in the presence of an attenuating medium Star's analytic solution no longer holds true and MC results are compared to an empirical solution. Finally, with the view to developing a fluence model more applicable to the highly asymmetric geometries of the thoracic cavity, we conduct a series of MC simulations for an oblate ellipsoidal cavity. At present, there is no analytic solution for cavities that are not radially symmetric in all directions.

The purpose of these studies is to verify the analytic model for fluence against simulation results previously unreported for light distribution in spherical air cavity geometries which account for the effect on fluence caused by multiple scattering in the cavity. And also to explore scenarios for which there is no analytic solution but more closely resemble what is observed in pleural PDT. The consideration of arbitrary cavity geometries presents a considerable challenge in modeling light distribution with respect to photon path tracking. The results of this modeling combined with the in vivo spectroscopy data presented in Chapter 3 are the first steps to developing patient-specific PDT dosimetry system.

## 4.2 Semi-Infinite Modeling

Calculating the fluence in a semi-infinite medium is the simplest geometry (beyond an infinite medium) considered when modeling photon transport and light distribution. The analytic solution presented in Section 2.3.1 is based on applying the diffusion approximation to a set of boundary conditions appropriate to a semi-infinite medium, where, unlike fluence in a cavity, there is no multiple scattering to consider. This solution breaks down, however, when the reduced scattering coefficient is not considerably greater than the absorption coefficient, as in the instance of clinical cases where blood is present. To solve analytically for the fluence for a

semi-infinite medium with greater accuracy, the $P_3$ approximation discussed in section 2.3.2 is applied[68, 134, 135]. The $P_3$ approximation requires continuity of each moment of radiance at the boundary. Recall that eqn. ( 2.18 ) describes the fluence for a semi-infinite medium and is a complicated expression (see A.1 ).

Steve L. Jacques [133] determined a simpler empirical expression using MC simulations for a collimated light source incident on a planar medium. His expression for the fluence in the medium for an incident broad beam (radius>2 cm) is:

$$\phi(z) = S_0 k e^{(-\mu_{eff} z)}, \tag{4.1}$$

where $S_0$ is the light source (W/cm), z is the depth of measurement, $\mu_{eff}=(3\mu_a\mu_{tr})^{1/2}$, and $k$, the backscattering coefficient, is given by:

$$k = 3 + 5.1\rho - 2e^{(-9.7\rho)}. \tag{4.2}$$

Where, in relation to eqns.( 4.1 ) and ( 4.2 ), $R_d$ is determined from the simulation results. Jacques approximated $\rho$ to be [133]:

$$\rho \approx e^{(-7.8\delta\mu_a)} = e^{\left(-7.8/\sqrt{1+\mu_s'/\mu_a}\right)}. \tag{4.3}$$

The factors in eqns.( 4.2 ) and ( 4.3 ) were determined from a rigorous series of MC simulations performed by Jacques[133]. In this work, we improve upon constants in eqn.( 4.2 ). Instead of using eqn. ( 4.3 ), however, we will fit our MC results with ( 2.35 ), as it is a by obtaining new fits of fluence from our own MC simulations for a semi-infinite medium for varying circular field sizes, from broad beams to small fields (radius<2 cm).

## 4.3 Semi-Infinite Monte Carlo Simulations

### *4.3.1 Monte Carlo Methods for a Semi-Infinite Medium*

Previous work modeled light distributions for broad beam light sources in air or water incident on semi-infinite media[43, 132, 133]. In PDT, however, often the treatment of surface lesions require a light field size less than 2 cm in radius[136]. The total fluence rate is affected by this small light field size as less light scattering occurs and significantly reduces the fluence in the medium (recall there is no multiple scattering of light in this scenario). Building upon the work of Zhu et al. [81, 136], we conduct a series of MC simulations to determine new empirical expressions for $R_d$ and $k$ for the fluence of small fields sizes. An expression for $k$ and values for $\mu$ (from eqns.( 4.1 ), ( 4.2 ), and ( 2.35 ) ) are fitted for large to small field radius, and these new values increase modeled fluence accuracy compared to the previously published expressions determined for broad beam light sources.

The MC simulation is setup using a slab of optical homogeneous medium with infinite length and finite depth that is surrounded by air according to the method developed by Zhu et al. [81]. The indices of refraction of the tissue medium and air are 1.4 and 1 respectively. The absorption and reduced scattering coefficients of the simulation medium were varied according to Table 4.1.

For scoring efficiency, the light source is a pencil-beam that is incident on the medium with varying angle. When calculating the fluence from simulation results, the pencil beam is convoluted according to eqn.( 4.4 ):

$$\phi(x,y,z)/\phi_{air} = p \otimes I = \iint p(x'-x, y'-y, z) \cdot I(x', y') dx' dy' . \quad (4.4)$$

Table 4.1: Optical property combinations for MC simulations

| Absorption Coefficient ($cm^{-1}$) | Reduced Scattering Coefficient ($cm^{-1}$) |
|---|---|
| 0.01 | 5 |
| 0.1 | 5 |
| 0.5 | 5 |
| 1.0 | 5 |
| 0.01 | 10 |
| 0.1 | 10 |
| 0.5 | 10 |
| 1.0 | 10 |
| 0.01 | 15 |
| 0.1 | 15 |
| 0.5 | 15 |
| 1.0 | 15 |
| 0.01 | 25 |
| 0.1 | 25 |
| 0.5 | 25 |
| 1.0 | 25 |
| 0.01 | 40 |
| 0.1 | 40 |
| 0.5 | 40 |
| 1.0 | 40 |

The pencil-beam kernel is denoted by *p* and is calculated by the simulation. *I* is 1 inside the light field and zero outside the light field. The photons are launched and scattered in the forward direction (g~0.9)[137], where the photon density, $\rho_n$, is scored via cylindrically

symmetric voxels of 0.01 cm thickness, 0.2 cm width, and 1° size. The recorded $\rho_n$ is then used to calculate the fluence per unit incident light power of the light source in the medium using the number of incident photons, $N_{inc}$, as $\phi=\rho_n/N_{inc}/\mu_a$.

### *4.3.2 Semi-Infinite MC Results for $\rho$ and k*

The fits for $\mu$, *k* and $\rho$ were obtained via the fitting process for a non-linear function using the optimization fitting function from MATLAB™ *fitfun*. The function *fitfun* utilizes the MATLAB™ function *fminsearch* (mentioned previously in Section 3.3), which uses an unconstrained non-linear optimization technique. This function finds the minimum of a scalar function of several variables of a specified functional form using an initial estimate for the minimum. The determined minimum is the best-fit value for the scalar in question.

### *4.3.3 Fitting results k in terms of fluence*

Equation ( 4.1 ) is well suited for large field size (radius>2 cm), but this solution for fluence breaks down at smaller field sizes. In considering smaller field sizes we fit for $\mu$ and *k*:

$$\frac{\phi(z)}{\phi_{air}} = ke^{(-\mu z)}, \qquad (4.5)$$

The resulting fitted curves are plotted with the MC results using the optical properties listed in Table 4.1.

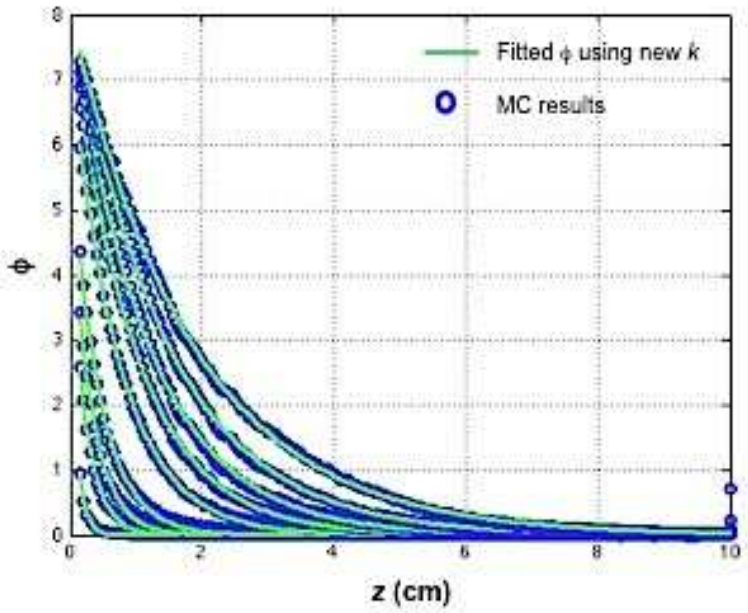


Figure 4.1: MC results for fluence compared to fit with new values for *k* and $\mu$

Fields size from lower left corner to upper right:

0.1 cm, 0.25 cm, 0.35 cm, 0.5 cm, 1.0 cm, 1.5 cm, 2.0 cm, 3 cm, and 8.0 cm

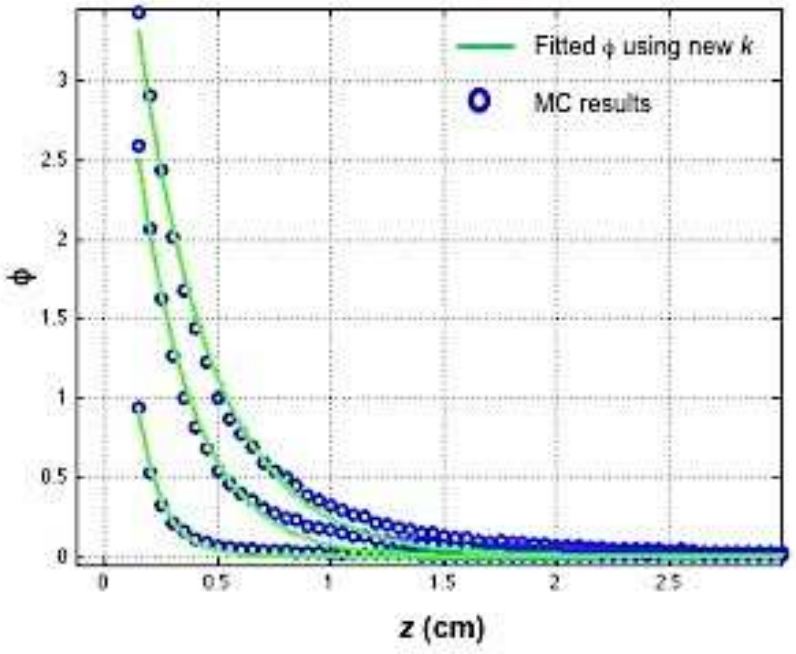


Figure 4.2: MC results for fluence compared to fit with new values of *k* for small field sizes

Fields sizes from lower left corner to upper right: 0.1 cm, 0.25 cm, 0.35 cm

Equation ( 4.1 ) states that $\phi(x)$ is a function of $k$ and $\mu_{eff}$ for broad beams, and by eqn. ( 4.2 ), a function of $\rho$ . This relationship holds only for field sizes greater than 2 cm. In generating Figure 4.2, a new $\mu$ had to be fitted for numerically in order to obtain an accurate fit.

Table 4.2 lists $\mu_{eff}$ for the simulations run ($\mu_a$ listed in the columns, $\mu_s$' listed in the rows).

Table 4.3 lists these new values to replace $\mu_{eff}$ in eqn. ( 4.1 ) for smaller field sizes, which generate the curves generated in Figure 4.1 and Figure 4.2[*].

Table 4.2: $\mu_{eff}$ for the optical properties used in the MC simulations

| | **0.01 cm$^{-1}$** | **0.1 cm$^{-1}$** | **0.5 cm$^{-1}$** | **1 cm$^{-1}$** |
|---|---|---|---|---|
| **5 cm$^{-1}$** | 0.387 | 1.225 | 2.739 | 3.873 |
| **10 cm$^{-1}$** | 0.548 | 1.732 | 4.743 | 5.477 |
| **15 cm$^{-1}$** | 0.671 | 2.121 | 4.743 | 6.708 |
| **25 cm$^{-1}$** | 0.866 | 2.739 | 6.124 | 8.660 |
| **40 cm$^{-1}$** | 1.095 | 3.464 | 7.746 | 10.954 |

[*] Note that these fits are the results of simulations run for the optical properties listed in Table 4.1

Table 4.3: Values of μ determined numerically to replace $\mu_{eff}$ in eqn. ( 4.5 )for small beam sizes

| **Circular Field Size, radius = 0.1 cm** | | | | |
|---|---|---|---|---|
| | **0.01 cm$^{-1}$** | **0.1 cm$^{-1}$** | **0.5 cm$^{-1}$** | **1 cm$^{-1}$** |
| **5 cm$^{-1}$** | 2.021 | 2.336 | 2.844 | 3.230 |
| **10 cm$^{-1}$** | 2.417 | 2.822 | 3.557 | 4.140 |
| **15 cm$^{-1}$** | 2.514 | 3.115 | 4.043 | 4.753 |
| **25 cm$^{-1}$** | 2.799 | 3.434 | 4.744 | 5.561 |
| **40 cm$^{-1}$** | 2.936 | 3.701 | 5.446 | 6.574 |
| **Circular Field Size, radius =0.25 cm** | | | | |
| | **0.01 cm$^{-1}$** | **0.1 cm$^{-1}$** | **0.5 cm$^{-1}$** | **1 cm$^{-1}$** |
| **5 cm$^{-1}$** | 2.021 | 2.336 | 2.844 | 3.230 |
| **10 cm$^{-1}$** | 2.417 | 2.822 | 3.557 | 4.140 |
| **15 cm$^{-1}$** | 2.514 | 3.115 | 4.043 | 4.753 |
| **25 cm$^{-1}$** | 2.799 | 3.434 | 4.744 | 5.561 |
| **40 cm$^{-1}$** | 2.936 | 3.701 | 5.446 | 6.574 |
| **Circular Field Size, radius =0.35 cm** | | | | |
| | **0.01 cm$^{-1}$** | **0.1 cm$^{-1}$** | **0.5 cm$^{-1}$** | **1 cm$^{-1}$** |
| **5 cm$^{-1}$** | 2.021 | 2.336 | 2.844 | 3.230 |
| **10 cm$^{-1}$** | 2.417 | 2.822 | 3.557 | 4.140 |
| **15 cm$^{-1}$** | 2.514 | 3.115 | 4.043 | 4.753 |
| **25 cm$^{-1}$** | 2.799 | 3.434 | 4.744 | 5.561 |
| **40 cm$^{-1}$** | 2.936 | 3.701 | 5.446 | 6.574 |

In the same manner, when fitting ρ we used the functional form of ( 2.35 ), fitting for parameter *c(1), c(2), c(3)*:

$$\rho = \frac{a'}{2}\left(c(1) + e^{-\sqrt{c(2)(1-a')}}\right) e^{\sqrt{c(3)(1-a')}}, \qquad (4.6)$$

where the parameters *c(1), c(2), and c(3)* were optimized using *fitfun*. Figure 4.3 shows the fits obtained from MC results $\rho$. *The resulting fitting parameters for broad beams (radius r larger than 2 cm) are shown in Table 4.4.*

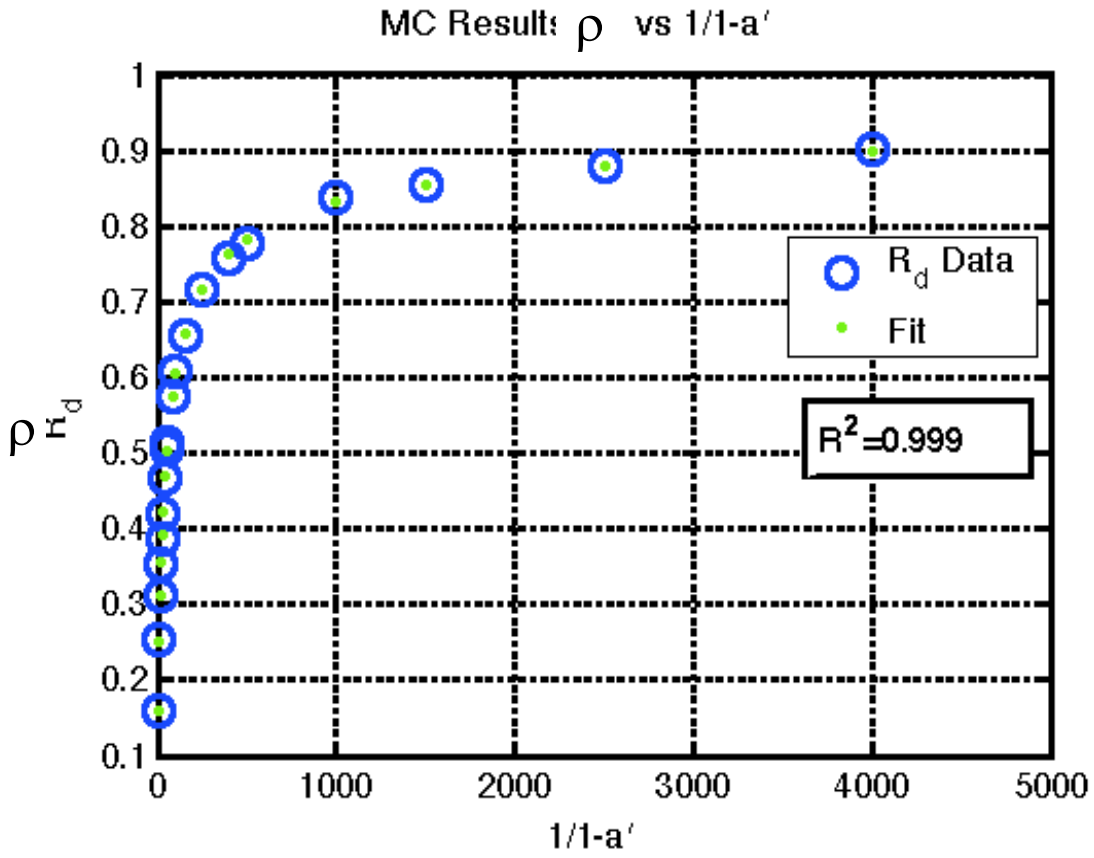


Figure 4.3: ρ as a function of albedo, comparing MC results to model fit for broad circular beams with radius larger than 2 cm.

Table 4.4 Fitting parameters for Eq. 4.6 for broad beam MC simulated diffuse reflectance ρ and reduced albedo a′.

| c(1) | c(2) | c(3) |
|---|---|---|
| 0.941 | 20.389 | 6.614 |

Table 4.5: $R^2$ between the respective fits to the MC data

| | |
|---|---|
| Jacques | 0.810 |
| Zhu and Meo | 0.982 |

Figure 4.3 demonstrates the robustness of our fitting process. The functional form for the backscattering coefficient, *k,* used for fitting optimization then becomes, with respect to eqn.( 4.2 ):

$$k = m(1)\rho^{m(2)} + m(3) \tag{4.7}$$

The parameters *m(1), m(2),* and *m(3)* again were optimized for the best fit of *k* as a function of $\rho$. As shown in Figure 4.4, we obtained a closer fit for *k*:

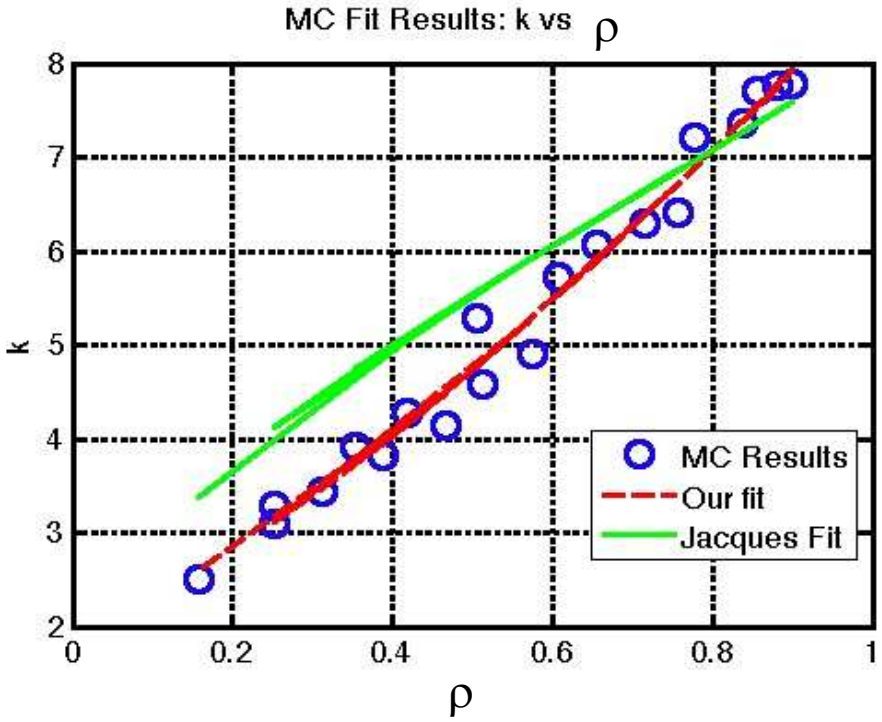


Figure 4.4: Comparison of MC generated k vs. ρ for broad beams.Symbols are MC simulation. The red line is our new fit. The blue solid line is taken from Jacques fit Eq. 4.3 [132].

Table 4.6: New Parameters for k as a function of ρ

| m(1) | m(2) | m(3) |
|---|---|---|
| 6.8085 | 1.3107 | 1.9884 |

The fit for *k* by Farrell et al. gives an $R^2$=0.974 while our fit gives $R^2$=0.999. This study of fluence in a semi-infinite medium establishes the validity of our MC simulation methods in the simplest treatment geometry and our fitting techniques. We determined new constants for Jacques' empirical models that provide much greater accuracy. The following sections build upon this work to simulate photon transport in cavity geometries with varying degrees of symmetry, which more closely simulate treatment regions seen in the clinic.

## 4.4 Spherical Cavity Modeling

The semi-infinite approach to calculating fluence is most useful for PDT applications where the treatment tissues are approximated as semi-infinite media. PDT fluence dosimetry used in topical treatment, such as for skin, is well approximated by the theory discussed in Section 2.4. In the instance of a treatment cavity geometry, such as the thoracic cavity or the bladder, scattered fluence exhibits an overall increase beyond predicted by that on a semi-infinite medium, due to photons that are scattered repeatedly into the cavity wall. This increased fluence is known as the integrating sphere effect (ISE). Total fluence rate at the cavity wall was observed to increase fluence by nearly a factor of five for an isotropic light source[1]. A solution to the diffusion approximation for spherical air cavity, then, is needed to most accurately calculate the true fluence rate at the cavity wall. The analytical derivation for fluence in a the spherical cavity follows strict diffusion approximation (unlike that used in Star's original derivation), based and expanded on solutions available in the literature[3, 7, 8, 69].

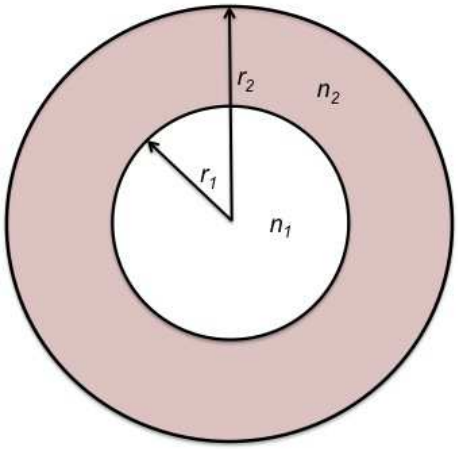


Figure 4.5: Spherical cavity with inner radius $r_1$ and $r_2$

Given a two-layer spherical "slab" with inner radius $r_1$ and outer radius $r_2$ (see Figure 4.5), the expressions for radiant flux *F(r)* and scattered fluence $\phi_s(r)$ (shown below) first introduced in Chapter 2, are expressed in the spherical polar coordinates of *r,* $\theta$, and $\phi$,

$$\nabla \cdot F(\vec{r}) = -\mu_a \phi_s(\vec{r}) + \mu_s' S(\vec{r}), \tag{4.8}$$

$$F(\vec{r}) = -\frac{1}{3\mu_{tr}} \nabla \phi_s(\vec{r}) + \frac{\mu_s' g}{\mu_{tr}} S(\vec{r}). \tag{4.9}$$

Where *S(r)* is the light source. The radiant flux and scattered fluence are related in the following way:

$$\phi_s = 2[F_+(\vec{r}) + F_-(\vec{r})], \tag{4.10}$$

$$F(\vec{r}) = F_+(\vec{r}) - F_-(\vec{r}) \tag{4.11}$$

Using eqns. ( 4.10 ) and ( 4.11 ), eqns. ( 4.8 ) and ( 4.9 ) become eqns. ( 4.12 ) and ( 4.13 ) respectively:

$$\nabla \cdot \left(F_+(\vec{r}) - F_-(\vec{r})\right) = -2\mu_a[F_+(\vec{r}) + F_-(\vec{r})] + \mu_s S(\vec{r}) \quad (4.12)$$

$$F_+(\vec{r}) + F_-(\vec{r}) = -\frac{2}{3\mu_{tr}}\nabla[F_+(\vec{r}) + F_-(\vec{r})] + \frac{\mu_s{}'}{\mu_{tr}} S(\vec{r}) \quad (4.13)$$

By symmetry, eqns. ( 4.12 ) and ( 4.13 ) reduce from $\vec{r}$ to *r*, the radial distance from the center of the sphere and become the following:

$$\frac{1}{r^2}\frac{\partial}{\partial r}[r^2(F_+(\vec{r}) - F_-(\vec{r}))] = -2\mu_a[F_+(\vec{r}) + F_-(\vec{r})] + \mu_s{}' S(r) \quad (4.14)$$

$$\frac{\partial}{\partial r}[F_+(\vec{r}) + F_-(\vec{r})] = -\frac{3}{2}\mu_{tr}[F_+(\vec{r}) - F_-(\vec{r})] + \frac{3}{2}\mu_s S'(r) \quad (4.15)$$

We assume the light source, *S(r)*, is an isotropic point source of the form $\frac{P}{4\pi r^2} e^{\mu_t(r-r_1)}$, where *P* is power of the light source. To solve for the fluence both in the inner sphere, i.e., the cavity surrounding tissue, the distance between $r_1$ and $r_2$, we must solve for the quantities $[F_+(r)+F_-(r)]$ and $[F_+(r)-F_-(r)]$. Solving eqn.( 4.14 ) for $r^2[F_+(r)-F_-(r)]$ and then substituting this solution into eqn.( 4.15 ) we arrive at an expression for $[F_+(r)+F_-(r)]$ by multiplying both expressions by $r^2$.

$$r^2\frac{\partial}{\partial r}[F_+(\vec{r}) + F_-(\vec{r})] = -\frac{3}{2}\mu_{tr}[F_+(\vec{r}) - F_-(\vec{r})] + \frac{3}{2}\frac{\mu_s{}'}{4\pi} e^{-\mu_t(r-r_1)} \rightarrow r^2[F_+(\vec{r}) - F_-(\vec{r})]$$

$$= \frac{2}{3}\frac{1}{\mu_{tr} r^2}\left[\frac{3}{2}\frac{\mu_s{}' S}{4\pi} e^{-\mu_t(r-r_1)} - r^2\frac{\partial}{\partial r}[F_+(\vec{r}) + F_-(\vec{r})]\right]$$

Plugging this expression for $r^2[F_+(r)+F_-(r)]$ into eqn. ( 4.14 ):

$$\frac{1}{r^2}\frac{\partial}{\partial r}\left\{\frac{2}{3}\frac{1}{\mu_{tr}r^2}\left(\frac{3}{2}\frac{\mu_s{}'P}{4\pi}e^{-\mu_t(r-r_1)} - r^2\frac{\partial}{\partial r}[F_+(\vec{r}) + F_-(\vec{r})]\right)\right\}$$

$$= -2\mu_a[F_+(\vec{r}) - F_-(\vec{r})] + \frac{\mu_a S}{4\pi}e^{-\mu_t(r-r_1)}$$

Using the identity $\left(\frac{\partial}{\partial r}\left\{r^2\frac{\partial f(r)}{\partial r}\right\}\right) = r\frac{\partial^2}{\partial r^2}rf(r)$ the above expression becomes the inhomogeneous differential equation:

$$\frac{\partial^2}{\partial r^2}\left[r \quad (F_+(\vec{r}) + F_-(\vec{r}))\right] - 3\mu_a\mu_{tr}[F_+(\vec{r}) + F_-(\vec{r})]$$

$$= -\frac{S(S_+ + S_-)}{4\pi r}e^{-\mu_t(r-r_1)} \qquad (4.16)$$

Where $S_+$ and $S_-$ equal:

$$S_+ = \frac{\mu_s}{4}[\mu_a(5 + 9g) + 5\mu_s{}'] \qquad (4.17)$$

$$S_- = \frac{\mu_s}{4}[\mu_a(1 - 3g) + \mu_s{}'] \qquad (4.18)$$

Recall we want to solve for the scattered fluence in a cavity, $\phi_s=2[F_+(r)+F_-(r)]$, we can therefore solve for the quantity $[F_+(r)+F_-(r)]$. Equation ( 4.16 ) can be solved for $[F_+(r)+F_-(r)]$ by taking the sum of the particular solution and the solutions of the source free equation, multiplied by constants . These constants will be determined using the appropriate boundary conditions. The source free equation becomes homogeneous, and is then expressed as:

$$\frac{\partial^2}{\partial r^2}\left[r \quad (F_+(\vec{r}) + F_-(\vec{r}))\right] - 3\mu_a\mu_{tr}[F_+(\vec{r}) + F_-(\vec{r})] = 0 \qquad (4.19)$$

The solution to this familiar homogeneous equation takes the form:

$$[F_+(\vec{r}) + F_-(\vec{r})] = B_\pm \frac{1}{r} e^{\pm \mu_{eff} r} \tag{4.20}$$

Applying this solution to eqn. ( 4.15 ) gives a solution for $[F_+(r)+F_-(r)]$:

$$\frac{\partial}{\partial r}\left(B_\pm \left(\frac{1}{r}\right) e^{\pm \mu_{eff} r}\right) = B_\pm \left[\frac{\pm \mu_{eff}}{r} - \frac{1}{r^2}\right] e^{\pm \mu_{eff} r}$$

$$B_\pm \left[\frac{\pm \mu_{eff}}{r} - \frac{1}{r^2}\right] e^{\pm \mu_{eff} r} = -\frac{3}{2}[F_+(r) + F_-(r)]$$

$$[F_+(r) - F_-(r)] = B_\pm \left[\frac{2}{r^2}\left(1 - \mu_{eff} r\right)\right] e^{\pm \mu_{eff} r}$$

With solution for $[F_+(r)-F_-(r)]$ determine from the homogeneous equation, it remains for us to determine $[F_+(r)+F_-(r)]$ by solving the inhomogeneous equation, eqn.( 4.19 ), where the source is reintroduced. Let $H_b(r)=r[F_+(r)+F_-(r)]$:

$$\frac{\partial^2}{\partial r^2} H_b(r) - \mu_{eff}^2 H_b(r) = \frac{S\left(S_+(r) + S_-(r)\right)}{4\pi r} e^{-\mu_t (r - r_1)}$$

Allowing the right-hand side of the equation to go to $\frac{S(S_+(r)+S_-(r))}{4\pi r} e^{-\mu_t (r-r_1)} = h_b(r)$, the known particular solution of the inhomogeneous equation is of the form:

$$H_b(r) = \frac{1}{2\mu_{eff}} \int_r^{r_0} \left[e^{\mu_{eff} r} e^{-\mu_{eff} x} - e^{-\mu_{eff} r} e^{\mu_{eff} x}\right] h_b dx \tag{4.21}$$

To solve the integral in eqn.( 4.21 ), we let $r_0 = \infty$. The solution for $H_B$ then becomes:

$$H_B = P \frac{3\mu_s e^{\mu_t r_1}}{16\pi \mu_{eff}} [(1+g)\mu_a + \mu_s] \left[e^{\mu_{eff} r} B_0\left(\left(\mu_t + \mu_{eff}\right) r, \infty\right)\right.$$
$$\left. - e^{-\mu_{eff} r} B_0\left(\left(\mu_t - \mu_{eff}\right) r, \infty\right)\right] \tag{4.22}$$

The coefficient $B_0$ is an exponential integral of the form:

$$B_0(a,b) = \int_a^b \frac{e^{-u}}{u}\,du \qquad (4.23)$$

The solution for $B_0$ is well approximated by a polynomial, which will be of further use as we come to a complete expression for fluence in a spherical cavity with mismatched indices of refraction between cavity and the surrounding medium. Combining eqns.( 4.20 ) and ( 4.41 ) we arrive at an expression for $\phi_s$=2[$F_+$(r)-$F_-$(r)]:

$$\begin{aligned}\phi_t = B_+\frac{2}{r}e^{\mu_{eff}r} + B_-\frac{2}{r}e^{-\mu_{eff}r} \\ + S\frac{3\mu_s e^{\mu_t r_1}}{16\pi\mu_{eff}}[(1+g)\mu_a \\ + \mu_s]\left[e^{\mu_{eff}r}B_0\left((\mu_t+\mu_{eff})r,\infty\right)\right. \\ \left. - e^{-\mu_{eff}r}B_0\left((\mu_t-\mu_{eff})r,\infty\right)\right]\end{aligned} \qquad (4.24)$$

It now remains to apply the appropriate boundary conditions and approximations to solve for the coefficients $B_+$, $B_-$, and $B_0$. The first approximation we make is $\lim_{r_2\to\infty}\phi_t = 0$. This approximation is reasonable as fluence rapidly decreases as the distance from the light increases, particularly in an absorbing, scattering medium. To fulfill this approximation, $B_+=0$, eliminating several terms in eqn.( 4.24 ). We then make the approximation for $B_0$, saying that $B_0(a) \to \frac{e^{-a}}{a}$. Equation ( 4.24 ) then simplifies to:

$$\phi_t = \frac{B_-}{r}e^{-\mu_{eff}r} + S\frac{3\mu_s e^{-\mu_t(r_1-r)}}{8\pi r^2}\left[\frac{(1+g)\mu_a+\mu_s}{\mu_t^2-\mu_{eff}^2}\right] \qquad (4.25)$$

Recall that we assume $\mu_{eff} << \mu_t$ because $\mu_a << \mu_s$. This allows us to make the approximation $\mu_t \approx \mu_s$. Equation ( 4.43 ) then becomes:

$$F_+ + F_- = \frac{B_-}{r} e^{-\mu_{eff} r} + S \frac{3\mu_s e^{-\mu_t (r_1 - r)}}{8\pi r^2} \quad (4.26)$$

To solve for $B_-$ we must return to the boundary condition $F_+(r_1)=F_-(r_1)$ and the original differential equation, eqn.( 4.15 ):

$$\frac{\partial}{\partial r}[F_+ + F_-] = \frac{B_-}{r} e^{-\mu_{eff} r} \left\{ \frac{1}{r} - \mu_{eff} \right\} + PS \left\{ \frac{2}{r} - \mu_t \right\} \quad (4.27)$$

Solving for $B_-$:

$$\frac{-B_-}{r} e^{-\mu_{eff} r} \left\{ \frac{1}{r} + \mu_{eff} \right\} + S \frac{3\mu_s e^{-\mu_t (r_1 - r)}}{8\pi r^2} = \frac{3}{2} g \mu_s \left( \frac{S}{4\pi r^2} \right) e^{-\mu_t (r - r_1)}$$

$$B_- = \frac{3S}{8\pi} e^{\mu_{eff} r_1} \frac{\mu_{tr}}{1 + \mu_{eff} r_1} \quad (4.28)$$

Using this value for $B_-$, we arrive at a full expression for fluence in the medium surrounding the spherical cavity:

$$\phi_t(r) = \frac{3S}{4\pi} \left\{ \frac{\mu_{tr} e^{-\mu_{eff}(r - r_c)}}{r\left(1 + \mu_{eff} r_c\right)} - \frac{2}{3} \frac{e^{-\mu_t (r - r_c)}}{r^2} \right\}. \quad (4.29)$$

When eqn.( 4.29 ) is evaluated for $r=r_1$ (i.e. at the cavity wall), and recalling the optical penetration depth is small, $\mu_{eff} r_1 >> 1$, it simplifies to:

$$\phi_t(r_1) = \frac{3S}{4\pi r_1^2} \left\{ \frac{\mu_{eff}}{\mu_a} - 2 \right\}. \quad (4.30)$$

To arrive at an expression for the fluence in the cavity, we must introduce the refection factor, $r_{21}$. The reflection factor is dependent on the Fresnel coefficients of the medium and the cavity and requires that light scattering occurs only on one side of the cavity-medium boundary, meaning there is no scattering present in the cavity. The reflection coefficient is defined as:

$$r_{21} = \int_0^{\theta_c} 2R_{fres} \cos\theta_i \sin\theta_i \, d\theta_i + \int_{\theta_i}^{\pi/2} 2\cos\theta_i \sin\theta_i \, d\theta_i. \quad (4.31)$$

Where $\theta_c$ is the critical angle, $\theta_i$ is the angle of incidence, and $R_{fres}$ is defined as:

$$R_{fres} = \frac{1}{2}\left(\frac{n_1 \cos\theta_R - n_2 \cos\theta_i}{n_1 \cos\theta_i + n_2 \cos\theta_R}\right)^2 + \frac{1}{2}\left(\frac{n_1 \cos\theta_i - n_2 \cos\theta_R}{n_1 \cos\theta_i + n_2 \cos\theta_R}\right)^2 \quad (4.32)$$

where $n_1$ is the index of refraction of the cavity, $n_2$ is the index of refraction of the surrounding medium, $\theta_R$ is the angle of refraction, and $\theta_i$ is the angle of incidence. The flux reflected back into the cavity is then $(1-r_{21})F_{r\text{-}}(r_1)$. The non-scattered fluence in the cavity is the direct light from the isotropic source, $S/4\pi r_1^2$. The scattered light in the air cavity for a centrally located source, is the total light in the medium, minus the direct light, multiplied by the reflection factor term:

$$\phi_{sc}(r_1) = \frac{S}{4\pi r_1^2}(1 - r_{21})\left(\frac{\mu_{eff}}{\mu_a} - 3\right). \quad (4.33)$$

The total fluence at the cavity wall, inside the cavity is then:

$$\phi_{tc}(r_1) = \frac{S}{4\pi r^2} + \frac{S}{4\pi r_1^2}(1 - r_{21})\left(\frac{\mu_{eff}}{\mu_a} - 3\right) \quad (4.34)$$

## 4.5 Spherical Monte Carlo Simulations: No Attenuation

We conducted a series of MC simulations for a spherical air cavity with a centrally located isotropic source to verify the fluence model derived in Section 4.4 and to establish our treatment of multiple scattering within the cavity. We simulate the random walk of photons in the surrounding medium with a specified mean free path and scattering angle in the medium to determine fluence at the cavity wall and surrounding tissue can be determined. The absorption

coefficients and scattering coefficients are homogeneous in the surrounding tissue and indices of refraction are 1 for air and 1.4 for tissue.

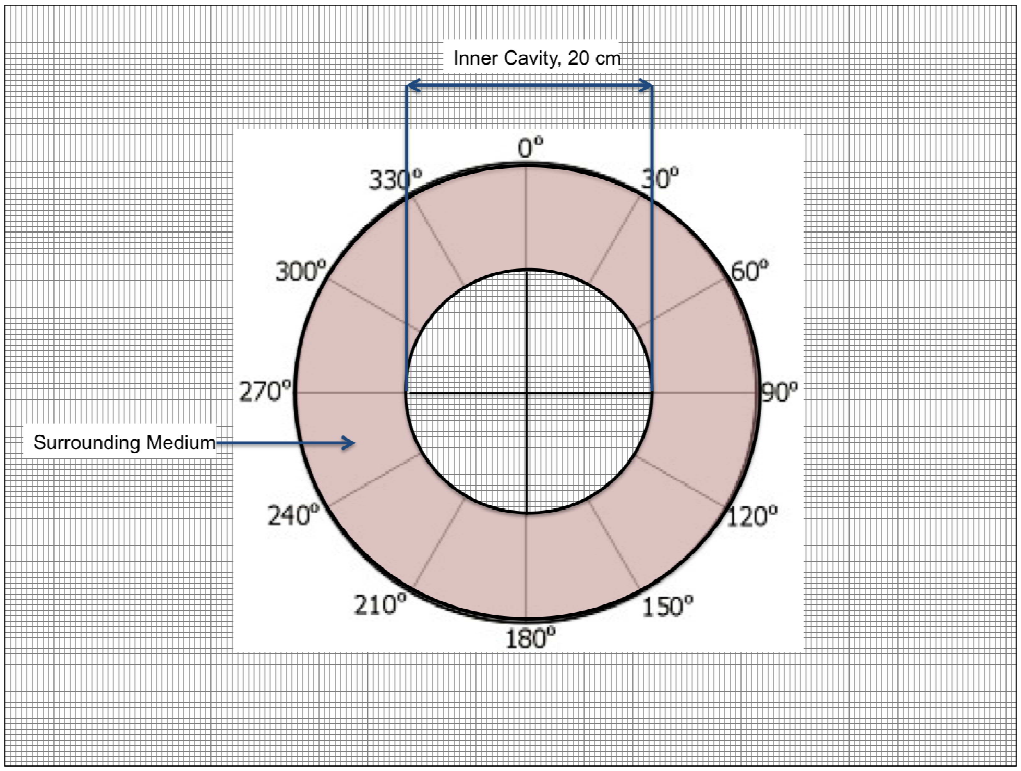


Figure 4.6: Schematic of a slice of the spherical cavity

The origin of the system is set at the center of the inner sphere (0,0,0), of radius 10 cm. The surrounding medium (depicted in red), represents the surrounding tissue and is assigned different combinations of optical properties, uniform over the entire medium.

### *4.5.1 Monte Carlo Photon Transport Modeling*

We developed a MC simulation for a spherical cavity with uniform optical properties and no attenuation in the cavity (see Figure 4.6) in the MATLAB™ platform. This simulation is an adaption of work done by Zhu et al. [81, 136] which simulated photon transport for a semi-infinite planar surface. A spherical cavity geometry is initialized, with the inner radius set to 10 cm and the outer radius set to 15 cm. Each voxel in this geometry is a 0.005 cm x 0.005 cm cube. As each photon passes through each voxel, the photon's location and weight are recorded.

Photons are followed in this manner until they escape the outer radius, or when the photon weight becomes insignificant. It is this recorded photon density, $\rho_n$, that is used in post-simulation analysis to determine the fluence rate. For scoring efficiency, the light source for the simulation is a pencil beam that is perpendicularly incident on the cavity surface (to compare results to the diffusion approximation solution, this light source is convolved to an isotropic point source, as described below). $10^4$ photons were propagated through the simulation. The photon step size, $\Delta s$, is determined by the optical properties and uniformly distributed random number, ε: $\Delta s = mfp \cdot \ln \varepsilon$, where the mean free path, *mfp*, is defined as $mfp = 1/(\mu_a + \mu_s)$. We assume the tissue surface is Lambertian, therefore the radiant intensity from the tissue surface follows $\cos\theta$ for the azimuthal angle, θ [138].

The pencil-beam light source was placed at the cavity-tissue boundary, sending photons into the surrounding tissue in a concentrated region determined by the size of the beam (see Figure 4.7). The resulting kernel of the pencil beam is then convolved with an isotropic point-source (eqn. ( 4.35 )) for comparison purposes with our analytic solution.

$$\int_{4\pi} k\big((r-r'),\theta\big)\frac{S}{4\pi}\sin\theta\, d\theta\, d\varphi = \frac{S}{4\pi}\left(\frac{2\pi}{n}\right)\sum_{j}^{n-1} k\left(r,\frac{2\pi j}{n}\right)\sin\frac{2\pi j}{n}, \qquad (4.35)$$

where $r$ is the radius of the cavity, $r'$ is the location of the photon, and $S$ is the strength of the light source. The convolution was taken to a standard quadrature sum and the resulting fluence was then compared with the fluence from our analytic model both within and without the cavity.

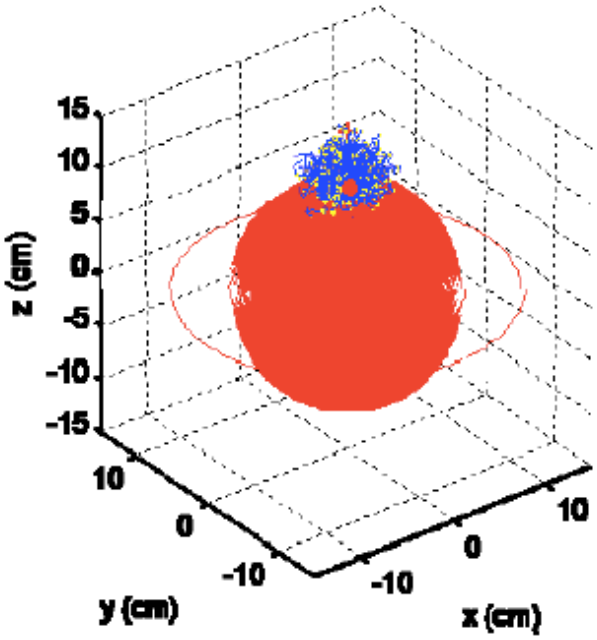


Figure 4.7: Depiction of MC simulation for a spherical cavity with a pencil beam light source

Results from preliminary run of Monte Carlo simulation for a cavity of inner radius of 10 cm and outer radius of 15 cm, $\mu_a$=1cm$^{-1}$, $\mu_s$'=18 cm$^{-1}$, g=0.9 for a tissue-air interface for a pencil-beam light source located at the center of the cavity. The fluence for the pencil-beam source is then convolved with the fluence of an isotropic point source for comparison with our analytic model.

The simulation records the following quantities: the photon density $\rho_n$ as a function of emitting angle, the fraction of diffusely reflected photons by the inner radius, the fraction of diffusely reflected photons by the outer radius, and the kernel as a function of emitting angle. The light fluence rate, $\phi$, per unit incident light power of the source is taken to be $\phi=\rho_n/N_{inc}/\mu_a$, where $N_{inc}$ is the number of incident photons. The reciprocity theorem[139] is used to calculate ratio of the light fluence rate φ to the incident irradiance (or light fluence rate in air $\varphi_{air}$) on the central axis of a circular field with radius $R$ by an area integral:

$$\frac{\phi}{\phi_{air}} = \int_0^R \frac{\rho_n}{N_{inc}\mu_a} 2\pi r \, dr \, . \qquad (4.36)$$

The reciprocity theorem is applied again to calculate the angular distribution of differential diffuse reflectance, $r_d$, as a function of beam radius and emitting angle, $\theta$. Reflection of photons at the cavity boundary is modeled according the Fresnel reflection coefficient for unpolarized light (eqn. ( 4.32 )). The multiple scattering of photons within the cavity, causing the ISE, is described in the following section.

### *4.5.2 Multiple Scattering*

The MC simulation code developed by Zhu et al. [81, 136] does not account for the multiple scattering observed in spherical cavities. To accurately simulate the photon migration the cavity, we added a treatment of multiple scattering to the existing simulation. The multiple scattering treatment utilizes basic ray tracing, incorporating the Fresnel coefficients for transmission and reflection for unpolarized light and is described schematically in Figure 4.8. We consider multiple scattering first for a sphere, whose complete symmetry allows the calculation of scattering angles to be simplified.

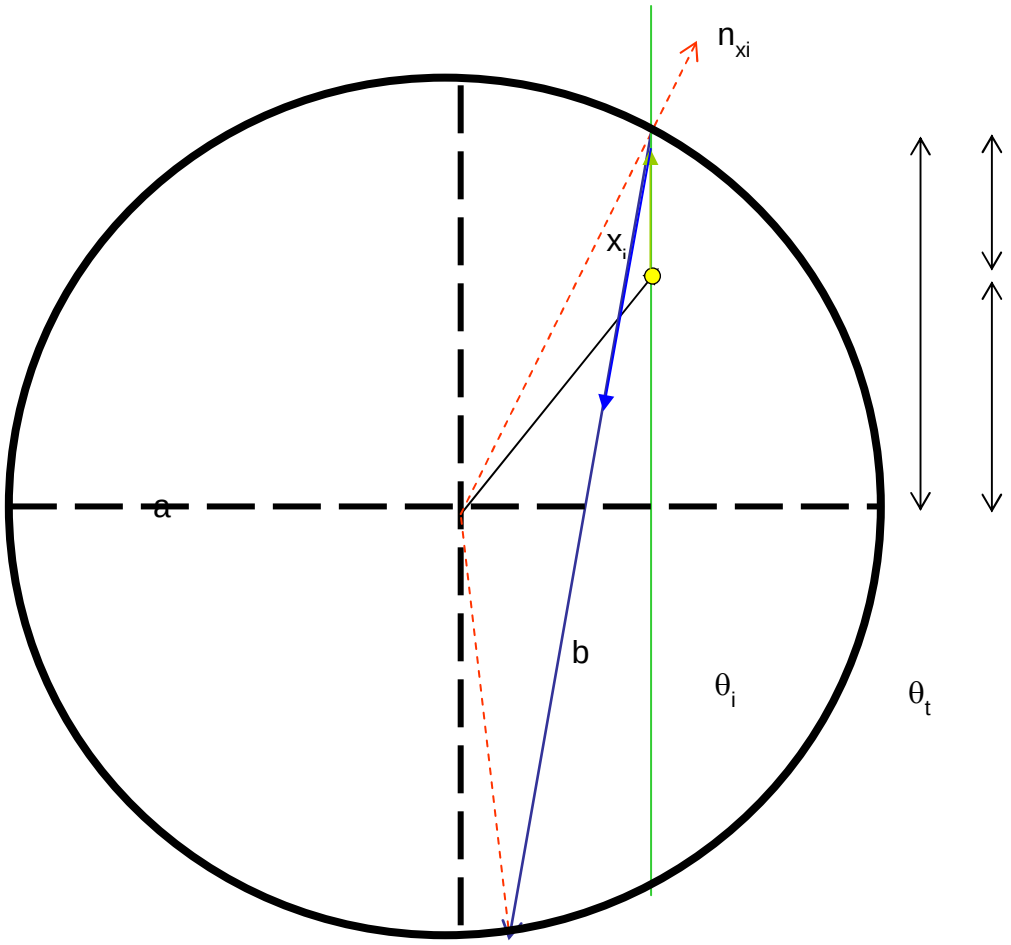


Figure 4.8: Schematic of multiple scattering treatment in a spherical cavity

The point nxi is the point where two photons interact a distance r0 from the cavity center. The photon which hits the cavity wall with direction u0, a distance x0 from the cavity center and then travels a distance l and is incident on the cavity wall with direction ut. See definitions of quantities and the derivation of ut below.

### Definitions for Multiple Scattering

$$r_0 = \sqrt{x_{0,x}^2 + x_{0,y}^2 + x_{0,z}^2}$$
$$a = \mid x_0 \cdot u_0 \mid$$
$$b = \sqrt{a^2 - (r_0^2 - r_1^2)}$$
$$x_i = x_0 - u_0 \cdot t_i$$
$$n_{xi} = \frac{x_i}{\sqrt{x_i^2}}$$
$$\theta_i = \pi - arccos(u_0 \cdot x_{xi})$$
$$l = 2r_1 cos\theta_t$$

### Derivation of $u_t$

$$u_t = (u_t \cdot n_x)n_x + (u_t \cdot n_y)n_y$$
$$u_0 \cdot n_x = cos\theta_i; u_t \cdot n_x = cos\theta_t$$
$$u_0 = -cos\theta_i \cdot n_x + sin\theta_i \cdot n_y$$
$$u_t = -cos\theta_t \cdot n_x + sin\theta t \cdot n_y$$
$$u_t = \frac{n_1}{n_0}u_0 + n_x(cos\theta_i - \frac{sin\theta_i}{sin\theta_t} \cdot cos\theta_t)$$
$$u_t = u_0\frac{n_1}{n_0} + n_{xi}(\frac{n_1}{n_0}cos\theta_i - cos\theta_t)$$

### *4.5.3 Spherical Cavity MC Results for a centrally located source*

MC simulations were run for $\mu_a$=0.01 cm$^{-1}$, 0.1 cm$^{-1}$, 0.5 cm$^{-1}$, 1.0 cm$^{-1}$ and $\mu_s$'=5 cm$^{-1}$, 10 cm$^{-1}$, 15 cm$^{-1}$, 25 cm$^{-1}$, 40 cm$^{-1}$. $10^5$ photons were launched at an incidence angle of 0$^o$ from the center of the cavity as pencil beam (see Figure 4.6). This light source was later convolved to an isotropic point source as described in Section 4.5.1. The cavity had a radius of 10 cm, and the surrounding medium had an outer radius of 20 cm. No attenuation was present in the cavity, which was treated as air with an index of refraction of 1. Optical properties were uniform throughout the medium surrounding the cavity. Figure 4.10, Figure 4.11, Figure 4.12, and Figure 4.13 show the comparison of the calculated total fluence and scattered fluence from the cavity center using eqns.( 4.33 ) and ( 4.34 ) to the results of our simulations.

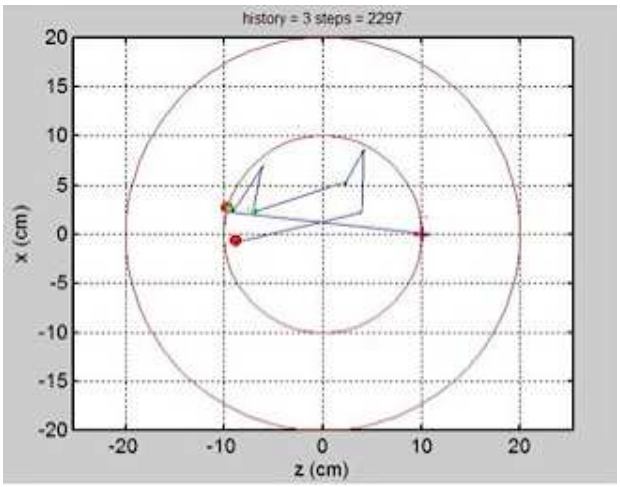


Figure 4.9: Bird's eye view of a photon scattering multiple times off the cavity wall

As one can observe, there is excellent agreement between the calculated fluence in the cavity and the fluence derived from the MC simulations. The results diverge slightly from one another with increasing $\mu_a$, but are still in overall agreement. These results indicate our treatment of multiple scattering within the cavity is a suitable technique for spherical cavities of homogenous optical properties. The results from this simulation allow us to determine the fluence as a function of angle about the cavity, at the cavity-tissue boundary. We observe the scattered portion of the fluence is uniform, as expected since eqn. ( 4.34 ) is dependent only on the radius of the cavity.

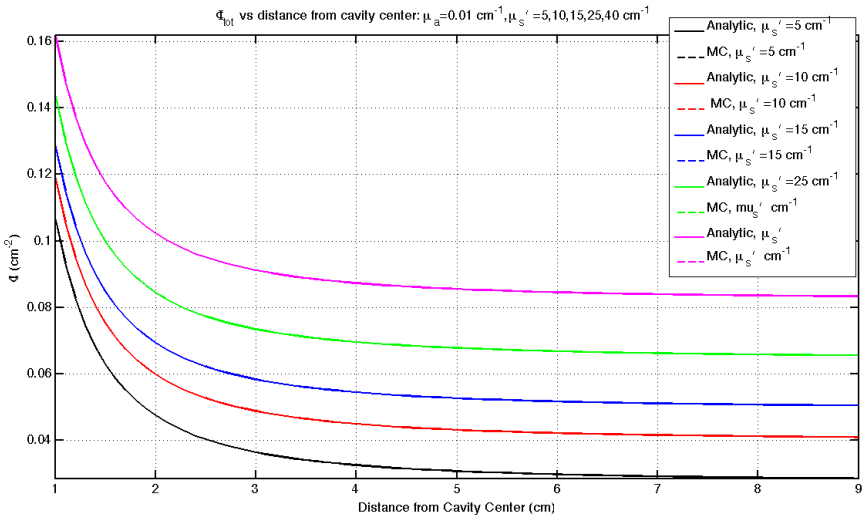


(a)

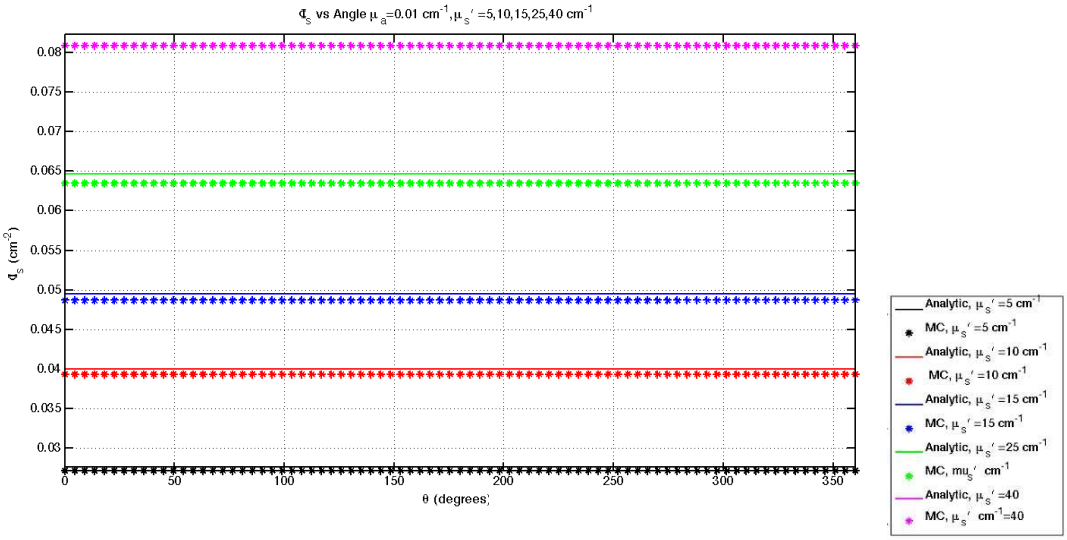


"'9b)

Figure 4.10: MC simulated scatter fluence rate per source power ($\Phi_s$/S) results compared to eqn. ( 4.33 )

Scatter fluence and total fluence for $\mu_a$=0.01 cm$^{-1}$ and $\mu_s$' = 5, 10, 15, 25 cm-1. (a) Total fluence rate vs. distance from cavity center. (b) Scattered fluence rate vs angle about entire cavity wall. See corresponding legend below.

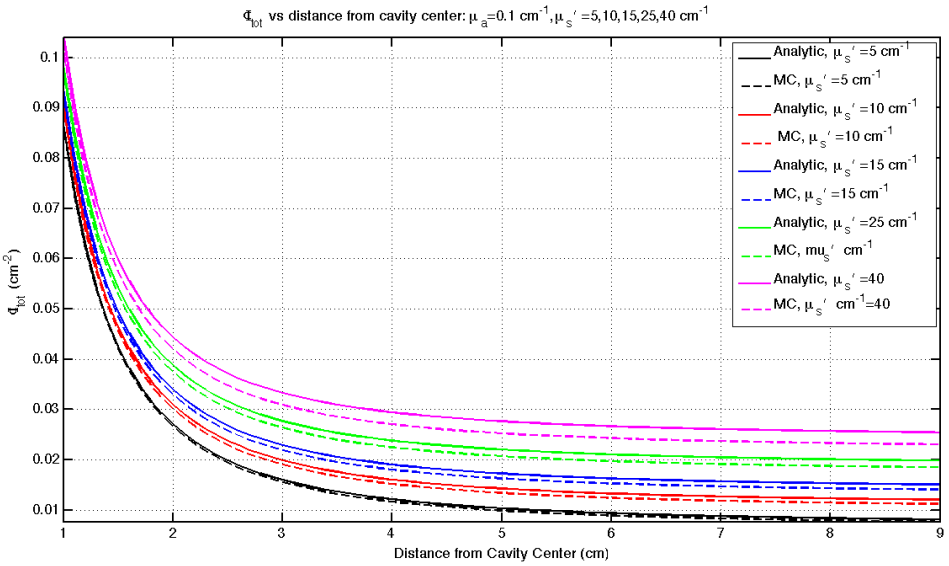


(a)

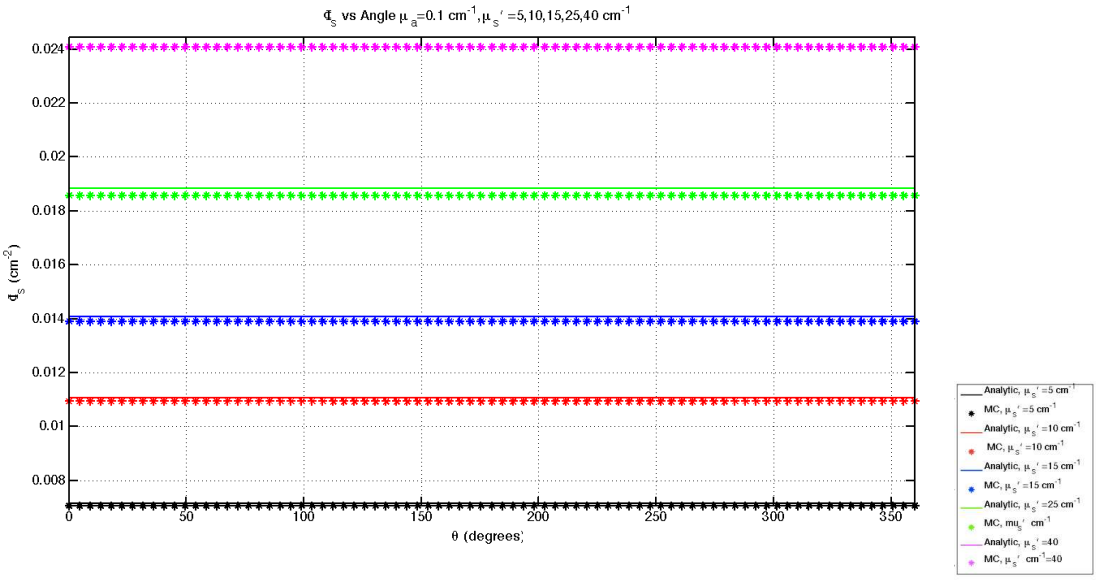


(b)

Figure 4.11: MC fluence rate results ($\Phi_s$/S) compared to eqn.( 4.33 ) and (4.34)

Scatter and total fluence rate, for $\mu_a$=0.5 cm$^{-1}$and $\mu_s$' = 5, 10, 15, 25 cm-1. (a) Total fluence rate vs. distance from cavity center. (b) Scattered fluence rate vs angle about entire cavity wall. See corresponding legend.

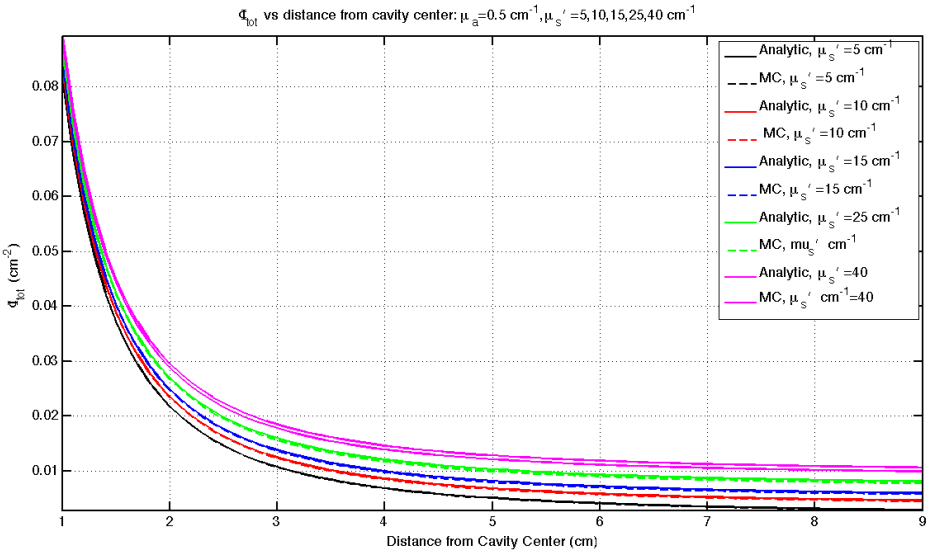


(a)

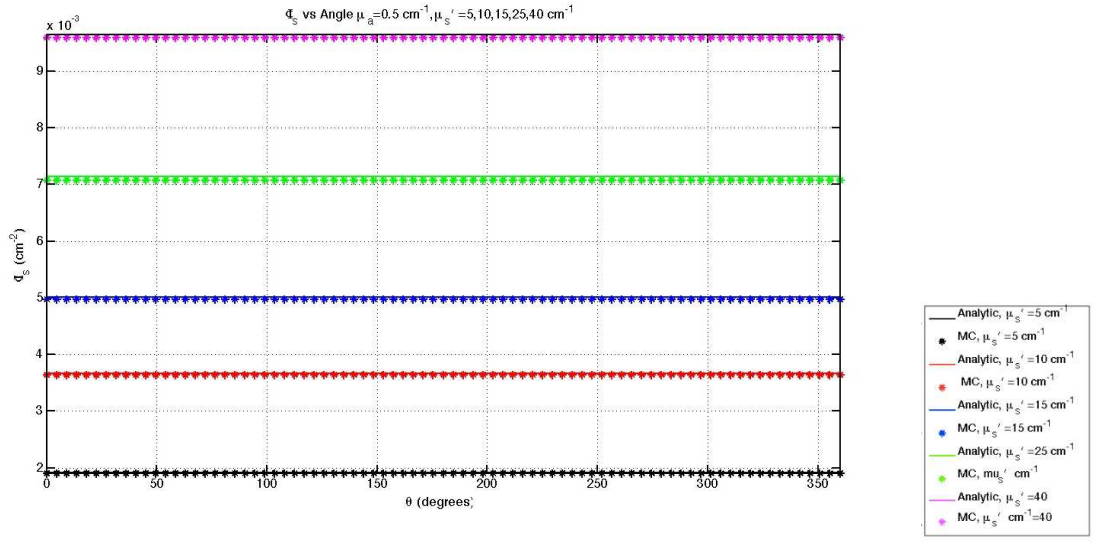


(b)

Figure 4.12: MC fluence rate results ($\Phi_s$/S) compared to equation ( 4.33 ) and (4.34)

Comparing scatter and total fluence rate, for $\mu_a$=0.5 cm$^{-1}$and $\mu_s$' = 5, 10, 15, 25 cm-1. (a) Total fluence rate vs. distance from cavity center. (b) Scattered fluence rate vs angle about entire cavity wall. See corresponding legend.

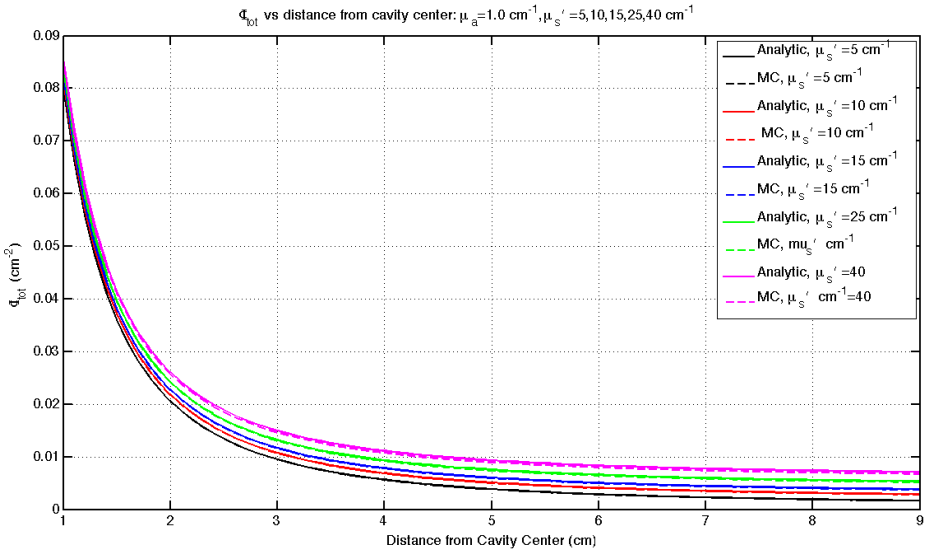


(a)

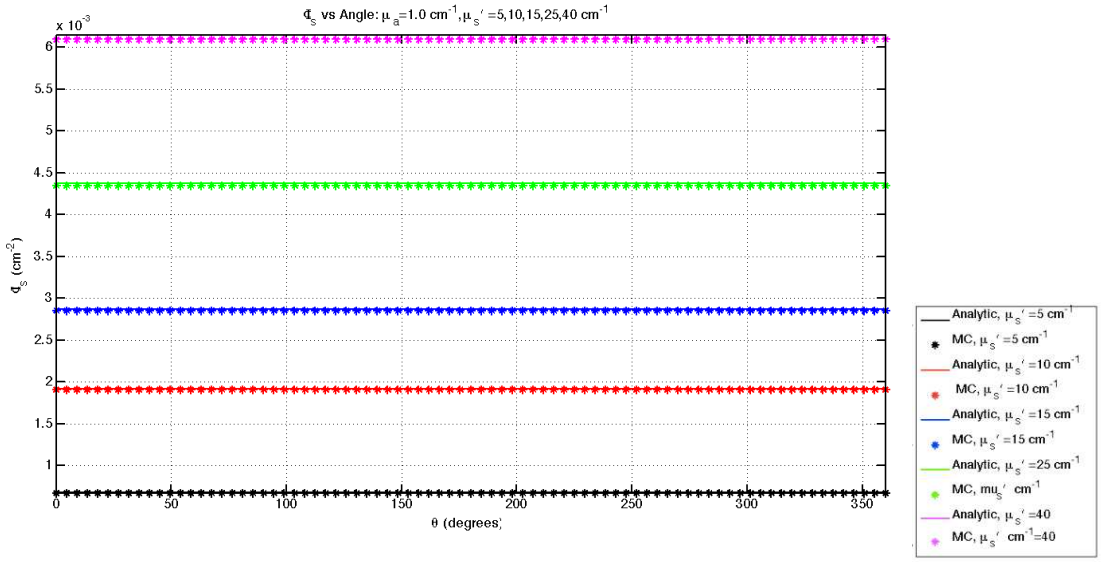


(b)

Figure 4.13: MC fluence rate results ($\Phi_s$/S) compared to equation ( 4.33 ) and (4.34)

Scatter and total fluence rate, for $\mu_a$=1.0 $cm^{-1}$and $\mu_s$' = 5, 10, 15, 25 cm-1. (a) Total fluence rate vs. distance from cavity center. (b) Scattered fluence rate vs angle about entire cavity wall. See corresponding legend.

## 4.6 Spherical Monte Carlo Simulations: Attenuation

In the clinic, when treating a patient's thoracic cavity, several key factors arise that were not accounted for in the preceding MC simulations. The thoracic cavity is extremely asymmetrical (see Figure 4.14) with varying optical properties (as seen in Chapter 3). Furthermore, during PDT treatment, the thoracic cavity is filled with a diluted 0.01% Intrallipid™ solution to help scatter the treatment light more uniformly. This solution mixes with blood present, creating an attenuating medium with negligible scattering filling the cavity. Star's solution for fluence in an air cavity does not in the presence of attenuation. The effects of an attenuating medium in a cavity are explored here via MC simulations for a spherical cavity and later for an ellipsoidal cavity.

### *4.6.1 Monte Carlo Methods for attenuation*

To model photon transport in a cavity in the presence of attenuation is a more complicated simulation. The MC simulation developed here is a modified version of the code developed in C by Boas et al. [140]. Their simulation, whose photon transport method is described in detail by Wang and Jacques[132], is able to track photons as they travel through a grid laid over the entire geometry with each region able to be assigned its own optical properties. This tracking method is particularly useful for our purposes, where the simulation cavity has either no absorption or scattering (no attenuation) or minimal absorption (attenuating) media. In the simulations discussed in Section 4.5, we did not track the photons in the cavity, only those in the surrounding medium. By tracking the photon at any point in the geometry we again further knowledge of how photon transport is affected by different geometries.

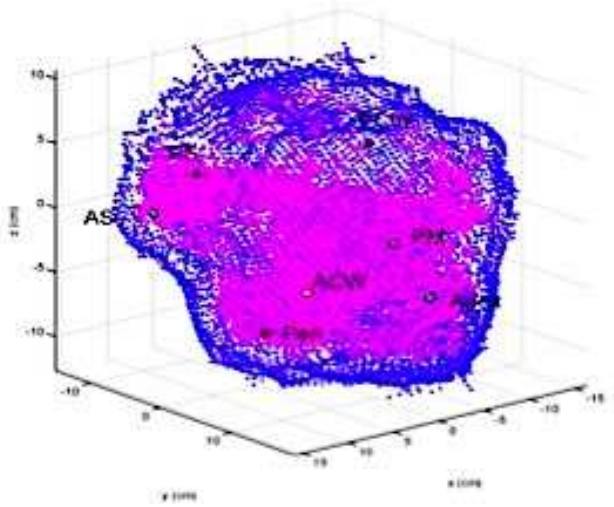

Figure 4.14: Contour of the thoracic cavity taken during treatment

The blue lines represent the outer contour of the thoracic cavity, while the pink lines represent the movement of the treatment wand (see Chapter 5). The detectors sutured into the cavity wall are marked.

First, a spherical cavity is initialized with user-specified voxel size (see Figure 4.15). A photon is launched in a user-specified direction from a given location. To achieve an isotropic point source, each photon is launched in a random direction from ranging from 0 to $2\pi$ from the center of the cavity (determined by using a uniformly distributed random number). The length to the first scattering event is calculated using an exponential distribution. Photon absorption is determined by decreasing the photon weight by $e^{(-\mu aL)}$ where L is the length the photon travels[132]. The Henyey-Greenstein phase function is used to determine the new scattering angle of the photon. The new scattering length of the photon is then determined by an exponential distribution as before. The photon is propagated this new length in the new direction. This propagation process continues until the photon exits the medium or the photon traveled for 10 ns, which at this point, its weight can be regarded as negligible[140]. When a photon encounters a boundary, the probability of reflection is calculated using Fresnel's equation[132]. If the photon is reflected back into the cavity, our multiple scattering treatment

described in Section 4.5.2 determines the photon's path in the cavity. An empirical solution for scattered fluence at a spherical cavity wall is given by eqn.( 4.37 ) [128] for a non-attenuating cavity:

$$\phi_s = \frac{4S}{4\pi r_1^2}\left[\frac{\rho}{1-\rho(1-f)}\right], \quad (4.37)$$

Where *f* is the ratio between the open surface area to total surface area. Since we are only considering completely closed geometries, *f* will always equal 0.The factor $\rho$ earlier in chapter 2 (eqn. ( 2.35 )), is defined as:

$$\rho = \frac{a'}{2}\left[1 + e^{-4/3\left(A\sqrt{3(1-a')}\right)}\right] e^{-\sqrt{3(1-a')}}, \quad (4.38)$$

Where *a'* is the albedo and is defined as $a'=\mu'_s/\mu'_s+\mu_a$ and *A* is the reflection factor (A=2.9 in this instance). To account for the attenuation now present in the cavity eqn.( 4.37 ) becomes:

$$\phi_s = \frac{4S}{4\pi r_1^2}\left[\frac{\rho e^{-\mu_{atten} r_1}}{1-\rho(1-f)e^{-\mu_{atten} r_1}}\right], \quad (4.39)$$

This term, $e^{-\mu_{atten} r_1}$, describes the exponential decay caused an atenuating medium, described by $\mu_{atten}$ . As $\rho$ is also dependent on the optical properties of the system, it stands to reason that where ever $\rho$ appears, it should be multiplied by the attenuation term. We compare eqn. ( 4.37 )to the MC simulation results for an air cavity, and to eqn.( 4.39 ) when an attenuating medium is present in the cavity. The total fluence for an attenuating cavity then becomes:

$$\phi_t = \frac{S}{4\pi}\left[\frac{e^{-\mu_{atten}r}}{r^2} + \frac{1}{r_1^2}\left(\frac{4\rho e^{-\mu_{atten}r_1}}{1-\rho(1-f)e^{-\mu_{atten}r_1}}\right)\right], \qquad (4.40)$$

where r is the position from the source and $r_1$ is the radius of the cavity. The optical properties of the cavity and surrounding medium are assigned voxel by voxel (each voxel is 1 $mm^3$) and each photon is tracked voxel by voxel.

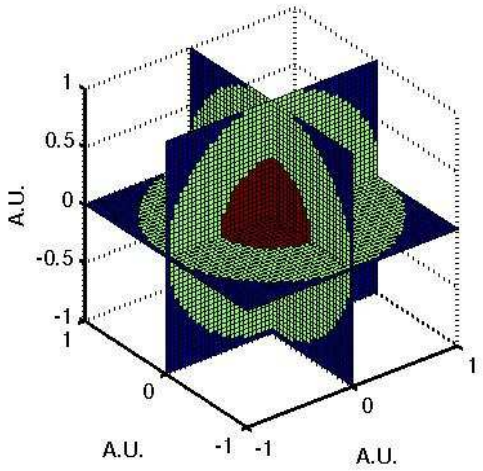


Figure 4.15: Visualization of the spherical cavity generated by MATLAB™

For plotting purposes the geometry's size was normalized by the outmost radius. Photons were launched from the center of this volume. The code used allows the user to track photons at any location. For this study, photons were tracked at different locations along the cavity-medium boundary, where the red and green spheres meet.

### *4.6.2 Spherical Cavity MC Results in the presence of attenuation*

The MC simulations presented here were performed for spherical cavities of radius 10 cm. $10^8$ photons were launched for each simulation, with the direction of the photon chosen by a uniformly distributed random number to effect a centrally located isotropic point source. The absorption coefficient of the surrounding medium ranged from 0.01 to 0.05 and 0.1 $cm^{-1}$, while the reduced scattering coefficient was kept constant at 10 $cm^{-1}$. Simulations were run for an air

cavity ($\mu_a=\mu_s'=0$) and an attenuating cavity with matching index of refraction ($\mu_{att}=$□□□05, 0.05 $cm^{-1}$), as well as for a water filled cavity. Simulations were also run for $\mu_s'$=2 cm, 10 cm, 20 cm, and 40 cm. The resulting fluence data from these simulations did not display any change in the relationships observed in Figure 4.16-Figure 4.18 with changing $\mu_s'$. For this reason we focus on the results from one set of simulations with changing absorption in the surrounding tissue.

We observe, as for an air cavity, the scattered fluence is uniform at the cavity wall at all angles. With increasing surface area (SA), here equal to $S/4\pi r^2$, the total fluence at the cavity wall decreases as 1/SA. Our results also demonstrate that the introduction of a non-air medium into the cavity decreases both total and the scatter fluence. We observe that, as expected, when attenuation is present, the scatter fluence decreases from that of an air cavity. And as attenuation increases, scattered fluence accordingly decreases. Furthermore, eqn. ( 4.39 ) correctly predicts this change in fluence caused by attenuation. The symmetry of a homogeneous sphere is the simplest cavity scenario to simulate. It remains to be seen if the relationships that hold for a sphere will hold for a cavity with less symmetry.

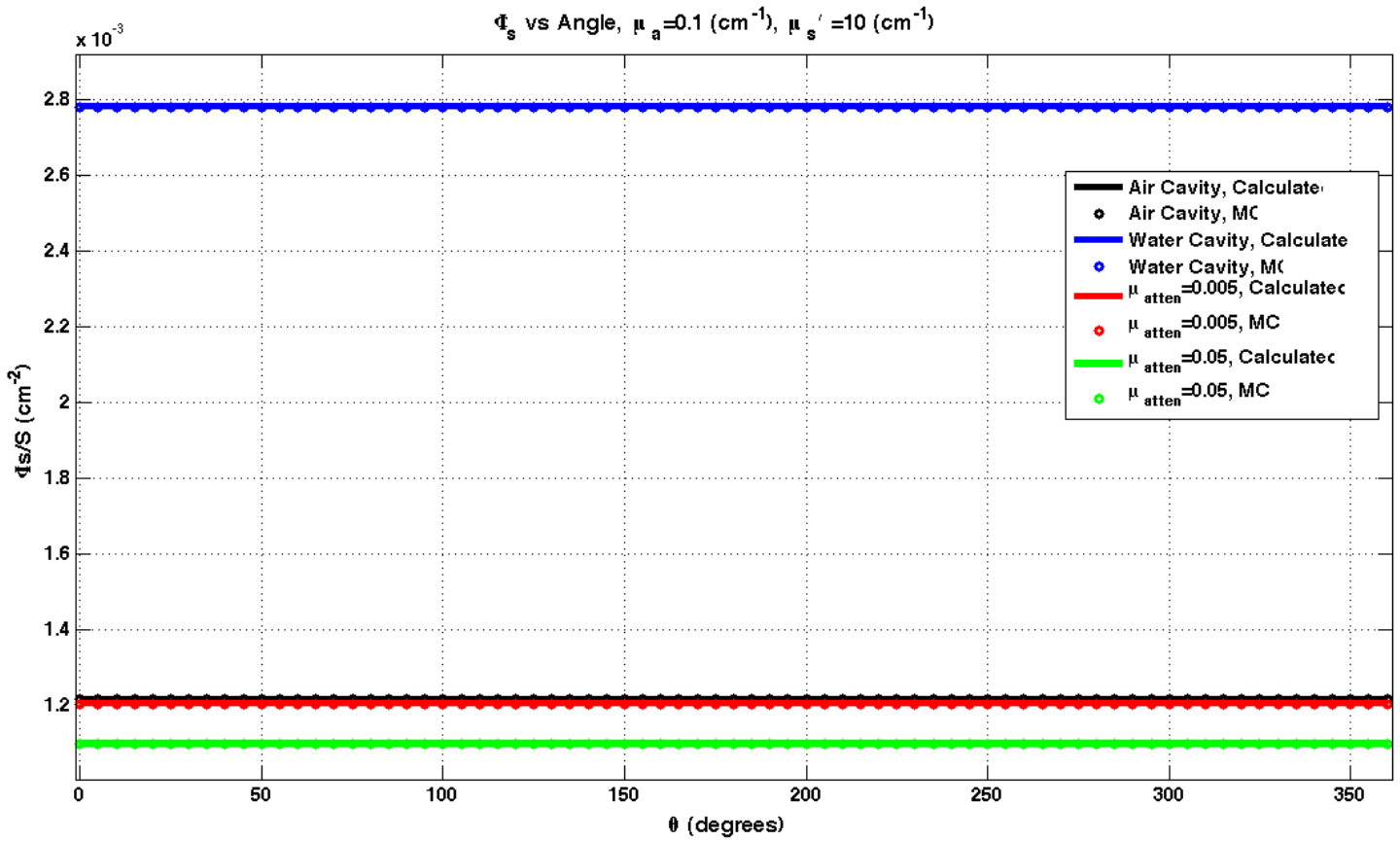


Figure 4.16: Φs/S over angle at spherical cavity boundary, MC results compared to empirical solution for different $\mu_{atten}$

Scattered fluence rate per source power as a function of angle, for a centrally located source in at cavity wall of radius=10 cm, MC results compared to empirical equation, eqn. .( 4.39 )

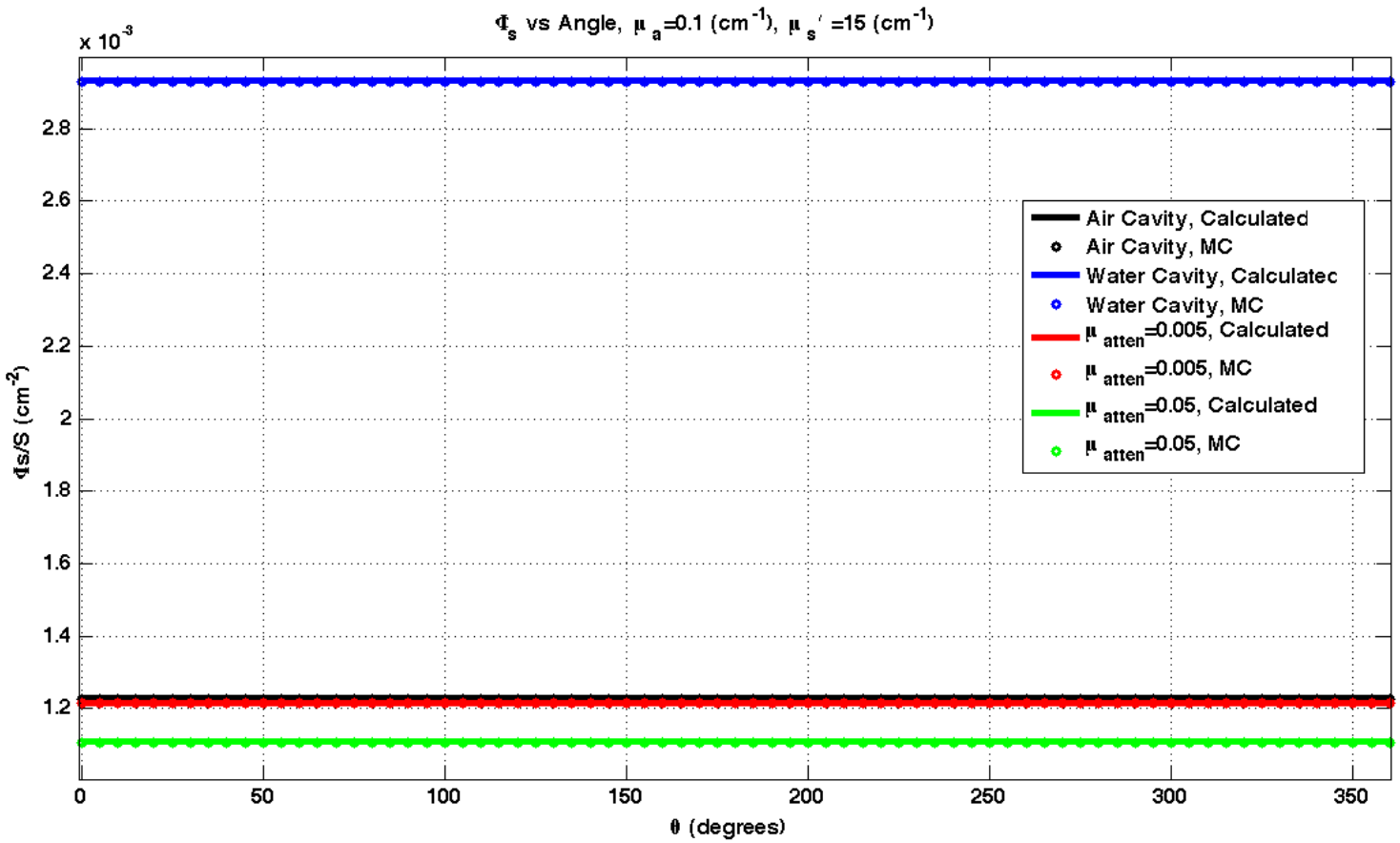


Figure 4.17: Φs over angle at spherical cavity boundary, MC results compared to empirical solution for different $\mu_{atten}$

Scattered fluence rate as a function of angle, for a centrally located source in at cavity wall of radius=10 cm, MC results compared to empirical equation, eqn.( 4.39 )

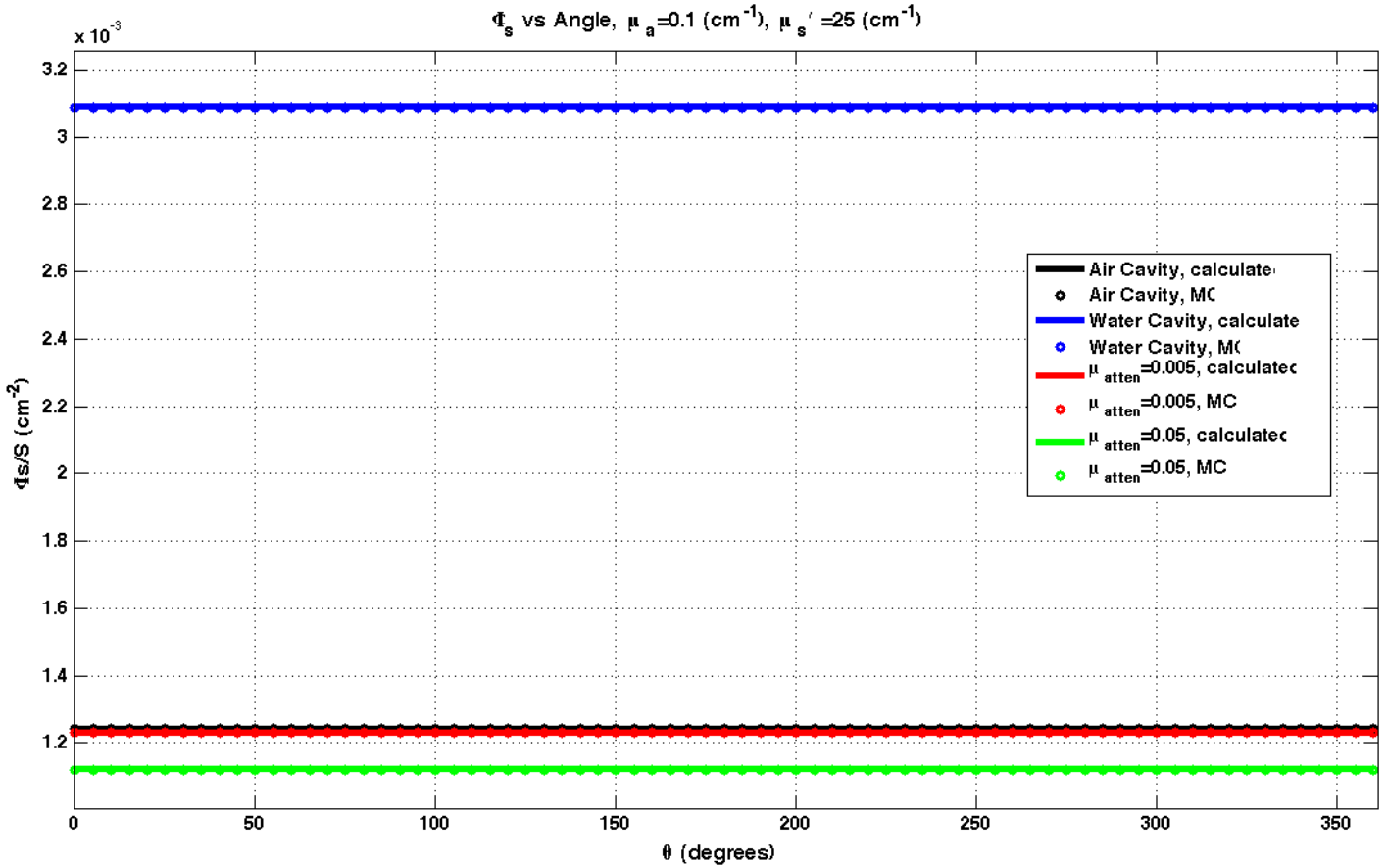


Figure 4.18: Φs over angle at spherical cavity boundary, MC results compared to empirical solution for different $\mu_{atten}$

Scattered fluence rate as a function of angle, for a centrally located source in at cavity wall of radius=10 cm, MC results compared to empirical equation, eqn.( 4.39 )

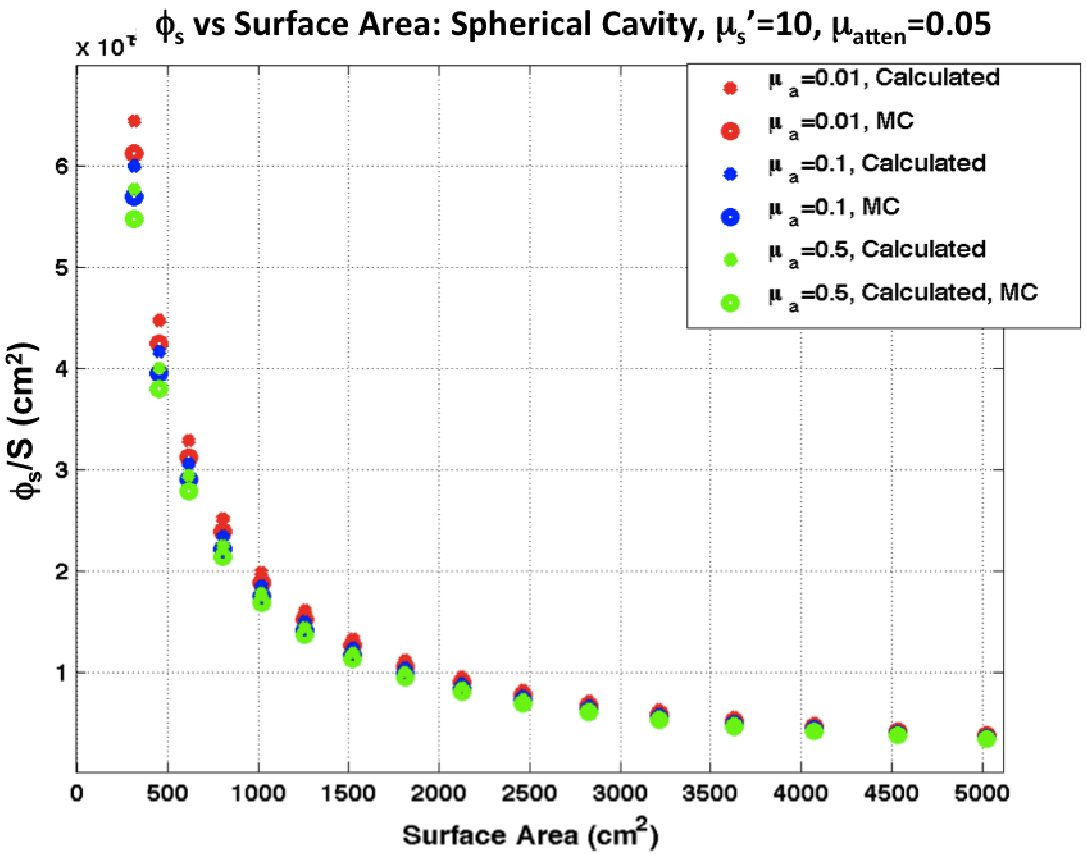


Figure 4.19: Scattered fluence as a function of surface area for a spherical air cavity

The scattered fluence was calculated using eqn. ( 4.39 )

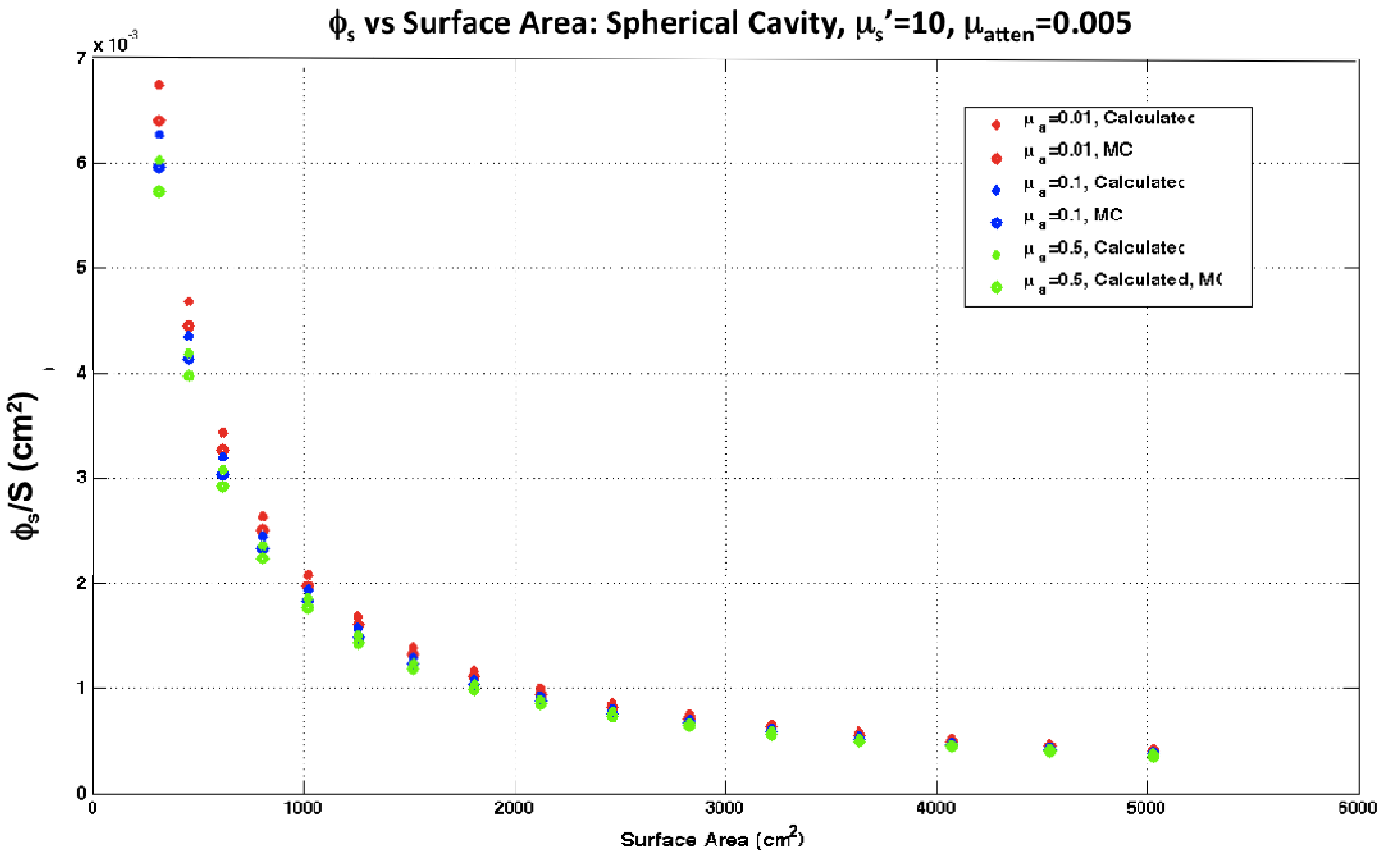


Figure 4.20: Scattered fluence rate per source power as a function of surface area for a spherical cavity with $\mu_{attn}$=0.005, $\mu_s'$=10

The scattered fluence was calculated using eqn.( 4.39 )

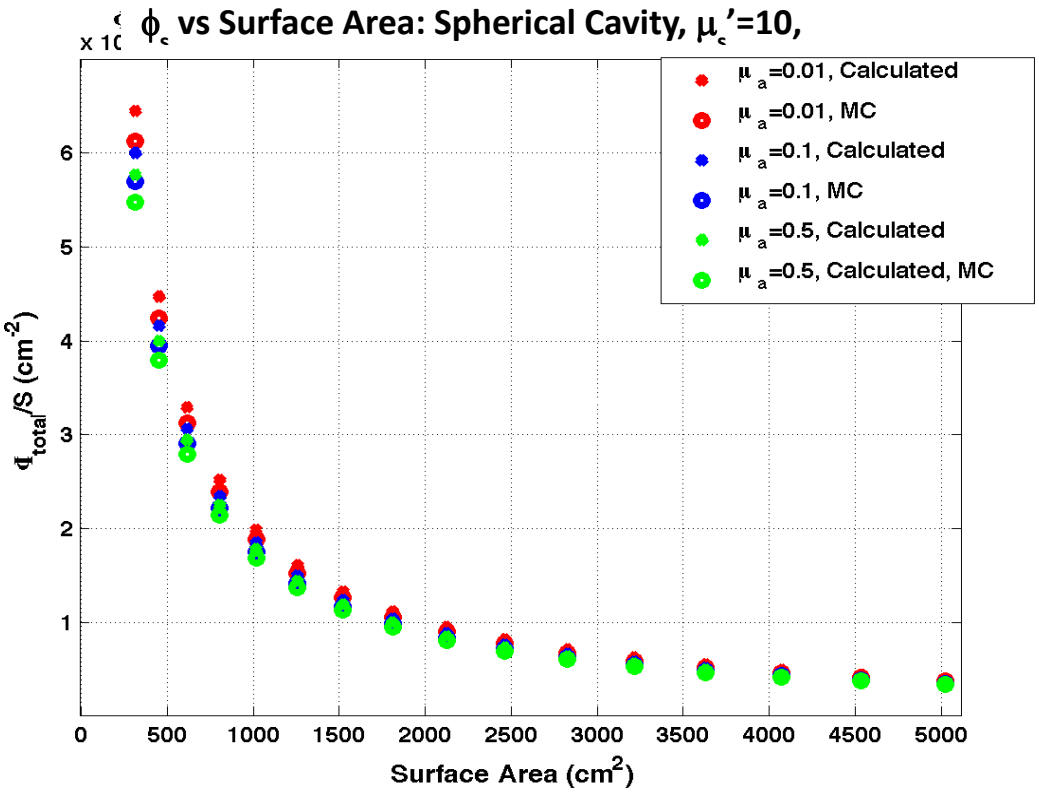


Figure 4.21: Scattered fluence rate per source power as a function of surface area for a spherical cavity with $\mu_{attn}$=0.05, $\mu_s'$=10

The scattered fluence was calculated using eqn. ( 4.39 )

*4.5.4 Spherical Cavity MC Results for an off-center source*

The same MC simulation method used in 4.6.1 was applied once more, only this instance the light source was placed at 5 cm from the cavity center along the y-axis. Our aim was to verify that not only is scattered fluence in the cavity uniform along the cavity boundary at all degrees for a centrally located source, but also is also uniform when the light source is placed in an off-center location (see **Error! Reference source not found.**Figure 4.14). $10^5$ photons were launched for $\mu_a$=0.5 $cm^{-1}$, and $\mu_s'$=5, 10, 15, 25, and 40 $cm^{-1}$. We observe that indeed the scattered fluence is independent of source position and remains uniform at the cavity wall (see

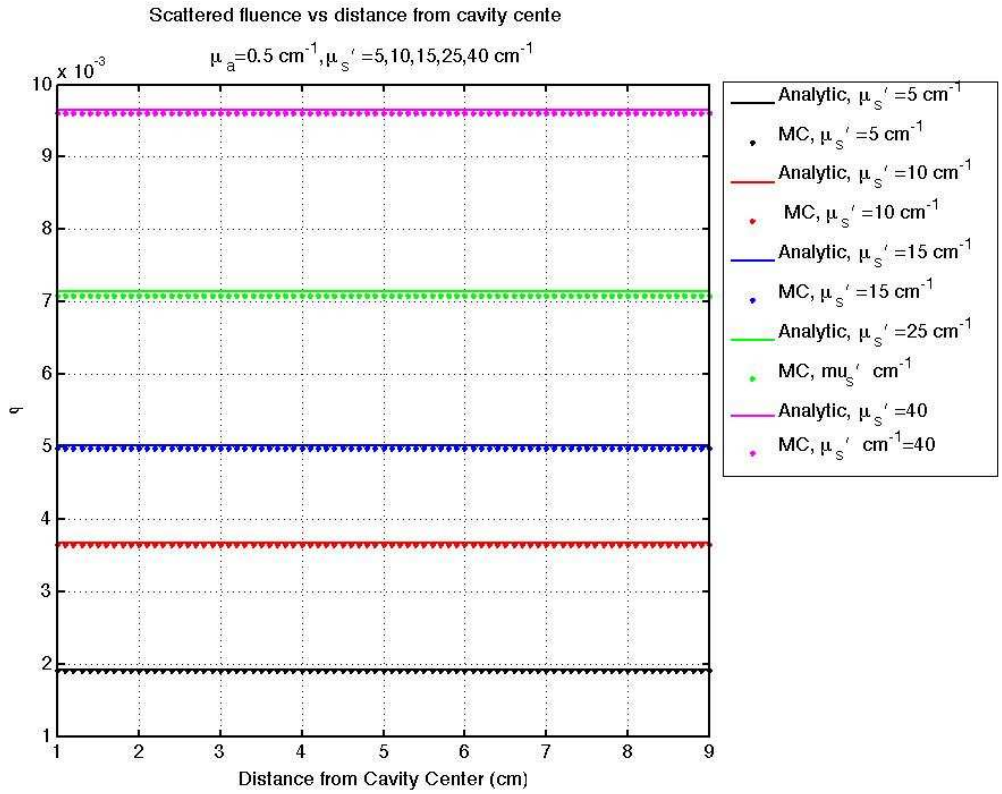


Figure 4.23).

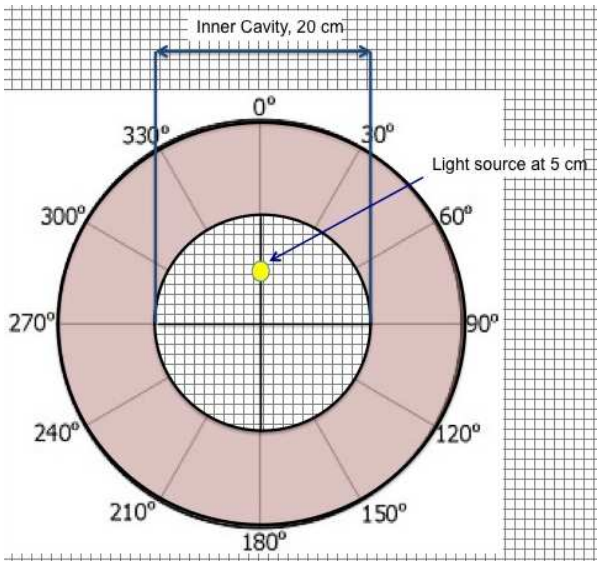


Figure 4.22: Schematic of sphere with the light source off center at (0,5,0)

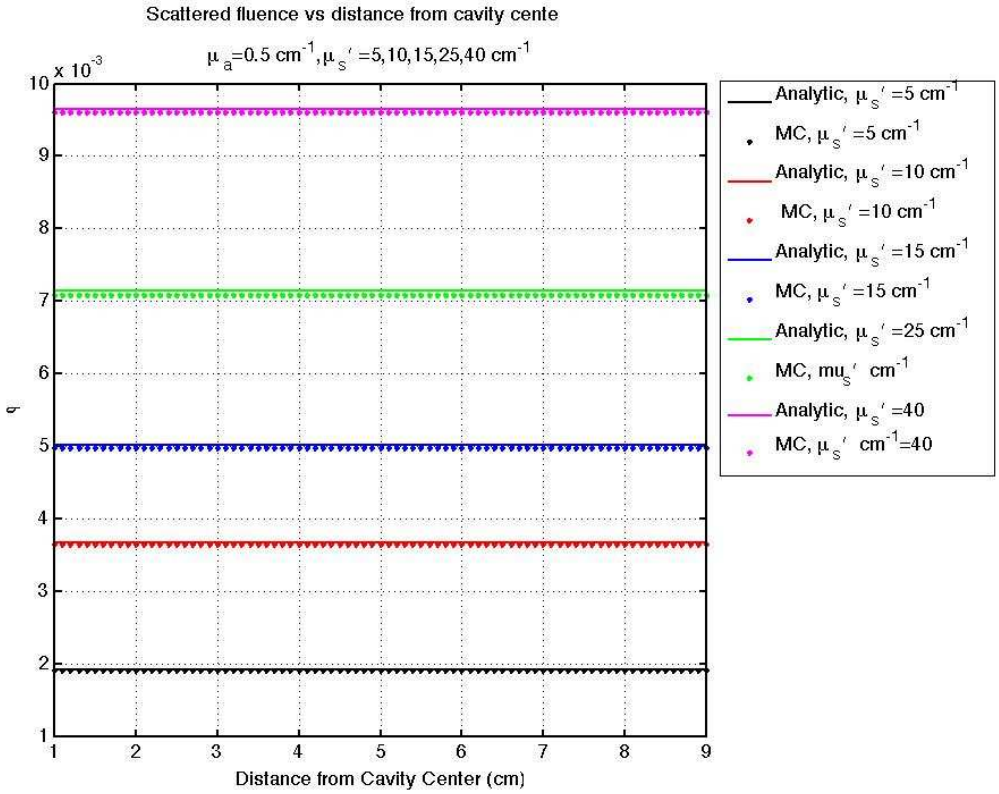


Figure 4.23: Scattered fluence rate per source power from MC simulation for an off-center source compared to analytic solution.

Note that not only is the scattered fluence uniform, but is also the same for the corresponding simulations run for a centrally located source.

## 4.7 Ellipsoidal Monte Carlo Simulations

### *4.7.1 Monte Carlo Methods for an Oblate Ellipsoidal Cavity*

The same MC simulation code used in 4.6.1 was applied for an oblate ellipsoid, where one axis of symmetry is lost compared to a sphere (see Figure 4.24). The empirical solution for fluence in a sphere (see eqn.( 4.37 ) is a function of the surface area, *SA*, of the cavity (for air):

$$\phi_s = \frac{4S}{SA}\left[\frac{\rho}{1-\rho(1-f)}\right], \quad (4.41)$$

The surface area of an oblate ellipsoid is given by the following:

$$SA = 2\pi a^2\left(1+\frac{1-e^2}{e}\tanh^{-1}e\right), \quad (4.42)$$

Where *a* and *c* are the semi-principle axes of the ellipsoid (with a>b=c defining an oblate ellipsoid) and *e* is calculated by the following:

$$e^2 = 1-\frac{c^2}{a^2}. \quad (4.43)$$

For an ellipsoidal cavity with an attenuating medium eqn.( 4.41 ) becomes:

$$\phi_s = \frac{4S}{SA}\left[\frac{\rho e^{-\mu_{atten}r_{avg}}}{1-\rho(1-f)e^{-\mu_{atten}r_{avg}}}\right], \quad (4.44)$$

Where $r_{avg}$ is the average between the semi-major axis, *a*, and the semi-minor axes, *b* and *c*:

$$r_{avg} = \frac{a+b+c}{3}. \quad (4.45)$$

The total fluence, with *r* representing the position from the source is then:

( 4.46 )

The multiple scattering of the photons was handled in the same manner as described above for the spherical cavity. However, because of the loss of symmetry along one axis, a uniformly distributed random number generator chose the angle the photon was scattered off the cavity wall beyond the first two times a photon scattered off the cavity wall, should the photon be scattered back into the cavity. This method was chosen because without symmetry in all directions it becomes impossible to determine the following scattering angle.

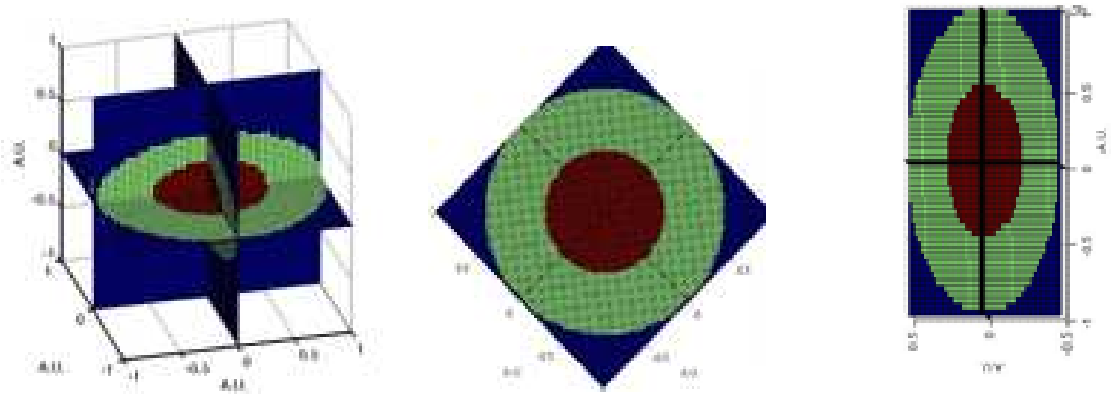

Figure 4.24: Visualization of ellipsoidal cavity

(a)Visualization of the ellipsoidal cavity used for simulation, with the geometry normalized to outer semi-major axis (20 cm). (b) The ellipsoidal cavity used in this study is an oblate ellipsoid, where the two semi-major axes are equal with the semi-minor axis< semi-major axes. A cross section of the ellipsoidal cavity is depicted here along the semi-minor axis. (c) Cross section of the cavity along the semi-major axis.

### *4.7.2 MC Results for an Ellipsoidal Cavity*

The MC simulations presented here were performed for an ellipsoid of semi-major axis 10 cm and semi-minor axis of 5 cm (this is, by definition, an oblate ellipsoid). $10^8$ photons were run for each simulation. The absorption coefficients of the surrounding medium are $\mu_a$= 0.01, 0.05, and 0.1 $cm^{-1}$, while the reduced scattering coefficient was kept constant at $\mu_s$'=10 $cm^{-1}$. Simulations were run for an air cavity and an attenuating cavity ($\mu_{atten}$=0.005 and ???? $cm^{-1}$). The voxel size of the geometry was 1 $mm^3$. As with the spherical cavity simulations, simulations were run for changing $\mu_s$' as well but we focus on one typical dataset. Again the scatter fluence is found by subtracting *P/SA* from eqn.( 4.3 ) where *P* represents the power of the light source.

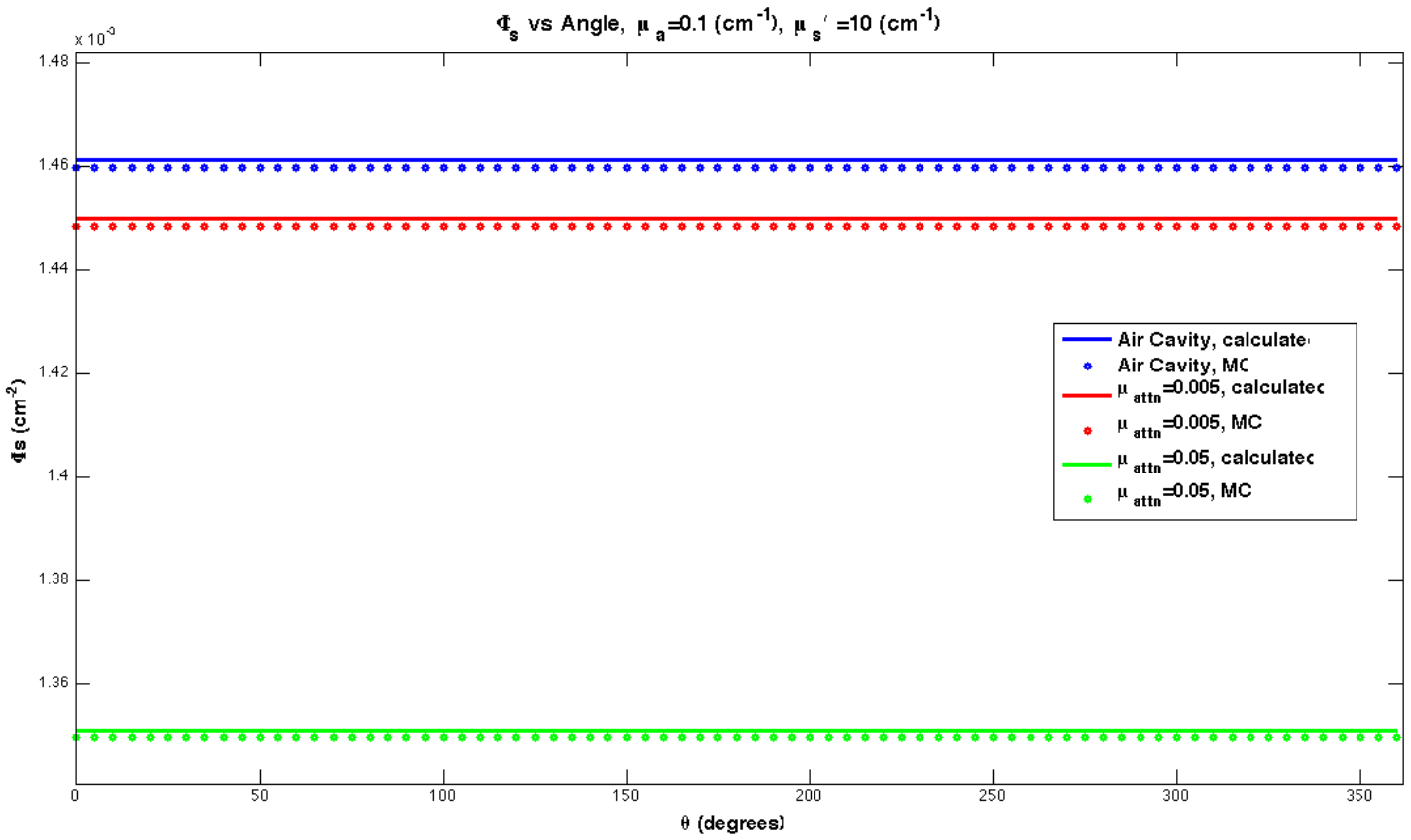


Figure 4.25: Scattered fluence rate per source power (fs/S) at the ellipsoidal cavity boundary as a function of angle, for a centrally located source, in an ellipsoidal cavity. MC results compared to values from eqn. ( 4.41 )

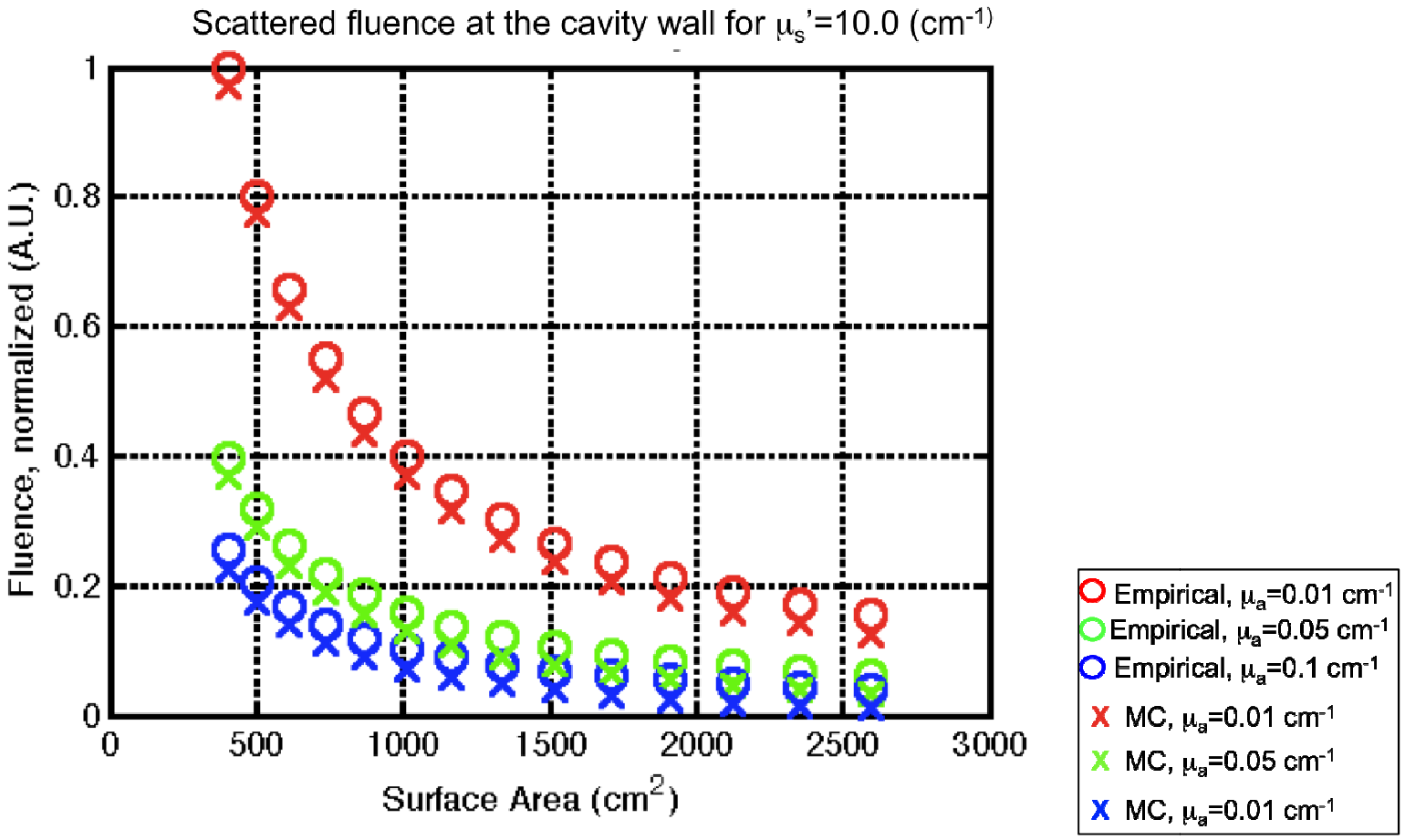


Figure 4.26: $\phi_s$ rate per source power at the wall of an air cavity vs surface area: MC results compared to empirical solution, eqn.( 4.44 ) for $\mu_s'$=10.0 ($cm^{-1}$)

Where the fluence was normalized by dividing the results by maximum value for fluence for $\mu_a$=0.01 ($cm^{-1}$)

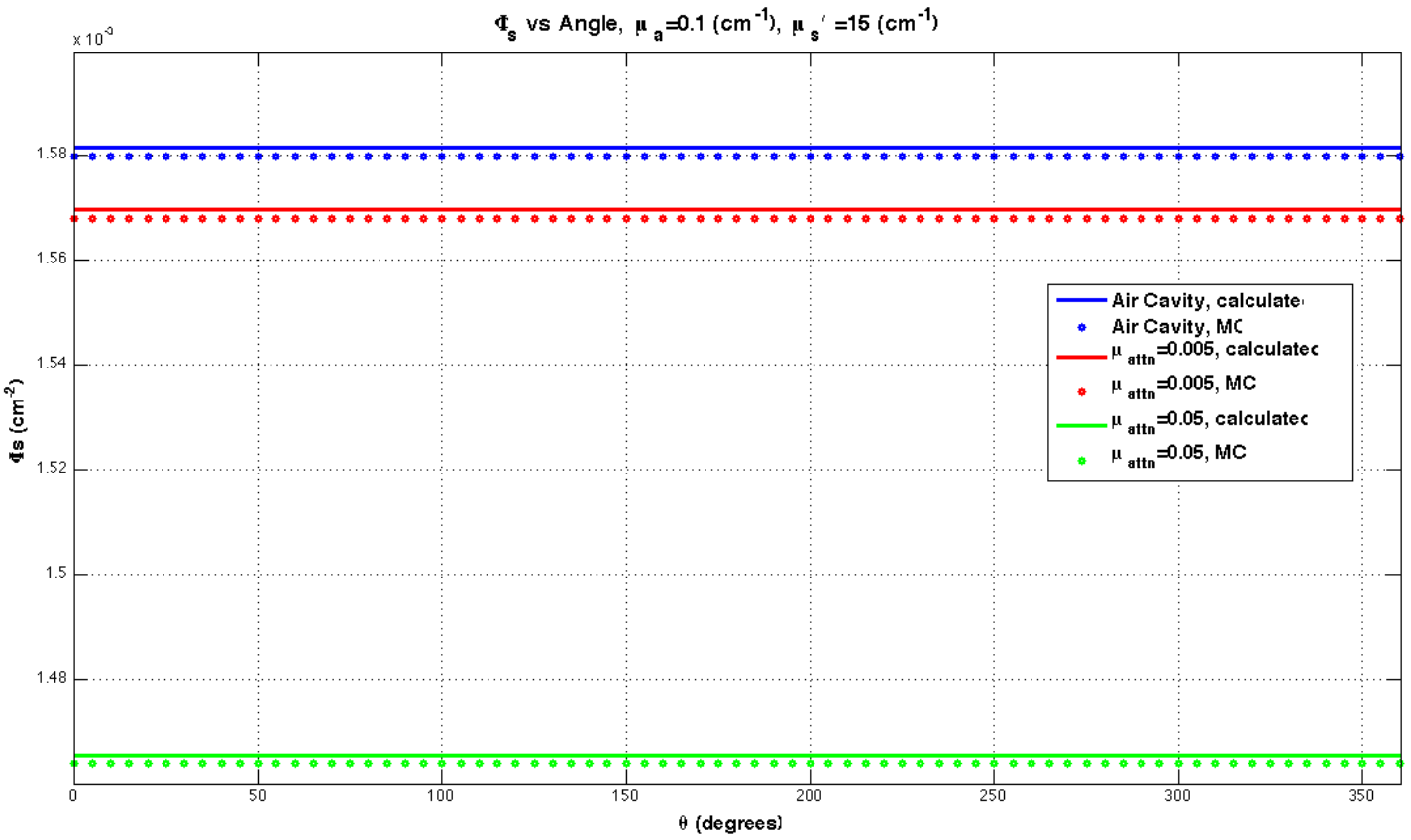


Figure 4.27: Scattered fluence rate per source power at the boundary of an ellipsoidal cavity as a function of angle. Scattered fluence rate, for a centrally located source, in an ellipsoidal air cavity. MC results compared to values from eqn. eqn.( 4.46 ).

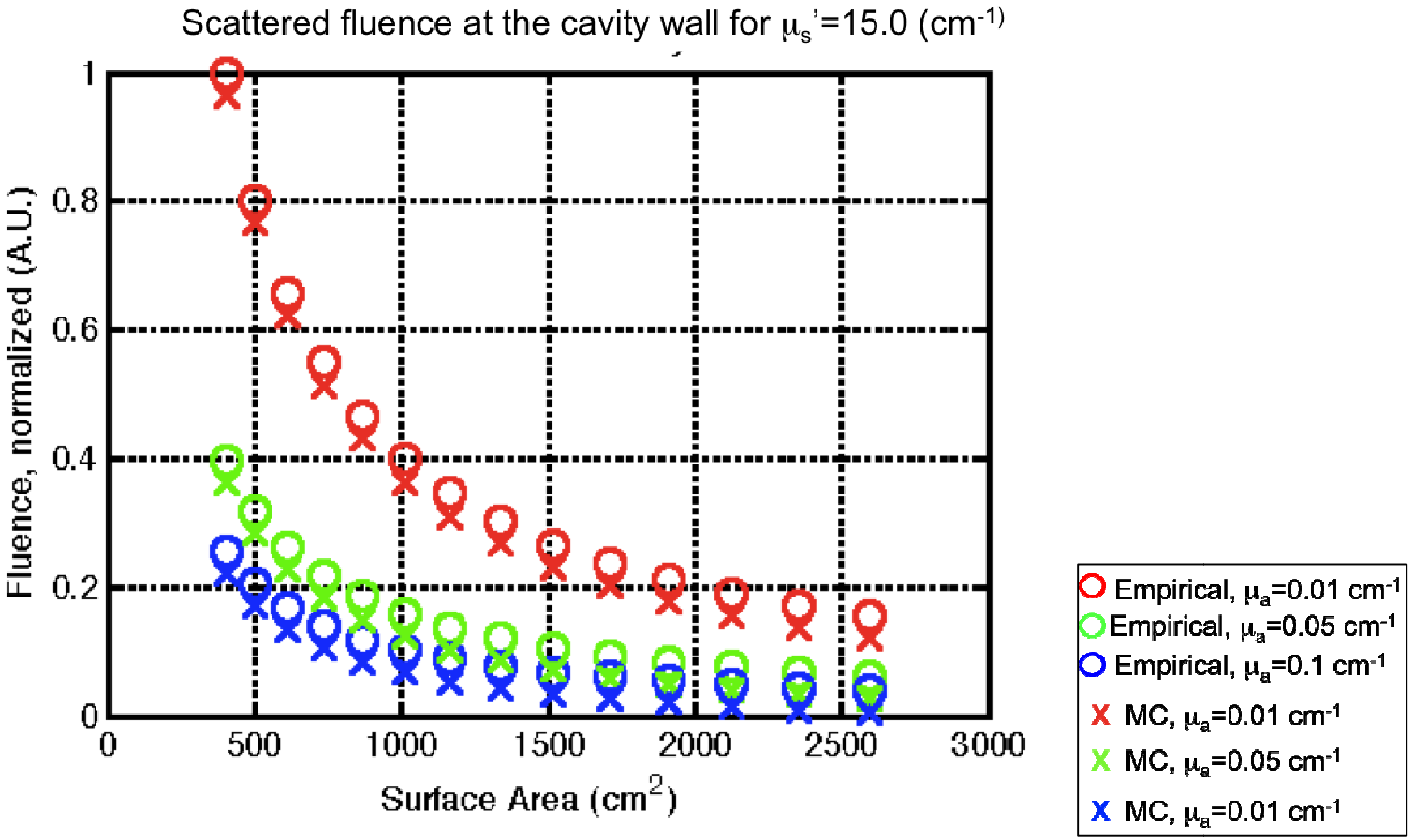


Figure 4.28: : $\phi_s$ rate per source power at the wall of an air cavity vs surface area: MC results compared to empirical solution, eqn.( 4.44 ) for $\mu_s'$=15.0 ($cm^{-1}$)

Where the fluence was normalized by dividing the results by maximum value for fluence for $\mu_a$=0.01 ($cm^{-1}$)

.

## 4.8 Spherical Cavity Phantom Study

This study presents the results of an extensive phantom study that uses different sized acrylic spheres and optical properties (both absorption and scattering). An isotropic detector measured the fluence at the inner cavity wall. These measurements are compared to fluence calculations using eqn.( 4.33 ).

The fluence as a function of angle along the cavity wall (Figure 4.28) agrees well with eqn. ( 4.33 ), but the analytic solution for the total fluence at the cavity wall overestimates the fluence compared to the MC results (Figure 4.28) for total fluence as a function of surface area. This indicates a need to modify the analytic solution, either numerically based on simulation results or via a different analytic approach. The results of these simulations do verify that the total fluence at the cavity wall decreases cavity surface area as 1/SA regardless of cavity symmetry.

### *4.8.1 Experimental Setup*

The experimental setup for dose verification in a phantom used four different cavity geometries (three spheres of radius=4.14, 5.46, and 7.78 cm) submerged in solutions of varying optical properties. Two phantom treatments were conducted using the navigation system with human torso geometry submerged in a solution of $\mu_a$=0.78 $cm^{-1}$ and $\mu_s'$= 11.2 cm-1. A contour and detector positions were measured twice using the contour navigation tool. Treatments were performed for a period of five minutes each at a power of 3 W at 70% efficiency. The light source position on the treatment wand was determined using the method described in section 5.2.1. All data was processed using programs developed in Matlab™. Black India ink was used for the absorption component and 20% concentration Intralipid™ was used for the scattering component. Intralipid™ has been shown to produce scattering similar to that observed in biologic tissues[86, 141] while the absorption spectra of the concentration of black ink used is

similar to that of hemoglobin.

For each sphere, an isotropic detector was placed on the inside cavity wall and another placed on the outside cavity wall to measure fluence monitored by an in-house made dosimetry system (see Figure 4.29).


Figure 4.29: In-house built dosimetry system to measure fluence

An isotropic light source was used for the spherical cavities and a cylindrically diffusing light source was used for the human torso geometry, both at 730 nm, at a power ranging from 1-2 W (see Figure 4.30 for setup schematic, and Figure 4.31 for photos of the various setups). Each cavity was submerged in a solution of nine different optical property combinations ($\mu_a$=0.1 $cm^{-1}$, 0.5 $cm^{-1}$, 1.0 $cm^{-1}$, $\mu_s$'=2 $cm^{-1}$, 10 $cm^{-1}$, 20 $cm^{-1}$) for each cavity condition (air, water, and attenuating solution). Optical properties were measured using a motorized parallel catheter system described previously in [11, 24], with the detector and source at 3 mm separation and the detector moving an overall distance of 5 mm. For each solution, optical properties were measured three times and fluence measured five times, with the resulting value of optical properties and fluence being the average of the measurements respectively. For each solution

combination, the light source was placed at both the center of the cavity and at an off-center location in order to observe source location affects on fluence at the cavity wall. Measurements were made in darkened room to prevent overhead lights from affecting overall fluence levels while cavities were submerged in solutions contained in clear plastic containers.

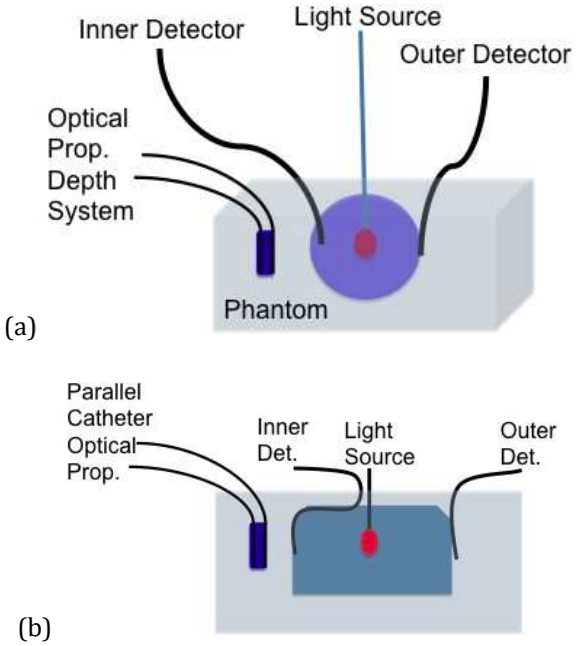


Figure 4.30: Schematics for experimental setup of phantom study

(a) Schematic of experimental setup for a spherical cavity. Optical properties were measured three times before the light source was placed within the cavity. (b) Schematic of experimental setup for the human torso geometry. The "radius" of this geometry was determined by measuring the volume of the cavity and treating the cavity as a sphere.

(a) 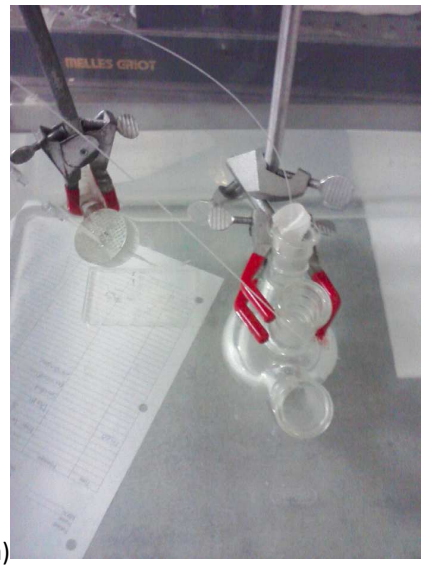


(b) 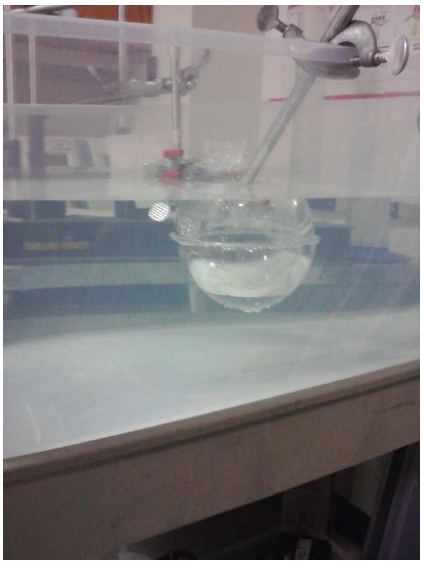

(c) 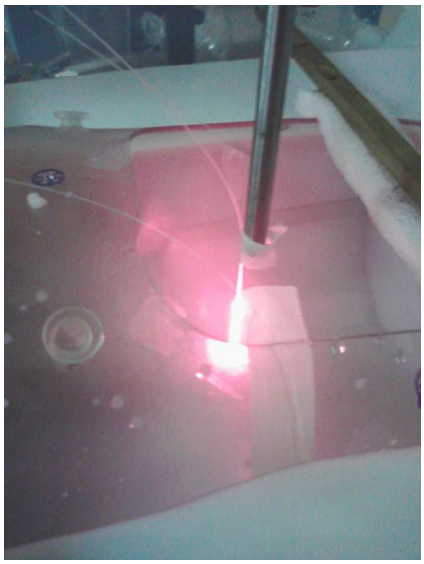

Figure 4.31: Setup for spherical cavity and torso phantom study

(a) and (b) Setup for spherical cavities submerged in solution. Note the parallel catheter system on the left of Figure 4.31a used to measure the optical properties of the solution. (c) Setup for the human torso phantom submerged in solution with a cylindrically diffusing light source located at the center of the cavity.

### *4.8.2 Results for Spherical Cavity Phantoms*

Figure 4.32-Figure 4.34 display the results from the spherical cavity measurements for spheres of varying radius. For a spherical air cavity, there is good agreement between the averaged measured fluence values and the calculated values (calculated using Eqn.( 5.2 )). As the absorption coefficient of the solution surrounding the cavity increases we see the expected decrease in fluence flatten out. We also observe the expected overall increase in observed fluence with increasing reduced scattering. Once a medium other than air is introduced into the cavity, this agreement begins to break down, with the theory overestimating the fluence. These results are independent of cavity size.

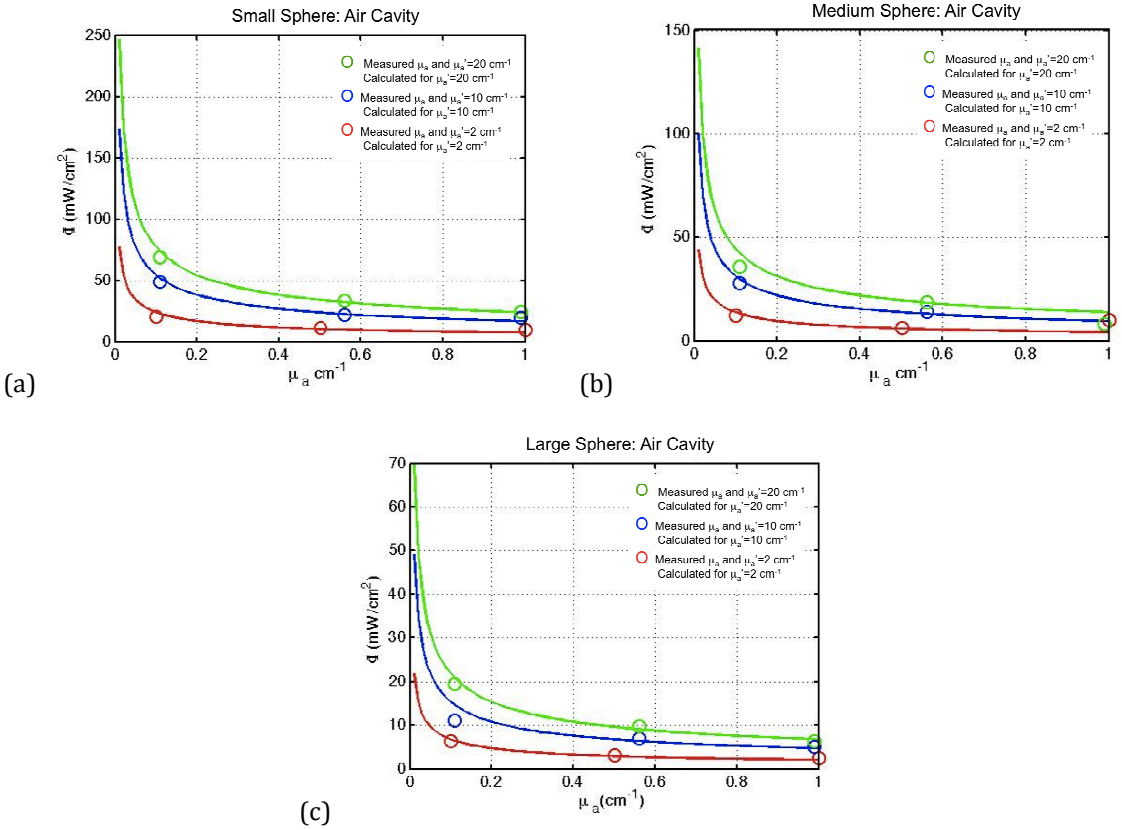


Figure 4.32: Spherical air cavity phantoms measured fluence compared to analytic solution

(a-c) Fluence as a function of $\mu_a$ for $\mu_s$'=2 (red), 10 (blue), and 20 cm-1 (green). Fluence calculated using ( 5.1 ) is represented by a solid line.

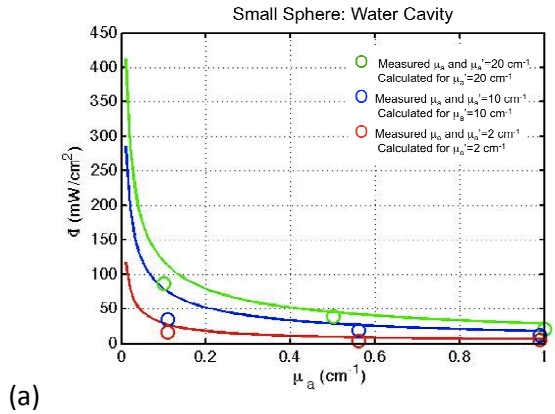


(a)

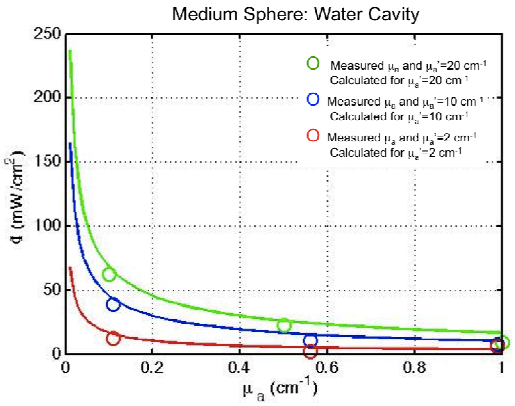


(b)

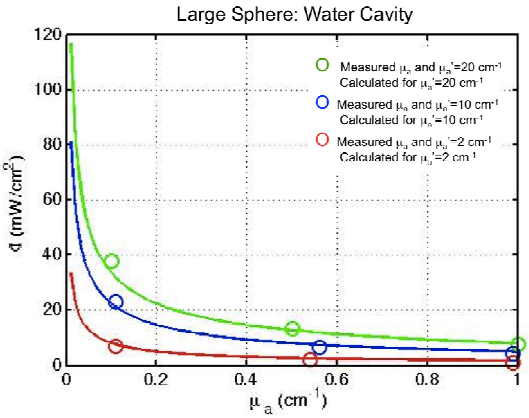


(c)

Figure 4.33: Spherical water cavity phantoms measured fluence compared to analytic solution

(a-c) Fluence as a function of $\mu_a$ for $\mu_s'$=2 (red), 10 (blue), and 20 cm-1 (green). Fluence calculated using ( 5.1 ) is represented by a solid line.

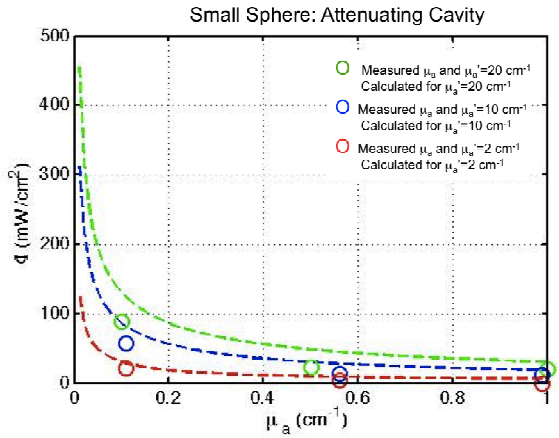


(a)

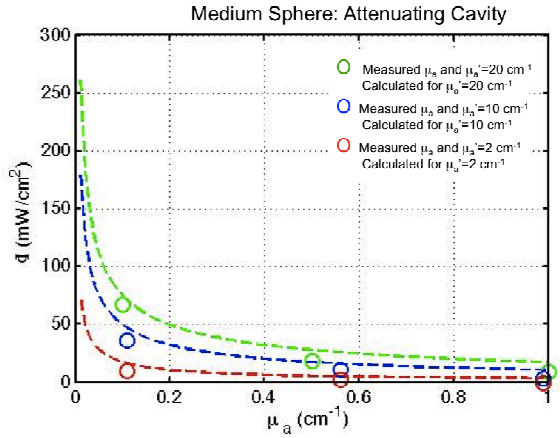


(b)

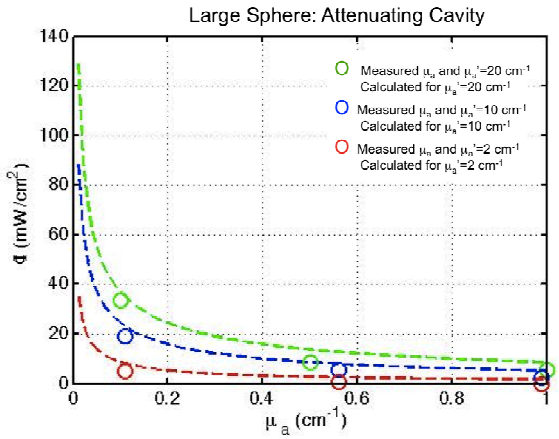


(c)

Figure 4.34: Spherical cavity with attenuating medium phantoms measured fluence compared to analytic solution

(a-c) Fluence as a function of $\mu_a$ for $\mu_s'$=2 (red), 10 (blue), and 20 cm-1 (green). Fluence calculated using ( 5.1 ) is represented by a dashed line.

## 4.9 Light Fluence as a function of optical properties

Our MC simulations consider on an isotropic point source, or a pencil beam that is convolved to simulate isotropic point source. In reality, the fluence is also affected by the type of light source: linear, planar, and point sources. In addition to the effects the type of light have on the fluence, whether multiple scattering occurs becomes important in determining the fluence. Furthermore, the effect of optical properties becomes even more pronounced on fluence inside the tissue itself. Figure 4.35a-c shows the light fluence rate, normalized to $P/4\pi r^2$, vs. $\mu_{eff}$ for a range of $\mu_s'$ between 2 and 20 $cm^{-1}$ for a multiple scattering (MS) point source inside a 10 cm radius sphere at 0.5 cm depth. Comparing the MS point source (dashed-dotted lines) to the planar source (dashed line) at the same depth in tissue (0.5 cm), the former is 3–7 times higher than the later, depending on the optical properties. This increased value is due entirely to the effect of multiple scattering, with minor influence due to the curvature of the 10 cm sphere compared to that of the flat semi-infinite geometry.

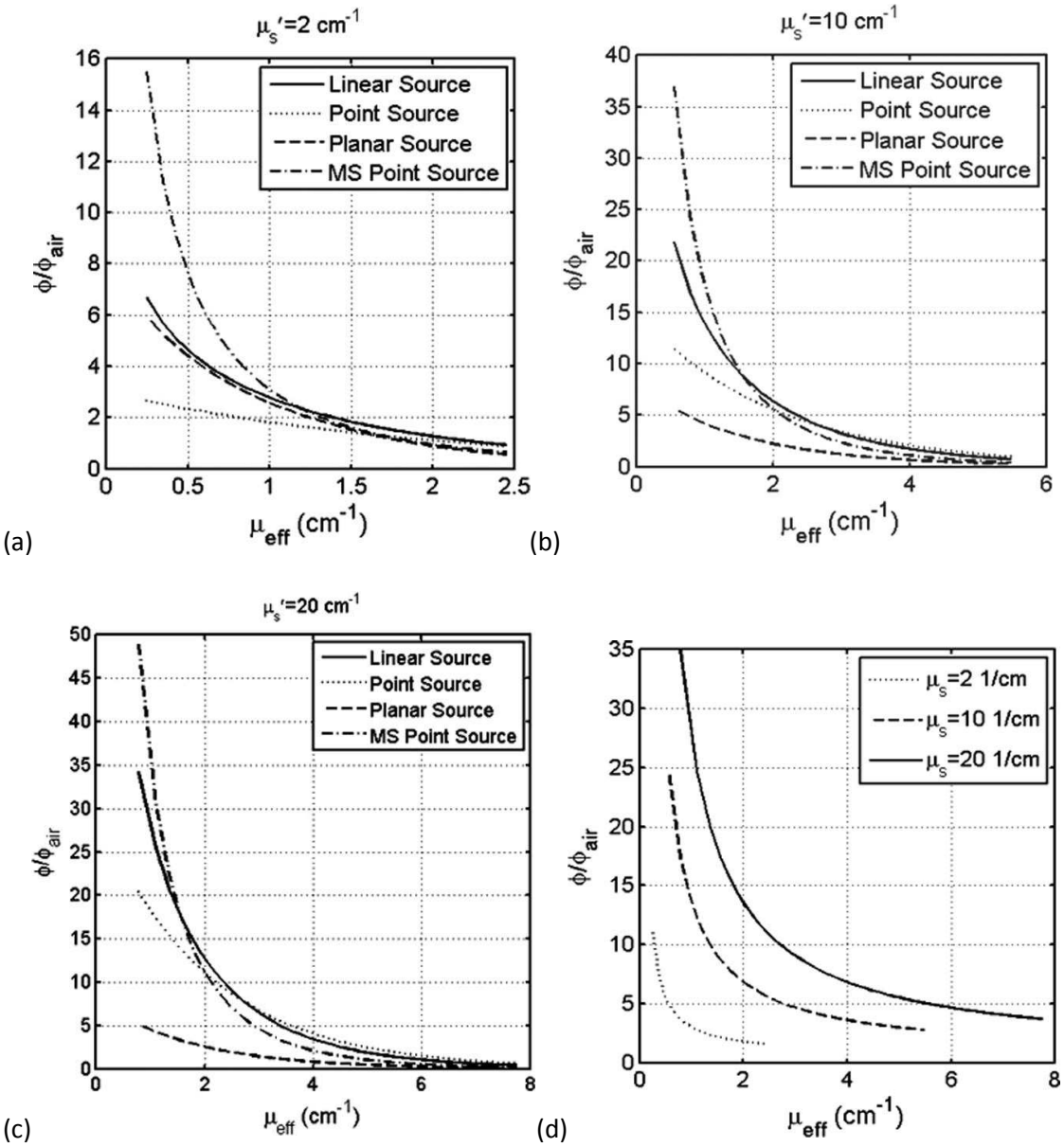


Figure 4.35: Fluence versus $\mu_{eff}$ for different light sources

Fluence rate, normalized to in-air fluence rate, versus $\mu_{eff}$ for linear, point sources inside an infinite medium, planar light sources (dotted line) on a semi-infinite medium below an air-tissue interface, and point source with multiple scattering (MS) inside a spherical cavity of 10 cm radius at 0.5 cm from the light source (for point or linear sources) or 0.5 cm depth in tissue (planar or MS point sources) for $\mu_s'$= (a) 2.0, (b) 10.0 , (c) 20 $cm^1$. (d) $\phi/\phi_{air}$ in a spherical cavity at the air-tissue boundary.

From our MC simulations, we are able to consider how scattered fluence (Figure 4.36) at the cavity boundary is a function of the optical properties of the surrounding medium. We used

the MC results from Section 4.3.3 for a spherical air cavity with a 10 cm radius and a centrally located source to observe how the fluence changes with $\mu_{eff}=(3\mu_a\mu_{tr})^{1/2}$. The scattered fluence was calculated for the corresponding $\mu_{eff}=(3\mu_a\mu_{tr})^{1/2}$ using eqn.( 4.33 ) for an isotropic point source. For each $\mu_s$' we see a unique curve when plotted against scattered fluence (also observed in Figure 4.35). The agreement between theory and the MC results begins to diverge at low $\mu_{eff}$, which corresponds to low $\mu_a$. The $\chi^2$ values of Figure 4.36 is 0.0494.

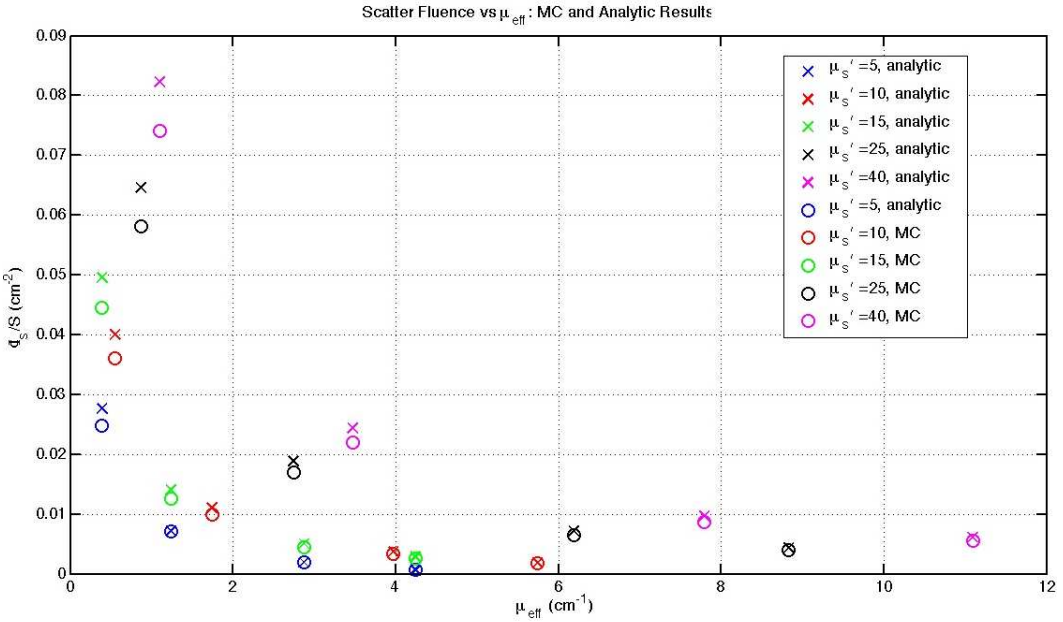


Figure 4.36: Scattered fluence at the cavity wall vs $\mu_{eff}$ for a spherical air cavity of radius 10 cm

Scattered fluence is plotted for the optical properties listed in Table 4.1 and using eqn. ( 4.33 ) for the analytic solution.

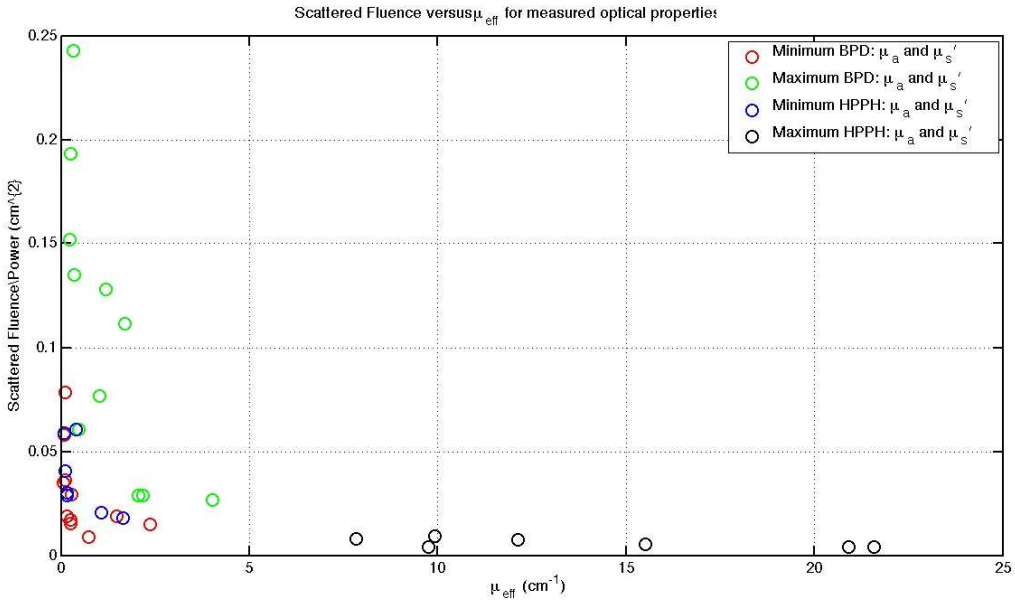


Figure 4.37: Scattered Fluence versus $\mu_{eff}$ for the minimum and maximum values of measure optical properties

Scattered fluence calculated using data from Table 3.4, Table 3.5, Table 3.6, and Table 3.7 and eqn.( 4.33 ).

While our work focuses primarily on using MC simulations to determine the fluence in a cavity, finite element models (FEM) is another method used to model the fluence. A simple FEM simulation was run for an air cavity of radius=10 cm. The model was given the diffusion approximation equations and boundary conditions discussed in chapter 2 to solve for the fluence in the medium surrounding the cavity (Figure 4.38). This method again verifies that scattered fluence is uniform at the cavity boundary for homogeneous optical properties, regardless of source location.

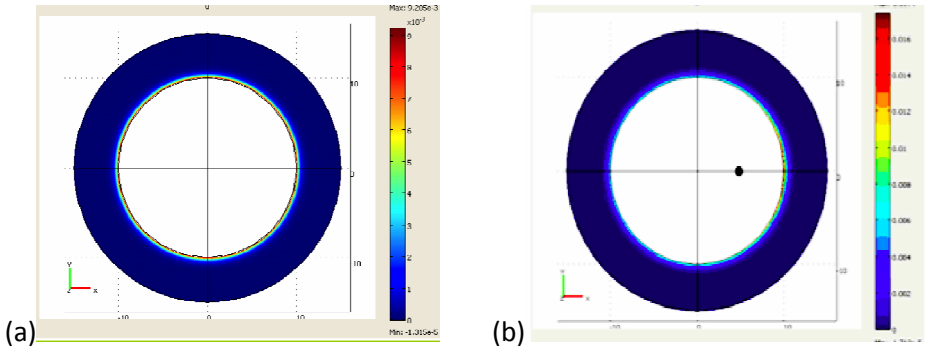

Figure 4.38: Depiction of FEM solution for an air cavity

(a) Fluence for a centrally located source, (b) fluence for a source located at x=5 in an air cavity with $\mu_a$ = 0.3 $cm^{-1}$, $\mu_s'$=14 $cm^{-1}$, r = 10 cm

The MC simulations developed here do not consider how fluence is affected by inhomogeneous optical properties in the surrounding medium. As observed from our results in chapter 3, the optical properties in the thoracic cavity vary greatly, and how this great variation affects total and scattered fluence is unknown. The MC simulation developed for attenuation has the potential to assign different optical properties to each voxel of the system. Without an analytic solution for this scenario, the results from such a simulation would need to be verfied both by FEM and by phantom studies before an empirical formal could be developed. In a brief study, we ran a FEM for a spherical air cavity where half the cavity had a uniform range of optical properties from $0^o$ to $180^o$. Just from this simple FEM run, we see that inhomogenous

optical properties have a significant effect on fluence in the surrounding tissue. In future studies, a relationship between this change in optical properties and fluence both in the cavity and in the surrounding medium should be explored.

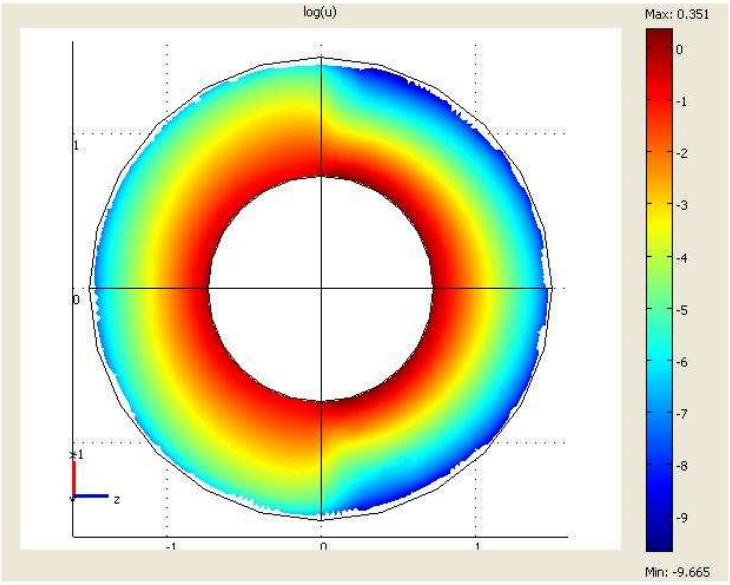


Figure 4.39: FEM fluence results for changing optical properties

$\mu_a$ went from 0.01-1.0 in 0.01 increments over 180$^o$, $\mu_s$' went from 2.0-10 in 0.5 increments over 180$^o$

# Chapter 5

# Fluence Modeling and IR Navigation

The preceding chapters discuss several key elements of implementing more accurate and efficient light fluence delivery during PDT mediated plural PDT in the thoracic cavity. The spectroscopic evaluation of the thoracic cavities if patient enrolled in the Phase I study at UPHS demonstrate the wide ranging variety of the optical properties both throughout a single thoracic cavity and between patients. The fluence modeling developed and verified via MC simulations provide an analytical solution for light distribution within a cavity and in the surrounding medium, given a set of optical properties. Utilizing our spectroscopic data in our fluence models we have the potential to calculate patient specific light fluence, a novel approach to pleural PDT.

## 5.1 Introduction

In collaboration with Drs. X. Liang, C. Chang, and T.Zhu, B. Lui and Michele Kim, an infrared (IR) tracking camera was used to develop a treatment guidance system. This tracking system provides the missing piece of the puzzle of real-time, patient-specific PDT light fluence. This system tracks obtains a contour of the patient's thoracic cavity during surgery and then tracks the position of the light source relative to the cavity walls. With this position data, we can improve the uniformity of light treatment[42]. Current light fluence protocol provides only discrete light fluence information; seven isotropic detectors are sutured at strategic points in the thoracic cavity[112, 113]. The detected fluence of these detectors is displayed to clinician in

real-time, and once all seven detectors reach the prescribed light fluence, the light treatment is ended. Using the IR tracking system, in contrast, provides guidance to the clinician over the entire cavity in 3D, when real-time light source position data is displayed. The initial development and application of this tracking system is presented in the following sections.

## 5.2 Infrared Camera System

### *5.2.1 Instrumentation*

This navigation system is based on an IR camera (Polaris® Spectra, North Digital Inc., Waterloo, Canada), which has been used in medical fields such as spinal surgery, position control of surgical robot, and abdominal therapy intervention [142, 143]. Utilizing the IR camera shown in Figure 5.1a, the navigation system is able to obtain a contour of the patient's thoracic cavity, and track the position of the light source during treatment in 3D. The accuracy of the system was ~0.5 mm in 3D, and the maximum volume for the system was ~ 205 ° x 186 ° x 147 $cm^3$, which was sufficient for operations on our patient population. The tracking tool in the navigation system is a rigid body built on passive reflective markers (Figure 5.1b). The markers are used as the tracking target for the navigation system to track motion of the light source.

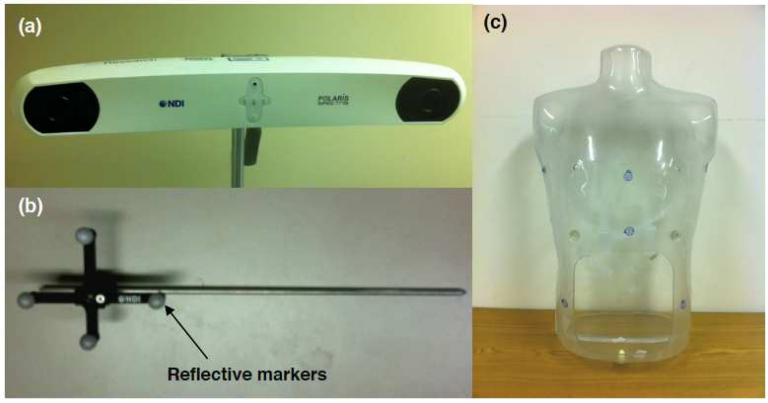


Figure 5.1: IR tracking system and torso phantom

Photographs of (a) pleural PDT navigation camera, (b) tracking tool for the navigation system, and (c) human-shape phantom.

Once the tracking tool is in the working volume, the IR camera system starts to track the position of the markers in 3D, and track the position of the tip of the rigid body by applying a vector to the position of the markers. The tip position data are transferred to a computer at a rate of 20-60 Hz, and can be displayed in real-time. When taking a surface contour in phantoms, the tip of the tracking tool is used to gently slide against the inner surface. The tracking tool tip positions over time represented the surface positions or raw contour data in 3D, based on which the inner surface contour is determined, given enough position samples. Before this system was implemented and further developed in the operating room, extensive phantom studies were conducted in order to determine wand design and overall procedure.

### *5.2.2 Treatment Guidance Procedure*

The procedure of the image-guidance system for pleural PDT is shown in Figure 5.2. Two positioning wands were used in this procedure to complete the image guidance. One wand was used for taking detector and treatment surface contour, while the other one was used for tracking the light source position during PDT treatment. They are referred to as contour wand and treatment wand respectively. Both wands are calibrated to locate their tip positions by pivoting them around a fixed point. Then an optimization algorithm was used to determine the shift between the treatment wand tip and the laser point source. The contour wand is then used to locate the seven detectors on the cavity surface, and also to determine the cavity contour. When the PDT treatment begins, the treatment wand is used and the light fluence distribution on the cavity surface is calculated simultaneously from the position data. The scattered portion of light fluence is given by[144]:

$$\phi_{sc} = \frac{4S}{SA} \cdot \rho e^{-\mu_{atten} r_{avg}} \cdot [1 + \rho e^{-\mu_{atten} r_{avg}} (1 - f) + \rho^2 (1 - f)^2]$$

$$= \frac{4S}{SA} \cdot \frac{\rho e^{-\mu_{atten} r_{avg}}}{1 - \rho e^{-\mu_{atten} r_{avg}} (1 - f)}, \quad (5.1)$$

where $S$ is the light source (W), $A_s$ is the surface area of the cavity, $R_d$ is defined in Eqn.( 2.35 ), and $f$ is the fraction of open area to the surface area of the cavity. The total fluence then becomes:

$$\phi_{cavity} = \frac{S}{4\pi r^2} e^{\mu_{eff} r} + \frac{4S}{SA} \cdot \frac{\rho e^{-\mu_{atten} r_{avg}}}{1 - \rho e^{-\mu_{atten} r_{avg}} (1 - f)}, \quad (5.2)$$

Where $r$ is the distance between the cavity wall and the light source. Using Eqn.( 5.2 ) the light fluence can be calculated in real-time to achieve a uniform light fluence in the cavity. To verify the image-guidance procedure, the isotropic detectors sutured to the thoracic cavity surface are used to compare the calculated fluence from the tracking data with the detectors measurements at several positions.

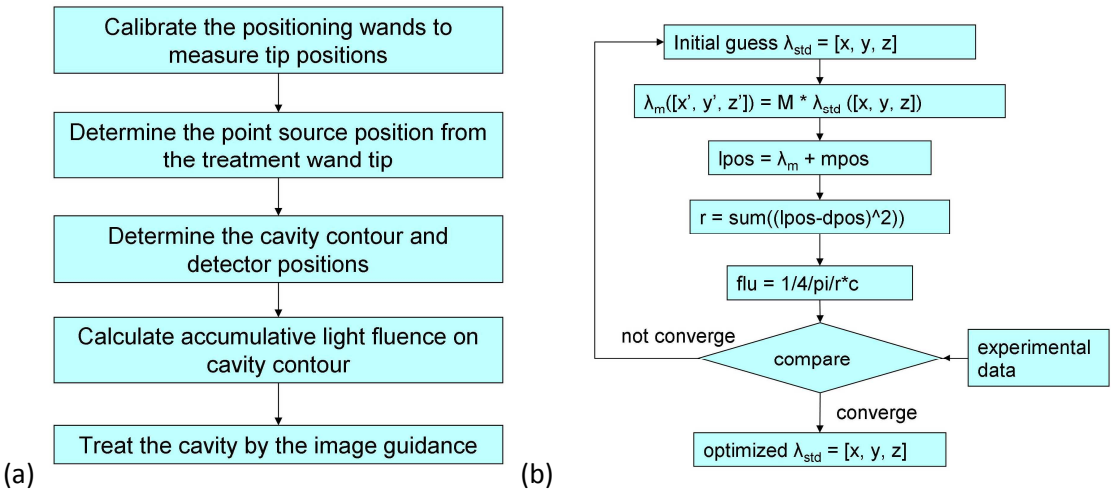


Figure 5.2: Schematics for treatment procedure and optimization algorithm

(a) Schematics for the treatment procedure for image guided treatment. (b) Schematics for the optimization algorithm to determine iteratively the position of the laser source relative to the wand tip ($\lambda_m$).

## 5.3 IR Camera Study for Human Torso Cavity

This study is a continuation of the phantom study discussed in section4.8. The experiment setup was similar to that of section 4.8.1, with the human torso submerged in a tub of a liquid solution with optical properties similar to that of tissue. Position data of the treatment is collected from the IR navigation system while concurrently light distribution measurements were made using t isotropic detectors. These measurements were compared to fluence calculations made using data from the IR navigation system to verify our light distribution theory (using eqn. ( 5.1 )) is correct and applicable in patient-like settings.

### *5.3.2 Results: Human Torso Cavity*

The human torso phantom picture in Figure 5.1c was submerged in a solution of varying optical properties, and the fluence experienced at the cavity was measured using two isotropic detectors. Figure 5.3 displays the results of these measurements compared to the calculated fluence, treating the torso cavity as a sphere of the same volume. Unlike the spherical cavity, there appears to be greater agreement between theory and observation for a water cavity as

compared to the air cavity.

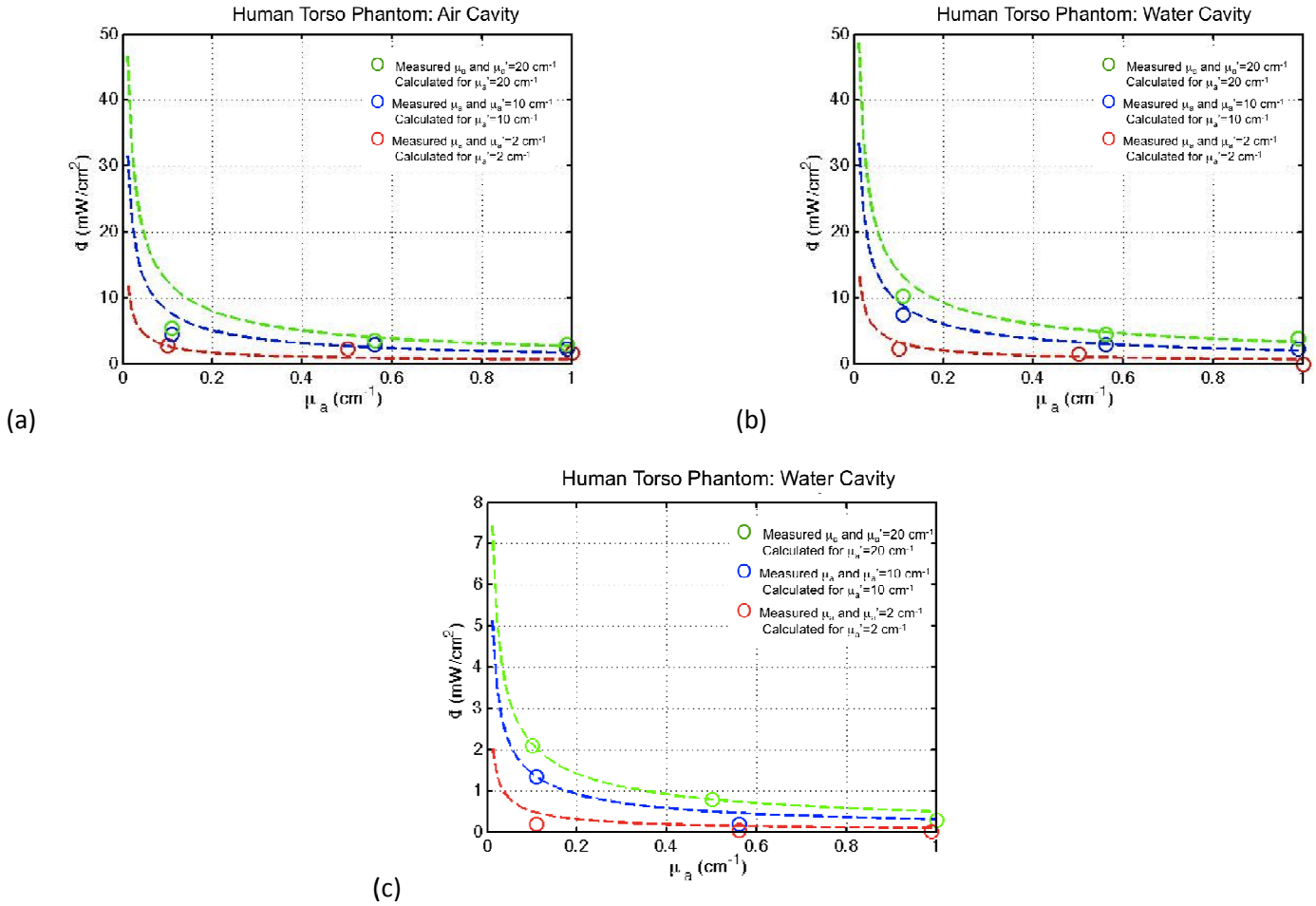


Figure 5.3: Averaged measured fluence per source power for human torso phantom compared to analytic solution. The averaged fluence measured (circles) compared the fluence calculated (dashed line) for the human torso cavity for an (a) air cavity, (b) water cavity, and (c) attenuating medium cavity.

### *5.3.3 Navigation System Application to human torso phantom*

Using the procedure presented in [145], two treatments were conducted using the human torso cavity. Using the position tracking data coupled with Eqn.( 5.2 ) where *r* is the distance between the light source and the cavity wall (the location of which is determined using the contour displayed in Figure 5.5a), a comparison is made between measured and observed fluence. By including the scattered light in the calculation, greater agreement is achieved between observation and theory, as seen in Figure 5.5.

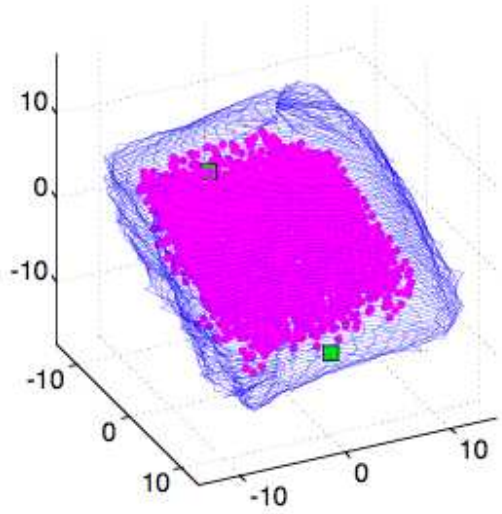


Figure 5.4: Contour of human torso taken with IR camera

The walls of the phantom are represented by blue, the movement of the light source is represented by pink, and the two isotropic detectors measuring fluence are represented by green squares.

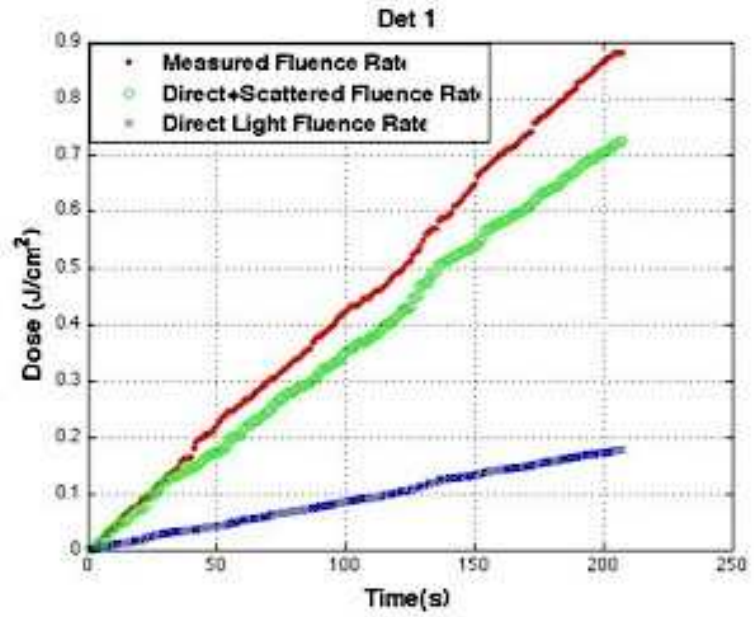


(a)

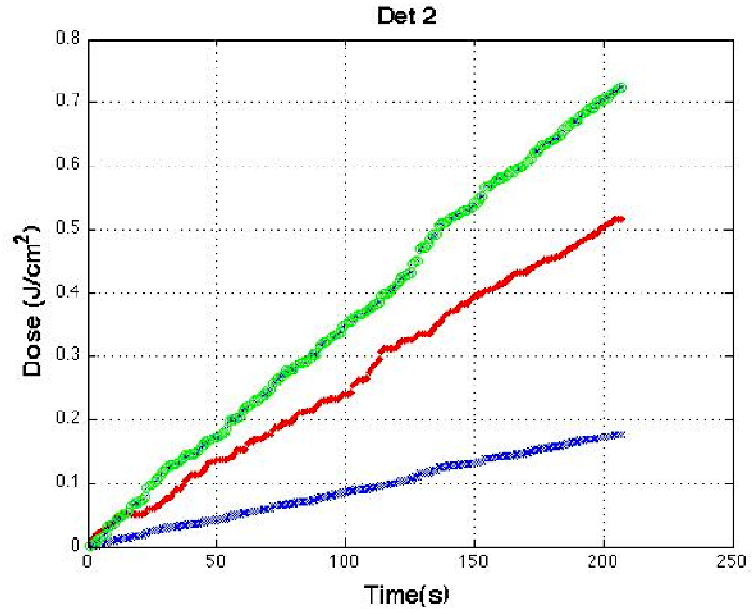


(b)

Figure 5.5: Results for IR system applied to torso phantom. (a-b) the overall fluence rate measured as a function of time (red) compared to the direct light calculation (blue) and the direct plus scattered light calculation (green).

The results for a spherical air cavity are in good agreement with the theory presented in Eqn. ( 5.2 ). Upon the introduction a medium within the cavity, however, this agreement begins to break down and the theory consistently overestimates the amount of fluence experienced by the cavity wall. Further investigation is needed to determine the cause of this disagreement. When considering a cavity of arbitrary geometry such as an empty human torso, the geometry can effectively be approximated as a sphere of the same volume and still achieve good agreement between fluence observations and calculated fluence. Again, with the introduction of an attenuating medium in the cavity, our theory overestimates the fluence at the cavity wall.

## 5.4 Recent Developments

The development of this guidance system is ongoing and the result of the collaborative efforts of the entire PDT group at UPenn. The earliest stages of development, worked on by Dr. Chang, Dr. Liang, Dr. Zhu, and myself, included wand design, methods of light source determination, and proper procedure in the OR. The phantoms studies discussed above aided in verifying light fluence calculations using this system. The most recent developments are the product of the work of Michele Kim, Baochang Liu, Xing Liang, and Tim C. Zhu and are included here to present readers with the most recent developments of this ongoing project.

### *5.4.1 Improved real-time determination of light source position [146]*

The light source is placed inside an ellipsoidal balloon that is filled with an Intrallipd™ solution. This setup makes it challenging to accurately determine the location of the light source in relation to the trip of the treatment wand. Several generations of tools were developed to address these issues. The most recent tool uses eight different isotropic detectors in known locations (Figure 5.6), as opposed to the first generation of light source positioning tool, which used one detector and required the measurement of eight different positions (see Figure

5.6a)[42]. With this new light source position tool, a reference wand is used to measure the relative positions of the detectors in the OR (see arrow in Figure 5.6). This new tool provides a faster and more accurate method of determining the light source position.

(a) 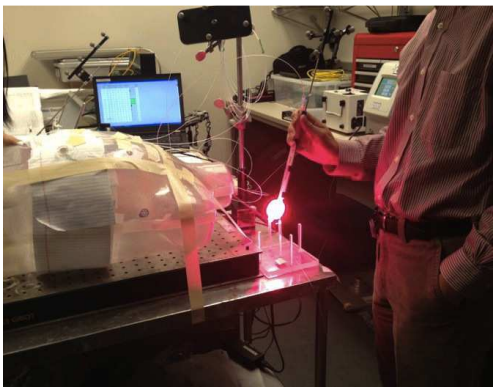 (b) 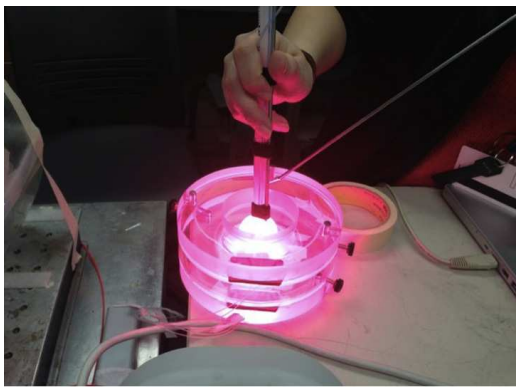

Figure 5.6: Light source position tool

Laser source position determination using (a) a single isotropic detector and (b) modified laser source calibration tool that incorporates 8 isotropic detectors so that all 8 measurements can be performed at once. The arrow points to the positioning wand for the tool.

### *5.4.2 Real-time feedback of light fluence calculations*

In order to provide real-time feedback to the measured values, Xing Liang and Baochang Liu developed another Matlab™-based GUI to display the calculated light fluence on a 2D unwrapped surface. OpenIGTLink™ was used to provide a platform communicating between the NDI Polaris camera and a PC. The light source position data were acquired at a frequency of 20 Hz from the NDI™ data acquisition driver. When the PC receives the light source position data, Matlab™ was used to calculate the cumulative light fluence on every point of the pleural cavity contour, and to display/update the unwrapped light fluence distribution map at the frequency of 20 Hz. In the light fluence distribution map, 3D points on the pleural cavity contour were unwrapped into 2D $\phi$-z maps, given the condition that on each x-y plane of the cavity contour, there is only one point for each angle $\phi$, where $\phi=\text{atan}(y/x)$. Calculation is based on the direct light term of Eqn.( 5.2 ) and displayed the cumulative light fluence in real-time during treatment.

# Chapter 6

# Conclusions and Future Work

## 6.1 Summary

The goal of this work was to address to key factors in PDT light dosimetry for treatment in cavity-like geometries: the modeling of light dose in a cavity and the determination of in vivo optical properties via spectroscopic methods. Prior to this work, understanding and reliable modeling of how applied light during PDT is affected by treatment in a cavity was developed only for spherical symmetric cavities. In vivo optical properties of both the canine interperitoneal and human thoracic cavities were unknown.

Building upon the existing theory of the diffusion approximation to the radiative transport equation, we successfully verified Willem Star's theory for total and scattered fluence in a spherical cavity with no attenuating medium. We built on this work by creating MC simulations of spherical cavities with air, attenuation, and off-center light sources to verify the scattered fluence at the cavity wall is uniform, regardless of attenuation or light source position. We went further to demonstrate that scattered fluence is not only uniform for spherically

symmetric cavities, but also oblate ellipsoids. The results of our simulations indicate to us that the scattered fluence is a function the cavity surface area. This result hold much promise as the IR navigation system developed and presented here will be able to determine the surface area of a patient's thoracic cavity in real-time. This tool, in combination with these results, may be further developed to calculate the patient-specific light dose in real-time during treatment.

An equally important aspect of this work was the successful in vivo measurements of canine and human tissues during treatment. As shown in the first chapter, in vivo human data of this nature is very limited and the data presented here does much to expand what is currently available in the literature. The spectroscopy data not only informs our light fluence model but also provides vital information concerning tissue oxygenation, drug concentration, and total hemoglobin levels in treated tissue. The high variability between patients and tissue types indicates the need for real-time in vivo spectroscopy to fully and most accurately inform our fluence model; work that is already being explored.

Add a paragraph to discuss the magnitude of scatter fluence for the range of optical properties observed above.

Further developing a fluence model for a completely arbitrary treatment cavity geometry, and combining this model with the IR navigation remains to be completed. Once this is accomplished, combined with real-time spectroscopy holds significant potential to implement a patient-specific PDT light dose and improve PDT efficacy overall.

# Appendices

## A.1 $P_3$ Approximation for a Semi-Infinite Medium

The $P_3$ approximation, which is used to determine the Green's function of the radiative transport equation, was developed to overcome the two major limitations of diffusion theory: $\mu_a << \mu_s'$ and is only valid for source-detector distances larger than one mean free path. Recall the mean free path is $1/(\mu_a+\mu_{s'})$. We present the following derivation developed by Hull and Foster[68] for the $P_3$ approximation.

The Boltzman equation is a widely accepted method of describing light propagation in turbid media. Here we use the time independent Boltzmann equation as all our work assumes a steady state solution:

$$\frac{1}{c}\frac{\partial L(\vec{r},\hat{s},t)}{\partial t} = -\nabla\cdot L(\vec{r},\hat{s},t) - \mu_t L(\vec{r},\hat{s},t) + \mu_s \int_{4\pi} L(\vec{r},\hat{s},t)\, f(\hat{s},\hat{s}')d\Omega' + S(\vec{r},\hat{s},t), \quad \text{(A. 1)}$$

Where *L* is the radiance at a position ***r*** in direction ***s*** and has units of power per unit area per unit solid angle. The function *f* is the scattering phase function, describing the probability a photon with direction ***s*** will be scattered into direction ***s'***. Equation (A. 1) is difficult to solve analytically and several different approaches to determine a solution have been developed. Here, we consider a $P_n$ approximation, expanding up to *n=3*. The angular quantities of eqn.(A. 1) are expanded in spherical harmonics $Y_{lm}$:

$$L(\vec{r},\hat{s},t) = \sum_{l=0}^{N}\sum_{m=-l}^{l}\left(\frac{2l+1}{4\pi}\right)\phi_{lm}(\vec{r},t)Y_{lm}(\hat{s})$$

$$S(\vec{r},\hat{s},t) = \sum_{l=0}^{N}\sum_{m=-l}^{l}\left(\frac{2l+1}{4\pi}\right)\sigma_{lm}(\vec{r},t)Y_{lm}(\hat{s}) \quad \text{(A. 2)}$$

Where $\phi_{lm}$ is the moment of radiance and $\sigma_{lm}$ is the moment of the source distribution. Here, the fluence is defined as the isotopic component of the radiance, which is given by:

$$\phi_{00} = \int_{4\pi} L(\vec{r}.t)\, d\hat{s} \quad \text{(A. 3)}$$

We assume that the scattering amplitude is a function of the scattering angle, but independent of the spatial location and direction of the incident light. The scattering phase function can then be expressed by a series of Legendre polynomials:

$$f(\vec{r},\cdot\,\hat{s}') = \sum_{l=0}^{N}\left(\frac{2l+1}{4\pi}\right)g_l P_l(\hat{s}\cdot\hat{s}') \quad \text{(A. 4)}$$

For an infinite slab geometry, the radiance is dependent on the *z* coordinate and the cosine of the angle between the *z* axis and the observation direction $\hat{s}$. This quantity will be referred to as $\eta$. Equations (A. 2) and (A. 4) are then expanded to the following:

$$L(z,\eta) = \sum_{m=0}^{3}\left(\frac{2m+1}{4\pi}\right)\varphi_m(z)P_m(\eta)$$

$$S(z,\eta) = \sum_{m=0}^{3}\left(\frac{2m+1}{4\pi}\right)q_m(z)P_m(\eta) \quad \text{(A. 5)}$$

$$f(\hat{s}\cdot\hat{s}') = \sum_{m=0}^{3}\left(\frac{2m+1}{4\pi}\right)g_m(z)P_m(\hat{s}\cdot\hat{s}')$$

Where $P_m$ is a Legendre polynomial of order $m$ and $\varphi_m$ and $q_m$ are the moments of radiance source distribution respectively. We use the expressions in eqn. (A. 5) in eqn. (A. 1) by multiplying by $P_l(\eta)$ and integrating over all solid angles, resulting in a first order linear ordinary differential equation:

$$\frac{1}{2l+1}\left[l\frac{d}{dz}\varphi_{l-1}+(l+1)\frac{d}{dz}\varphi_{l+1}\right]+(\mu_t-\mu_s g_l)\varphi_l=q_l \tag{A. 6}$$

Expanding (A. 6) to $l=3$:

$$\begin{aligned}
\mu_a\varphi_0+\varphi_1{}'&=q_0,\\
\frac{1}{3}\varphi_0{}'+\mu_t^{(1)}\varphi_1+\frac{2}{3}\varphi_2{}'&=q_1,\\
\frac{1}{5}\varphi_1{}'+\mu_t^{(2)}\varphi_2+\frac{3}{5}\varphi_3{}'&=q_2,\\
\frac{1}{7}\varphi_2{}'+\mu_t^{(3)}\varphi_3&=q_3,
\end{aligned} \tag{A. 7}$$

where the prime denote differentiation, $\mu_a^{(l)}=\mu_a+\mu_s(1-g_l)$, and $\mu_t^{(0)}=\mu_a$. To find a complete solution for the radiance in the $P_3$ approximation, we determine four single-exponential solutions to homogeneous version of eqns. (A. 7) for the source-free regions for the moment of radiance. We assume a solution for $\varphi_l$ of the form:

$$\varphi_l(z)=\sum_{j=0}^{3}A_{l_j}e^{\nu_j z} \tag{A. 8}$$

Substituting eqn.(A. 8)into eqns.(A. 7) for $l=0,1,2,3$:

$$\nu[(l+1)A_{l+1}+lA_{l-1}]+(2l+1)\mu_t^{(l)}A_l=0 \tag{A. 9}$$

By requiring the determinants of eqns.(A. 9) to vanish, nontrivial solutions for $\nu$:

$$\nu = \pm\nu^{+} = \pm\left(\frac{\beta + \sqrt{\beta^2 - \gamma}}{18}\right)^{1/2}$$
$$\nu = \pm\nu^{-} = \pm\left(\frac{\beta - \sqrt{\beta^2 - \gamma}}{18}\right)^{1/2} \quad \text{(A. 10)}$$

where:

$$\beta = 27\mu_a\mu_t^{(1)} + 28\mu_a\mu_t^{(3)} + 35\mu_t^{(2)}\mu_t^{(3)}$$
$$\gamma = 3780\mu_a\mu_t^{(1)}\mu_t^{(2)}\mu_t^{(3)} \quad \text{(A. 11)}$$

The values for $\nu^{\pm}$ were previously determined by Star[147] and Boas *et al.*[134]. The coefficients $A_{l_j}$ are determined by solving eqn. (A. 9) which are related to $A_{0_j}$ and are functions of the optical properties of the medium, $h_l(\nu_j)$:

$$A_{0_j} = A_{0_j}h_1(\nu_j) \qquad h_1(\nu_j) = \left(-\frac{\mu_a}{\nu_j}\right) \quad \text{(A. 12)}$$

$$A_{2_j} = A_{0_j}h_2(\nu_j) \qquad h_2(\nu_j) = \left(-\frac{1}{2} + \frac{3\mu_a\mu_t^{(1)}}{2\nu_j^2}\right) \quad \text{(A. 13)}$$

$$A_{2_j} = A_{0_j}h_2(\nu_j) \qquad h_2(\nu_j) = \left(-\frac{1}{2} + \frac{3\mu_a\mu_t^{(1)}}{2\nu_j^2}\right) \quad \text{(A. 14)}$$

Recall that the $h_0(\nu_j)$ are equal to unity.

The radiance in the source-free region of the media with planar symmetry is given by:

$$L(z,\eta) = \sum_{l=0}^{3}\left(\frac{2l+1}{4\pi}\right)\varphi_l P_l(\eta) \quad \text{(A. 15)}$$

Where $\varphi_l(z)$ is given by eqn.(A. 8), the attenuation coefficients $\nu_j$ are given by eqns.(A. 10) and constants defined by eqns.(A. 12),(A. 13), and (A. 14). The constants are determined by the source distribution and boundary conditions.

For a slab of infinite length and finite width of thickness *2b* and a homogeneous distribution of isotropic sources, we can determine the fluence using the above approach. First, we take the limit as the slab width goes to zero, the source strength goes to infinity, and the product $2q_0b$ is equal to unity (unit source per unit area).

As observed in Figure A. 1, there are two regions of interest: the internal region, where $|z|<b$, and the external region, where $|z|>b$. In the internal region, all possible values of $\nu$ are permissible (see eqn.(A. 10)) while in the external region only decaying solutions, meaning , are permissible.

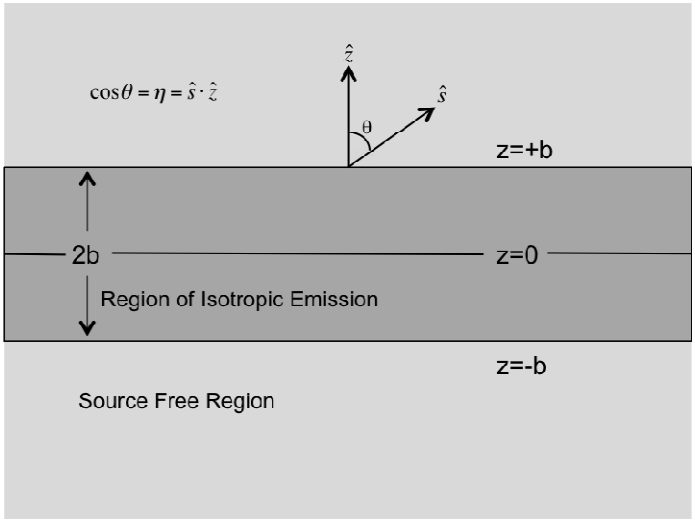


Figure A. 1: Semi-infinite geometry slab used in the derivation of the $P_3$ approximation

By symmetry about the z=0 axis, and the $h_l(\nu_l)$ are of odd parity with respect to $\nu$ for odd *l* and even parity for even *l*, the following expressions are obtained for the internal region:

$$\begin{aligned}
\varphi_{0_{in}}(z) &= E\cosh(z\nu^-) + F\cosh(z\nu^+),\\
\varphi_{1_{in}}(z) &= Eh_1(\nu^-)\sinh(|z\nu^-|) + Fh_1(\nu^+)\sinh(|z\nu^+|),\\
\varphi_{2_{in}}(z) &= E\,h_2(\nu^-)\cosh(z\nu^-) + F\,h_2(\nu^+)\cosh(z\nu^+),\\
\varphi_{3_{in}}(z) &= Eh_3(\nu^-)\sinh(|z\nu^-|) + Fh_3(\nu^+)\sinh(|z\nu^+|),
\end{aligned} \tag{A. 16}$$

And for the external region:

$$\begin{aligned}
\varphi_{0_{out}}(z) &= Ce^{-\nu^-(|z|-b)} + De^{-\nu^+(|z|-b)}\\
\varphi_{0_{out}}(z) &= Ce^{-\nu^-(|z|-b)} + De^{-\nu^+(|z|-b)}\\
\varphi_{2_{out}}(z) &= Ch_2(-\nu^-)e^{-\nu^-(|z|-b)} + Dh_2(-\nu^+)e^{-\nu^+(|z|-b)}\\
\varphi_{3_{out}}(z) &= Ch_3(-\nu^-)e^{-\nu^-(|z|-b)} + Dh_3(-\nu^+)e^{-\nu^+(|z|-b)}
\end{aligned} \tag{A. 17}$$

We are interested in the external region coefficients *C* and *D*, which describe the radiance outside the source region. At the boundaries $z = \pm b$, we require continuity of each moment of radiance and assume an isotropic source ($q_l$*=0* for all $l \geq 1$). The solution to eqn.(A. 7) then becomes:

$$\varphi_0(z,\eta) = \frac{q_0}{\mu_a}, \qquad \varphi_l(z,\eta) = 0 \qquad (l > 0) \tag{A. 18}$$

With these conditions, we solve the following system of equations at the boundary for the coefficients *C* and *D*:

$$\varphi_{0_{in}}(\pm b) + \frac{q_0}{\mu_a} = \varphi_{0_{out}}(\pm b) \tag{A. 19}$$

$$\varphi_{1_{in}}(\pm b) = \varphi_{1_{out}}(\pm b)$$

$$\varphi_{2_{in}}(\pm b) = \varphi_{2_{out}}(\pm b)$$

$$\varphi_{3_{in}}(\pm b) = \varphi_{3_{out}}(\pm b)$$

The resulting expression for *C* and *D*, taking the limit $b \to 0, q_0 \to \infty, 2q_0 b = 1$:

$$C = \frac{\nu^{-3}\left[3\mu_a\mu_t^{(1)} - \nu^{-2}\right]}{6\mu_a^2\mu_t^{(1)}\left(\nu^{-2} - \nu^{+2}\right)}$$

$$D = \frac{\nu^{+3}\left[3\mu_a\mu_t^{(1)} - \nu^{-2}\right]}{6\mu_a^2\mu_t^{(1)}\left(\nu^{+2} - \nu^{-2}\right)} \qquad \text{(A. 20)}$$

To conclude, the fluence for a semi-infinite medium with an infinite place source is:

$$\varphi_0 = Ce^{-\nu^- z} + De^{-\nu^+ z} \qquad \text{(A. 21)}$$

Where the coefficients *C* and *D* are defined in eqn. (A. 20).

## A.2 Absorption Spectra of HPPH in Solvents

### *A.2.1 Methods*

The absorption spectra of HPPH used in the Phase I study ongoing at UPenn was measured using an Ocean Optics cuvette holder, our Avantes white light source, and our LN-cooled CCD spectrograph. Two transfer fibers were connected by a variable attenuator and carried the light from the source to the cuvette holder. The attenuator was adjusted prior to measurements to prevent saturation of the CCD. Three different solvents were used: PBS, dextrose-5, and "Solvenator", a homemade detergent (SDS (10%)+NaOH(1%)+dd$H_2O$(89%)).

Solvents were measured at 0, 5, 10, and 20 minutes in two different cuvettes (for a total of eight measurements). Between measurements each cuvette was removed from the holder and replaced at the next time interval. Following these measurements, a solution of 1 ml solvent and 0.05 g of bovine serum albumin (BSA) for a 5% concentration of BSA was made (again, measurements were made using two different cuvettes for each solvent-BSA combination for a total of eight measurements). A solution of 1 ml solvent and 20 μL of HPPH (aqueous solution at 1.37 mg/ml) was then made and measured using the schema described above (four measurements total for one cuvette). Following this series of measurements, a solution of 1 ml solvent, 0.05 g BSA, and 10 μL HPPH was made and measured in a similar fashion. HPPH was measured using the Eppendorf 10-100 μL (Serial No. 410455) pipette.

Emission spectra of two lasers were characterized using the same spectrograph and overlaid on the absorption spectra of HPPH to determine a relative effectiveness.

### *A.2.2 Results*

Measurements made over time were averaged and the standard deviation was found. The error bars were created by taking *(standard deviation)/($N^{1/2}$)* where *N* is the number of measurements made (*N*=8 for solvent-only and solvent+BSA measurements, *N*=4 for HPPH+solvent and HPPH+BSA+solvent measurements). Table 1 lists the values of the raw data, $\mu_a$, and transmission with the corresponding standard deviations for 661 and 665 nm for HPPH+BSA+solvent solutions and HPPH+solvent solutions.

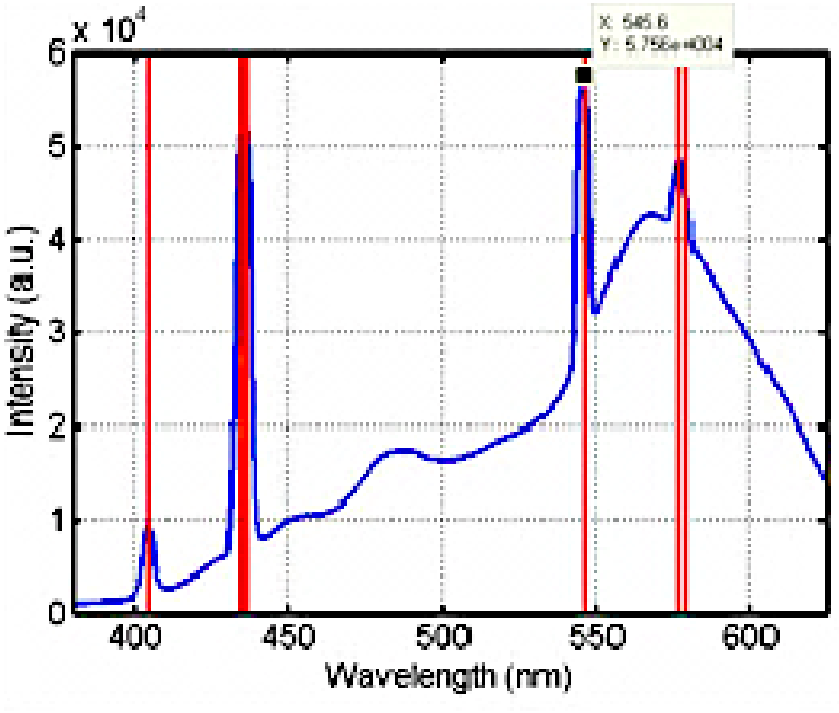


Figure A. 2: Overhead mercury lamp with known spectral peaks

Measurement of overhead mercury lamp (blue curve) overlaid with the known spectral peaks (vertical lines) of mercury emission. There is good agreement (maximum deviation is ~0.5 nm) between the two spectra, indicating the wavelength calibration for the spectrograph is correct.

Table A. 1: Measurements of HPPH and HPPH solvents

| HPPH+BSA | Peak (nm) | wv (nm) | $\mu_a$ | stdev | $\Sigma \phi_{661}/\Sigma\phi_{665}$ | $\Sigma \phi_{658}/\Sigma\phi_{661}$ | $\Sigma \phi_{658}/\Sigma\phi_{665}$ |
|---|---|---|---|---|---|---|---|
| PBS | | 658 | 2.08E+00 | 2.61E-03 | | | |
| | 665.40 | 661 | 2.65E+00 | 2.63E-03 | 0.8912 | 0.8047 | 0.7172 |
| | | 665 | 3.01E+00 | 3.15E-03 | | | |
| Solvenator | | 658 | 7.45E-01 | 2.16E-01 | | | |
| | 663.80 | 661 | 8.84E-01 | 2.93E-01 | 0.9505 | 0.8542 | 0.8119 |
| | | 665 | 9.17E-01 | 3.11E-01 | | | |
| D5W | | 658 | 2.17E+00 | 8.04E-03 | | | |
| | 664.60 | 661 | 2.69E+00 | 8.68E-03 | 0.9208 | 0.8372 | 0.7709 |
| | | 665 | 2.92E+00 | 9.87E-03 | | | |
| **HPPH** | **Peak (nm)** | **wv (nm)** | $\mu_a$ | **stdev** | $\Sigma \phi_{661}/\Sigma\phi_{665}$ | $\Sigma \phi_{658}/\Sigma\phi_{661}$ | $\Sigma \phi_{658}/\Sigma\phi_{665}$ |
| PBS | | 658 | 1.33E+00 | 9.28E-03 | | | |
| | 665.00 | 661 | 1.64E+00 | 8.91E-03 | 0.9012 | 0.8374 | 0.7547 |
| | | 665 | 1.84E+00 | 9.31E-03 | | | |
| Solvenator | | 658 | 1.47E+00 | 1.31E-02 | | | |
| | 664.20 | 661 | 1.90E+00 | 1.18E-02 | 0.9066 | 0.8229 | 0.7461 |
| | | 665 | 2.11E+00 | 1.04E-02 | | | |
| D5W | | 658 | 1.90E+00 | 1.34E-02 | | | |
| | 664.60 | 661 | 2.38E+00 | 1.34E-02 | 0.9002 | 0.8229 | 0.7487 |
| | | 665 | 2.65E+00 | 1.22E-02 | | | |
| Roswell | 667.70 | | | | 0.8307 | 0.7774 | 0.6458 |

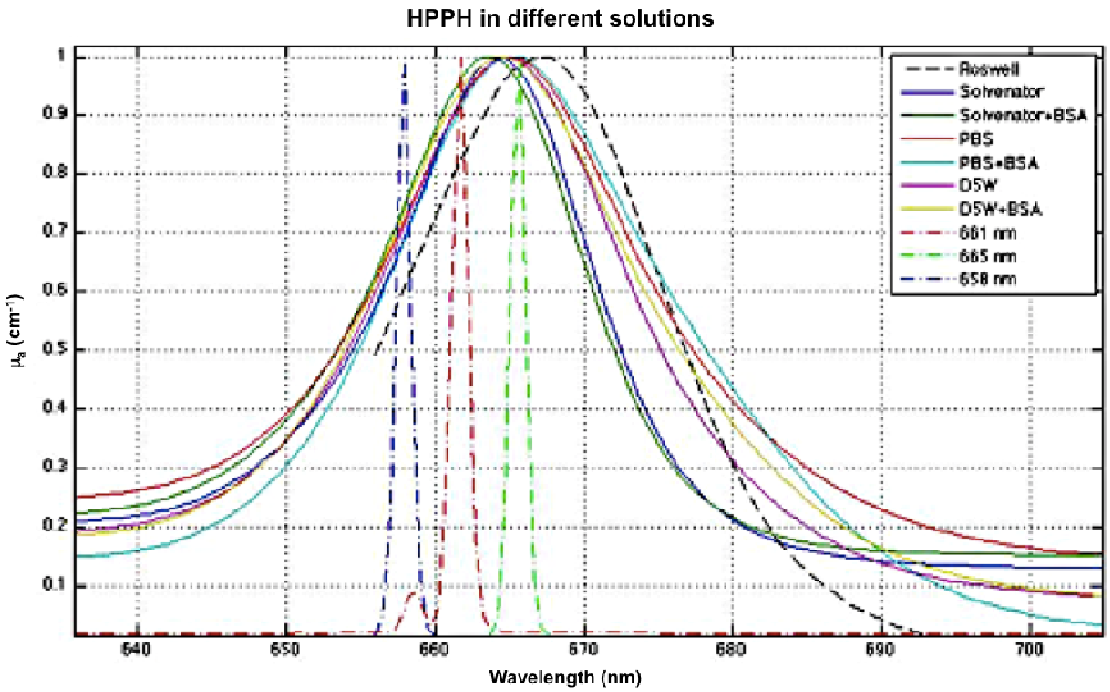


Figure A. 3: HPPH in different solutions

## A.3 Verification of the wavelength of three B&W Tek diode lasers

### *A.3.1 Purpose*

A new 665 nm diode laser was purchased from B&W Tek. A series of measurements were done on both the new 665 nm and the existing 661 nm to quantify the emission spectrum and power setting dependence.

### *A.3.2 Methods & Materials*

The two lasers measured are listed in Table A. 1. In each case, the laser being measured as coupled to a 400 micron core, 0.39 NA optical cable (Thorlabs M28L02). The power out of the fiber was measured using a thermopile power meter (Coherent LM-10). Care was taken to ensure that the beam projected by the fiber under-filled and was concentric with the active area of the detector. To measure the spectrum, the same fiber was coupled into one port of a 6-inch integrating sphere (Labsphere). A second port, blocked from the first by a baffle (661 nm laser

measurements were not blocked by the baffle), was coupled to an SMA patch cable, through a manual attenuator (OZ optics), and into a CCD based spectrograph. The attenuator was adjusted to prevent saturation of the detector. Multiple spectra were acquired at each power setting of each laser to ensure that the spectrum was stable over time. Multiple spectra were also taken at different slit widths to observe how sharp the spectral peak becomes. To verify the wavelength calibration of the spectrograph, a measurement of the spectrum of the lab's overhead mercury lights was recorded.

### *A.3.3 Results*

Figure A. 2 shows the correspondence between the measured spectrum of the overhead mercury fluorescence lights (data) and known emission lines (vertical red lines). The maximum different between known emission and measured emission is ~1.7 nm. Table A. 1 lists the measured power, wavelength peaks, and FWHM for both the 661 and 665 nm lasers at different powers. For both lasers, the wavelength peak gradually shifts higher in the spectrum as power increases. The 661 nm displays a greater shift in spectral peak than the new 665 laser, which shifts about ~0.5 nm (see Figure A. 4). In both cases, the wavelength measurements made with the spectrograph were in agreement with rough measurements made with a handheld dial monochromator.

Table A. 2: BWF-5-665 Laser

| Power setting (mA) | Total power (mW) | Peak center (nm) | FWHM (nm) |
|---|---|---|---|
| 0.5 | 0.48 | 665.8 | 2.5 |
| 1 | 0.96 | 665.8 | 2.5 |
| 1.5 | 1.46 | 665.8 | 2.5 |
| 2 | 1.98 | 665.8 | 2.5 |
| 3 | 2.98 | 665.8 | 2.5 |
| 4 | 3.90 | 665.8 | 2.5 |
| 6 | 5.80 | 666.3 | 2.5 |
| 8 | x | 666.3 | 2.6 |

Table A. 3: BWF-5-661 Laser

| Power setting (mA) | Total power (mW) | Peak center (nm) | FWHM (nm) |
|---|---|---|---|
| 0.5 | X | 660.4 | 2.5 |
| 1 | X | 660.4 | 2.7 |
| 1.5 | X | 660.7 | 2.6 |
| 2 | X | 660.9 | 2.7 |
| 3 | X | 660.9 | 2.6 |
| 4 | X | 661.4 | 2.6 |
| 6 | X | 661.9 | 2.6 |
| 8 | X | 662.4 | 2.6 |

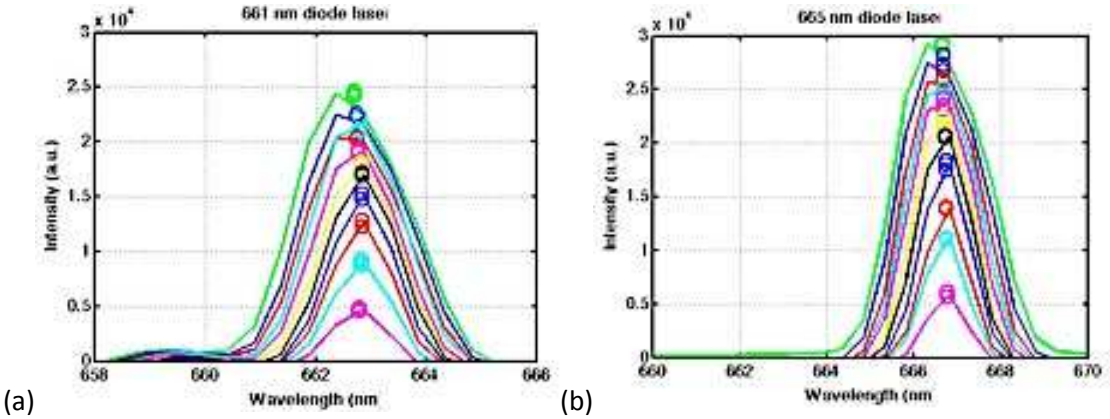


(a) (b)

Figure A. 4: Measured spectra of the 661 and 665 diode lasers

## A.4 List of Presentations and Publications

### *A.4.1 Presentations*

J.L. Sandell[3], J.C. Finlay, T. Zhu, J. Friedberg, K.A. Cengel, In Vivo Determination of Optical Properties from Pleural PDT in Humans. 35th Annual Meeting. American Society for Photobiology. June 12-16, 2010, Providence, RI.

J.L. Sandell, C. Chang, T.C. Zhu, Light Fluence Rate Calculation for Intracavity Photodynamic Therapy. 52nd Annual Meeting. American Association for Physicists in Medicine. Imaging General Poster Discussion. July 18-22, 2010. Philadelphia, PA.

J.L. Sandell, T.C. Zhu, J.C. Finlay, X. Liang. Monte Carlo Simulation of Arbitrary Geometries and Heterogeneous Optical Properties for Treatment Planning in PDT. 53rd Annual Meeting, American Association of Physicists in Medicine. Therapy General Poster Discussion. July 31-August 4. Vancouver, BC.

### *A.4.2 Presentation Proceedings*

Jarod C. Finlay; Julia L. Sandell; Timothy C. Zhu; Robert Lewis; Keith A. Cengel; Stephen M. Hahn: Spectroscopic evaluation of photodynamic therapy of the intraperitoneal cavity. Proc SPIE 7551: 755109, March 2010.

Julia Sandell; Chang Chang; Jarod C. Finlay; Timothy C. Zhu (senior author): A treatment planning system for pleural PDT. Proc SPIE 7551: 75510C, March 2010.

Julia L. Sandell; Timothy C. Zhu; Jarod C. Finlay: A study of light fluence rate distribution for PDT using MC simulation Proc SPIE 7886: 788619, Feb 2011.

Julia Sandell; Jarod C. Finlay; Timothy C. Zhu: Determining how uncertainties in optical properties affect light dose calculations for PDT Proc SPIE 7886: 78860N, Feb 2011.

Timothy C. Zhu; Xing Liang; Chang Chang; Julia Sandell; Jarod C. Finlay; Andreea Dimofte; Carmen Rodriguez; Keith Cengel; Joseph Friedberg; Eli Glatstein; Stephen M. Hahn: An IR navigation system for real-time treatment guidance of pleural PDT. Proc SPIE 7886: 28860L, Feb 2011.

Julia L Sandell, Xing Liang, Timothy C. Zhu: Light dose verification for pleural PDT. Proc

SPIE 8210: 821010, April 2012.

Timothy C. Zhu, Xing Liang, Julia Sandell, Jarod C. Finlay, Andreea Dimofte, Carmen Rodriguez, Keith Cengel, Joseph Friedberg, Stephen M Hahn, Eli Glatstein: A real-time treatment guidance system for pleural PDT Proc SPIE 8210: 821009, April 2012.

Dimofte A, Anna Sharikova, Julia Meo, Chuck Simone, Joseph Friedberg, and Timothy C. Zhu: Light dosimetry and dose verification for pleural PDT. Proc SPIE 8568: 85680V, April 2013.

Julia L. Meo and Timothy Zhu: Monte Carlo simulation of light fluence calculation during pleural PDT. Proc SPIE 8568: 85680U, April 2013.

### *A.4.3 Publications*

J.L. Sandell, T.C. Zhu, *A review of in-vivo optical properties of human tissues and its impact on PDT*. Journal of Biophotonics, 2011. **4**: p. 773-787

J.L. Meo, T.C. Zhu, R. Lewis, K.A. Cengel, S.M. Hahn, J.C. Finlay. *In vivo Spectroscopic Evaluation of the Intraperitoneal Cavity in Canines*. Manuscript in Preparation.

J.L. Meo, T.C. Zhu, K.A. Cengel, C. Simone M. Cullighan, C. Edmonds, J. Friedberg, S.M. Hahn, J.C. Finlay. *Diffuse reflectance and fluorescence spectroscopy in the human thoracic cavity in-vivo*. Manuscript in Preparation.

X. Liang, J. Meo, C. Chang, K.A. Cengel, J.C. Finlay, T.C. Zhu. *Real-time treatment planning for pleural photodynamic therapy – Determining cavity contour.* Manuscript submitted to Physics in Medicine and Biology. 2013

# BIBLIOGRAPHY


1. Marijnissen, J.P.A., W. Star, H.J.A. Zandt, M.A. D'Hallewin, and L. Baert, *In situ light dosimetry during whole bladder wall photodynamic therapy: clinical results and experimental verification.* Physics in Medicine and Biology, 1993. **38**: p. 567-582.
2. Shackley, D., C. Whitehurst, J. Moore, N. George, C. Betts, and N. Clarke, *Light penetration in bladder tissue: implications for the intravesical photodynamic therapy of bladder tumours.* BJU International, 2000. **86**: p. 638-43.
3. Star, W.M., J. Marijnissen, M. Keijzer, and M.J.C. van Gamert, *Light Dosimetry for photodynamic therapy by whole bladder wall irradiation.* Photochemistry and Photobiology, 1987. **46**: p. 619-624.
4. Staveren, H., J. Beek, M. Keijzer, and W. Star, *Integrating sphere effect in whole-bladder-wall photodynamic therapy: II. The influence of urine at 458, 488,514 and 630 nm optical irradiation.* Physics in Medicine and Biology, 1995. **40**: p. 1307-1315.
5. Staveren, H., J. Beek, J. Ramaekers, M. Keijzer, and W. Star, *Integrating sphere effect in whole bladder wall photodynamic therapy: I. 532 nm versus 630 nm optical irradiation.* Physics in Medicine and Biology, 1994. **39**: p. 947-959.
6. Staveren, H., M. Keijzer, T. Keesmaat, H. Jansen, W. Kirkel, J. Beek, and W. Star, *Integrating sphere effect in whole-bladder-wall photodynamic therapy: III. Fluence multiplication, optical penetration and light distribution with an eccentric source for human bladder optical properties.* Physics in Medicine and Biology, 1996. **41**: p. 579-590.
7. van Gemert, M.J.C., W.F. Cheong, A.J. Welch, and W. Star, *Light Delivery for Whole-Bladder Photodynamic Therapy.* Lasers in Surgery and Medicine, 1987. **2**: p. 273-284.

8. van Staveren, H.J., M. Keijzer, T. Keesmaat, H. Jansen, W. Kirkel, J.F. Beek, and W.M. Star, *Integrating sphere effect in whole-bladder-wall photodynamic therapy: III. Fluence multiplication, optical penetration and light distribution with an eccentric source for human bladder optical propertie.* Physics in Medicine and Biology, 1996. **41**(4): p. 579-590.

9. Altschuler, M., T. Zhu, J. Li, and S. Hahn, *Optimization of light sources for prostate photodynamic therapy.* Proceedings SPIE, 2005. **5689**: p. 186-197.

10. Davidson, S., R. Weersink, M. Haider, M. Gertner, A. Bogaards, D. Giewercer, A. Scherz, J. Trachtenberg, and B. Wilson, *Treatment planning and dose analysis for interstitial photodynamic therapy of prostate cancer.* Physics in Medicine and Biology, 2009. **54**: p. 2293-2311.

11. Finlay, J., T. Zhu, A. Dimofte, D. Stripp, S. Malkowicz, R. Whittington, J. Miles, E. Glatstein, and S. Hahn, *In vivo determination of the absorption and scattering spectra of the human prostate during photodynamic therapy.* Proc. SPIE, 2004. **5315**: p. 132-142.

12. Finlay, J.C., T.C. Zhu, A. Dimofte, D. Stripp, S.B. Malkowicz, T.M. Busch, and S.M. Hahn, *Interstitial Fluorescence Spectroscopy in the Human Prostate During Motexafin Lutetium-Mediated Photodynamic Therapy.* Photochemistry and Photobiology, 2006. **82**: p. 1270-1280.

13. Li, J., M. Altschuler, S. Hahn, and T. Zhu, *Optimization of light source parameters in the photodynamic therapy of heterogeneous prostate.* Physics in Medicine and Biology, 2008. **53**: p. 4107-4121.

14. Li, J. and T. Zhu, *Determination of in vivo light fluence distribution in a heterogeneous prostate during photodynamic therapy.* Physics in Medicine and Biology, 2008. **53**: p. 2103-2114.

15. Moore, C., C. Mosse, C. Allen, H. Payne, M. Emberton, and S. Bown, *Light penetration in the human prostate: a whole prostate clinical study at 763 nm.* Journal of Biomedical Optics, 2011. **16**(1): p. 015003.

16. Solenenko, M., R. Cheung, T. Busch, A. Kachur, G. Griffin, T. Vulcan, T. Zhu, H.-W. Wang, S. Hahn, and A. Yodh, *In-vivo reflectance measurement of motexafin lutetium uptake, optical properties, and oxygenation of canine large bowels, kidneys, and prostates.* Physics in Medicine and Biology, 2002. **47**: p. 857-873.

17. Svensson, T., E. Alerstam, M. Einarsdottir, K. Svanberg, and S. Andersson-Engels, *Towards accurate in vivo spectroscopy of the human prostate.* Journal of Biophotonics, 2008. **1**(3): p. 200-203.

18. Svensson, T., S. Andersson-Engels, M. Einardsdottir, and K. Svanberg, *In vivo optical characterization of human prostate tissue using near-infrared time-resolved spectroscopy.* Journal of Biomedical Optics, 2007. **12**(1): p. 0140221-01402210.

19. Swartling, J., J. Axelsson, G. Ahlgren, K. Kalkner, S. Nilsson, S. Svanberg, K. Svanberg, and S. Andersson-Engels, *System for interstitial photodynamic therapy with online dosimetry: first clinical experiences of prostate cancer.* Journal of Biomedical Optics, 2010. **15**(5): p. 058003.

20. Weersink, R.A., A. Bogaards, M. Gertner, S.R.H. Davidson, K. Zhange, G. Netchev, J. Trachtenberg, and B.C. Wilson, *Techniques for delivery and monitoring of TOOKAD (WST09)-mediated photodynamic therapy of the prostate: Clinical experience and*

*practicalities.* Journal of Photochemistry and Photobiology B: Biology, 2005. **79**: p. 211-222.

21. Zhu, T., A. Dimofte, J. Finlay, D. Stripp, T. Busch, J. Miles, R. Whitting, S.B. Malowicz, Z. Tochner, E. Glatstein, and S.M. Hahn, *Optical properties of human prostate at 732 nm measured in vivo during motexafin lutetium-mediated photodynamic therapy.* Photochemistry and Photobiology, 2005. **81**: p. 96-105.
22. Zhu, T., J. Li, J. Finay, A. Dimofte, D. Stripp, B. Malkowicz, and S. Hahn, *In-vivo light dosimetry of interstitial PDT of human prostate.* Proceedings SPIE, 2006. **6139**.
23. Zhu, T.C. and J. Finlay, *Prostate PDT dosimetry.* Photodiagnosis and Photodynamic Therapy, 2006. **3**: p. 234-246.
24. Zhu, T.C., J.C. Finlay, and S.M. Hahn, *Determination of the distribution of light, optical properties, drug concentration, and tissue oxygenation in-vivo human prostate during motexafin luteium-mediated photodynamic therapy.* Journals of Photochemistry and Photobiology B: Biology, 2005. **79**(3): p. 231-241.
25. Sunar, U., D. Rohrbach, N. Rigual, E. Tracy, K.R. Keymel, M.T. Cooper, H. Baumann, and B.H. Henderson, *Monitoring photobleaching and hemodynamic responses to HPPH-mediated photodynamic therapy of head and neck cancer: a case report.* Optics Express, 2010. **18**(14): p. 14969-14978.
26. Johansson, A., T. Johansson, M. Thompson, N. Bendsoe, K. Svanberg, S. Svanberg, and S. Andersson-Engels, *In vivo measurement of parameters of dosimetric importance during interstitial photodynamic therapy of thick skin tumors.* Journal of Biomedical Optics, 2006. **11**(3): p. 030429-1-030429-10.

27. Liu, B., T. Farrell, and M.J. Patterson, *Comparison of noninvasive photodynamic therapy dosimetry methods using a dynamic model of ALA-PDT of human skin.* Physics in Medicine and Biology, 2012. **57**(3): p. 825.

28. Marchesini, R., A. Bono, and M. Carrara, *In vivo characterization of melanin in melanocytic lesions: spectroscopic study on 1671 pigmented skin lesions.* Journal of Biomedical Optics, 2009. **14**(014027).

29. Marchesini, R., C. Clemente, E. Pignoli, and M. Brambilla, *Optical properties of in vitro epidermis and their possible relationship with optical properties of in vivo skin.* Journal of Photochemistry and Photobiology, 1992. **16**(2): p. 127-140.

30. Meinhardt, R., A. Anders, U. Heinrich, and H. Tronnier, *Effect of ultraviolet adaptation on the ultraviolet absorption spectra of human skin in vivo.* Photodermotology, Photoimmunology, and Photobiology, 2008. **24**(2): p. 76.

31. Zonios, G., A. Dimou, I. Bassukas, D. Galaris, A. Tsolakidis, and E. Kaxiras, *Melanin absorption spectroscopy: new method for noninvasive skin investigation and melanoma detection.* Journal of Biomedical Optics, 2008. **13**(1): p. 014017.

32. Stringer, M.R., C.J. Kelty, R. Ackroyd, and S.B. Brown, *Light dosimetry measurements during ALA-PDT of Barrett's oesophagus.* Photodiagnosis and Photodynamic Therapy, 2006. **3**: p. 19-26.

33. Allison, R.R., H.C. Mota, and C.H. Sibata, *Clinical PD/PDT in North America: An historical review.* Photodiagnosis and Photodynamic Therapy, 2004. **1**(4): p. 263-277.

34. Friedberg, J. and K. Cengel, *Pleural malignancies.* Semin Radiat Oncol., 2010. **20**: p. 208-214.

35. Wilson, B., M. Patterson, and L. Lilge, *Implicit and Explicit Dosimetry in Photodynamic Therapy: A New Paradgm* Lasers in Medicine and Science, 1997. **12**: p. 182-99.

36. Allison, R.R., G. Downie, R. Cuenca, X.-H. Hu, C.J. Childs, and C.H. Sibata, *Photosensitizers on Clinical PDT.* Photodiagnosis and Photodynamic Therapy, 2004. **1**: p. 27-42.

37. Agostini, P., K. Berg, K.A. Cengel, T.H. Foster, A.W. Girotti, S.O. Gollnick, S.M. Hahn, M.M. Hamblin, A. Juzeniene, D. Kessel, M. Korbeli, J. Moan, P. Mroz, D. Nowis, J. Piette, B.C. Wilson, and J. Golab, *Photodynamic Therapy of Cancer: An Update.* CA: A Cancer Journal for Clinicians, 2011. **61**: p. 250-281.

38. Hahn, S., R. Smith, and J. Friedberg, *Photodynamic Therapy for Mesothelioma.* Current Treatment Options in Oncology, 2001. **2**: p. 375-383.

39. Jett, J. and M. Aubry, *Malignant Pleural Mesothelioma.*, in *Clinical Respiratory Medicine*, R.K. Albert, S.G. Spiro, and J.R. Jett, Editors. 2004, Elsevier Health Sciences.

40. Pass, H.I., B.K. Temeck, K. Kranda, G. Thomas, A. Russo, P. Smith, W. Friauf, and S.M. Steinber, *Phase III Randomized Trial of Surgery With or Without Intraoperative Photodynamic Therapy and Postoperative Immunochemotherapy for Malignant Pleural Mesothelioma.* Annals of Surgical Oncology, 1997. **4**(8): p. 628-633.

41. Friedberg, J., *Photodynamic Therapy as an innovative treatment for malignant pleural mesothelioma.* Thoracic and Cardiovacular Surgery, 2009. **21**: p. 177-187.

42. Zhu, T.C., X. Liang, C. Chang, J. Sandell, J. Finlay, A. Dimofte, C. Rodriguez, K. Cengel, J. Friedberg, E. Glatstein, and S. Hahn, *An IR navigation system for real-time treatment guidance of pleural PDT.* SPIE Proc., 2011: p. 78860L.

43. Jacques, S. and W. LH, *Monte Carlo Modeling of Light Transport in Tissues*, in *Optical-thermal response of laser irradiated tissues*, A. Welch and M. van Gemert, Editors. 1995, Plenum Press: New York.

44. Jacques, S. and B. Pogue, *Tutorial on diffuse light transport.* Journal of Biomedical Optics, 2008. **13**(4).

45. Star, W.M., *Light dosimetry in vivo.* Physics in Medicine and Biology, 1997. **42**: p. 763-787.

46. Johansson, A., *Spectroscopic Techniques for Photodynamic Therapy Dosimetry*, in *Thesis*2007, Lund University: Lund. p. 224.

47. Wang, H.W., J. Finay, L.K. Lee, T. Zhu, M. Putt, E. Glatsein, C. Koch, S. Evans, S. Hahn, T. Busch, and A. Yodh, *Quantitative comparison of tissue oxygen and motexafin lutetium uptake by ex-vivo and noninvasive in-vivo techniques in patients with intraperitoneal carcinomatosis,.* Journal of Biomedical Optics, 2007. **12**(3): p. 1-11.

48. Wang, K.K.-H., J. Finlay, T.M. Busch, S. Hahn, and T.C. Zhu, *Explicit dosimetry for photodynamic therapy: macroscopic*

*singlet oxygen modeling.* Journal of Biophotonics, 2010. **3**(5-6): p. 304-318.

49. Allison, R.R., K. Moghissi, G. Downie, and K. Dixon, *Photodynamic therapy (PDT) for Lung Cancer.* Photodiagnosis and Photodynamic Therapy, 2011. **8**: p. 231-239.

50. Castano, A.P., P. Mroz, and M.M. Hamblin, *Photodynamic therapy and anti-tumour immunity.* Nature Reviews Cancer, 2006. **6**: p. 535-545.

51. Jarvi, M.T., M.J. Patterson, and B.C. Wilson, *Insights into Photodynamic Therapy Dosimetry: Simultaneous Singlet Oxygen Luminescence and Photosensitizer Photobleaching Measurements.* Biophysical Journal, 2012. **102**: p. 661-671.

52. McIlroy, B.W., T.S. Mann, J. Dysart, and B.C. Wilson, *The effects of oxygenation and photosensitizer substrate binding on the use of fluorescence photobleaching as a dose metric for photodynamic therapy.* Vibrational Spectroscopy, 2002. **28**(25-35).

53. Georgakoudi, I. and T.H. Foster, *Singlet oxygen- versus nonsinglet oxygen-mediated mechanisms of sensitizer photobleaching and their effects on photodynamic dosimetry.* Photochemistry and Photobiology, 1998. **67**: p. 612-625.

54. Dougherty, T.J., D.J. Gomer, B.W. Henderson, G. Jori, D. Kessel, M. Korbelik, J. Moan, and Q. Peng, *Photodynamic therapy.* J. Natl. Cancer Inst., 1998. **90**(12): p. 889-905.

55. Amelink, A., A. van der Ploeg van der Heuvel, W.J. de Wolf, D.J. Robinson, and H.J.C.M. Sterenborg, *Monitoring PDT by means of superficial reflectance spectroscopy.* Journal of Photochemistry and Photobiology B, 2005. **79**: p. 243-51.

56. Mang, T.S., *Dosimetric Concepts for PDT.* Photodiagnosis and Photodynamic Therapy, 2008. **5**: p. 217-223.

57. Cottrell, W.J., A. Oseroff, and T.H. Foster, *Portable instrument that integrates irradiation with fluorescence and reflectance spectroscopies during clinical photodynamic therapy of cutaneous disease.* Review of Scientific Instruments, 2006. **77**(6): p. 064302 - 064302-8.

58. Cottrell, W.J., A.D. Paquette, K.R. Keymel, T.H. Foster, and A. Oseroff, *Irradiance-Dependent Photobleaching and Pain in δ-Aminolevulinic Acid-Photodynamic Therapy of Superficial Basal Cell Carcinomas.* Clinical Cancer Research, 2008. **14**.

59. Svensson, T., *Pharmaceutical and Biomedical Applications of Spectroscopy in The Photon Migration Regime*, in *Physics*2008, Lund University: Lund. p. 319.

60. Keinle, A. and M. Patterson, *Improved solutions of the steady state and the time-resolved diffusion equations for reflectance from a semi-infinite turbid medium.* Journal of the Optical Society of America, 1997. **14**(1): p. 246-254.

61. Liu, H., D.A. Boas, Y. Zhange, A. Yodh, and B. Chance, *Determination of optical properties and blood oxygenation in tissue using continuous NIR light* Physics in Medicine and Biology, 1995. **40**(11): p. 1983-1993.

62. Yu, G., T. Durduran, D. Furuya, J. Greenberg, and A. Yodh, *Frequency-Domain Multiplexing System for in vivo Diffuse Light Measurements of Rapid Cerebral Hemodynamics.* Applied Optics, 2003. **42**(16): p. 2931-2939.

63. Patterson, M., *Principles and Applications of Frequency Domain Measurements of Light Propagation*, in *Optical-Thermal Response of Laser-Irradiated Tissue*, A. Welch and M. Van Gemert, Editors. 1995, Plenum Press: New York.

64. Pogue, B. and M. Patterson, *Frequency-domain optical absorption spectroscopy of finite tissue volumes using diffusion theory* Physics in Medicine and Biology, 1994. **39**(7): p. 1157-1180.

65. Torricelli, A., P. Taroni, E. Giambattistelli, and R. Cubeddu, *In vivo optical characterization of human tissues from 610 nm to 1010 nm by time-resolved reflectance spectroscopy.* Physics in Medicine and Biology, 2001. **46**: p. 2227-2237.

66. Farrell, T., M. Patterson, and B. Wilson, *A diffusion theory model of spatially resolved, steady-state diffuse reflectance for the noninvasive determination of tissue optical properties in vivo.* Medical Physics, 1992. **19**(4): p. 879-888.

67. Cubeddu, R., A. Pifferi, P. Taroni, A. Torricelli, and G. Valentini, *Noninvasive absorption and scattering spectroscopy of bulk diffusive media: An application to the optical characterization of human breast.* Applied Physics Letters, 1999. **74**(6): p. 874-876.

68. Hull, E. and T. Foster, *Steady-State reflectance spectroscopy in the P3 approximation.* Journal of the Optical Society of America, 2001. **18**: p. 584-599.

69. Star, W., *The relationship between integrating sphere and diffusion theory calculations of fluence rate at the wall of a spherical cavity.* Physics in Medicine and Biology, 1995. **40**: p. 1-8.

70. Wang, H.W., T. Zhu, M. Putt, M. Solenenko, J. Mets, A. Dimofte, J. Miles, D. Fraker, E. Glatsein, S. Hahn, and A. Yodh, *Broadband reflectance measurements of light penetration, blood oxygenation, hemoglobin concentration, and drug concentration in human intraperitoneal tissues before and after photodynamic therapy.* Journal of Biomedical Optics, 2005. **10**(1): p. 0140041-01400413.

71. Ishimaru, A., *Wave propagation and scattering in random media*1997, New York: IEEE Press.

72. Henyey, L.G. and J.L. Greenstein, *Diffusion Radiation in the Galaxy.* Astrophysical Journal, 1941. **93**: p. 70-83.

73. Welch, A., M.J.C. Van Gemert, and H. Kogelnik, *Optical Thermal Response of Laser-Irradiated Tissue*. Lasers, Photonics, and Electro-Optics1995, New York: Plenum Press.

74. Prahl, S.A., A. Welch, and v.G. J., *The Adding-Doubling Method*, in *Optical-Thermal Response of Laser-Irradiated Tissue*, H. Kogelnik, Editor 1995, Plenum Press: New York.

75. Dunderstadt, J.J. and L.J. Hamilton, *Nuclear Reactor Analysis*1976, New York: Wiley.

76. Keijzer, M., W.M. Star, and P.R. Storchi, *Optical Diffusion in Layered Media.* Appl. Optics, 1988. **27**: p. 1820-1824.

77. Groenhuis, R., H. Ferwerda, and J. Ten Bosch, *Scattering and absorption of turbid materials determined from reflection measurements. 1: Theory.* Applied Optics, 1983. **22**(16): p. 2452.

78. Egan, W.G. and T.W. HIlgeman, *Optical properties of inhomogeneous materials*1979, New York: Academic.

79. Haskell, R., L. Svaasand, T.T. Tsay, T.C. Feng, M. McAdams, and B. Tromberg, *Boundary Conditions for the diffusion equation in radiative transfer.* Journal of the Optical Society of America, 1994. **11**(10): p. 2727-2741.

80. Finlay, J.C. and T.H. Foster, *Hemoglobin oxygen saturations in phantoms and in vivo from measurements of steady-state diffuse reflectance at a single, short source-detector separation.* Med Phys, 2004. **31**(7): p. 1949-1959.

81. Zhu, T., J. Finlay, A. Dimofte, and S. Hahn, *Light Dosimetry at Tissue Surfaces for Oblique Incident Circular Fields.* Proceedings SPIE, 2004. **5315**: p. 113-124.

82. Patterson, M.J., S.J. Madsen, J.D. Moulton, and B.C. Wilson, *Diffusion representation of photon migration in tissue.* IEEE Microwave Theory and Techniques Symposium Digest, 1991. **BB-1**: p. 905-908.

83. Finlay, J.C., *Reflectance and Fluorescence Spectroscopies in Photodynamic Therapy*, in *Physics and Astronomy*2003, University of Rochester: Rochester. p. 368.

84. Jacques, S., R. Joseph, and G. Gofstein, *How photobleaching effects dosimetery and fluorescence monitoring of PDT in turbid media.* SPIE Proc., 1993. **1881**: p. 168-179.

85. Mourant, J.R., J. Freyer, A. Hielscher, A. Eick, D. Shen, and T. Johnson, *Mechanisms of light scattering from biological cells relevant to non-invasive optical tissue diagnostics.* Applied Optics, 1998. **37**(16): p. 3586-3593.

86. Mourant, J.R., T. Fuselier, J. Boyer, T. Johnson, and I.J. Bigio, *Predictions and measurements of scattering and absorption over broad wavelength ranges in tissue phantoms.* Applied Optics, 1997. **36**(4): p. 948-957.

87. Mourant, J.R., M. Canpolat, C. Brocker, O. Esponda-Ramos, T. Johnson, A. Matanock, K. Stetter, and J. Freyer, *Light scattering from cells: the contribution of the nucleus and the effects of proliferative status.* Journal of Biomedical Optics, 2000. **5**(2): p. 131-137.

88. van Veen, R., H. Sterenborg, A. Marinelli, and M. Menke-Pluymers, *Intraoperatively assessed optical properties of malignant and healthy breast tissue used to determine the optimum wavelength of contrast for optical mammography.* Journal of Biomedical Optics, 2004. **9**(6): p. 1129-1136.

89. Spinelli, L., A. Torricelli, A. Pifferi, P. Taroni, G. Danesini, and R. Cubeddu, *Bulk optical properties and tissue components in the female breast from multiwavelength time-resolved optical mammography.* Journal of Biomedical Optics, 2004. **9**(6): p. 1137-1142.

90. Mo, W., T. Chang, L. Chen, and N. Chen, *Quantitative characterization of optical and physiological parameters in normal breasts using*

*time-resolved spectroscopy: in vivo results of 19 Singapore women.* Journal of Biomedical Optics, 2009. **14**(6): p. 064004.

91. Pifferi, A., J. Swartling, E. Chikoidaze, A. Torricelli, P. Taroni, A. Bassi, S. Andersson-Engels, and R. Cubeddu, *Spectroscopic time-resolved diffuse reflectance and*

*transmittance measurements of the female breast at different interfiber distances.* Journal of Biomedical Optics, 2004. **9**(6): p. 1143-51.

92. Nair, M., N. Ghosh, N. Raju, and A. Pradan, *Determination of optical parameters of human breast tissue from spatially resolved fluorescence: a diffusion theory model.* Applied Optics, 2002. **41**(9): p. 4024-4035.

93. Rajaram, R., D. Kovacic, M. Migden, J. Reichenberg, T. Nguyen, and J. Tunnell, *In Vivo Determination of Opitcal Properties and fluorophore characteristics of non-melanoma skin cancer.* SPIE Proceedings, 2009. **7161**: p. 716102.

94. Fantini, S., S.A. Walker, M.A. Franceschini, M. Kaschke, P.M. Schlag, and K.T. Moesta, *Assessment of the size, position, and optical properties of breast tumors in vivo by noninvasive optical methods.* Applied Optics, 1998. **37**(10): p. 1982-9.

95. Matcher, S., M. Cope, and D. Delpy, *In vivo measurements of the wavelength dependence of tissue-scattering coefficients between 760 and 900 nm measured with time-resolved spectroscopy.* Applied Optics, 1997. **36**(1): p. 386-396.

96. Taroni, P., A. Pifferi, A. Torricelli, D. Comelli, and R. Cubeddu, *In vivo absorption and scattering spectroscopy of biological tissues.* Photochemistry and Photobiology, 2003. **2**: p. 124-129.

97. Zhu, T., S.M. Hahn, A.S. Kapatkin, A. Dimofte, C.E. Rodriguez, T. Vulcan, E. Glatstein, and R.A. Hsi, *In vivo Optical Properties of Normal Canine Prostate at 732 nm Using motexafin lutetium-mediated photodynamic therapy.* Photochemistry and Photobiology, 2003. **77**: p. 81-88.

98. Lee, L., C. Whitehurst, M. Pantelides, and J. Moore, *In situ comparison of 665 nm and 633 nm wavelength light penetration in the human prostate gland.* Photochemistry and Photobiology, 1995. **62**: p. 882-6.

99. Pifferi, A., A. Torricelli, P. Taroni, A. Bassi, E. Chikoidaze, E. Giambattistelli, and R. Cubeddu, *Optical biopsy of bone tissue: a step toward the diagnosis of bone pathologies.* Journal of Biomedical Optics, 2004. **9**(3): p. 474-80.

100. Beck, T., W. Beyer, T. Pongratz, W. Stummer, R. Waidelich, H. Stepp, S. Wagner, and R. Baumgartner, *Clinical Determination of Tissue Optical Properties in vivo by Spatially Resolved Reflectance Measurements.* SPIE Proceedings, 2003. **5138**: p. 96-105.

101. Driver, I., C. Lowdell, and D. Ash, *In vivo measurement of optical interaction coefficients of human tumours at 630 nm.* Physics in Medicine and Biology, 1991. **36**(6): p. 805-13.

102. Wilson, B., P. Muller, and Y. JC, *Instrumentation and light dosimetry for intra-operative photodynamic therapy (PDT) of malignant brain tumours.* Physics in Medicine and Biology, 1986. **31**(2): p. 125-33.

103. Ijichi, S., T. Kusaka, K. Isobe, K. Okubo, K. Kawada, M. Namba, H. Okada, T. Nishida, T. Imai, and S. Itoh, *Developmental Changes of Optical Properties in Neonates Determined by Near-Infrared Time-Resolved Spectroscopy.* Pediatric Research, 2005. **58**(3): p. 568-573.

104. Choi, J., M. Wolf, V. Toronov, U. Wolf, C. Polzonetti, D. Hueber, L. Safanova, R. Gupta, A. Michalos, W. Mantulin, and E. Gratton, *Noninvasive determination of the optical properties of adult brain: near-infrared spectroscopy approach.* Journal of Biomedical Optics, 2004. **9**(1): p. 221-229.

105. Zhao, J., H. Ding, X. Hou, C. Zhou, and B. Chance, *In vivo determination of the optical properties of infant brain using frequency-domain near-infrared spectroscopy.* Journal of Biomedical Optics, 2005. **10**(2): p. 024048.

106. Cerussi, A., N. Shah, D. Hsiang, A. Durkin, J. Butler, and B. Tromberg, *In vivo absorption, scattering, and physiologic properties of 58 malignant breast tumors determined by broadband diffuse optical spectroscopy.* Journal of Biomedical Optics, 2006. **11**(4): p. 044005.

107. Durduran, T., R. Choe, J. Culver, L. Zubkov, M. Holboke, J. Gaimmarco, B. Chance, and A. Yodh, *Bulk optical properties of healthy female breast tissue.* Physics in Medicine and Biology, 2002. **47**: p. 2847-2861.

108. Suzuki, K., Y. Yamashita, K. Ohta, M. Kaneko, M. Yoshida, and B. Chance, *Quantitative measurement of optical parameters in normal breast using time-resolved spectroscopy: in vivo results of 30 Japanese women.* Journal of Biomedical Optics, 1996. **1**(3): p. 330.

109. Heusmann, H., J. Kolzer, and G. Mittick, *Characterization of female breast tissue in vivo by time resolved and spectroscopic measurements in nread infrared spectroscopy.* Journal of Biomedical Optics, 1996. **1**(4): p. 425.

110. Shah, N., A. Cerussi, D. Jakubowski, D. Hsiang, J. Butler, and B. Tromberg, *Spatial variations in optical and physiological properties of healthy breast tissue.* Journal of Biomedical Optics, 2004. **9**(3): p. 534-40.

111. Wang, H.W., T. Zhu, M. Solenenko, S. Hahn, J. Metz, A. Dimofte, J. Mile, and A. Yodh, *In-vivo measurements of penetration depth, oxygenation, and drug concentration using broadband absorption spectroscopy in human tissues before and after photodynamic therapy* Proc. SPIE, 2003. **68**: p. 857-873.

112. Dimofte, A., T. Zhu, J. Finay, M. Cullighan, C. Edmonds, J. Friedberg, K. Cengel, and S. Hahn, *In-vivo light dosimetry for HPPH-mediated pleural PDT.* Proceedings SPIE, 2010. **7551**: p. 755115.

113. Dimofte, A., T. Zhu, J. Finlay, M. Culligan, C. Edmonds, J. Friedberg, K. Cengel, and S. Hahn, *In vivo light dosimetry for pleural PDT.* Proceedings SPIE, 2009. **7164**.

114. Lee, L.K., C. Whitehurst, M.K. Pantelides, and J.V. Moore, *An interstitial light assembly for photodynamic therapy in prostatic carcinoma.* BJU International, 1999. **84**: p. 821-826.

115. Levy, D., J. Schwartz, M. Ostermeyer, S. Jacques, and A. von Eschenbach, *Transurethral In Vivo Optical Properties.* SPIE Proceedings, 1996. **2671**: p. 329-34.

116. Larsson, M., H. Nilsson, and T. Stromberg, *In vivo determination of local skin optical properties and photon path length by use of spatially resolved diffuse reflectance with applications in laser Doppler flowmetry.* Applied Optics, 2003. **1**: p. 124-134.

117. Zonios, G. and A. Dimou, *Melanin Optical Properties Provide Evidence for Chemical and Structural Disorder In Vivo.* Optics Express, 2008. **16**(11): p. 8263.

118. Sun, P., R. Yang, F. Xie, J. Ding, F. Zhang, and X. Cao, *A method for determining optical properties of human tissues by measuring diffuse reflectance with CCD* SPIE Proceedings, 2010. **7845**: p. 784522.

119. Nichols, M.G., E.L. Hull, and T.H. Foster, *Design and testing of a white-light, steady-state diffuse reflectance spectrometer for determination of optical properties of highly scattering systems.* Appl. Optics, 1997. **36**(1): p. 93-104.

120. Lagarias, J.C., J.A. Reeds, M.H. Wright, and P.E. Wright, *"Convergence Properties of the Nelder-Mead Simplex Method in Low Dimensions,".* SIAM Journal of Optimization, 1998. **9**(1): p. 112-47.

121. Hull, E., M.G. Nichols, and T. Foster, *Quantitative broadband near infrared spectroscopy of tissue-simulating phantoms containing erythrocytes.* Physics in Medicine and Biology, 1998. **43**: p. 3381-3404.

122. Prahl, S.A. *Optical absorption of hemoglobin*. 2002

123. Finlay, J.C., D. Conover, E.L. Hull, and T.H. Foster, *Porphyrin Bleaching and PDT-induced Spectral Changes are Irradiance Dependent in ALA-sensitized Normal Rat Skin In Vivo.* Photochemistry and Photobiology, 2001. **73**(1): p. 54-63.

124. Wu, J., M.S. Feld, and R.P. Rava, *Analytical model for extracting intrinsic fluorescence in turbid media.* Appl. Optics, 1993. **32**: p. 3585–3595.

125. Press, W.H., S.A. Teukolsky, W.T. Vetterling, and B.P. Flannery, *Numerical Recipes in C: The Art of Scientific Computing*1992, New York: Cambridge University Press.

126. Hahn, S.M., D.L. Fraker, R. Mick, J. Metz, T.M. Busch, D. Smith, T. Zhu, C. Rodriguez, A. Dimofte, F. Spitz, M. Putt, S.C. Rubin, C. Menon, H.-W. Wang, D. Shin, A. Yodh, and E. Glatstein, *A Phase II Trial of Intraperitoneal Photodynamic Therapy for Patients with Peritoneal Carcinomatosis and Sarcomatosis.* Clinical Cancer Research, 2006. **12**(8): p. 2517-2525.

127. Lodeman, P., G. Schorer, and B.M. Frey, *Wrong molar hemoglobin reference values—a longstanding error that should be corrected.* Ann. Hematol, 2010. **89**: p. 209.

128. Dimofte, A., A.V. Sharikova, J.L. Meo, C.B. Simone II, J.S. Friedberg, and T.C. Zhu, *Light dosimetry and dose verification for pleural PDT.* SPIE Proc., 2013. **8568**: p. 85680V-1-85680V-12.

129. Beutler, E. and J. Waalen, *The definition of anemia: what is the lower limit of the normal blood hemoglobin concentration?* Bllod, 2006. **107**: p. 1747–1750.

130. Baas, P., L. Murrer, F. Zoetmulder, F. Stewart, H. Ris, N. van Zandwijk, J. Peterse, and E. Rutgers, *Photodynamic therapy as adjuvant therapy in surgically treated pleural malignancies.* Br J Cancer, 1997. **76**(6): p. 819-826.

131. Solonenko, M., T. Zhu, and T. Vulcan, *Commissioning of the isotropic light dosimetry system for photodynamic therapy.* Med Phys, 1999. **26**: p. 1124.

132. Wang, L., S. Jacques, and L. Zheng, *MCML-Monte Carlo modeling of light transport in multi-layered tissues.* Computer Methods and Programs in Biomedicine, 1995. **47**: p. 131-146.

133. Jacques, S., *Light Distributions from Point, Line and Plane Sources for Photochemical Reactions and Fluorescence in Turbid Biological Tissues.* Photochemistry and Photobiology, 1998. **67**(1): p. 23-52.

134. Boas, D.A., H. Liu, M. O'leary, B. Chance, and A. Yodh, *Photon Migration within the P3 approximation.* Proceedings SPIE, 1995. **2389**: p. 240-247.

135. Dickey, D.J., R.B. Moore, D.C. Rayner, and J. Tulip, *Light dosimetry using the P3 approximation.* Physics in Medicine and Biology, 2001. **46**(9): p. 2359-2370.

136. Zhu, T., A. Dimofte, S. Hahn, and R. Lustig, *Light Dosimetry at Tissue Surfaces for Small Circular Fields.* Proceedings SPIE, 2003. **4952**: p. 56.

137. Cheong, W.F., S.A. Prahl, and A.J. Welch, *A Review of Optical Properties of Biological Tissues.* IEEE Journal of Quantum Electronics, 1990. **26**(12): p. 2166-2185.

138. Marijnissen, J. and W.M. Star, *Calibration of isotropic light dosimetry probes based on scattering bulbs in clear media.* Physics in Medicine and Biology, 1996. **41**: p. 1191–1208.

139. Attix, F., *Introduction to Radiological Physics and Radiation Dosimetr*1983, New York: John Wiley and Sons.

140. Boas, D.A., J.A. Culver, J.J. Stott, and A.K. Dunn, *Three dimensional Monte Carlo code for photon migration through complex heterogeneous media including the adult human head.* Optics Express, 2002. **10**(3): p. 159-170.

141. van Staveren, H.J., C.J.M. Moes, J. van Marle, S.A. Prahl, and M.J.C. van Gamert, *"Light scattering in Intralipid-10 in the wavelength range of 400-1100 n.* Appl. Optics, 1991. **30**: p. 4507-4515.

142. Korb, W., D. Engel, R. Boesecke, G. Eggers, B. Kotrikova, R. Marmulla, J. Raczkowsky, H. Worn, J. Muhling, and S. Hassfeld, *Development and first patient trial of a 364 surgical robot for complex trajectory milling.* Comput Aided Surg, 2003. **8**: p. 247-56.

143. Kalfas, I.H., *Image-guided spinal navigation: application to spinal metastases.* Neurosurg Focus, 2001. **11**: p. e5.

144. *Integrating Sphere Design and Applications Technical Information*2007: SphereOptics. 4.

145. Zhu, T.C., X. Liang, C. Chang, J. Sandell, J. Finlay, A. Dimofte, C. Rodriguez, K. Cengel, J. Friedberg, E. Glatstein, and S. Hahn, *An IR navigation system for real-time treatment guidance of Pleural PDT* Proc. SPIE, 2010. **7886**: p. 78860L.

146. Zhu, T.C., M.M. Kim, X. Liang, B. Liu, J.L. Meo, J.C. Finlay, A. Dimofte, C. Rodriguez, C.B. Simone II, K. Cengel, and J.S. Friedberg, *Real-time treatment feedback guidance of Pleural PDT.* SPIE Proc., 2013. **8568**: p. 85680O-1-85680O-6.

147. Star, W.M., *Comparing P3 approximation with diffusion theory and with Monte Carlo calculations of light propagation in slab geometry.* SPIE Inst. Ser., 1989. **IS5**(146-154).